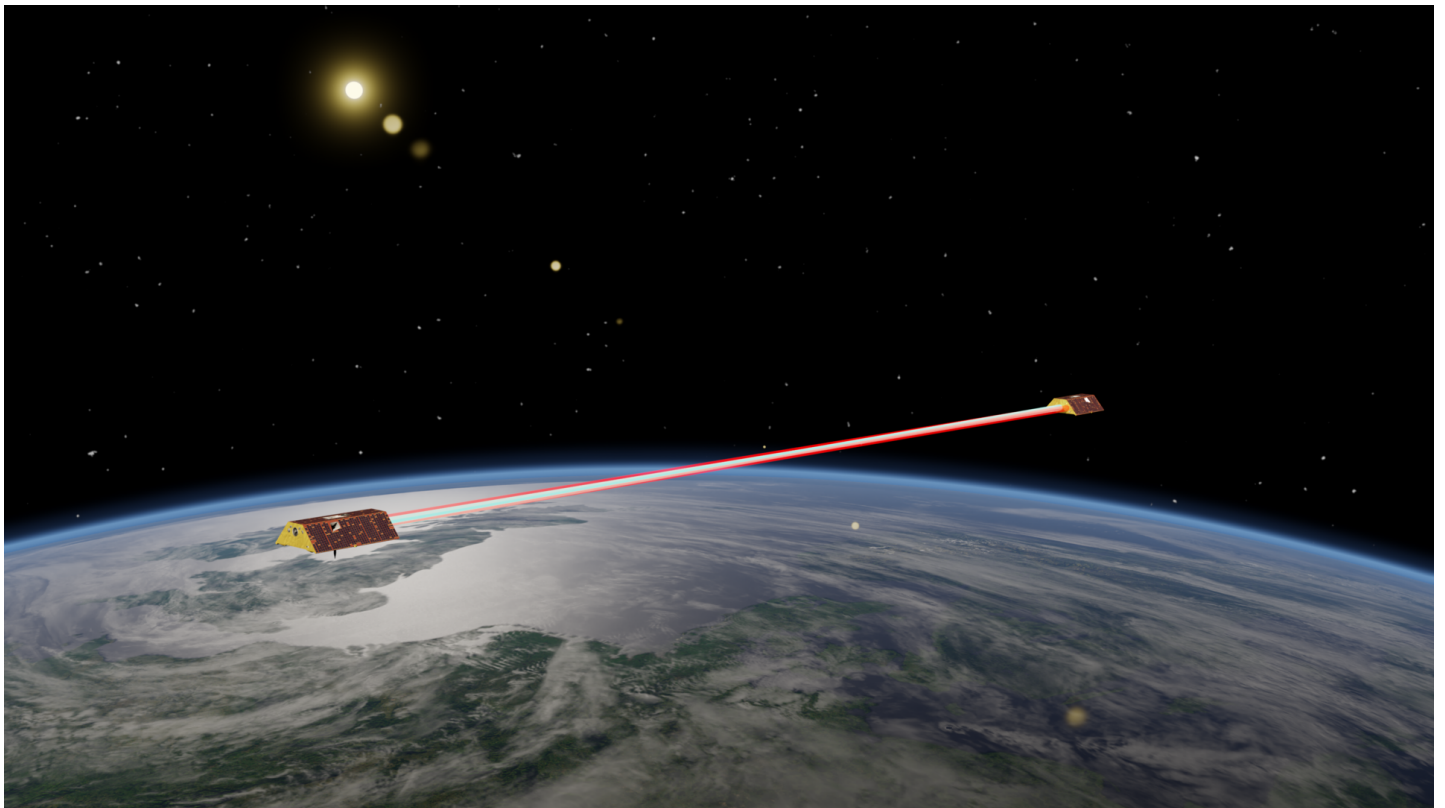
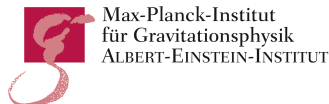


In-Depth Characterization of the First Inter-Satellite Laser Ranging Interferometer on GRACE Follow-On



Dissertation
of
Malte Misfeldt
2023



MAX-PLANCK-GESELLSCHAFT

Cover Image: Artistic view of the GRACE-FO satellites by Malte Misfeldt
Earth Textures: NASA – The Blue Marble
Satellite Model: NASA – VTAD

**In-Depth Characterization of the First
Inter-Satellite Laser Ranging Interferometer
on GRACE Follow-On**

Von der QUEST-Leibniz-Forschungsschule
der Gottfried Wilhelm Leibniz Universität Hannover
zur Erlangung des Grades

DOKTOR DER NATURWISSENSCHAFTEN
– Dr. rer. nat. –

genehmigte Dissertation
von

M. Sc.
Malte Matthias Misfeldt

Referent	Apl. Prof. Dr. Gerhard Heinzl Institut für Gravitationsphysik, Leibniz Universität Hannover
Korreferent	Prof. Dr. Kirk McKenzie Centre for Gravitational Astrophysics, Australian National University
Korreferent	Univ.-Prof. Dr.-Ing. Torsten Mayer-Gürr Institut für Geodäsie, Technische Universität Graz
Tag der Promotion	27.10.2023

Abstract

The GRACE Follow-On (GRACE-FO) satellite mission was launched in May 2018. It continues the time series of monthly estimates of the Earth's gravity field, started by its predecessor, the Gravity Recovery And Climate Experiment (GRACE). Scientists all around the globe use these monthly snapshots to study hydrological processes and the climate crisis. The GRACE-FO twin satellites orbit the Earth approximately every 90 minutes in a polar orbit, with an along-track distance of about 220 km. The Earth's gravity information is encoded in subtle distance variations between the two, which are measured by the conventional Microwave Instrument (MWI), and in GRACE-FO also by the novel Laser Ranging Interferometer (LRI). The LRI is an optical interferometer split into two units, one on each spacecraft. Its sensitivity of $200 \text{ pm}/\sqrt{\text{Hz}}$ at 5 Hz surpasses the MWI by several orders of magnitude. Further, it has proven very reliable, with very few instrument-related outages.

This dissertation is concerned with data analysis of the various telemetry channels of the LRI to deepen the understanding of the instrument. It begins with explaining the LRI instrument and its subunits. New formulas for converting the measured optical phase to the inter-spacecraft range in meter are presented, considering the effect of a time-varying laser frequency. Furthermore, the dominant error sources in the data processing, namely the determination of the absolute value of the laser frequency and a time-tag error of the measurements, are modeled.

Lasers form the heart of the LRI, and their reliability and stability are closely monitored. The two LRI lasers show no sign of performance degradation after five years in orbit, but a small bi-modal behavior of some laser telemetry channels was observed. Further, short periods with increased laser frequency noise are investigated.

The absolute optical frequency of the LRI lasers acts as the conversion factor between the measured phase variations and the desired ranging signal. It is not measured directly on board and must be inferred in post-processing on ground. Therefore, a large part of this work is taken by developing different models for the absolute optical frequency of the LRI lasers, including the assessment of thermally induced tone errors.

The triple mirror assembly is a key component in the LRI, and the perpendicular alignment of its three mirrors ensures the parallelity of the two laser beams traveling between the spacecraft. Hence, their alignment is closely monitored in orbit by analyzing particular diagnostic scans. These scans can further be used to assess various properties of the beam, like the Gaussian divergence angles, the heterodyne efficiency variations, and the effects of a particular kind of tilt-to-length coupling.

In the end, single event upsets within the ranging data are investigated, which are short-lived disturbances of the ranging measurement due to charged particles that interact with the onboard electronics.

Keywords: Interferometer, GRACE Follow-On, Data Analysis, Laser Frequency Determination, Tone Errors

Kurzzusammenfassung

Die Satellitenmission *GRACE Follow-On (GRACE-FO)* wurde im Mai 2018 gestartet. Sie setzt die Zeitreihe monatlicher Schätzungen des Schwerefelds der Erde seines Vorgänger, dem *Gravity Recovery And Climate Experiment (GRACE)*, fort. Wissenschaftler rund um den Globus nutzen diese monatlichen Momentaufnahmen, um hydrologische Prozesse und die Klimakrise zu untersuchen. Die *GRACE-FO* Zwillingssatelliten umkreisen die Erde etwa alle 90 Minuten auf einer polaren Umlaufbahn mit einem Abstand von etwa 220 km. Die Informationen über die Schwerkraft der Erde sind in den feinen Abstandsschwankungen zwischen den beiden kodiert, die mit dem herkömmlichen *Microwave Instrument (MWI)* und in *GRACE-FO* auch mit dem neuartigen *Laser Ranging Interferometer (LRI)* gemessen werden. Das LRI ist ein optisches Interferometer, das in zwei Einheiten aufgeteilt ist, eine auf jedem Satelliten. Seine Empfindlichkeit von $200 \text{ pm}/\sqrt{\text{Hz}}$ bei 5 Hz übertrifft die des MWI deutlich. Darüber hinaus hat es sich als sehr zuverlässig erwiesen, mit wenigen gerätebedingten Ausfällen.

Diese Dissertation befasst sich mit der Datenanalyse der verschiedenen Telemetriekanäle des LRI, um das Verständnis für das Instrument zu vertiefen. Sie beginnt mit einer Erläuterung des LRI-Instruments und seinen Teileinheiten. Es werden neue Formeln für die Umrechnung der gemessenen optischen Phase in die Entfernung zwischen den Satelliten in Metern vorgestellt, wobei die Auswirkungen einer zeitlich veränderlichen Laserfrequenz berücksichtigt werden. Darüber hinaus werden die dominierenden Fehlerquellen bei der Datenverarbeitung modelliert, nämlich die Bestimmung des Absolutwerts der Laserfrequenz und ein Zeitstempelfehler der Messungen.

Laser bilden das Herzstück des LRI, und ihre Zuverlässigkeit und Stabilität werden genau überwacht. Die beiden LRI-Laser zeigen nach fünf Jahren in der Umlaufbahn keine Anzeichen einer Leistungsver schlechterung, aber es wurde ein geringfügiges bimodales Verhalten einiger Lasertelemetriekanäle beobachtet. Außerdem werden kurze Perioden mit erhöhtem Laserfrequenzrauschen untersucht.

Die absolute optische Frequenz der LRI-Laser dient als Umrechnungsfaktor zwischen den gemessenen Phasenschwankungen und dem gewünschten Entfernungssignal. Sie wird nicht direkt an Bord gemessen, sondern muss in der Datenverarbeitung am Boden abgeleitet werden. Daher besteht ein großer Teil dieser Arbeit in der Entwicklung verschiedener Modelle für die absolute optische Frequenz der LRI-Laser, einschließlich der Bewertung thermisch bedingter Tonfehler.

Die *triple mirror assembly* ist eine Schlüsselkomponente des LRI, und die rechtwinklige Ausrichtung seiner drei Spiegel gewährleistet die Parallelität der beiden Laserstrahlen, die sich zwischen den Satelliten bewegen. Daher wird ihre Ausrichtung durch die Analyse bestimmter Diagnose-Scans in der Umlaufbahn genau überwacht. Anhand dieser Scans können verschiedene Eigenschaften des Strahls bewertet werden, z. B. die Gaußschen Divergenzwinkel, die Schwankungen der Überlagerungseffizienz und die Auswirkungen eines besonderen Typs der Rotation-zu-Weglängen Kopplung.

Schließlich werden *single event upsets* in den Entfernungsmessungsdaten untersucht, bei denen es sich um kurzlebige Störungen der Entfernungsmessung aufgrund geladener Teilchen handelt, die mit der Bordelektronik wechselwirken.

Schlagnworte: Interferometer, GRACE Follow-On, Datenanalyse, Laserfrequenzbestimmung, Tonfehler

Table of Contents

Abstract	i
Kurzzusammenfassung	iii
Table of Contents	v
List of Figures	ix
List of Tables	xi
List of Acronyms	xiii
1. Introduction	1
1.1. The Changing Earth	1
1.2. Observing Gravity from Space	2
1.3. Beyond Classical Gravity	4
1.4. Thesis Structure and Objectives	5
2. Basics of Interferometry	9
2.1. Electromagnetic Waves in the Paraxial Approximation	9
2.2. Gaussian Beams	10
2.3. The Concepts of Interferometry	13
2.3.1. Phase Readout	14
2.3.2. Coherent and Incoherent Sum	15
2.3.3. Differential Wavefront Sensing (DWS)	15
2.3.4. Carrier-to-Noise Ratio (CNR)	17
2.3.5. Heterodyne Efficiency	18
2.4. Interferometer	20
3. The Laser Ranging Interferometer	21
3.1. Interferometric Intersatellite Laser Ranging	21
3.1.1. LRI Setup: An Overview	21
3.1.2. Reference Frames and Spacecraft Pointing	23
3.1.3. Laser and Cavity	24
3.1.4. Optical Bench Assembly and Electronics	27
3.1.5. Fast Steering Mirror (FSM)	28
3.1.6. Triple Mirror Assembly (TMA)	28
3.1.7. Laser Ranging Processor (LRP)	30
3.1.8. Other GRACE-FO Payloads	31
3.1.9. Mission Phases	33
3.2. In-Flight Sensitivity and Previous Studies	34
3.3. Measurement Noise Modeling	36
3.3.1. Introduction to Least Squares Parameter Estimation	36
3.3.2. Variance-Covariance Matrix and Autocorrelation Function	37

3.3.3. Derivation of LRI Noise Models at High Frequencies	38
3.4. Summary	42
4. The Interferometric Phase Observable	43
4.1. Relativistic Description of the Phase Observable	43
4.2. Relation between the Measured Phase and Biased Range	48
4.3. Scale and Timing Errors in the Instantaneous Biased Range	49
5. Laser Frequency Determination for the GRACE-FO LRI	51
5.1. Cross-Calibration using the MWI	51
5.2. Cavity Frequency Decay	53
5.3. Laser-Telemetry Frequency Model	54
5.3.1. Laser Telemetry Description	54
5.3.2. Ground-Calibration Measurement Campaigns	55
5.3.3. Empirical Refinement with Flight Data	58
5.4. Comparison of the Models	60
5.4.1. The Range Error	61
5.4.2. Global Scale and Timeshift Estimation	63
5.5. Thermal Coupling in KBR-LRI Residuals	64
5.5.1. Coupling Mechanisms: Frequency and Phase Domain	65
5.5.2. Unconstrained Parameter Estimation	65
5.5.3. Enforcing a Coupling of the Cavity	68
5.5.4. Enforcing AC Temperature Components (GF-2 only)	69
5.5.5. Variations of the Tone Error Amplitudes	69
5.5.6. Variations of Scale Factor and Timeshift	70
5.6. Discussion of Alternative Approaches for Future Gravity Missions	70
5.7. Summary	73
6. Experimental Verification of the RLU Frequency Drift	75
6.1. RLU-EM Description and EGSE Construction	75
6.2. Experimental Setup	76
6.3. RLU-EM Calibration	79
6.3.1. Optical Power to Frequency Coupling	79
6.3.2. Temperature to Frequency Coupling	80
6.4. Measurement Campaigns	81
6.5. Discussion and Summary	85
7. Analysis of DWS Scans	87
7.1. DWS Scan Types	87
7.2. Far-Field Beam Properties and TMA Co-Alignment Errors	88
7.2.1. Elliptical Gaussian Beam Model	89
7.2.2. Amplitude Profile Estimation and Discussion of Results	89
7.2.3. Temperature Stability of the TMA Co-Alignment	92
7.3. Local Heterodyne Efficiency	93
7.4. Phase Variations during DWS Scans	98
7.4.1. Beam Pointing-to-Pathlength Coupling: Linear and Quadratic	98
7.4.2. Beam Pointing-to-Pathlength Coupling: Beam Waist Offsets	100
7.5. Summary	104

8. RLU In-Flight Behavior	107
8.1. Time-Variability of the RLU Telemetry Channels	107
8.2. RLU Frequency Variations at High Frequencies	111
8.3. Pump Module Head (PMH) Frequency Noise	114
8.4. Summary	116
9. Disturbances from Radiation: Single Event Upsets	119
9.1. Radiation Environment in a Low-Earth Orbit	119
9.2. Recent and Future Solar Activity	120
9.3. Simulation of SEUs in the LRI Phase Data	120
9.4. Detection of SEUs in the LRI Phase Data	123
9.5. Discussion of the SEU Events	125
9.6. Summary	128
10. Summary and Outlook	129
Appendix	135
A. Wavemeter Calibration	135
B. RLU Calibration Actuator Signals	137
C. Thermal Coupling Coefficients for v51 and v53	139
D. DWS Scan Design Patterns	142
E. DWS Setpoint Wrapping	144
F. Error Propagation for the Phase Front Parameters	145
Bibliography	147
Acknowledgements	155

List of Figures

1.1.	Timeline of gravity missions and laser interferometers in space	3
2.1.	Quantities used to describe a Gaussian beam	10
2.2.	Schematic working principle of a DPLL	14
2.3.	Sketch of a QPD and the DWS principle	16
3.1.	Sketch of the LRI hardware	22
3.2.	Schematic of the light paths and frequencies in the LRI setup	23
3.3.	Sketch of the RLU interior	25
3.4.	ASD of laser frequency variations from the actuator signals	26
3.5.	Photographs of the NPRO laser and the optical cavity	27
3.6.	Concept of the local beam alignment using the FSM	29
3.7.	Photograph of the TMA flight model	30
3.8.	Sketch of the phasemeter processing chain	31
3.9.	Schematic view of the GRACE-FO satellite interior	32
3.10.	ASDs of the LRI measurement and its dominant noise sources	35
3.11.	PSD of the LRI one-way phase at high frequencies	39
3.12.	Autocorrelation functions $R_R(\tau)$ and $R_T(\tau)$	40
3.13.	PSD of a single channel phase combination	42
3.14.	Autocorrelation function of single channel combinations	42
4.1.	Minkowski-Diagram of the LRI Roundtrip Measurement	44
4.2.	Typical ASD of the LRI ranging signal	50
5.1.	Scale Factor ε_{SCF} and exponential fit ε^{Cav}	53
5.2.	Daily Mean/Min/Max values for the <code>lasTRP</code> thermistor	55
5.3.	Laboratory setup for the LRI flight laser frequency calibration	56
5.4.	Regression results for the GF-1 laser	57
5.5.	Regression results for the GF-2 laser	58
5.6.	Laser frequency models over time for both SC	60
5.7.	Thermal Actuator Frequency Variations	61
5.8.	TC fit v52 for both SC	62
5.9.	Thermal correction time series for 2022-Jan-01.	67
5.10.	1/rev and 2/rev tone error amplitudes of the TC models	70
5.11.	Residual scale ε_{SCF} and timeshift ζ of LRI1B-v52	71
6.1.	Photograph of the RLU EGSE during construction	77
6.2.	Photograph of the RLU-EM mounted on the Peltier cooled baseplate	77
6.3.	Screenshot of the RLU EGSE GUI	77
6.4.	Experimental setup for the RLU frequency stability experiment	80
6.5.	RLU-EM calibration: Optical frequency vs. optical power	80
6.6.	Temperature calibration measurement of the RLU-EM	81
6.7.	Example of an RLU-EM frequency calibration measurement	82
6.8.	Frequency drift results after 1.5 years of measurements for the RLU-EM.	84

7.1.	DWS Scan on GF-1 in June 2018 in time-domain	91
7.2.	Amplitude profile of GF-1 in June 2018	91
7.3.	Variations of the triple mirror assembly (TMA) coalignment angles	91
7.4.	TMA TRP temperature variations in June 2019	92
7.5.	Beam pointing offset over time with temperature fit	92
7.6.	Spatial distribution of the heterodyne efficiency on GF-1 and GF-2	94
7.7.	Post-fit residuals of the heterodyne efficiency	96
7.8.	Function for the non-gaussianity of the heterodyne efficiency	97
7.9.	Phase Front Scan in Time Domain	99
7.10.	Two spherical phase fronts, one with a waist offset Δz	102
8.1.	QPD DC Power and RLU telemetry of five years	108
8.2.	QPD DC, DPS, and FSM signals on GF-2	110
8.3.	RLU free-running laser frequency noise estimate based on the telemetry model $\nu_{\text{IL}}^{\text{TM}}$	112
8.4.	Equivalent free-running RLU frequency fluctuations	114
8.5.	PMH scan results	115
9.1.	Sun spot number progression and predictions	121
9.2.	Block diagram of the two FIR filter stages	121
9.3.	Simulated data of an SEU in filter <i>A</i>	123
9.4.	Simulated data of an SEU in filter <i>B</i>	123
9.5.	SEU Event #1: Fit example with low residuals	127
9.6.	SEU Event #3: Fit example with high residuals	127
9.7.	Simulation of two non-simultaneous SEU events	127
9.8.	World map showing the location of the SEU events	127
A.1.	Absolute frequency measurements of different hyperfine lines	135
A.2.	OGSE laser frequency, measured with two wavemeters	136
A.3.	Thermal Coupling calibration of the OGSE laser	136
B.4.	Actuator signals of the on-ground measurements for GF-1	137
B.5.	Actuator signals of the on-ground measurements for GF-2	138
C.6.	TC fit v51 and v53 and for both SC	139
C.7.	Residual scale ε_{SCF} and timeshift ζ of LRI1B-v51 and v53	141
D.8.	DWS Scan Type 1	142
D.9.	DWS Scan Type 2	142
D.10.	DWS Scan Type 3	142
D.11.	DWS Scan Type 4	143
D.12.	DWS Scan Type 5	143
D.13.	DWS Scan Type 6	143
E.14.	Bit Wrapping of the DWS Setpoints	144

List of Tables

2.1.	Electronic readout noise $S_{n,cs}$ and its contributors	18
2.2.	Local beam parameters and maximum heterodyne efficiency	18
2.3.	Polynomial coefficients for the heterodyne efficiency approximation	19
3.1.	TMA Mirror positions and their respective normal vectors	29
3.2.	Parameters for the PSD models S_T^m and S_R^m	38
5.1.	Estimated exponential cavity model ε^{Cav} parameters	54
5.2.	Measurement campaigns of the RLU frequency calibration	57
5.3.	Frequency coupling factors for the two LRI laser flight units	59
5.4.	Empirical parameters for telemetry model	62
5.5.	Pre- and postfit rms of the range error	63
5.6.	TC parameters for v52	66
5.7.	TC parameters for v52 when enforcing cavity thermistors	68
5.8.	TC parameters for GF-2-v52, only with T^{AC}	69
5.9.	Comparison of the scale factor determination methods	72
6.1.	Frequencies of some selected $^{127}\text{I}_2$ transitions	79
6.2.	Long-term RLU-EM optical frequency measurements	83
7.1.	DWS Scan Type Description	88
7.2.	Fit Parameters of all in-flight DWS Scans of types 1, 2, and 5	90
7.3.	Parameter estimates for the temperature coupling of the TMA	93
7.4.	Heterodyne Efficiency Model Parameters	95
7.5.	Beam pointing-to-pathlength coupling factors	100
7.6.	Beam waist offset parameters from DWS scans	104
9.1.	SEU parameters as detected in the LRI phase data	126
9.2.	Fractional bit numbers for two simultaneous bitflips	128
C.1.	TC parameters for v51	140
C.2.	TC parameters for v53	140

List of Acronyms

ACC accelerometer	GOCE Gravity field and steady-state Ocean Circulation Explorer
ACF autocorrelation function	GPS global positioning system
ACT attitude control thruster	GRACE Gravity Recovery And Climate Experiment
ADC analog to digital converter	GRACE-C GRACE-Continuity
ADPLL all-digital phase-locked loop	GRACE-FO GRACE Follow-On
AEI Albert-Einstein Institute	GSE ground support equipment
AOC antenna offset correction	GUI graphical user interface
AOCS attitude and orbit control system	HPF high-pass filter
ASD amplitude spectral density	ICU instrument control unit
BIPM Bureau International des Poids et Mesures	IL in-loop
CHAMP CHALLENGING Minisatellite Payload	IMU Inertial Measurement Unit
CHU Camera Head Unit	IOC in-orbit commissioning
CNR carrier-to-noise ratio	IPCC Intergovernmental Panel on Climate Change
COM center of mass	IPU MWI instrument processing unit
DLR German Aerospace Center (Deutsches Zentrum für Luft- und Raumfahrt)	JPL Jet Propulsion Laboratory
DPLL digital phase locked loop	KBR K-Band Ranging
DPS differential power sensing	LDB laser diode bench
DWS differential wavefront sensing	LEO low Earth orbit
EDAC error detection and correction	LEOP launch and early operations
EGSE electronic ground support equipment	LISA Laser Interferometer Space Antenna
ENBW equivalent noise bandwidth	LOF LRI optical frame
EOM electro-optical modulator	LOS line-of-sight
ESA European Space Agency	LRI Laser Ranging Interferometer
FFT Fast Fourier Transform	LRP laser ranging processor
FIA fiber injector assembly	LTC light time correction
FIR finite impulse response	LTP LISA technology package
FPGA field programmable gate array	LUT look-up table
FSM fast steering mirror	MTS modulation transfer spectroscopy
FSR free spectral range	MWI Microwave Instrument
GCRF geocentric celestial reference frame	NASA National Aeronautics and Space Administration
GFR gravity field recovery	NCO numerically controlled oscillator
GNSS global navigation satellite system	NGGM Next Generation Gravity Mission
	NPRO non-planar ring oscillator
	OBA optical bench assembly

OBC onboard computer	SDS science data system
OBE optical bench electronics	SEE single event effects
OGSE optical ground support equipment	SEFI single event functional interrupt
OOL out-of-loop	SET single event transient
PA phase accumulator	SEU single event upset
PDH Pound-Drever-Hall	SF satellite frame
PIR phase increment register	SLR satellite laser ranging
PJ phase jump	SRF science reference frame
PMH pump module head	STI SpaceTech Immenstaad GmbH
POD precise orbit determination	TC thermal coupling
PSD power spectral density	TIA transimpedance amplifier
PZT piezo-electric transducer	TM/TC telecommand and telemetry
QPD quadrant photodiode	TMA triple mirror assembly
RAM random access memory	TPR transponder photoreceiver
RIN relative intensity noise	TRP thermal reference point
RLAS reference laser	TTL tilt-to-length coupling
RLU reference laser unit	TWS terrestrial water storage
RTC range thermal coupling	ULE ultra-low expansion
SAA south-atlantic anomaly	USO ultra-stable oscillator
SAGB simple astigmatic Gaussian beam	VAFB Vandenberg Air-Force Base
SC spacecraft	VCM variance-covariance matrix
SCA Star Camera Assembly	VCO voltage controlled oscillator

“ *The world has changed.
I see it in the water.
I feel it in the Earth.
I smell it in the air.* ”

— J. R. R. TOLKIEN —
Author and Philologist

1.1. The Changing Earth

The sustainable management of planet Earth’s most vital resource, water, depends on a comprehensive understanding of its distribution, availability, and utilization. In this pursuit, monitoring global water storage is a central ambition that bridges environmental science, societal well-being, and climate resilience. A multidimensional tapestry interweaves the importance of global water storage monitoring, the significance of water to society, and its intricate impact on the climate.

As humanity struggles to avert the accelerating climate crisis, water emerges as both a protagonist and a sentinel. It is intimately tied to the hydrological cycle, playing a key role in understanding Earth’s climatic rhythm. The insights of the latest assessment report AR6 of the Intergovernmental Panel on Climate Change (IPCC) underscore that changes in water availability contribute to a spectrum of climate impacts, ranging from altered precipitation patterns to heightened risks of extreme weather events (IPCC AR6, Ch. 4, 2022), as already observed worldwide in the past months and years. The global ocean accentuates the interconnectedness of water and climate. IPCC’s report also examines how melting ice and thermal expansion of seawater instigate sea level rise, a central problem in the climate change narrative. The global mean sea level rise, currently at a rate of 3.6 mm/year, keeps accelerating (IPCC AR6, Ch. 4, 2022). This triggers cascading impacts on coastal regions, shaping ecosystems and human settlements alike. Furthermore, water influences temperature regulation and energy transfer, acting as a regulator in climate dynamics. Its role in modulating various climatic processes, such as ocean currents and heat distribution, is key to understanding and predicting climate patterns. (Jiménez Cisneros et al., 2014).

Geodetic satellite systems like Gravity Recovery And Climate Experiment (GRACE) and its successor GRACE Follow-On (GRACE-FO) play a pivotal role in assessing the current state and changes of Earth’s mass distribution (Jin et al., 2013; Wouters et al., 2019). By observing water’s subtle and intricate movements across and below Earth’s surface, GRACE-FO unveils the hidden dynamics that shape our world (Tapley et al., 2019). Such valuable data sets are analyzed by scientists worldwide, e. g., to observe groundwater basins, especially in remote regions and those grappling with water stress (Frappart et al., 2018).

By now, the two GRACE satellite missions sampled more than two decades of Earth gravity and thus terrestrial water storage (TWS), one observable to describe the amount of available water on and below the Earth’s surface, apart from the oceans. Within this time frame, the global TWS decreased by 1 cm per year on average, causing severe impacts on humanity (WMO, 2021). The scientific applications of the monthly gravity fields are widely spread and range from monitoring of polar ice-mass loss (Velicogna et al., 2020), glacier mass loss (Wouters et al., 2019) to earthquake studies (Han et al., 2006), and many more. With its higher precision, the Laser Ranging Interferometer (LRI) offers new analysis techniques in which direct time-domain along-track observations are used instead of a gravity map averaged over a long period. These new techniques allow observations with high time resolution (Ghobadi-Far et al., 2020; Pie et al., 2021).

This thesis is at the quantum frontier within the broad field of geodetic Earth observation technology. At its core, it delves into detailed data analysis of the LRI aboard the GRACE-FO satellite mission. This technology demonstrator has proven the feasibility of laser interferometers for long distance, high precision ranging measurements (Abich et al., 2019). By investigating the LRI’s capabilities and performance, this research presents novel observations and findings that will guide the design and refinement of future space-borne laser-ranging instruments. In doing so, this work contributes to advancing the technological frontier of Earth observation.

Moreover, this is my contribution to defeating the climate crisis.

1.2. Observing Gravity from Space

The history of space missions for quantifying the Earth’s gravity field reaches back to the first artificial satellites, Sputnik-1 and Sputnik-2, launched in late 1957. For the first time, the gravitational field was observed from space by precisely measuring the rotation of the orbital plane, which allowed determining Earth’s oblateness with unprecedented accuracy (Merson et al., 1958; Rummel, 2020). A first gravity field with higher order contributions was derived from the *LAsEr GEodynamics Satellites* (LAGEOS-I: 1976–now; LAGEOS-II: 1992–now; Yoder et al. (1983) and Gegout et al. (1991)), whose medium Earth orbit nearly 6000 km above Earth’s surface is precisely determined using Earth-to-space satellite-laser-ranging techniques. Studying the LAGEOS orbits already revealed time-variable effects in the gravity field, such as post-glacial rebound (Rubincam, 1984). Gravity field estimates have become more and more accurate with an increasing number of satellites and their observations, especially with using the global navigation satellite system (GNSS) for precise orbit determination.

A new era of gravity field determination, with a timeline depicted in figure 1.1, started with dedicated satellite gravimetry missions in the year 2000 when the German *CHALLENGING Minisatellite Payload* (CHAMP; 2000–2010; Reigber et al., 2003) was launched. The satellite was in a low Earth orbit (LEO) at approximately 450 km above sea level, and the whole spacecraft (SC) served as a test mass in the Earth’s gravity field. Its orbit was determined using the global positioning system (GPS), called high-low satellite-to-satellite tracking (hl-SST), and satellite laser ranging (SLR) observations. As a unique feature, the non-gravitational accelerations like air drag and solar radiation pressure were measured by an onboard electrostatic accelerometer (ACC).

The Earth’s gravitational potential is determined through a non-linear regression

1.2. OBSERVING GRAVITY FROM SPACE

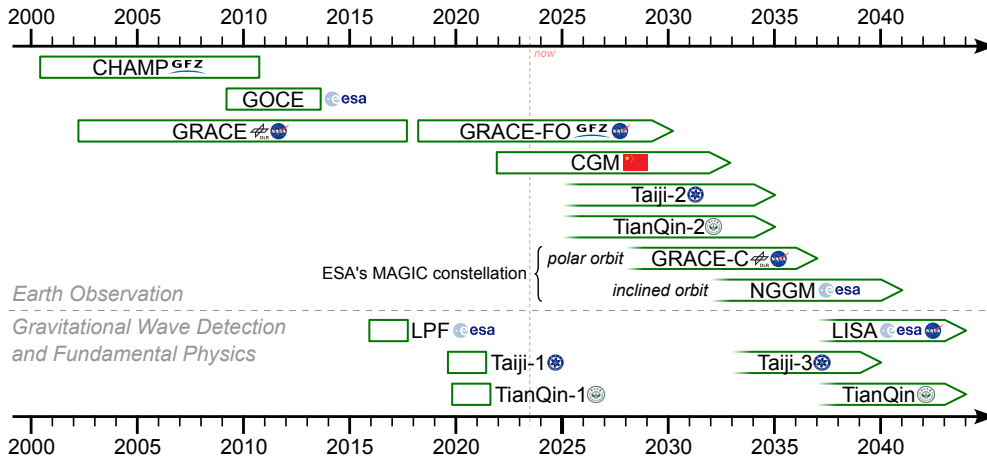


Figure 1.1. Timeline of recent and future Earth-observing gravity missions and other laser interferometers in space. LISA, Taiji, and TianQin are future gravitational wave observatories in space. Their respective pathfinder missions include Earth gravity missions. The CGM is a GRACE-like mission employing microwave ranging. Note that the duration of operation of each satellite mission is inaccurately represented in this figure, and that the launch dates of future missions are estimates and thus subject to change.

process, usually denoted as gravity field recovery (GFR), based on assessing the disturbance of the SC trajectory from known and precise force models. Deviations of the predicted orbits, and thus the expected satellite position, are attributed to previously unmodeled effects or deficiencies in the a-priori force models. The gravity field is typically expressed through coefficients of spherical harmonics (Reigber, 1989; Tapley et al., 2004).

The first geodetic space mission employing ranging measurements between two satellites flying in a formation, so-called low-low satellite-to-satellite tracking (ll-SST), was the US-German *Gravity Recovery And Climate Experiment* (GRACE; 2002–2017; Tapley et al., 2003; Tapley et al., 2004). It featured two identical satellites, following each other in a distance of about 220 ± 50 km in a polar LEO. The distance between the two SC was measured by microwave interferometry with a noise level of approximately $1 \mu\text{m}/\sqrt{\text{Hz}}$ at frequencies of 1 Hz. Gravitational and non-gravitational forces mainly determine their orbits, and the differential line-of-sight acceleration is inferred through that inter-satellite ranging measurement. An accelerometer on both SC again measures non-gravitational accelerations for removal in post-processing to disentangle gravitational and non-gravitational accelerations in the ranging measurement. Furthermore, precise position and a time reference are determined using GPS observations. The GFR process is comparable to the CHAMP-case sketched above but with the additional along-track ranging measurement from the ll-SST link. The polar orbit configuration with low eccentricity allows the derivation of global gravity field models every month, and the variations of these mainly reveal hydrological signals with annual and semi-annual periods and long-term trends that arise from groundwater variations, ice sheet mass loss, and similar effects. The GRACE mission has contributed significantly to understanding climate change (Tapley et al., 2019).

The successor mission *GRACE Follow-On* (GRACE-FO; 2018–now; Flechtner et al., 2015; Kornfeld et al., 2019; Landerer et al., 2020) was launched on 22nd of May

2018, shortly after the deorbiting of GRACE in November 2017. The new mission hosts an updated Microwave Instrument (MWI), alongside the novel LRI, a technology demonstrator that uses a laser interferometer for the range measurement (Sheard et al., 2012).

Like GRACE-FO was intended to provide continuity of the monthly GRACE gravity maps, several studies have been performed or are ongoing to foster a new generation of Earth gravity missions (Wiese et al., 2021; Massotti et al., 2021; Cesare et al., 2022; Nicklaus et al., 2022; Carraz et al., 2023). A successor of GRACE-FO, called *GRACE-Continuity* (GRACE-C) and again shared between US-German parties like GRACE-FO, is planned to launch in 2028. A second satellite pair with the name *Next Generation Gravity Mission* (NGGM) led by the European Space Agency (ESA) is expected in the early 2030s. GRACE-C and NGGM form the *Mass Change and Geosciences International Constellation* (MAGIC), a so-called Bender configuration (Bender et al., 2008; Wiese, 2011) with GRACE-C in a polar- and NGGM in an inclined orbit (Massotti et al., 2021).

A parallel development is currently ongoing in China. Their first GRACE-like mission using a microwave instrument, named CGM, was launched in late-2021 (Xiao et al., 2023). Two more gravity missions, Taiji-2 and TianQin-2, that both use laser interferometry, are currently being prepared for launch in the second half of this decade. They are both part of independent developments towards space-based gravitational wave observatories; see the next section.

A different concept of measuring Earth’s gravity field was pursued by the *Gravity field and steady-state Ocean Circulation Explorer* (GOCE; 2009-2013; Rummel et al., 2002; Johannessen et al., 2003). Its core technology was a 3-axis gradiometer with arm lengths of 50 cm to directly measure the gravity gradients along this short baseline. It flew at an even lower altitude, 250 km above Earth’s surface, to resolve the gravity field with higher spatial resolution. Unlike GRACE, it was designed to precisely measure the static gravity field, i. e., an average field over the mission duration for the benefit of higher spatial resolution and not to resolve temporal variations.

The GRACE principle of ll-SST has also been adapted to measure the lunar gravity with the so-called *GRAvity recovery and Interior Laboratory* (GRAIL; 2011–2012; Zuber et al., 2013). Like GRACE, these twin satellites also employed a microwave instrument for the ranging measurement. Recently, there has also been a proposal for a GRACE-like gravity mission orbiting the planet Mars (Wörner et al., 2023).

1.3. Beyond Classical Gravity

The LRI onboard GRACE-FO proved the concept of laser interferometric inter-satellite ranging measurements for the very first time. Hence, it is a successful demonstration for the planned *Laser Interferometer Space Antenna* (LISA; Danzmann et al. (2003) and Amaro-Seoane et al. (2017)), a space-borne gravitational wave detector. LISA consists of three SC flying approximately 20° in front or behind the Earth on its heliocentric orbit. Six laser interferometric links exist between the three SC, and the distance variations encode the variations in the curved spacetime, e. g., caused by gravitational waves. Like LRI, the three SC are equally equipped and utilize similar techniques. Generally speaking, both missions measure distance variations of test masses in a gravitational potential, either caused by classical gravity or gravitational waves. However, the tech-

nological challenges differ: higher beam powers and a beam telescope are needed in LISA due to the huge path length of $2.5 \cdot 10^6$ km as opposed to 220 km on GRACE-FO, and a reduced phase readout noise of the phasemeter at sub-mHz frequencies is necessary, in LISA (Bachman et al., 2017). Furthermore, the total ranging signal between two test masses on the distant SC is split into three parts in LISA: a so-called test mass interferometer on both ends of the link determines the motion of the free-floating test mass with respect to the SC body. The long-arm interferometer measures the relative motion of the two SC. While the LRI demonstrated parts of one LISA-arm, the test mass interferometer has, among other technologies, been demonstrated in *LISA Pathfinder* (2015–2017; Armano et al. (2015), Armano et al. (2017), and Armano et al. (2022)), a single-satellite mission in deep space.

LISA Pathfinder orbited the Lagrange point L1 between the Earth and the Sun, hosting the first laser interferometer in space, called the LISA technology package (LTP), for testing the optical readout of all six angular and lateral degrees of freedom of such free-floating test masses within the satellite. The LTP also has technological similarities to the LRI, as it uses a similar laser source. Its core technology, the optical test mass readout, has also been proposed for future gravity missions (Álvarez et al., 2022). Besides the interferometer, LISA Pathfinder also demonstrated the test mass housing and release mechanism, contactless discharging of the test mass, μ N-thrusters, and more.

Similar to the development of LISA, with LISA Pathfinder and the LRI testing critical components of the gravitational wave detector, two Chinese projects are currently in development. The design of Taiji-3 is similar to LISA: a triangular constellation with a slightly increased arm length of $3 \cdot 10^6$ km in a heliocentric orbit, led by the Chinese Academy of Sciences (Luo et al., 2020b). TianQin instead is orbiting Earth with an arm length in the order of $100 \cdot 10^3$ km and led by the Sun-Yat Sen University (Luo et al., 2016). Both projects face similar technological developments as LISA and have already launched their single-satellite pilot missions, both in mid to late-2019 (Taiji-1: Wu et al. (2021); TianQin-1: Luo et al. (2020a)). Their two-satellite demonstrations, featuring an LRI-like interferometer, are expected to launch between 2025 and 2030, and the entire gravitational wave constellations within the 2030s.

1.4. Thesis Structure and Objectives

The presented thesis is concerned with various aspects of analyzing the telemetry of the LRI. Precise knowledge of the laser frequency, or the wavelength, is needed as it represents the conversion factor from the measured phase to the desired inter-spacecraft ranging signal, and new determination schemes are required without the option to compare the range measurement of the LRI to the MWI. Therefore, a significant part of the investigation is driven by the question: “How do laser frequency variations influence the ranging measurements, and how can we determine the absolute value of the laser frequency?”, an important research question for future gravity missions. A second significant topic is the verification of the co-alignment of the retro-reflector mirrors and, in connection with that, the thorough investigation of the DWS scans. Lastly, some questions arose from the observation of non-nominal telemetry data and the aim to explain those.

The theoretical basis for the analysis performed in this thesis is set in chapter 2

by introducing the concept of interferometry. The working principle of the LRI and the individual subunits are explained in section 3.1.1, before the GRACE-FO mission is described in general, including a brief introduction to the other payloads and the current mission status. Furthermore, section 3.2 presents the in-flight sensitivity of the LRI and discusses previous studies regarding the LRI performance. Section 3.3 briefly presents the noise sources of the LRI at high-frequencies. Afterward, the actual in-flight measurement noise is modeled, as knowledge of the frequency-dependent noise shape is needed for many kinds of parameter estimation, like the weighted least squares or likelihood methods. Analytical functions for the noise power spectral density (PSD) and the corresponding autocorrelation functions are derived for the LRI in the transponder and reference roles, and also for a particular phase combination, which is needed for analyzing effects in single phase channels.

Special attention is drawn to a relativistically correct formulation of the ranging phase and, more importantly, to the relativistic shifts of the absolute frequency of the laser light traveling between the two SC in chapter 4. The absolute laser frequency, or similarly the laser wavelength, sets the ruler for converting the measured phase variations of the interferometer to an equivalent range in units of meter (sections 4.1 and 4.2). The dominant processing error sources in the instantaneous biased range are precise timing and the estimation of the laser frequency, and their effect is covered in section 4.3. The laser frequency stability is a key performance driver of the LRI, not only at high frequencies to mitigate laser frequency noise coupling in the ranging measurement but also at low frequencies, where the long-term stability of the instrument has to be ensured. These assessments conclude the theoretical part of this thesis.

The entire chapter 5 discusses different approaches to estimate the in-flight laser frequency of the LRI lasers. In principle, there are three possibilities: comparing LRI and K-Band Ranging (KBR) data and co-calibrate the LRI laser frequency (section 5.1); using a newly derived model of the (time-variable) cavity resonance frequency (section 5.2); model the optical laser frequency by deriving coupling factors for the telemetry of the laser, i. e., the setpoints of the frequency controllers (section 5.3). The latter model was derived from on-ground calibrations and showed a drift w. r. t. flight data that is not present in the other two models. It is potentially caused by the aging of the non-planar ring oscillator (NPRO) crystal within the laser and was corrected using an empirical model derived from in-flight data. Chapter 6 describes a laboratory experiment in which the free-running frequency of a comparable laser unit is tracked over the course of several months in order to observe such a drift on the ground as well. A comparison of the three models is performed in section 5.4. The residual differences between KBR and LRI measurements are investigated in section 5.5, and two possible coupling mechanisms of temperature variations into the measured range, also commonly known as tone errors, are developed. Parameters for this thermal coupling are estimated, and the tone error model performance, in terms of reduction of the KBR-LRI residuals, is verified. It is shown that the thermal coupling not only reduces the residuals between the two ranging instruments but is also capable of removing variations in the scale factor and timing offsets estimates from the cross-calibration method, which did arise on a seasonal period. This part is concluded by discussing alternative determination schemes for the absolute laser frequency in the context of future gravity missions in section 5.6.

The LRI features the possibility of diagnostic data capture. This mainly serves the

purpose of characterizing the LRI itself but has also proven to be helpful for diagnostics across different payloads onboard the satellites, e. g., to track the motion of the spacecraft's center of mass (Wegener et al., 2020). A particular type of these scans, called differential wavefront sensing (DWS) scans, is investigated in detail in chapter 7. During such DWS scans, extensively introduced in section 7.1, one of the LRI units adds a slight pointing deviation to the outgoing beam, which implies less received optical power at the distant SC and a degraded heterodyne efficiency locally. By modulating the pointing angle, the beams' intensity profile can be mapped (section 7.2), which allows the determination of the Gaussian beam parameters, as well as the co-alignment error of the triple mirror assembly (TMA). Further, the local heterodyne efficiency variations under relative beam tip and tilt are investigated in section 7.3. Both effects do not introduce path length noise into the measurement if there is no beam walk on the photodiodes and if the phase fronts of the Gaussian beams propagating between the two SC are perfectly spherical and centered at the reference point for the beam rotation. However, if the phase front does not have the right phase front curvature, any attitude jitter will cause an equivalent path length noise on the photodiode. Hence, the shape of the beams' phase front is recovered in section 7.4, and equivalent offsets of the beam waist positions of the astigmatic Gaussian beam are derived.

The optical light sources of the LRI are the two reference laser units (RLUs). Their frequency stability at frequencies above 1 mHz over the mission lifetime is investigated in chapter 8.

Last but not least, chapter 9 investigates the occurrence of so-called single event upsets (SEUs), which are disturbances in the digital processing chain within the laser ranging processor (LRP), evoked by radiation and charged particles that interact with the onboard electronics. The effect is simulated, detected, and removed from the LRI phase data.

Ultimately, chapter 10 summarizes this thesis' findings.

“*Interferometry, like surfing, is a search for the perfect wave. But physicists don't have to paddle around and wait.*”

— KEN GOLDBERG —

Artist and Professor at UC Berkeley

2.1. Electromagnetic Waves in the Paraxial Approximation

A (quasi-) monochromatic laser beam, commonly used in optical experiments, is an electromagnetic wave confined in space. The complex-valued electric field vector can generically describe the electric field of such a laser beam through

$$\vec{E}(\vec{r}, t) = E_0(\vec{r}) \cdot \vec{p}(\vec{r}) \cdot \exp(-i(\vec{k} \cdot \vec{r} - 2\pi\nu t + \phi(\vec{r}))) , \quad (2.1)$$

which depends on the spatial evaluation point \vec{r} and the evaluation time t . The complex-valued field amplitude is denoted as $E_0(\vec{r})$ with the unit of V/m, and \vec{p} is a complex unit vector denoting the polarization of the wave. As it is not further needed in the following, it will be neglected from now on. The optical frequency ν is related to the wavelength $\lambda = c/\nu$ through the speed of light c in vacuum. In the simple form of equation (2.1), the beams' frequency ν is assumed to be constant over time. Cases of a time-varying laser frequency $\nu(t)$ will be discussed later. The constant wave vector \vec{k} defines the propagation direction as well as the frequency through its norm as

$$k = |\vec{k}| = 2\pi n/\lambda_0 = 2\pi n\nu/c_0 , \quad (2.2)$$

with n being the refractive index of the propagation medium, e. g., $n = 1$ in vacuum. An additional phase, which may contain contributions from a particular phase front curvature, is denoted as $\phi(\vec{r})$. In the case of a planar wave front (or phase front), this phase term is $\phi(\vec{r}) \equiv \text{const.}$. The amplitude $E_0(\vec{r})$ of the electric field of equation (2.1) is a solution of the scalar Helmholtz equation ([Reider, 2016](#))

$$\nabla^2 E_0(\vec{r}) + k^2 E_0(\vec{r}) = 0 , \quad (2.3)$$

which contains the Laplace operator ∇^2 and assumes that the electric field amplitude to vary slowly along the propagation axis such that $|\partial E_0(\vec{r})/\partial z| \ll 2\pi |E_0(\vec{r})|/\lambda$. This condition is similar to the assumption that the angle Θ_{div} between the wave vector \vec{k} and the optical propagation axis z is $\Theta_{\text{div}} \ll 1$. This approximation allows neglecting the second derivative in z and to obtain the paraxial Helmholtz equation

$$\nabla_T^2 E_0(\vec{r}) - 2ik \frac{\partial E_0(\vec{r})}{\partial z} = 0 , \quad (2.4)$$

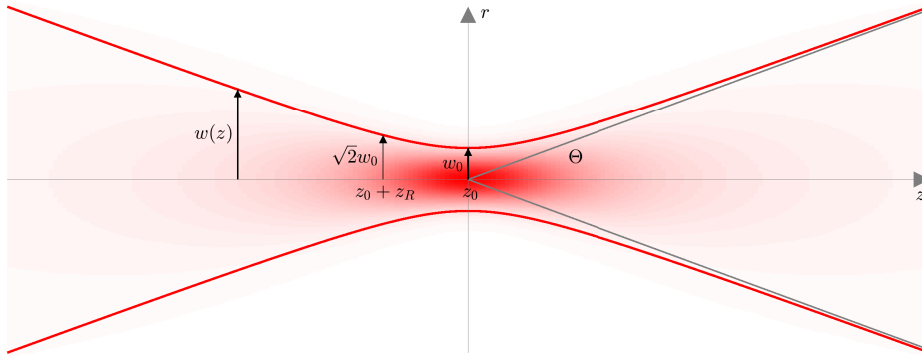


Figure 2.1. Quantities used to describe a Gaussian beam propagating along z . The radial component is $r = \sqrt{x^2 + y^2}$.

where ∇_T^2 denotes the 2-dimensional Laplace operator in the transverse directions x and y . Equation (2.1) satisfies this equation under the additional assumption that the polarization vector is orthogonal to the propagation axis. The instantaneous phase of this field is defined as

$$\Phi(\vec{r}, t) = \arg(|\vec{E}(\vec{r}, t)|) = -2\pi\nu t - \vec{k}_0 \cdot \vec{r} - \varphi(\vec{r}). \quad (2.5)$$

The phase $\varphi(\vec{r})$ describes the shape of the wavefront, which can be regarded as constant for plane waves or flat-top beams and parabolic in the case of a Gaussian beam.

Importantly, in the far field, where the distance between points of emission and measurement is much larger than the beam's transverse expansion, i. e., $z \gg r = \sqrt{x^2 + y^2}$, the phase

$$\Phi(z \rightarrow \infty, t) \rightarrow -2\pi\nu t - \frac{2\pi n\nu \cdot z}{c_0} \quad (2.6)$$

shows spherical symmetry (Carter, 1972).

2.2. Gaussian Beams

Without rigorous derivation, the electric field of a so-called Gaussian beam can be expressed as (Reider, 2016)

$$E(\vec{r}) = \underbrace{E_0(z)}_{\text{amplitude}} \underbrace{\exp\left[-\frac{r^2}{w^2(z)}\right]}_{\text{profile}} \underbrace{\exp\left[-ik\frac{r^2}{2R(z)}\right]}_{\text{phase curvature}} \underbrace{\exp(-i(k(z - z_0) - \eta_g(z)))}_{\text{carrier}}, \quad (2.7)$$

where $r = \sqrt{x^2 + y^2}$ denotes the radial component of the evaluation point \vec{r} .

A schematic picture of such a beam is shown in figure 2.1. The amplitude profile resembles a Gaussian bell curve with the width

$$w^2(z) = w_0^2 \left(1 + \left(\frac{z - z_0}{z_R} \right)^2 \right), \quad (2.8)$$

by definition the transverse offset at which the absolute amplitude $E_0(\vec{r})$ falls below $1/e^2$. The term z_0 describes the position of the beam's waist with respect to the coordinate systems' origin, w_0 is the waist radius, and

$$z_R = \frac{n\pi w_0^2}{\lambda} \quad (2.9)$$

is the so-called Rayleigh range. The waist radius w_0 furthermore defines the beam divergence angle

$$\Theta_{\text{div}} = \frac{\lambda}{w_0\pi} \quad w_0 = \frac{\lambda}{\Theta_{\text{div}}\pi}, \quad (2.10)$$

which describes the asymptotic beam divergence in the far field. The parabolic phase curvature term approximates the spherical phase front with curvature $1/R(z)$ for a small lateral offset $r = \sqrt{x^2 + y^2}$ from the main propagation axis z . Here,

$$R(z) = (z - z_0) \left(1 + \left(\frac{z_R}{z - z_0} \right)^2 \right). \quad (2.11)$$

The term $k(z - z_0)$ denotes the optical path length and

$$\eta_g(z) = \arctan\left(\frac{z - z_0}{z_R}\right) \quad (2.12)$$

is the so-called Gouy phase shift approaches $\pm\pi/2$ in the far field and features a fast zero-crossing at the waist position $z = z_0$.

The optical intensity distribution, which is defined by the first two factors in equation (2.7), can be expressed as

$$I(\vec{r}) = |E(\vec{r})|^2 = E_0(z)^2 \exp\left(\frac{-2r^2}{w(z)^2}\right). \quad (2.13)$$

The optical power in units of watts, sensed by a photodiode with radius r_{pd} , can be obtained by integrating equation (2.13) over the active area of the photodiode. It reads (Kochkina, 2013)

$$P = \int_0^\infty I(\vec{r}) 2\pi r \, dr \quad (2.14)$$

$$= \frac{\pi}{2} E_0^2 w(z)^2. \quad (2.15)$$

Given the optical power of the impinging laser beam power, $P = P_{\text{tx}}$, as normalization constant, and assuming the photodiode radius to be larger than the beam at the photodiode position, $r_{\text{pd}} > w(z_{\text{pd}})$, the normalization constant of the electric field can be expressed as

$$E_0(z) = \frac{1}{w(z)} \sqrt{\frac{2P_{\text{tx}}}{\pi}}. \quad (2.16)$$

The notation P_{tx} , with tx denoting the transmit beam, will become clear when the actual Laser Ranging Interferometer (LRI) setup is described in chapter 3. In the following, the power received by a photodiode at a certain distance L , at which large parts of the beam are clipped by a receiving aperture with a radius $r_{\text{rx,ap}} < w(L - z_{\text{ap} \rightarrow \text{pd}})$

before reaching the detector, is computed by using the previous equations. The on-axis distance $z_{\text{ap} \rightarrow \text{pd}}$ is written here for completeness but is usually much smaller than L and can be neglected. A potential misalignment $\alpha_{\text{rx,pd}}$ of the receiver's photodiode surface normal vector w. r. t. the beam propagation axis is introduced. It is sufficiently described in one dimension here due to the radial symmetry of the Gaussian beam. The effective area of the aperture is then given by

$$A_{\text{eff}} = \pi r_{\text{rx,ap}}^2 \cdot \cos(\alpha_{\text{rx,pd}}) \approx \pi r_{\text{rx,ap}}^2 \cdot \left(1 - \frac{\alpha_{\text{rx,pd}}^2}{2}\right) \approx \pi r_{\text{rx,ap}}^2. \quad (2.17)$$

However, the angle $\alpha_{\text{rx,pd}}$ is typically small and only couples into the area quadratically. It is thus neglected in the last approximation of equation (2.17). The power inside the clipping aperture area is finally given by the product of equations (2.13) and (2.17) as

$$P_{\text{rx,ap}} = A_{\text{eff}} \cdot I(\vec{r}) \quad (2.18)$$

$$\approx \pi r_{\text{rx,ap}}^2 \frac{2P_{\text{tx}}}{\pi w(L)^2} \exp\left(\frac{-2r_{\text{rx,ap}}^2}{w(L)^2}\right) \quad (2.19)$$

$$P_{\text{rx,ap}}(\alpha_{\text{tx}}) \approx \frac{2P_{\text{tx}} r_{\text{rx,ap}}^2}{(\Theta_{\text{div}} \cdot L)^2} \exp\left(\frac{-2\alpha_{\text{tx}}^2}{\Theta_{\text{div}}^2}\right), \quad (2.20)$$

where an angular misalignment α_{tx} was introduced in the last step to express the radial component $r = \sqrt{x^2 + y^2} \approx \alpha_{\text{tx}} \cdot L$ of the evaluation point. In addition, the approximation $w(L) \approx \Theta_{\text{div}} \cdot L$ for large $L \gg z_R$ is used and $I(\vec{r})$ is regarded constant over the small size of the clipping aperture, i. e., $r_{\text{rx,ap}} \ll w(L)$.

The equations introduced above for a radially symmetric Gaussian beam can be adapted for non-fundamental Gaussian beams such as, e. g., simple astigmatic or elliptic Gaussian beams of the form

$$E(\vec{r}) = E_0(z) \exp\left(-ik(z - z_0) - \sum_{i=1}^2 \left(ik \frac{r_i^2}{2R_i(z)} - \frac{i\eta_{g,i}(z)}{2} + \frac{r_i^2}{w_i^2(z)}\right)\right), \quad (2.21)$$

in which the beam propagates in z direction while the beam's principal axes are $r_i = [x, y]$. The principal axes of the beam are aligned with x and y for simplicity. These principal axes have their individual set of features, such as the waist position $r_{i,0}$, waist radius w_i , and radius of curvature R_i . The Gouy phase shift of both principal axes averages such that it still equals $\pm\pi/2$ in the far field. The amplitude of such a simple astigmatic Gaussian beam (SAGB) reads

$$\mathcal{A}^{\text{SAGB}}(\vec{r}, t) = E_0(z) \cdot \exp\left(-\sum_{i=2}^3 \frac{r_i^2}{w_i^2(z)}\right) \quad (2.22)$$

$$= E_0(z) \cdot \exp\left(-\sum_{i=2}^3 \frac{z^2 \alpha_i^2}{w_i^2(z)}\right), \quad (2.23)$$

wherein the second equation uses the small beam deflection angles α_i , the evaluation position along the propagation axis z as well as the approximation of small angles to describe the two lateral dimensions. The angles α_i can also be regarded as pointing angles of the beam w. r. t. the evaluation point \vec{r} .

The phase of an astigmatic Gaussian beam reads

$$\Phi^{\text{SAGB}}(\vec{r}) = \arg(E(\vec{r}, t)) = -k(z - z_0) + \sum_{i=1}^2 \left(\frac{\eta_{g,i}(z)}{2} - \frac{k \cdot r_i^2}{2R_i(z)} \right). \quad (2.24)$$

2.3. The Concepts of Interferometry

Interferometry describes the superposition (or vector addition) of two or more complex-valued electrical fields as defined by equation (2.1), which will be called \vec{E}_{lo} and \vec{E}_{rx} in the following. The notation “lo” for a local oscillator beam and “rx” for a received beam will become more intuitive in the subsequent chapters when actual interferometer designs are discussed. Given a recombination beam splitter with the reflectivity $\eta_{\text{BS}}^{\text{r}}$ and transmissivity $\eta_{\text{BS}}^{\text{t}} = 1 - \eta_{\text{BS}}^{\text{r}}$, the intensity I on a photodiode in the subsequent beam path, or similarly the amplitude of the electric field superposition, can be expressed as (Gerberding, 2014)

$$I(\vec{r}, t) = \frac{c_0 \varepsilon_0 n}{4} \left| i \sqrt{\eta_{\text{BS}}^{\text{t}}} E_{\text{lo}}(\vec{r}, t) + \sqrt{\eta_{\text{BS}}^{\text{r}}} E_{\text{rx}}(\vec{r}, t) \right|^2. \quad (2.25)$$

Here, $\varepsilon_0 = 8.85 \cdot 10^{-12} \text{ F/m}$ is the vacuum permittivity. The factor i arises from the 90° phase shift of the beam transmitted at the beam splitter. It can, w.l.o.g, also be applied to \vec{E}_{rx} , depending on the setup. The optical power that may be sensed by a photodiode within an optical experiment is given by integrating I over the active area of the photodiode, which is regarded to be large enough to sense the whole beam, and reads

$$P_{\text{pd}}(t) = \int_0^{r_{\text{rx,ap}}} I(\vec{r}, t) 2\pi r \, dr \quad (2.26)$$

$$= \frac{c_0 \varepsilon_0 n}{4} \left[\eta_{\text{BS}}^{\text{t}} P_{\text{lo}} + \eta_{\text{BS}}^{\text{r}} P_{\text{rx,ap}} + 2 \sqrt{\eta_{\text{het}} \eta_{\text{BS}}^{\text{t}} P_{\text{lo}} \eta_{\text{BS}}^{\text{r}} P_{\text{rx,ap}}} \cos(2\pi f_{\text{het}} t + \varphi(t)) \right] \quad (2.27)$$

$$= \frac{\mathcal{A}_b(t)}{\mathcal{R}}, \quad (2.28)$$

with the laser powers P_{lo} of the local oscillator and $P_{\text{rx,ap}}$ at the receiver side and the so-called heterodyne efficiency η_{het} , which is a measure for the similarity of the two interfering beams, see section 2.3.5. The last line defines the amplitude of the oscillating signal, or the AC-photocurrent, \mathcal{A}_b in units of ampere, and the responsivity of the photodiode, $\mathcal{R} \approx 0.6 \text{ A/W}$. In typical applications, the photocurrent is converted to a voltage using a transimpedance amplifier (TIA). It is then split into AC and DC parts in electronics to increase sensitivity to the small oscillations on top of a large static signal (Barranco et al., 2017). The argument of the cosine in equation (2.27) defines the heterodyne frequency $f_{\text{het}} = \nu_{\text{rx}} - \nu_{\text{lo}}$ of the two interfering beams. If the two beams have different optical frequencies, the superimposed beams’ measured power $P_{\text{pd}}(t)$ oscillates at that difference frequency. The phase term $\varphi(t)$ represents the (time-variable) path length difference of the two interfering beams, forming the quantity of interest in precision interferometry.

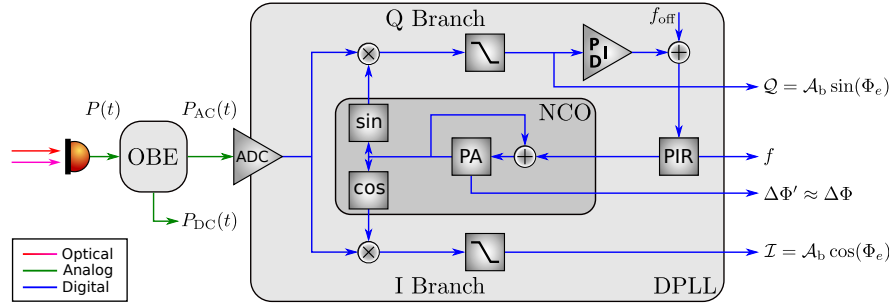


Figure 2.2. Schematic working principle of a DPLL. The incoming beat signal between the two incoming beams is split into AC- and DC-parts. The AC-signal at radio frequencies is digitized and multiplied with sine and cosine waves produced by an NCO. The error signal $\Delta\Phi_e$ from the Q branch is minimized by steering the NCO to the incoming signals' frequency. Hence, the I branch approximates the beatnote signal amplitude \mathcal{A}_b .

2.3.1. Phase Readout

The interferometric phase of equation (2.27),

$$\Delta\Phi = 2\pi f_{\text{het}}t + \varphi(t) , \quad (2.29)$$

is typically read using a so-called digital phase locked loop (DPLL). A DPLL, in principle, is a circuit with one analog input, featuring a numerically controlled oscillator (NCO)^[1] and a corresponding digital circuit that aims to maintain the NCO frequency at the same frequency as the incoming signal. A schematic drawing of such a circuit is shown in figure 2.2. As mentioned in the previous section, the photodiode current is split into AC and DC parts in analog domain. The AC part, containing the desired phase information, can be written as

$$P_{\text{AC}}(t) = g \cdot \mathcal{A}_b \cos(\Delta\Phi) , \quad (2.30)$$

where the time-dependency of the beat phase $\Delta\Phi$ is neglected for better readability. The newly introduced coefficient g is a variable gain-setting for signal conditioning in order to use the full bandwidth of the analog to digital converter (ADC). After digitization, the AC signal is multiplied with a sine and cosine wave, typically created from look-up tables (LUTs) within a field programmable gate array (FPGA), with a phase $\Delta\Phi'$, that is close to the actual incoming phase $\Delta\Phi$. Within this description, it is assumed that the phase of the incoming beam is roughly known while locking schemes for DPLLs are beyond the scope of this thesis. After multiplication, the signals in the so-called I- and Q-branch oscillate at

$$\text{I - branch :} \quad \cos(\Delta\Phi) \cos(\Delta\Phi') = \frac{1}{2}(\cos(\Delta\Phi + \Delta\Phi') + \cos(\Delta\Phi - \Delta\Phi')) \quad (2.31)$$

$$\text{Q - branch :} \quad \cos(\Delta\Phi) \sin(\Delta\Phi') = \frac{1}{2}(\sin(\Delta\Phi + \Delta\Phi') + \sin(\Delta\Phi - \Delta\Phi')) . \quad (2.32)$$

The oscillations at the sum frequency is removed by a low-pass filter in the individual branches, resulting in two signals oscillating at the phase difference $\Phi_e = \Delta\Phi - \Delta\Phi'$.

^[1]NCOs are typically used in DPLLs. In contrast, analog PLLs use voltage controlled oscillators (VCOs).

The signal of the Q-branch after the low-pass filter reads

$$Q = g \cdot \mathcal{A}_b \sin(\Phi_e) \quad (2.33)$$

and is typically small if the incoming and locally generated phases are similar, $\Delta\Phi \approx \Delta\Phi'$, and is used as an error signal in a controller. If needed, a frequency offset can be added before the phase error is stored in the phase increment register (PIR). The PIR contains a digital copy of the incoming signals' frequency. It is fed to the NCO, creating the phase from the frequency in an integrator called the phase accumulator (PA). The I-branch can be expressed as

$$I = g \cdot \mathcal{A}_b \cos(\Phi_e) \quad (2.34)$$

after the low-pass filter. The I - and Q -values, the frequency f , and most importantly, the desired digital copy of the signal phase $\Delta\Phi' \approx \Delta\Phi$ can be extracted from the DPLL and stored after suitable antialias filtering and downsampling. The total signal amplitude can be restored by computing

$$\mathcal{A}_b = \sqrt{I^2 + Q^2}/g . \quad (2.35)$$

2.3.2. Coherent and Incoherent Sum

In modern applications, quadrant photodiodes (QPDs) are typically used, in which the active area of the photoreceiver is split into four segments (quadrants), which are read out individually, each using one DPLL circuit. As defined in equation (2.27) for a circular, single-element photodiode, the ranging phase is the phase average over the four segments on the QPD. However, the sum of the four quadrants can be computed in two fundamentally different ways from the output of the DPLL introduced in the previous section. First, the incoherent sum reads

$$\mathcal{A}_{\text{ICS}} = \sum_{i=1}^4 \sqrt{I_i^2 + Q_i^2}/g_i = \sum_i \mathcal{A}_{b,i} , \quad (2.36)$$

where i numbers the four QPD segments. The coherent sum instead effectively represents the signal a circular photodiode would measure. It is obtained by forming the sum of the quadrants' phasors as

$$\mathcal{A}_{\text{CS}} = \sum_{i=1}^4 \mathcal{A}_{b,i} \cdot e^{i\Delta\Phi_i} . \quad (2.37)$$

The absolute value $|\mathcal{A}_{\text{CS}}|$ of the complex-valued coherent sum is a measure for the beat note amplitude on the QPD.

2.3.3. Differential Wavefront Sensing (DWS)

Using QPDs is furthermore beneficial, as the differential angles between the interfering beams can be inferred from linear combinations of the individual segments. This method is called differential wavefront sensing (DWS) (Morrison et al., 1994; Heinzl et al., 2020). Given the four segments A, B, C, and D as depicted in figure 2.3, the

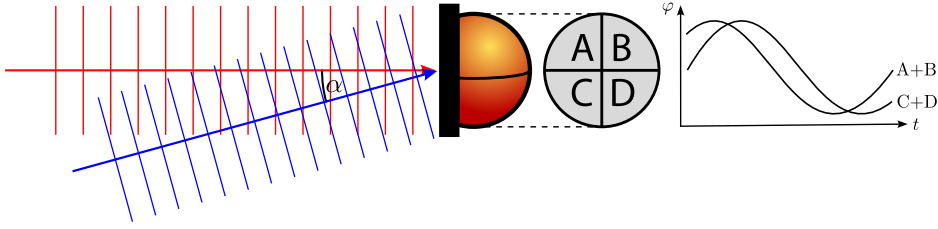


Figure 2.3. Sketch of a QPD and the differential wavefront sensing (DWS) principle. The two beams have a relative tilt α in one dimension. Hence, the average phase on the lower two segments, C and D, differs from that on segments A and B. Particular linear combinations of the individual channels' phase measurement and calibration provide an angular measurement, the DWS-derived beam pointing angles. Planar phase fronts are assumed in this simplified sketch.

horizontal and vertical DWS signals, which define the beams' relative tilt and tip, are defined as

$$\text{DWS}_h = \frac{\varphi_A - \varphi_B + \varphi_C - \varphi_D}{2} \quad (2.38)$$

$$\text{DWS}_v = \frac{\varphi_A + \varphi_B - \varphi_C - \varphi_D}{2} \quad (2.39)$$

A third linear combination without such a simple geometric interpretation is given by

$$\text{DWS}_x = \frac{\varphi_A - \varphi_B - \varphi_C + \varphi_D}{2} . \quad (2.40)$$

The heterodyne frequency cancels out in these combinations, as it is common in all segments. Only the phase difference on the upper two segments, due to the different optical path length of the phase fronts of the tilted beam (blue in the sketch, angle α), contributes to the phase difference of the DWS signals. These signals $\text{DWS}_{h,v}$ in units of electrical phase radian can be converted to the differential beam pointing angles ψ_{dws} and θ_{dws} in units of radian or degree through a linear calibration using the beam radius at the limiting aperture $r_{\text{rx,ap}} = 4$ mm and its wavelength $\lambda \approx 1064$ nm through (Sheard et al., 2012)

$$\begin{pmatrix} \psi_{\text{dws}} \\ \theta_{\text{dws}} \end{pmatrix} \approx \sqrt{2} \frac{16r}{3\lambda} \begin{pmatrix} \text{DWS}_h \\ \text{DWS}_v \end{pmatrix} \quad (2.41)$$

The exact conversion factors have been calibrated in the author's master's thesis and yield (Misfeldt, 2019)

$$\begin{pmatrix} \psi_{\text{dws,GF-1}} \\ \theta_{\text{dws,GF-1}} \end{pmatrix} = (-1)^R \cdot \begin{pmatrix} 30\,562.49 \text{ rad/rad} \cdot \text{DWS}_{h,\text{GF-1}} \\ 31\,112.70 \text{ rad/rad} \cdot \text{DWS}_{v,\text{GF-1}} \end{pmatrix} \quad (2.42)$$

for GF-1, and

$$\begin{pmatrix} \psi_{\text{dws,GF-2}} \\ \theta_{\text{dws,GF-2}} \end{pmatrix} = (-1)^R \cdot \begin{pmatrix} 30\,563.73 \text{ rad/rad} \cdot \text{DWS}_{h,\text{GF-2}} \\ 31\,594.28 \text{ rad/rad} \cdot \text{DWS}_{v,\text{GF-2}} \end{pmatrix} \quad (2.43)$$

for GF-2. The factor $(-1)^R$ denotes a sign flip due to the beams' frequency ordering. Its value is determined by the frequency ordering, i. e., $R = 1$ if $\nu_{\text{rx}} > \nu_{\text{lo}}$, and $R = 0$

otherwise. Here, ν_{rx} and ν_{lo} denote the optical frequencies of the received and local oscillator beams, respectively. These angles may be called yaw and pitch in some particular reference frame. An imaging system placed in front of the photodiodes can suppress potential beam walk on the photodiodes under beam rotation. If the imaging system is well-designed, the optical path length is kept constant as a side-effect, cf. section 3.1.5.

According to DWS, one can also define the normalized and unitless differential power sensing (DPS) signals as

$$\text{DPS}_h = \frac{P_{\text{left}} - P_{\text{right}}}{P_{\text{total}}} = \frac{P_A - P_B + P_C - P_D}{P_A + P_B + P_C + P_D} \quad (2.44)$$

$$\text{DPS}_v = \frac{P_{\text{top}} - P_{\text{bottom}}}{P_{\text{total}}} = \frac{P_A + P_B - P_C - P_D}{P_A + P_B + P_C + P_D}. \quad (2.45)$$

They provide information about the position of the beam spot on the QPD and are hence a measure for the beam walk.

2.3.4. Carrier-to-Noise Ratio (CNR)

One can define the carrier-to-noise ratio (CNR) as (Koch, 2020)

$$C/N_0 = 10 \cdot \log_{10} \left(\frac{A_b^2/2}{S_{\text{n,cs}}} \right), \quad (2.46)$$

wherein

$$A_b = 2\mathcal{R} \sqrt{\eta_{\text{het}} \eta_{\text{BS}}^t P_{\text{lo}} \eta_{\text{BS}}^r P_{\text{rx}}} \quad (2.47)$$

is the beatnote peak amplitude of the oscillating term (or AC part), cf. equation (2.28), in units of Ampere with the photodetector-specific responsivity $\mathcal{R} \approx 0.6 \text{ A/W}$ for In-GaAs sensors at a wavelength of 1064 nm. $S_{\text{n,cs}}$ is the single-sided power spectral density (PSD) of the cumulated additive noise of the photoreceivers and phase readout in units of A^2/Hz , which contains contributions from photodiode shot noise, detector input current noise, and relative intensity noise of the laser (Mahrdt, 2014). The detector noise per quadrant of a QPD is denoted $S_{\text{pd,q}}$, where the subscript q denotes the segment or quadrant. The combination of the total readout noise in the ranging signal is assessed afterward.

The PSD of shot noise is proportional to the optical power. Assuming that the power in the received beam is small, $P_{\text{rx}} \ll P_{\text{lo}}$, it can be expressed as

$$S_{\text{sn,q}} = 2q\mathcal{R}P_{\text{lo,q}} \quad (2.48)$$

with the elementary charge $q = 1.6 \cdot 10^{-19} \text{ C}$. The per-quadrant local oscillator power depends on the individual optical setup, i. e., on the total local oscillator power P_{lo} and the ratio of the beamsplitters in the optical path. Given that 10% of the local oscillator power is used for local readout, and two hot-redundant QPDs with a 50:50 splitter are used, then $P_{\text{lo,q}} = 0.1P_{\text{lo}}/8$.

The photodetector input current noise level is a property of any individual photodetector. It is in the order of $S_{\text{pd,q}} = (5 \cdot 10^{-12})^2 \text{ A}^2/\text{Hz}$ for the flight photodiodes in the LRI (Barranco et al., 2017).

Table 2.1. Electronic readout noise $S_{n,cs}$ and its contributors within the LRI setup.

Item	Symbol	Value	Unit	Note
Local laser power	P_{lo}	25	mW	Sheard et al. (2012)
Photodiode Responsivity	\mathcal{R}	0.6	A/W	Mahrdt (2014)
Laser RIN	RIN	$(3 \cdot 10^{-8})^2$	1/Hz	Mahrdt (2014)
Electronic noise	$S_{pd,q}$	$(5 \cdot 10^{-12})^2$	A ² /Hz	Barranco et al. (2017)
Shot noise	$S_{sn,q}$	$6.00 \cdot 10^{-23}$	A ² /Hz	eq. (2.48)
RIN noise	$S_{rin,q}$	$3.16 \cdot 10^{-23}$	A ² /Hz	eq. (2.49)
Quadrant Noise	$S_{n,q}$	$1.17 \cdot 10^{-22}$	A ² /Hz	eq. (2.50)
Coherent Sum Noise	$S_{n,cs}(n=8)$	$2.71 \cdot 10^{-21}$	A ² /Hz	eq. (2.51)

Table 2.2. Local beam parameters and maximum heterodyne efficiency

Item	Symbol	Value	Unit
Local waist radius	$w_{0,lo}$	2.5	mm
Clipping aperture radius	$r_{rx,ap}$	4	mm
Beam divergence	Θ_{div}	135	μrad
Maximum het. efficiency	$\eta_{het,0}$	0.669	–

The last noise source to be considered is relative intensity noise (RIN) of the laser, which depends on the square of the local oscillator power. It is expressed as (Mahrdt, 2014)

$$S_{rin,q} = (\mathcal{R}P_{lo,q})^2 \cdot \text{RIN} . \quad (2.49)$$

The total per-quadrant noise then reads

$$S_q = S_{pd,q} + S_{sn,q} + S_{rin,q} . \quad (2.50)$$

Of the three noise sources introduced above, the electronic detector noise and shot noise are uncorrelated among the quadrants. However, the RIN is correlated as it originates from the same light source for all quadrants. This property must be considered when computing the noise for a coherent sum of segments. Hence, the coherent sum for n photodiode segments reads

$$S_{n,cs} = n(S_{pd,q} + S_{sn,q}) + n^2 S_{rin,q} . \quad (2.51)$$

Although the working principle of the LRI is introduced later in section 3.1, table 2.1 lists realistic numerical values for the individual noise contributors.

2.3.5. Heterodyne Efficiency

The heterodyne efficiency η_{het} was implicitly used in previous sections. It is a function of the two interfering electric fields and is described by their overlap integral σ or phase front similarity on the photodiode, which can be computed as (Müller, 2017)

$$\sigma = \sqrt{\eta_{het}} \cdot e^{i\varphi} = \frac{\int_A \vec{E}_{rx}(\vec{r}) \cdot \vec{E}_{lo}^*(\vec{r}) dx dy}{\sqrt{P_{rx} \cdot P_{lo}}} , \quad (2.52)$$

i	p_i	q_i
0	0.9567	1.8663
1	1.0143	1.5448
2	-5.0297	-8.2989
3	10.1075	16.1162
4	-8.3148	-12.3148
5	3.1866	4.3253
6	-0.4688	-0.5788

Table 2.3. Polynomial coefficients for the heterodyne efficiency approximation f in equation (2.55) for a circular photodiode, $f_{\text{cpd}} = \sum_i p_i x^i$, and a single segment of a QPD, $f_{\text{seg}} = \sum_i q_i x^i$.

in which A denotes the photodiode's active area, and the star denotes the complex conjugate. The phase φ can be measured with a phasemeter. The heterodyne efficiency

$$\eta_{\text{het}} = |\sigma|^2 \quad (2.53)$$

takes values between zero and one and describes the real-valued overlap between the two interfering electric fields. The maximum heterodyne efficiency $\eta_{\text{het},0}$ for one local Gaussian and a received flat top or top hat beam is (Mahrdt, 2014)

$$\eta_{\text{het},0} = \frac{2w_{0,\text{lo}}^2}{r_{\text{rx,ap}}^2} \tanh\left(\frac{r_{\text{rx,ap}}^2}{2w_{0,\text{lo}}^2}\right). \quad (2.54)$$

Here, $r_{\text{rx,ap}}$ is the radius of the clipping aperture again, and $w_{0,\text{lo}}$ is the waist radius of the local oscillator. Table 2.2 lists the parameters as present in the LRI. The heterodyne efficiency remains constant under beam tip and tilt, common to both beams or phase front changes among the two beams. However, it decreases with a growing relative angle α_{tx} between the two beams' propagation axes. The drop-off can be regarded as having a Gaussian shape and reads (Müller, 2017)

$$\eta_{\text{het}}(\alpha_{\text{tx}}) = \eta_{\text{het},0} \cdot \exp\left(-2\alpha_{\text{tx}}^2 / (\Theta_{\text{div}} \cdot f_{\text{cpd}}(w_{0,\text{lo}}/r_{\text{rx,ap}}))^2\right), \quad (2.55)$$

wherein the angle α_{tx} is the angular misalignment of the two interfering beams as measured by the DWS. The unitless function $f_{\text{cpd}}(w_{0,\text{lo}}/r_{\text{rx,ap}})$ is a polynomial approximation of the heterodyne efficiency drop-off on a circular photodiode depending on the local beams' waist size, as derived by numerically solving the integral of equation (2.55) in Müller (2017, sec. 2.6.11)^[1]. The polynomial coefficients are given in table 2.3.

Note that equation (2.55) is valid for circular photodiodes only. However, the coherent sum over the four quadrants of a QPD approximates the behavior of such a single-element photodiode. One can express the heterodyne efficiency on a single element of a quadrant photodiode as well through equation (2.55), by replacing f_{cpd} by f_{seg} , whose coefficients are also given in table 2.3.

^[1]In the cited reference, the polynomial functions are called ψ and ψ_2 . As this Greek letter is used for the yaw angle within this thesis, it was replaced by a more generic function symbol f_{cpd} and f_{seg} . Further, eq. 2.349 in Müller (2017) contains a typographical error, which has been corrected in equation (2.55).

2.4. Interferometer

An interferometer refers to a device capable of converting a differential phase of two beams into a measurable voltage change using the interferometry principle introduced before. It typically consists of two or more light paths for the beams to travel, which are then recombined to produce an interference pattern. This pattern is then sensed by a photodiode with either a single element, four elements, or even with an entire camera-like photodiode array. Usually, the interfering beams originate from the same light source and thus have the same beam properties. One is regarded as the reference beam, and the other is the measurement beam. The measurement beam undergoes any physical process that changes its optical path length, such as a relative motion of a mirror or path length shifts, e. g., due to gravitational waves. The resulting interference pattern is detected using one of the photoreceivers as introduced earlier and then analyzed to infer the properties of the involved light waves, such as their wavelength λ , frequency ν , phase φ , or amplitude \vec{E} and power \vec{E}^2 .

The following section explains the concept of inter-satellite laser ranging using interferometry, and the phase relations are defined. Although the LRI is used as an example, the formulas are applicable more generally.

The Laser Ranging Interferometer

3

“ *Science is magic that works.* ”

— KURT VONNEGUT —
Science-Fiction Author

3.1. Interferometric Intersatellite Laser Ranging

Intersatellite laser ranging with interferometers is relatively new. It started with developing the Laser Interferometer Space Antenna (LISA); first proposals date back to the early 1990s (Amaro-Seoane et al., 2017). The first laser interferometer in space was LISA Pathfinder (Antonucci et al., 2012). In contrast, the first laser interferometric measurement between two spacecraft was achieved by the Laser Ranging Interferometer (LRI) onboard GRACE Follow-On (GRACE-FO) (Sheard et al., 2012), which was built in the 2010s, launched on 22nd of May 2018 and commissioned shortly after (Abich et al., 2019). The LRI consortium is a US-German partnership between the National Aeronautics and Space Administration (NASA) and German Aerospace Center (Deutsches Zentrum für Luft- und Raumfahrt) (DLR), including the Jet Propulsion Laboratory (JPL), SpaceTech Immenstaad GmbH (STI) and the Albert-Einstein Institute (AEI), among others.

This section serves as a foundational pillar and provides the essential principles of the instrument for readers new to the field. It aims to establish a common framework and terminology to facilitate understanding of subsequent chapters. However, for readers already familiar with the LRI, this section will contain already-known information and may be bypassed. Furthermore, this section makes some simplifying assumptions for easier understanding, which are not mentioned explicitly. However, some of these are addressed later in this thesis when in-depth instrument characterization is performed.

3.1.1. LRI Setup: An Overview

The LRI is a single instrument with equal units placed on the two spacecraft (SC), commonly denoted as GF-1 and GF-2, sometimes GRACE-C and GRACE-D. The setup has first been described in Sheard et al. (2012), and a schematic is shown in figure 3.1.

At first, an intuitive description of the LRI working principle is given in terms of the beams' frequencies of different paths, which are sketched in figure 3.2. Afterward, the individual subunits are explained in more detail. A reference laser unit (RLU) provides $P_{\text{lo}} = 25 \text{ mW}$ of laser light at an optical frequency of $\nu_{\text{R}} \approx 281 \text{ THz}$. 10% of which are used for frequency stabilization, and the remaining 90% are sent onto the optical bench assembly (OBA). It is reflected at the fast steering mirror (FSM) and the beamsplitter and traverses the triple mirror assembly (TMA) to be routed around the cold-gas tanks (not shown) and the K-Band Ranging (KBR) antenna at the satellites'

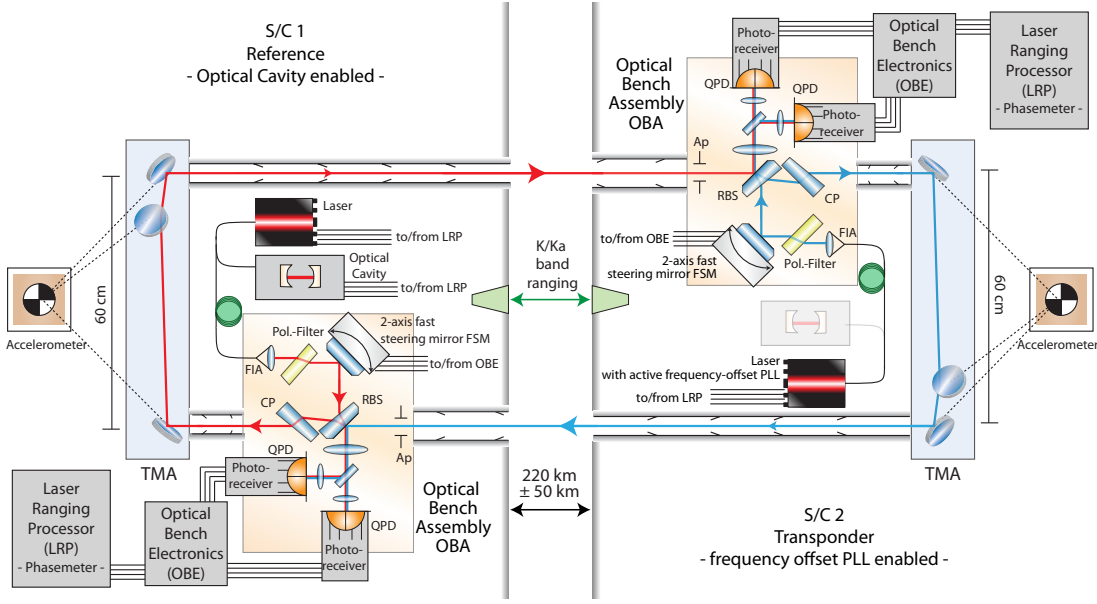


Figure 3.1. Sketch of the LRI hardware. TMA - Triple Mirror Assembly; FIA - Fiber Injector Assembly; FSM - Fast Steering Mirror; RBS - Recombination Beamsplitter; CP - Compensation Plate; Ap - Aperture; QPD - Quadrant Photodiode. Modified version of [Abich et al. \(2019, Fig. 1\)](#).

front surface. After propagating through the TMA, the beam leaves the reference SC and travels to the transponder SC. By traveling the distance of $L \approx 170$ km to 270 km between the two spacecraft, the optical power at the aperture of the receiving spacecraft is clipped, according to equation (2.20). Inserting the parameters of the LRI setup into that equation, i. e., the local oscillator power $P_{tx} = 0.9 \cdot P_{lo} = 22.5$ mW and a clipping aperture radius $r_{rx,ap} = 4$ mm, a received optical power of 0.5 nW to 1.4 nW is obtained in the perfectly aligned case of $\alpha_{tx} = 0$ rad. In practice, there might be an angular mispointing of the transmit beam, e. g., due to production tolerances of the TMA mirror perpendicularity. In case of such a misalignment of $\alpha_{tx} = 100$ μ rad, only 180 pW of optical power arrives at the distant spacecraft in the worst case. Nonetheless, the received beam interferes with the local oscillator and is sensed on the QPDs, which are hot-redundant on both sides. They feature four quadrants to provide angular relative beam tip and tilt information. The received beams' optical frequency is shifted by a Doppler shift f_D due to the relative motion of the SC when detected at the transponder. Other than on the reference side, where the local oscillator is locked to a reference cavity, the transponder laser is frequency-offset locked to the frequency of the incoming beam $\nu_R + f_D$ with an additional $f_{off} = 10$ MHz, which maintains the transponder lasers' frequency at

$$\nu_T = \nu_R + f_D + f_{off} . \quad (3.1)$$

The beam is again routed through a TMA and propagates back to the reference unit, picking up a second Doppler shift. The beat frequency f_R on the reference side is the difference between the local oscillators' and the incoming beams' frequency, i. e.,

$$f_R = (\nu_T + f_D) - \nu_R = f_{off} + 2f_D . \quad (3.2)$$

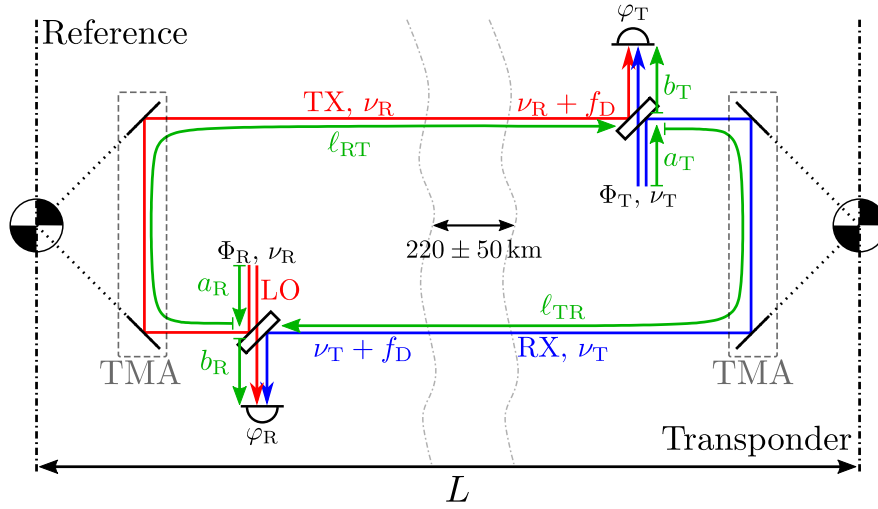


Figure 3.2. Schematic of the light paths and frequencies in the LRI setup. LO: Local oscillator; TX: transmit beam; RX: received beam. Optical frequencies are labeled with ν , while radio frequencies are labeled with f .

The frequency ordering is chosen such that the transponder laser frequency is always above the reference laser frequency. The scientific measurement of the inter-spacecraft range variations is encoded in the Doppler shift

$$f_D \approx -\frac{\dot{\rho}}{\lambda_R} \quad (3.3)$$

with $\dot{\rho}$ being first time-derivative of the inter-satellite range and $\lambda_R = c/\nu_R \approx 1064$ nm the wavelength of the reference oscillator (Sheard et al., 2012). Although the previous description was given in terms of frequencies, the measurement takes place in the phase domain, which is the integral of the frequency over time. Hence, the LRI measured phase difference represents the roundtrip length $2L = \ell_{RT} + \ell_{TR}$ up to an initial and constant bias, but not the orthogonal paths, since path length changes in these paths a_R, b_R, a_T, b_T cancel out as both beams propagate these segments. The conversion of the measured phase φ in units of cycles into a physical displacement or range ρ in units of meter can be done using the absolute laser frequency ν_R of the reference laser (or equivalently, its wavelength λ_R), as

$$\rho = \lambda_R \varphi = \frac{c}{\nu_R} \varphi. \quad (3.4)$$

Therefore, its knowledge and stability, known to be the limiting noise source of the LRI at high frequencies, are critical.

3.1.2. Reference Frames and Spacecraft Pointing

The different spatial reference frames onboard GRACE-FO are defined in Wen et al. (2019), of which a small excerpt is summarized in the following. The spacecraft itself provides the so-called satellite frame (SF) or science reference frame (SRF). Its origin is the nominal spacecraft center of mass, with the positive x -axis pointing towards the front surface at the position of the KBR horn, z pointing downwards, and y being

perpendicular to the right side of the satellite. All scientific data in the Level 1B data products is given in this particular reference frame. Typically, rotations in this frame are called roll, pitch, and yaw. Within this thesis, yaw and pitch are denoted as ψ and θ .

The accelerometer (ACC) has its own reference frame aligned with the SRF but with different axes naming. In essence,

$$x_{\text{acc}} = y_{\text{srf}} \quad , \quad y_{\text{acc}} = z_{\text{srf}} \quad , \quad z_{\text{acc}} = x_{\text{srf}} \quad . \quad (3.5)$$

This re-naming is a consequence of the fact that the x -axis in the ACC frame is the least-sensitive one, which, for the scientific benefit, shall point in the SRF cross-track direction. The design sensitivity levels are

$$\text{ASD}[x_{\text{acc}}](f) \leq 10^{-9} \text{ m/s}^2/\sqrt{\text{Hz}} \cdot \sqrt{\left(1 + \frac{f}{0.5 \text{ Hz}}\right)^4 + \frac{0.1 \text{ Hz}}{f}} \quad (3.6)$$

$$\begin{aligned} \text{ASD}[y_{\text{acc}}](f) &= \text{PSD}[z_{\text{acc}}](f) \\ &\leq 10^{-10} \text{ m/s}^2/\sqrt{\text{Hz}} \cdot \sqrt{\left(1 + \frac{f}{0.5 \text{ Hz}}\right)^4 + \frac{0.005 \text{ Hz}}{f}} \quad , \quad (3.7) \end{aligned}$$

where both noise amplitude spectral densities (ASDs) increase towards lower frequencies (Kornfeld et al., 2019).

The most important reference frame in the scope of this thesis is the LRI optical frame (LOF), as the pointing of the LRI beams is defined within this frame. It is also defined per spacecraft, with the center co-aligned to the frames introduced before. Ideally, the SRF and LOF are identical, and the transformation between them is given as the unity matrix. Still, residual angular deviations might arise from integration errors during spacecraft construction. These small residual angles were calibrated in-flight during the commissioning of the LRI with the so-called initial acquisition scan, see e. g. Abich et al. (2019). In this LOF, the x_{lof} axis points parallel to the nominal beam propagation axis that is defined through the line-of-sight between the two spacecraft, more precisely between the two virtual intersection points of the TMAs. Rotations, or pointing angles, around the z_{lof} axis (yaw) are denoted with ψ , while rotations around the y_{lof} axis (pitch) are represented with θ throughout this thesis. They are measured with the calibrated DWS signals, cf. section 2.3, where the horizontal and vertical combinations are equivalent to yaw and pitch, ψ and θ , respectively.

The GRACE-FO spacecraft use an attitude and orbit control system (AOCS) for maintaining the desired pointing (Kornfeld et al., 2019; Cossavella et al., 2022). In nominal operations, the two spacecraft point towards each other, along the (estimated) line-of-sight (LOS) within (Kornfeld et al., 2019)

$$\text{ASD}[\theta_{\text{aocs}}](f) = \text{ASD}[\psi_{\text{aocs}}](f) < 0.5 \text{ mrad}/\sqrt{\text{Hz}} \quad (3.8)$$

by employing accelerations through either magnetic torque rods or cold-gas thrusters.

3.1.3. Laser and Cavity

The two reference laser unit (RLU) are the light sources, providing $P_{\text{RLU}} = 25 \text{ mW}$ optical power at an optical frequency of $\nu_{\text{R}} \approx 281 \text{ THz}$. 90% of which are split internally

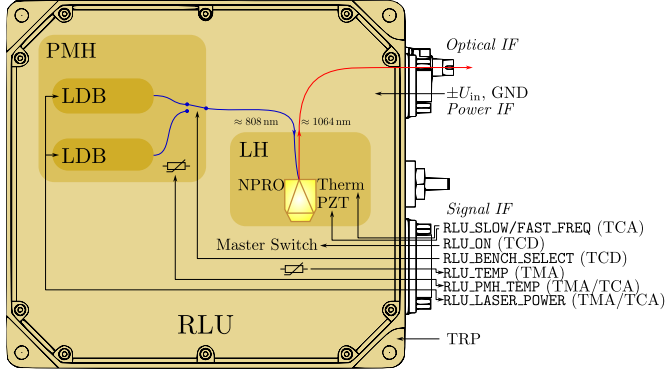


Figure 3.3. Sketch of the RLU interior. It hosts two laser diode benches (LDBs) for redundancy. The pump light at 808 nm is guided to the laser head and the NPRO crystal, which is resonant for a wavelength of about 1064 nm. The RLU features several TM/TC data streams through the signal interface; some are shown in the sketch.

and guided through the principal optical fiber to a fiber coupler onto the OBA. A secondary output fiber, carrying the remaining 10% laser power, is connected to the optical reference cavity after an electro-optical modulator (EOM). The RLUs are similar to the ones already flown on LISA Pathfinder and are also foreseen for future gravity missions (Nicklaus et al., 2020) and are one option for the seed lasers for the space-based gravitational wave detector LISA (Armano et al., 2017).

The RLU is based on the principle of a solid-state non-planar ring oscillator (NPRO) laser, see e. g., Kane et al. (1985). It is controlled through the laser ranging processor (LRP) (see below). It features several telecommand and telemetry (TM/TC) channels for setting the desired output power by increasing the pump current and optical output frequency by thermally or mechanically changing the optical properties of the NPRO crystal. Furthermore, the temperature of the pump diode bench can be controlled. The telemetry channels comprise internal temperature, current consumption, and optical power measurements. The RLU provides partial redundancy through one of the two cold-redundant laser diode benches (LDBs) within the pump module head (PMH). A schematic of the RLU interior is shown in figure 3.3. The RLU is controlled through the signal interface, a two-way interface between the RLU and the LRP, where several TM/TC channels are connected. Besides controlling the laser frequency and power, selecting the active LDB, and turning the RLU on and off, the telemetry channels comprise a readout of the PMH temperature and optical power, as well as the general RLU temperature and current consumption of the unit. The light propagates freely within the RLU but is coupled into a fiber before the optical interface at the output. The RLU optical power is likely measured by splitting a small part of the light leaving the NPRO and guiding it onto a photodiode.

A constant optical frequency is achieved by stabilizing the RLU to the optical reference cavity by employing the Pound-Drever-Hall (PDH) scheme (Drever et al., 1983). The requirement on residual laser frequency fluctuations is $\delta\nu_R < 30 \text{ Hz}/\sqrt{\text{Hz}}$ for Fourier frequencies above 10 mHz, with a relaxation towards lower Fourier frequencies. This relaxation accounts, e. g., for thermal noise (Thompson et al., 2011; Sheard et al., 2012). The actual in-flight laser stability, expressed as an ASD, is better, namely

$$\text{ASD} [\delta\nu_R] (f) \approx \frac{10^{-15} \cdot \nu_R}{\sqrt{f}} \approx 0.3 \frac{\text{Hz}}{\sqrt{f}} \quad (3.9)$$

for Fourier frequencies above 200 mHz, where the laser frequency stability dominates the measurement (Spero, 2021). Laser frequency variations couple directly into the

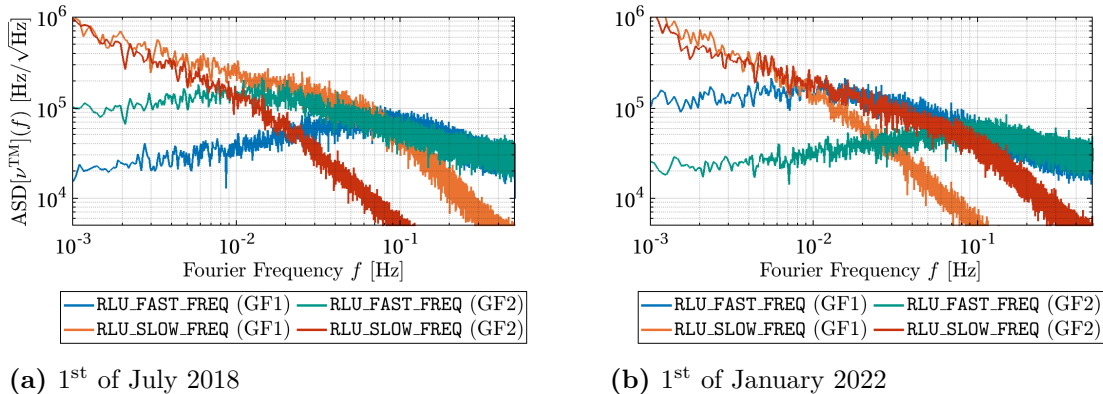


Figure 3.4. ASD of laser frequency variations from the actuator signals using the nominal frequency coupling coefficients. **(a)** GF-1 in transponder, GF-2 in reference role. **(b)** GF-1 in reference, GF-2 in transponder role.

ranging measurement ρ through

$$\text{ASD}[\delta\rho](f) = \frac{\Delta L}{\nu_R} \text{ASD}[\delta\nu_R](f), \quad (3.10)$$

where $\Delta L \approx L = 220 \pm 50$ km is the length difference of the two interferometer arms, which in this case is approximately the absolute distance between the two spacecraft (Sheard et al., 2012).

The tuning of the laser frequency, which is needed for the stabilization strategies, is provided through the frequency tuning telecommands. These analog voltages are connected to a thermal element for slow variations and a piezo-electric transducer (PZT) for fast actuation. They induce thermal or mechanical stress on the NPRO, slightly changing the crystalline structure. That structural change alters the refractive index and thus also the resonance frequency of the optical light path in the NPRO. A tuning of approximately ± 5 GHz can be achieved in the case of the RLUs implemented in the LRI. The cross-over Fourier frequency between the slower thermal and faster PZT actuator is at about 100 mHz in the PDH setup (reference mode) and at 10 mHz in the transponder mode. Typical ASDs of these signals are shown in figure 3.4 for both spacecraft, either in the transponder or reference role. It is apparent that the cross-over frequency between the two frequency actuators is at around 0.1 Hz for the transponder phase lock and at 0.01 Hz for the PDH lock on the reference unit.

A laser frequency model can be formulated, with calibrated coupling coefficients between the frequency actuator signals, as

$$\nu^{\text{TM}}(t) = \begin{pmatrix} c_{\text{pztIL}} \\ c_{\text{pztOOL}} \\ c_{\text{thermIL}} \\ c_{\text{thermOOL}} \\ c_{\text{lasTRP}} \end{pmatrix} \cdot \begin{pmatrix} \text{pztIL}(t) \\ \text{pztOOL}(t) \\ \text{thermIL}(t) \\ \text{thermOOL}(t) \\ \text{lasTRP}(t - \tau) - 26^\circ\text{C} \end{pmatrix} + \nu_{0,\text{Air}} + \Delta\nu_{\text{AirToVac}}. \quad (3.11)$$

This simple, linear model relates the true laser frequency to the actuator signals and RLU temperature, measured at the thermal reference point (TRP) and called `lasTRP`.

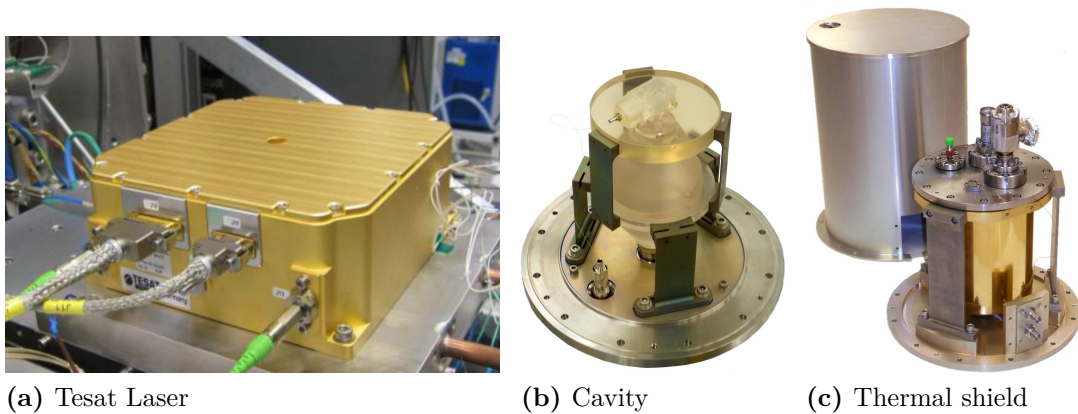


Figure 3.5. Photographs of the NPRO laser for GRACE-FO from Tesat-Spacecom GmbH (image from [Dubovitsky et al. \(2018\)](#)) and the 77.5 mm optical cavity and its thermal housing (images from [Thompson et al. \(2011\)](#)).

The TRP for these RLUs is located at one of their feet, which are the thermal interface to their mounting plate, cf. figure 3.3. The static absolute offset $\nu_{0,\text{Air}}$ is determined on-ground in a laboratory, while the frequency deviation between a laboratory environment and vacuum conditions, $\Delta\nu_{\text{AirToVac}}$, is provided by the manufacturer. The calibration of these coupling factors is described in detail in section 5.3.

The lasers were manufactured by the German company Tesat Spacecom ([Dubovitsky et al., 2018](#)), while the cavity was produced by Ball Aerospace, a US company ([Thompson et al., 2011](#)). Photographs of both are shown in figure 3.5.

3.1.4. Optical Bench Assembly and Electronics

The frequency-stabilized light from the laser and cavity system is injected into the OBA by a fiber injector assembly (FIA). The optical bench functionalities are to launch the laser beam to the distant SC, to superimpose the received and local oscillator beams and convert that heterodyne beat signal to an electric signal, and to enable active beam steering ([Nicklaus et al., 2017](#)).

The beam waist size w_0 on the optical bench is approximately 2.5 mm, while the clipping aperture for the incoming beam has a radius of 4 mm ([Heinzel et al., 2012](#)). The divergence is in the order of $\Theta \approx 135 \mu\text{rad}$. A compensation plate is placed in the transmit path to reduce tilt-to-length coupling (TTL), arising from the propagation of the transmit beam in the recombination beam splitter, which has its high-reflective coating on the side facing the incoming beam.

The OBA features a small imaging system between the recombination beam splitter and the QPDs. The imaging system provides several valuable features: First, the optical path length through that system of two lenses is invariant under different beam incident angles before the first lens. That means no TTL arises after the beam splitter, as it would without these lenses. Furthermore, the system's pupil plane image is on the surface of the QPD to reduce beam-walk [Sheard et al. \(2012\)](#).

3.1.5. Fast Steering Mirror (FSM)

The beam pointing requirement of the LRI is determined by the properties of the Gaussian beams and their amplitude profile. Given the beams' divergence angle $\Theta \approx 135 \mu\text{rad}$, the beams' amplitude at the receiving spacecraft drops by $1/e^2 \approx -8.5 \text{ dB}$ for a beam mispointing of $w(L) \approx L \cdot \Theta \approx 30 \text{ m}$ at the receiving spacecraft, for $L = 220 \text{ km}$, cf. equation (2.8). The electric field amplitude (or power) at the distant spacecraft has to maintain specific requirements for successfully tracking the beatnote signal within the LRP, which require smaller pointing offsets than the capabilities of the AOCS of $0.5 \text{ mrad}/\sqrt{\text{Hz}}$, cf. equation (3.8). Hence, active beam steering is needed for the LRI in order to firstly maximize the local heterodyne efficiency, and secondly maximize the beam power at the receiving spacecraft. The beam steering is achieved by the combination of the DWS technique (cf. section 2.3) to measure the angular misalignment of the local and the received beam, and a two-axis steering mirror, the FSM, which ultimately compensates for that misalignment (Sheard et al., 2012). The FSM movement is induced through voice coils, while an internal position sensing system using a Kaman-sensor is used for determining the actual mirror position (Langenbach et al., 2005). By utilizing the FSM, the beam leaving the LRI is antiparallel to the incoming beam, or in other words, the two roundtrip beams of the LRI travel along the LOS, independently of the actual satellite attitude, under the assumption of a perfect TMA, see the next section.

In a closed loop operation, the measured DWS-derived beam pointing angles, ψ_{dws} and θ_{dws} , which represent the angle between the local and the incoming beam, are zeroed by using the FSM as an actuator to align the local oscillator beam to the incoming beam in both axes (Abich et al., 2019). Aligning the two beams does not only maximize the heterodyne efficiency and signal strength on the QPDs, but it also ensures that the outgoing beam is (anti-)parallel to the incoming one, under the assumption of a perfect TMA. The active beam alignment concept is pictured in figure 3.6. The left panel shows the nominal situation in which the local and received beams are perfectly aligned after the beam splitter. Consequently, the wave fronts on the QPD are also aligned. In the center panel, the incoming beam arrives at an angle α , either due to local spacecraft rotation or because the distant spacecraft moved in the lateral direction. As a result, the received beam takes a different path through the imaging system and impinges the QPDs at an angle α/m with $m = 1/8$. This angle is measured using the DWS technique. It is then used as a control signal to the FSM servo, which consequently rotates the FSM, as depicted in the right panel. After rotation, the two beams are co-aligned again, and the DWS signal is zero. The transmit beam towards the TMA is parallel to the incoming RX beam. After propagating through the TMA, it is perfectly antiparallel to the incoming beam and propagates in the direction of the distant spacecraft.

3.1.6. Triple Mirror Assembly (TMA)

The TMA is needed to route the beams around the cold-gas tanks and the KBR antenna, which occupy the direct route between the centers of mass of the two SC (Sheard et al., 2012). It uses the principle of a corner cube, or a cat-eye, and consists of three mirrors, all perpendicular to each other. By that, the TMA introduces a lateral and vertical shifts of 600 mm and 48 mm, respectively, between the beams entering and exit-

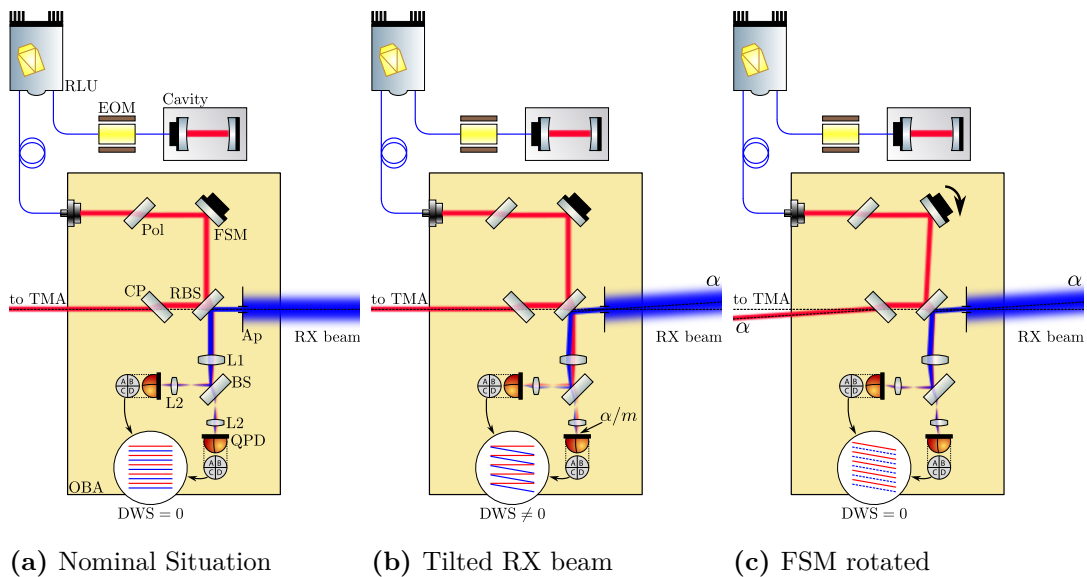


Figure 3.6. Concept of the local beam alignment using the FSM. **(a)** Local and RX beams are perfectly aligned, and their phase fronts are orthogonal to the QPD surface. **(b)** The local spacecraft rotated; hence the incoming beam arrives at an angle α . The DWS signal is non-zero. **(c)** The FSM is actuated to match the angle of the incoming beam. The DWS signal is again zero. The local beam that was reflected at the beamsplitter is parallel to the received beam.

Table 3.1. TMA Mirror positions w. r. t. the TMA vertex $V = (0, 0, 0)^T$ and their respective normal vectors. Units in mm.

	center			normal vector		
	c_x	c_y	c_z	n_x	n_y	n_z
M1	+300	+300	-24	$+1/\sqrt{2}$	+1/2	+1/2
M2	+300	-266	-24	$-1/\sqrt{2}$	+1/2	+1/2
M3	+333.9	-300	+24	0	$+1/\sqrt{2}$	$-1/\sqrt{2}$

ing the structure. The positions of the individual mirrors w. r. t. the virtual intersection point are listed in table 3.1, alongside the normal vectors of the mirror surfaces. A photograph of the TMA flight model is shown in figure 3.7. As the virtual intersection point of the three mirrors is actually outside the device, it can be mounted to the ACC, which occupies the SC center of mass (COM), such that the intersection point is co-located to the COM as well, which minimizes TTL (Sheard et al., 2012). The design of the TMA structure clips the maximum beam incidence angle above ± 3 mrad, being the initial acquisition scan range (Abich et al., 2019). The TMA provides three essential features:

1. The lateral beam separation of the incoming and outgoing beams is constant (600 mm)
2. The outgoing beam is always antiparallel to the incoming beam
3. The path length of a beam propagating through the TMA is independent of the

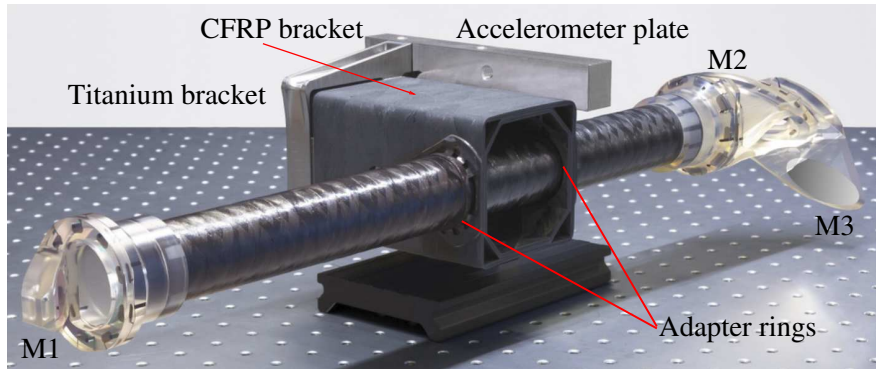


Figure 3.7. Photograph of the TMA flight model. Image Courtesy: SpaceTech GmbH.

beams' incidence angle. It is constantly twice the distance between the vertex and any arbitrary reference plane, that is perpendicular to the beams.

In addition to the active beam steering, the second property ensures that the outgoing beam always points toward the distant spacecraft. However, in case of imperfect angular alignment of the three mirrors, the transmitted beam is not antiparallel to the incoming beam. This effect will be investigated in chapter 7.

3.1.7. Laser Ranging Processor (LRP)

The LRP is the instrument computer of the LRI, relying on fast and precise data acquisition and handling using an FPGA. It was developed and built by the JPL (Bachman et al., 2017). Its main tasks are running the control loops for laser stabilization and the FSM steering, and tracking the interferometric path length signal. Furthermore, it digitizes the incoming analog data and provides them to the onboard computer (OBC) for being downlinked to Ground. The phase tracking of the MHz beat signal is based on DPLLs. More information about electronic phase readout for interferometric applications can be found in Gerberding (2014), Schwarze (2018), and Bachman et al. (2017).

The readout noise of the phasemeter is mainly driven by the CNR C/N_0 (cf. equation (2.46)) and can be computed as

$$\text{ASD}[\delta\varphi_{\text{LRP}}](f) \approx \frac{\lambda}{2\pi\sqrt{10^{C/N_0/10}}} \approx 50 \text{ pm}/\sqrt{\text{Hz}}, \quad (3.12)$$

where a $C/N_0 \approx 70 \text{ dB-Hz}$ was assumed to derive the numerical value, which is also the LRP requirement for reliably tracking the phase. At a higher CNR of 90 dB-Hz , the readout noise reduces to $5 \text{ pm}/\sqrt{\text{Hz}}$. The readout noise was also discussed in Müller et al. (2022).

Within the LRP, the data acquisition is performed at a rate of approximately 40 MHz and is subsequently converted to lower sampling rates. The final data rate of the scientific data, i. e., the phase measurement of the four QPD channels, are downlinked at a rate of roughly 10 Hz while housekeeping data packets have lower resolution.

The following paragraph focuses on data acquisition, filtering, and decimation, which will be needed later in this thesis. A simplified sketch of the anticipated working of the

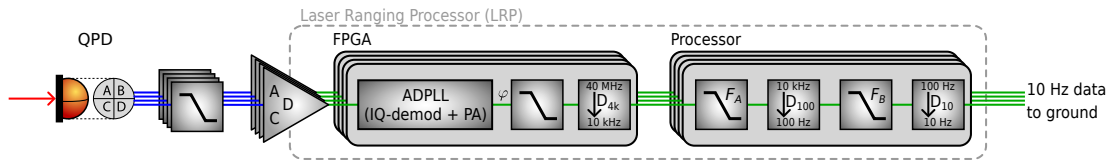


Figure 3.8. Sketch of the phasemeter processing chain. The optical signal (red) is converted to a voltage by the QPD and its electronics. The voltage is filtered in the analog domain and digitized at a rate of 40 kHz before the phase is extracted in an all-digital phase-locked loop and filtered.

decimation chain within the LRP principle is shown in figure 3.8. The optical signal of the interfering light rays is sensed on the QPD, which allows retrieving the ranging and beam tilt information from the four phase channels per spacecraft. Technically, there is also a fifth channel, which directly contains the coherent sum of the four quadrants and is used internally for the phase lock. However, this fifth channel is not downlinked to the ground. The photocurrents are converted into voltages within the optical bench electronics (OBE) through TIAs and digitized at a rate of approximately 40 MHz. The nominal clock rates are defined by the ultra-stable oscillator (USO) and read 38.656 000 MHz and 38.656 792 MHz for GF-1 and GF-2, respectively. However, the approximate value is used in the text for better readability. The phase information is subsequently extracted by an all-digital phase-locked loop (ADPLL), that is based on IQ-demodulation, a PIR and a PA (Ware et al., 2006; Wand et al., 2006; Gerberding, 2014), see section 2.3.1. The phase information is passed to the processor part, where a two-stage decimation takes place: first to a rate of 100 Hz for internal intermediate data streams and housekeeping, and second down to the 10 Hz output data rate. Low-pass filters are used before the decimators to avoid aliasing (Ware et al., 2006) of higher frequencies into the measurement band of 2 mHz to 100 mHz using two finite impulse response (FIR) filters A and B of length l_A and l_B , with $l_A > l_B$. The decimation is by a factor of 100 and 10 for filters A and B , respectively, giving a total decimation factor of 1000 to obtain the output data rate of 9.664 Hz (9.664 198 Hz on GF-2). The two filters each consist of a few hundred filter coefficients $c_{A/B}$ and corresponding registers m . The filter coefficients represent the impulse response of such a filter, while the registers m are memory cells, like a computer random access memory (RAM). The whole phase extraction and decimation are executed individually on the four phase channels and the fifth sum channel. The three filters, in the FPGA and processor, have a combined phase delay of exactly 28 802 038 clock ticks ≈ 0.745 s (Wen et al., 2019).

3.1.8. Other GRACE-FO Payloads

This section briefly introduces the payloads of the GRACE-FO mission apart from the LRI. It is not intended to explain every detail thoroughly but provide an overview. The information in this section is an excerpt of Kornfeld et al. (2019).

Microwave Instrument (MWI)

The Microwave Instrument (MWI) is the primary scientific instrument for measuring ranging data. It is based on the heritage design of the original Gravity Recovery And

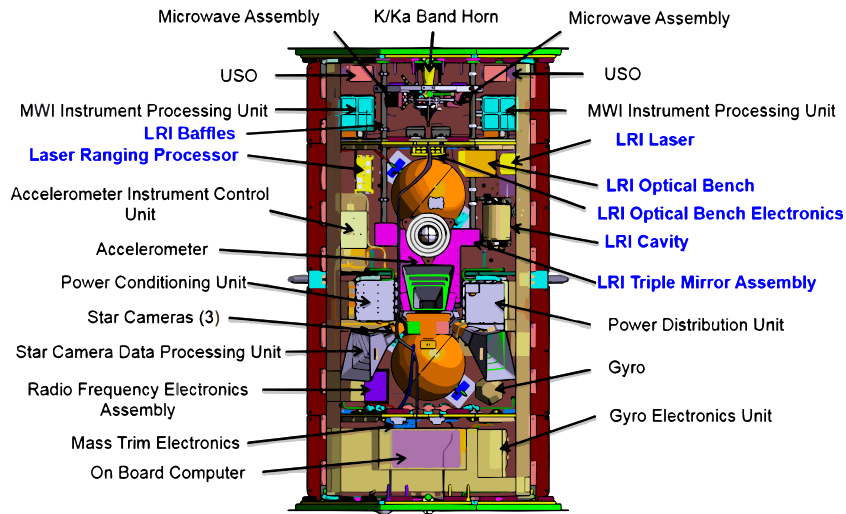


Figure 3.9. Schematic view of the GRACE-FO satellite interior. The parts belonging to the LRI are written in blue. Image based on [Dubovitsky et al. \(2018\)](#).

Climate Experiment (GRACE) mission. It is based on the principle of interfering electromagnetic waves, but in contrast to the LRI, the frequency is in the K- and Ka-bands of the microwave spectrum, at about 24.5 GHz and 32.7 GHz. These K/Ka-frequencies are derived by upsampling an USO frequency. Dual frequencies are used to remove delays due to ionospheric refraction effects. Although the exact delay is unknown and depends on the density and electron content of the atmosphere, the ratio of the delay between those frequencies is known precisely. The two measurements at different frequencies are then combined into an ionosphere-free combination. The measurement scheme is hence called Dual One-Way Ranging (DOWR). The KBR has a large TTL, which is caused by the offset of the KBR phase center to the SC center of mass of approximately 1.4 m. This antenna offset can be calibrated, and the erroneous signal is corrected in post-processing.

Furthermore, the global positioning system (GPS) antenna and the corresponding data processing is part of the MWI to provide the SC real-time position, velocity, and time information.

Accelerometer (ACC)

The ACC is the second scientific instrument on board. It features a test mass within an electrode housing. The test mass is freely floating within the housing but connected to it with a thin platinum wire to keep it at a well-defined electrostatic potential. The reference point of the ACC is the center of mass of the test mass, which is ideally co-located to the SC center of mass. Hence, the test mass flies on a geodesic in Earth's gravitational potential. The electrodes control and measure the test mass position using a capacitive readout scheme. If the SC encounters non-gravitational accelerations that act on the spacecraft but not on the internal test mass, the electrode housing moves w. r. t. the test mass, which is then recentered using the electrodes. The voltages applied to the electrodes to keep the test mass in the center of the housing are converted to the accelerations of the SC w. r. t. the test mass' geodesic motion. Using differential readout

per axis, linear and angular accelerations can be measured. The ACCs on GRACE-FO were manufactured by Onera.

Star Camera Assembly (SCA) and Inertial Measurement Unit (IMU)

Star cameras are used for absolute attitude measurement in inertial space. Three Camera Head Units (CHUs) on the top and side panels of the spacecraft hull record images from the stars above the SC. These images are compared to an onboard star catalog to determine the camera heads' line of sight and thus the orientation of the SC in inertial space. Three independent camera heads with different boresights are used to minimize the off-time due to sun- or moon-blindings, which saturate the cameras.

The Inertial Measurement Unit (IMU) comprises four fiber-ring laser gyroscopes in a tetrahedral arrangement. Each uses the Sagnac effect. Light is sent through the fiber-optic ring in two directions. On rotation, the two counterpropagating light waves travel different optical path lengths, causing a relative phase shift. The IMU does not provide absolute rotation angles, but only rotation rates. Three of the four rings are used simultaneously for redundancy, providing complete three-dimensional rotation information. The absolute angular information of the Star Camera Assembly (SCA) is merged with the more precise but biased IMU measurement in post-processing.

On Board Computer (OBC)

The OBC hosts the central command and data handling system. Based on the flight heritage of, e.g., Swarm and GOCE, it is responsible for the AOCS, thermal control systems, data packet timing and payload synchronization. It is internally redundant and provides memory storage for the science- and housekeeping data and telecommand modules for data up- and downlink at up to 3 Mbit/s.

3.1.9. Mission Phases

This section briefly overviews the mission phases, focusing on non-nominal events when the LRI was not recording science data. After the GRACE-FO satellites were launched on 22nd of May 2018, the launch and early operations (LEOP) phase started. That phase ended on 26th of May, with successful communication established and both SC reached a stable orbit. In the current configuration, GF-1 is leading the constellation and is flying “backward”, i. e., rotated by 180° around the local z -axis (yaw). GF-2 is trailing in a distance of 220 ± 50 km and the two front surfaces of the SC are facing each other. That implies that the SC are not oriented along the orbit to minimize air drag but towards each other to maximize the microwave and laser signal amplitudes at the distant spacecraft. After the LEOP phase, the scientific instruments were turned on and checked out within the in-orbit commissioning (IOC) phase, which included the commissioning of the LRI. The LRI subsystems on each spacecraft were turned on individually before the dual-SC checkout started, and the laser link was established for the first time on 14th of June 2018 with GF-2 in reference role.

Shortly after the commissioning, the nominal MWI instrument processing unit (IPU) on GF-2 autonomously shut down due to an undercurrent, which could not be recovered (NASA/JPL, 2018; Webb et al., 2018). Since then, the redundant IPU has been operating on GF-2. That IPU failure caused a long non-operational period of the LRI;

it was reactivated on 12th of December 2018 with GF-1 in reference role. Smaller gaps in the LRI operations in 2019 and 2020 were caused by other platform-related events, like an OBC problem (Webb et al., 2019b) or a corrupted on-board clock due to single event upsets (Webb et al., 2019a).

In mid-2021, several short periods started, in which the SC are in a so-called nadir pointing mode. They typically lasted two days per week until the beginning of 2022. In this nadir pointing mode, the spacecraft platforms do not face each other but are oriented along the orbit. This offset of approximately 2° is beyond the FSM field-of-regard, and hence, the LRI was switched off. The aim was to help the accelerometer transplant product generation, as the ACC on GF-2 is malfunctioning. Other periods in nadir pointing were July & August 2022 and January & February 2023. From 2023-Jul-01 on, the LRI is commanded to a diagnostic mode for six months, while the AOCS of both SC is in a wide range mode, with less strict requirements on the relative pointing. Again, these wider angular variations are beyond the LRI field-of-regard.

In some figures within this thesis, the background coloring indicates such phases: green denotes a science phase with GF-1 as the reference spacecraft, GF-2 was in reference role for yellow colors, and the LRI was not in science mode for gray colors.

3.2. In-Flight Sensitivity and Previous Studies

Understanding the instrument noise is vital for developing future ranging interferometers based on LRI heritage technology. However, the accurate assessment of the instrument noise is challenging, as it is usually superimposed with noise sources or measurements beyond the instrument-internal errors.

In general, the state of the LRI is good at the time of this writing, i. e., after more than five years in orbit. The scientific outcome, i. e., the ranging signal, shows good agreement with the microwave instrument but with significantly increased sensitivity, and is furthermore well understood (Abich et al., 2019). Figure 3.10 shows amplitude spectral densities of a four-day LRI ranging measurement in March 2023. The orbital peak and higher harmonics stand out clearly, while the gravitational signals (static and dynamic) roll off at a Fourier frequency of about 37 mHz. The LRI signal is dominated by non-gravitational accelerations up to 200 mHz, e. g., from residual air drag or solar radian pressure (Misfeldt, 2019). The highest frequencies are limited by the cavity coating thermal noise. A projection of an on-ground assessment of that noise source is shown in green. It matches well with the observation at the highest frequencies. The second noise source expected to limit the sensitivity of the LRI is TTL. It has been studied in detail by Wegener (2022), and a simple model of its magnitude is shown in dashed pink. TTL can be calibrated and removed in post-processing. The pink trace shows the effect before calibration. The cavity coating thermal noise and the TTL noise are both well below the sensitivity requirement of the LRI, which is $80 \text{ nm}/\sqrt{\text{Hz}}$. The KBR sensitivity is at about $1 \mu\text{m}/\sqrt{\text{Hz}}$, shown by the level of the post-fit residuals of gravity field recovery (GFR) at frequencies $f > 10^{-2} \text{ Hz}$ (green). The post-fit residuals of the GFR describe the residuals in the ranging data that the newly estimated gravity potential could not explain. For the LRI, that post-fit residual level (red) is well below the KBR residuals. The limiting effect in the post-fit residuals at highest frequencies $f > 30 \text{ mHz}$ is deficiencies in the ACC measurement, which is not resolving the non-linear accelerations well enough to correctly remove them from

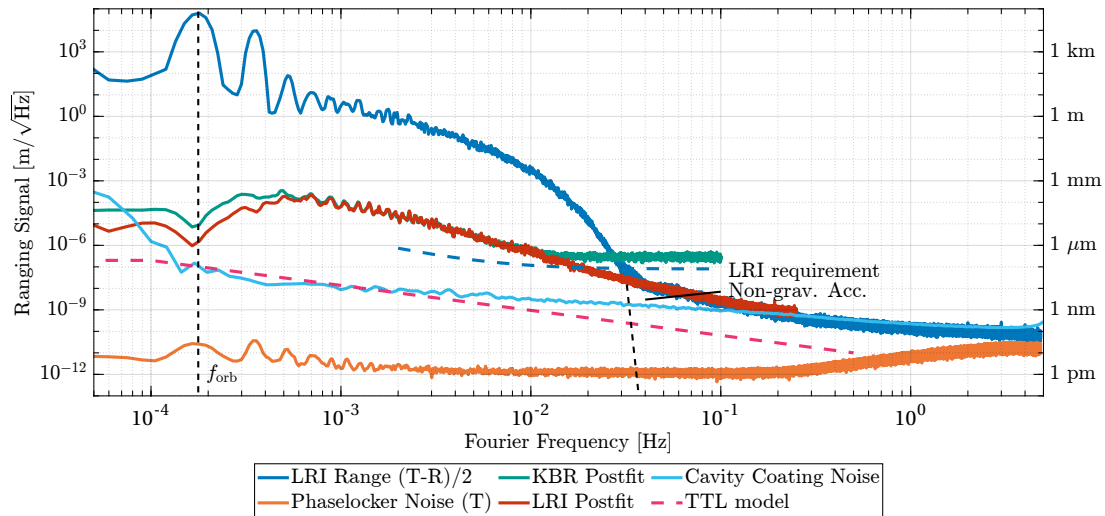


Figure 3.10. ASDs of the LRI measurement and its dominant noise sources. The big bulge in the blue ranging signal is the actual gravitational signal, which rolls off at around 37 mHz (dashed black). The light blue (Cavity Coating Noise) and dashed pink (TTL model) lines show the dominant noise sources of the measurement. The transponder measurement (orange) represents the phase readout noise. The region between 37 mHz to 200 mHz is dominated by the non-gravitational signal that also limits the gravity fields in this frequency region. KBR and LRI postfit residuals are shown in green and red. The spectral densities show data from 2023-Mar-02 until including 2023-Mar-04. Postfit residuals were calculated by Yihao Yan using the `GSOFT` software package (Wang et al., 2015).

the LRI data (Misfeldt, 2019). The orange trace shows the raw phase measurement of the transponder spacecraft, which mainly represents the LRP readout noise, cf. equation (3.12).

Spurious and unphysical jumps or glitches were found in the LRI ranging data shortly after the commissioning of the instrument, which are called phase jumps (PJs). They have been studied and explained in Abich et al. (2019) and Misfeldt (2019). Large parts of the phase jumps are removed by on-ground data processing through a template-based deglitching algorithm, and an update of the LRP flight software was performed in early September 2022 to mitigate this particular noise source. However, even before that update, the GFR was not limited by the PJs due to the excellent removal algorithm. Some sparse events look like phase jumps but have a magnitude of 10^6 cycles, which are consequently called mega-phasejumps. They are still not understood but are regarded as non-critical as they occur rarely and can be removed largely in post-processing.

The LRI has proven to discover new science. For example, deficiencies in the static gravity background model were found by (Ghobadi-Far et al., 2020) for frequencies between 20 mHz to 30 mHz. Furthermore, new data processing strategies using the LRI ranging data in the time domain enable the discovery of localized and small gravity changes with sub-monthly time resolution which are caused, e.g., by earthquakes or local flooding events (Ghobadi-Far et al., 2020; Ghobadi-Far et al., 2022). These new techniques can directly be related to the increased sensitivity of the LRI instrument. In terms of monthly gravity field maps, Pie et al. (2021) concludes that the monthly time-varying gravity field maps from the LRI can be retrieved at least as good as their

KBR counterpart, but with increased sensitivity in high frequencies, which reveal new gravitational attributes in the spectral and temporal domains. Furthermore, the LRI has fewer instrument reboots compared to the KBR instrument.

3.3. Measurement Noise Modeling

Knowledge of the noise shape and its correlation is required to analyze short-lived, high-frequency signals or disturbances like phase jumps in the LRI data. This section first introduces the concept of parameter estimation using the least squares method before the noise of the LRI at high Fourier frequencies is modeled.

3.3.1. Introduction to Least Squares Parameter Estimation

The simple least squares algorithm solves linear, algebraic problems of the form

$$\mathbf{A} \cdot \mathbf{c} = \mathbf{b} \quad \Rightarrow \quad \hat{\mathbf{c}} = \left(\mathbf{A}^\top \mathbf{A} \right)^{-1} \mathbf{A}^\top \mathbf{b} \quad (3.13)$$

in a sense that the sum of squared residuals

$$\chi^2 = \sum_i (\mathbf{b}_i - \mathbf{A}_i \cdot \hat{\mathbf{c}}_j)^2 \quad (3.14)$$

is minimized, hence the name *least squares*. The solution on the right-hand side of equation (3.13) is obtained by forming the gradient with respect to the parameter estimates $\hat{\mathbf{c}}$ and setting it to zero. The summation in equation (3.14) regards the process' independent variables, which are represented column-wise in the design matrix \mathbf{A} , $\hat{\mathbf{c}}$ is the estimator for the unknown parameters \mathbf{c} and \mathbf{b} is the observation or measurement. Note that bold capital letters denote matrices, bold lowercase letters denote vectors, and lowercase letters denote scalars. The previous expressions assume a white noise distribution in the measurement \mathbf{b} , but they can be generalized by applying weights to the measured data. Let

$$\mathbf{b} = \mathbf{A}\mathbf{c} + \boldsymbol{\varepsilon} , \quad (3.15)$$

with the noise term $\boldsymbol{\varepsilon}$ with an expectation value $E[\boldsymbol{\varepsilon}|\mathbf{X}] = 0$ and the variance-covariance matrix (VCM) being defined through $\boldsymbol{\Sigma} = \text{Cov}[\boldsymbol{\varepsilon}|\mathbf{X}]$, which ideally is non-singular and thus invertible. In case of uncorrelated noise, the VCM has diagonal form, $\text{diag}(\boldsymbol{\Sigma}) = \sigma_i^2$, where σ_i is the standard deviation of the measurement at the data point i . The algebraic solution to the newly formulated problem reads

$$\Rightarrow \quad \hat{\mathbf{c}} = \left(\mathbf{A}^\top \boldsymbol{\Sigma}^{-1} \mathbf{A} \right)^{-1} \mathbf{A}^\top \boldsymbol{\Sigma}^{-1} \mathbf{b} \quad (3.16)$$

A more general method for non-white input data is the so-called likelihood method, where the likelihood of the parameters \mathbf{c} given the measured data \mathbf{b} is computed as (Koch, 1999)

$$\mathcal{L}(\mathbf{b} | \mathbf{c}) = \frac{1}{\sqrt{|2\pi\boldsymbol{\Sigma}|}} \cdot \exp \left(-\frac{1}{2} \mathbf{r}(\mathbf{c})^\top \cdot \boldsymbol{\Sigma}^{-1} \cdot \mathbf{r}(\mathbf{c}) \right) . \quad (3.17)$$

In this expression, $\boldsymbol{\Sigma}$ denotes the variance-covariance matrix, which will be described in section 3.3.2 and employs a particular noise model of the input data \mathbf{b} . Those will

be derived in section 3.3.3. Further, $|\Sigma|$ denotes the determinant of Σ . The residuals of the input data after subtracting a potential model is denoted as

$$\mathbf{r}(\mathbf{c}) = \mathbf{b} - \mathbf{m}(\mathbf{c}) , \quad (3.18)$$

with the model $\mathbf{m}(\mathbf{c})$. The best-fit model $\mathbf{m}(\mathbf{c})$ can be identified by the maximum value of the likelihood function \mathcal{L} over the parameter space. Equivalently, but computationally less expensive, is to compute the negative logarithm of \mathcal{L} ,

$$\begin{aligned} \ell(\mathbf{b} | \mathbf{c}) &= -\ln \mathcal{L}(\mathbf{b} | \mathbf{c}) \\ &= \frac{1}{2} \ln (|2\pi\Sigma|) + \frac{1}{2} \mathbf{r}(\mathbf{c})^\top \cdot \Sigma^{-1} \cdot \mathbf{r}(\mathbf{c}) , \end{aligned} \quad (3.19)$$

which saves the evaluation of the exponential function. Ultimately, the negative log-likelihood ℓ is minimized by employing a generalized least squares, i. e., by computing an estimator $\hat{\mathbf{c}}$ of the parameters \mathbf{c} through

$$\hat{\mathbf{c}} = \underset{\mathbf{c}}{\operatorname{argmin}} \mathbf{r}(\mathbf{c})^\top \cdot \Sigma^{-1} \cdot \mathbf{r}(\mathbf{c}) . \quad (3.20)$$

Typically, modern computer-algebra systems use the so-called QR decomposition instead of solving this matrix expression, which is computationally more efficient. The art of noise modeling for physical processes now involves finding a suitable choice for the VCM Σ .

3.3.2. Variance-Covariance Matrix and Autocorrelation Function

The VCM Σ can be derived from the expectation value E of the measurement noise \mathbf{n} as

$$\Sigma_{ij} = E[n_i \cdot n_j] = R(t_i - t_j) , \quad (3.21)$$

which in turn is defined through the autocorrelation function (ACF) $R(\tau)$ (Jenkins et al., 1968).

The ACF $R(\tau)$ can be found from the actual measurement noise through the PSD of actual data, as the autocorrelation and the PSD of a measurement form a Fourier-transform pair according to the Wiener-Khinchin theorem (Chatfield, 1975; Jenkins et al., 1968). The PSD $S(f)$ is obtained from spectral analysis of the measured data, which usually is the LRI phase data within this thesis. From a numerically computed PSD $\hat{S}(f)$ using a simple Fast Fourier Transform (FFT) algorithm or an advanced PSD with logarithmic frequency axis (LPSD, Heinzl et al., 2002), the shape of the PSD can be modeled, e. g., using a polynomial or square-root law, yielding the PSD model $S_m(f)$. Usually, when working with real data which has a finite sampling frequency f_s , a rectangular cropping window in the frequency domain is needed to remove frequencies above f_s . Furthermore, a divisor two is needed to convert the double-sided PSD into its single-sided equivalent. Thus,

$$S(f) = \frac{1}{2} S_m(|f|) \cdot \operatorname{rect} \left(\frac{f}{f_s} \right) . \quad (3.22)$$

After finding a suitable model S_m , the ACF $R(\tau)$ is obtained through the inverse unitary Fourier transform \mathcal{F}^{-1} , where the following convention for the Fourier transform is used:

$$R(\tau) = \int_{-\infty}^{\infty} S(f) e^{-2\pi i \tau f} df \quad (3.23)$$

$$= \frac{1}{2} \int_{-f_s/2}^{f_s/2} S_m(|f|) e^{-2\pi i \tau f} df, \quad (3.24)$$

where the edge frequencies of the rectangle window in equation (3.22) can be used as integral limits.

A common mean for confirming that the analytical ACF $R(\tau)$ actually describes the measurement can be achieved through computing the unbiased autocorrelation of the (real-valued) data \mathbf{x} through

$$\text{xcorr}(\mathbf{x}) = \hat{R}_{\mathbf{x}}(\tau) = \begin{cases} \frac{1}{N - \tau} \sum_{i=0}^{N-\tau-1} x_{i+\tau} x_i, & \tau \geq 0 \\ \hat{R}_{\mathbf{x}}(-\tau), & \tau < 0 \end{cases} \quad (3.25)$$

and comparing both methods.

The following sections provide examples and solutions for the most common use cases of PSD and ACFs for the LRI instrument. They are evaluated at the highest frequencies of approximately $f > 1$ Hz, as this is the region where the noise is directly accessible and not hidden below the gravitational and non-gravitational signals. The analytical models and VCMs will be utilized in later sections, when the least squares formalism is used to estimate parameters of physical models.

3.3.3. Derivation of LRI Noise Models at High Frequencies

Transponder Role

In principle, the measured phase signal on the LRI transponder unit yields a constant phase ramp, cf. equation (4.12). After subtracting that ramp, it only comprises the readout or phaselocker noise. Thus, information on the measurement noise can directly be inferred from that data. Figure 3.11 shows a PSD of the transponder phaselocker signal (blue) and a corresponding fourth-order polynomial fit (orange),

$$S_T^m(f) = p_4 \cdot f^4 + p_2 \cdot f^2 + p_0, \quad (3.26)$$

in a log-log representation. The estimated model parameters are listed in table 3.2. This model is valid for frequencies above 1 Hz, or equivalently, when analyzing events

Table 3.2. Parameters for the transponder PSD model S_T^m , cf. equation (3.26), and reference PSD model S_R^m , cf. equation (3.29).

Parameter	p_0	p_2	p_4	A_R
Unit	[cycles ² /Hz]	[cycles ² /Hz ³]	[cycles ² /Hz ⁵]	[cycles ² /Hz]
Value	$-3.505 \cdot 10^{-11}$	7.836e-11	$-0.184 \cdot 10^{-11}$	$7.155 \cdot 10^{-13} \cdot L$

3.3. MEASUREMENT NOISE MODELING

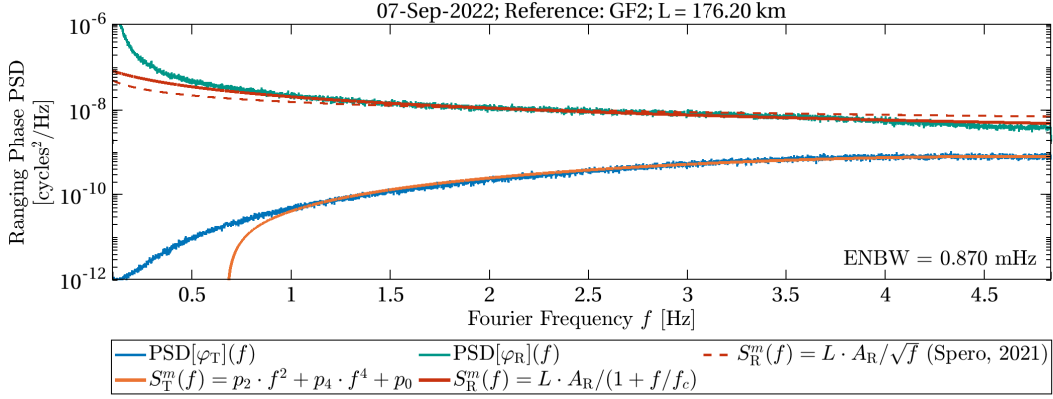


Figure 3.11. PSD of the measured one-way phase on the reference and transponder unit of the LRI, recorded on 2022-Sep-07 with GF-2 in reference role for frequencies above 0.1 Hz. The modeled PSDs $S_{R/T}^m$ (cf. equations (3.26) and (3.29)) are shown in orange and red, respectively. Here, $L = 176.20$ km.

shorter than 1 s or 10 samples at the typical 10 Hz data rate. The ACF $R_T(\tau)$ as computed through equation (3.23) reads

$$\begin{aligned}
 R_T(\tau) &= \mathcal{F}^{-1} \left[\frac{S_m^T(f)}{2} \cdot \text{rect} \left(\frac{f}{f_s} \right) \right] (\tau) \quad (3.27) \\
 &= \begin{cases} \frac{1}{32\pi^5\tau^5} \left[4\pi\tau f_s \left(\pi^2\tau^2 (p_4 f_s^2 + 2p_2) - 6p_4 \right) \cos(\pi\tau f_s) \right. \\ \quad \left. + \pi^4\tau^4 (p_4 f_s^4 + 4p_2 f_s^2 + 16p_0) \sin(\pi\tau f_s) \right. \\ \quad \left. - \left(4\pi^2\tau^2 (3p_4 f_s^2 + 2p_2) - 24p_4 \right) \sin(\pi\tau f_s) \right] & \text{if } \tau \neq 0 \\ \frac{f_s}{480} (240p_0 + 20f_s^2 p_2 + 3f_s^4 p_4) & \text{if } \tau = 0 . \end{cases} \quad (3.28)
 \end{aligned}$$

Its graphical representation is shown in orange in the left panel of figure 3.12, together with the numerical autocorrelation $\hat{R}_T(\tau)$ of the measured phase data φ_T . By comparing the model and the finitely sampled data, it is apparent that the decimation filter is designed to align the sampling after decimation with the zero-crossings of the ACF. Hence, the decimated sampling rate is at the nulls of the ACF, which minimizes aliasing (Ware et al., 2006). The data is only self-correlated to the first neighboring samples, and the computed covariance matrix (cf. equation (3.21)) is thus having non-zero entries in the diagonal and the first minor diagonals, but is (almost) zero elsewhere.

Reference Role

The spectrum $\text{PSD}[\varphi_R](f)$ for the one-way phase of reference role of the LRI is shown in green in figure 3.12. Although Spero (2021) suggests a $1/\sqrt{f}$ -behavior (dashed red, cf. figure 3.11) for the high-frequency cavity noise, a low-pass filter function (solid red) is chosen for the model

$$S_R^m(f) = \frac{L \cdot A_R}{1 + \frac{f}{f_c}}, \quad (3.29)$$

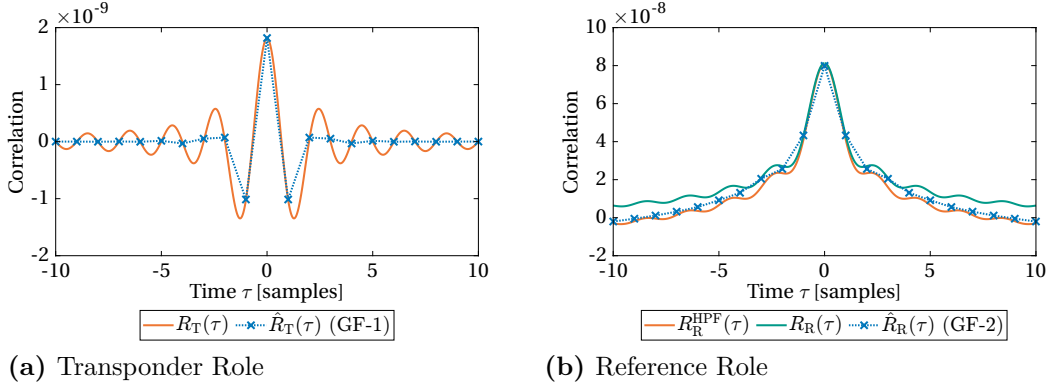


Figure 3.12. Analytical autocorrelation functions and their corresponding numerical estimate from flight data. **(a)** Transponder role, $R_T(\tau)$, cf. equation (3.28). **(b)** Reference role, $R_R(\tau)$, cf. equation (3.31).

as it is a better approximation to the data. The filter cutoff frequency is chosen to be $f_c = 0.2$ Hz and the numerical value for the fitted magnitude A_R is shown in table 3.2. The laser frequency noise from the cavity on the reference side scales with the absolute spacecraft separation (cf. equation (3.10)), which was approximately $L \approx 176.2$ km at that particular day.

The solution to equation (3.23) using the model $S_R^m(f)$ yields

$$R_R(\tau) = \mathcal{F}^{-1} \left[\frac{S_R^m(f)}{2} \cdot \text{rect} \left(\frac{f}{f_s} \right) \right] (\tau) \quad (3.30)$$

$$= 2LA_R f_c (\cos(2\pi\tau f_c) (\text{cosint}(\pi\tau(2f_c + f_s)) - \text{cosint}(2\pi\tau f_c)) \\ + \sin(2\pi\tau f_c) (\text{sinint}(\pi\tau(2f_c + f_s)) - \text{sinint}(2\pi\tau f_c))) . \quad (3.31)$$

However, as the low-frequency gravitational and non-gravitational signal dominates the measurement on the reference side, this analytical form of the ACF can not directly be compared to a numerical estimate using real data. Hence, a high-pass filter (HPF) employing a Kaiser window ($\beta \approx 0.021$), also at $f_c = 0.2$ Hz, is applied before computing the numerical autocorrelation \hat{R} , cf. equation (3.25). Furthermore, an average of autocorrelation results over 10 000 short segments of 50 samples ≈ 5 s = $1/f_c$ duration is shown, with an outlier/peak detection and removal to prevent falsifying the shape. This second filter must also be represented in the analytical ACF. It is covered by splitting the integral into two parts and cutting the limits at f_c , i. e.,

$$R_R^{\text{HPF}}(\tau) = \mathcal{F}^{-1} \left[\frac{S_R^m(f)}{2} \cdot \text{rect} \left(\frac{f}{f_s} \right) \right] (\tau) \Big|_{|f| > f_c} \quad (3.32)$$

$$= \frac{1}{2} \left(\int_{-f_s/2}^{-f_c} S_R^m(|f|) e^{-2\pi i \tau f} df + \int_{f_c}^{f_s/2} S_R^m(|f|) e^{-2\pi i \tau f} df \right) \quad (3.33)$$

$$= 2LA_R f_c [\cos(2\pi\tau f_c) (\text{cosint}(\pi\tau(2f_c + f_s)) - \text{cosint}(4\pi\tau f_c)) \\ + \sin(2\pi\tau f_c) (\text{sinint}(\pi\tau(2f_c + f_s)) - \text{sinint}(4\pi\tau f_c))] . \quad (3.34)$$

As the sharp edge of the integral limit does not model the smooth roll-off of the actual filter implementation, the numerical values for the amplitude A_R and f_c are replaced by

an effective cutoff $f_{c,\text{eff}} = f_c/2$ and $A_{R,\text{eff}} = 2A_R$ for compensating the total magnitude. This effective cutoff simplifies the true transfer function of the additional HPF. One should know that filtering, in general, has non-negligible effects on the ACF.

The two variants of the ACFs, R_R and R_R^{HPF} , are shown in figure 3.12. It is observed that omitting the HPF would cause a slight difference in the ACFs, originating from the factor four instead of two in the argument of the sine- and cosine-integral functions in equations (3.31) and (3.34). The ACF considering the HPF matches well with the numerical autocorrelation $\hat{R}_R(\tau)$ of the high-pass filtered phase data of the reference spacecraft, despite the simplified representation of the HPF.

Single Channel Phase Combination

Sometimes, individual channels of the QPD are analyzed. In this case, there are, in principle, two possibilities: First, process the phase data “as is” and use the transponder/reference ACF as defined in the previous two sections. Secondly, suppose there is a specific event in one channel. In that case, the common gravitational and non-gravitational signals over all four channels can be removed by subtracting the mean over the three unaffected channels. This phase channel combination is called $\kappa(t_i)$ or κ_i in the following, with t_i being the discrete-time samples. Exemplarily, for some kind of event in channel A, the phase combination reads

$$\kappa^A(t_i) = \varphi_A(t_i) - \frac{1}{3}(\varphi_B(t_i) + \varphi_C(t_i) + \varphi_D(t_i)) , \quad (3.35)$$

with $\varphi_{A\dots D}$ denoting the measured phase of the individual QPD channels. This expression rejects the ranging signal (on the reference side) and common-mode noise sources like laser frequency noise.

Following the previous sections, exemplary numerically computed PSDs of one single channel phase combination, $\text{PSD}[\kappa^A]$, on both SC as defined in equation (3.35) are computed and shown in figure 3.13. A combination of high- and lowpass transfer functions

$$S_\kappa^m(f) = \frac{A}{1 + \left(\frac{f}{f_{c1}}\right)^4} + \frac{B}{1 + \left(\frac{f_{c2}}{f}\right)^2} \cdot \frac{1}{1 + \left(\frac{f}{f_{c2}}\right)^4} \quad (3.36)$$

is fitted in the spectral domain for frequencies $f > 5 \cdot 10^{-2}$ Hz. The level of the DC value, i. e., the numerical value of A in equation (3.36), is spread between $1 \cdot 10^{-10}$ to $3 \cdot 10^{-10}$ for the two spacecraft in different roles and at different times. Similarly, the first cutoff frequency f_{c1} varies slightly. The value spread is larger in GF-1 than on GF-2. However, the more critical numerical values for $B \approx 2.65 \cdot 10^{-10}$ and $f_{c2} \approx 4.5$ Hz, which define the high-frequency bump above 1 Hz, are consistent between both SC in both roles and over time. The corresponding correlation function R_κ is again defined by inserting the PSD model (equation (3.36)) into the definition of equation (3.23). The inverse Fourier transform was solved using the computer algebra software MATHEMATICA. For reducing complexity, the inverse Fourier transform was computed individually for the two summands of equation (3.36) and then added afterward. The overall analytical formula for the ACF $R_\kappa(\tau)$ is not explicitly written out here, as it is a rather lengthy expression, but it is shown in figure 3.14 for both spacecraft (differing in their magnitude A ; orange: GF-1; cyan: GF-2) alongside their numerical correspondent $\hat{R}_\kappa(\tau)$. Obviously, the analytical solution is not stable for values of $\tau > 5$, however, it

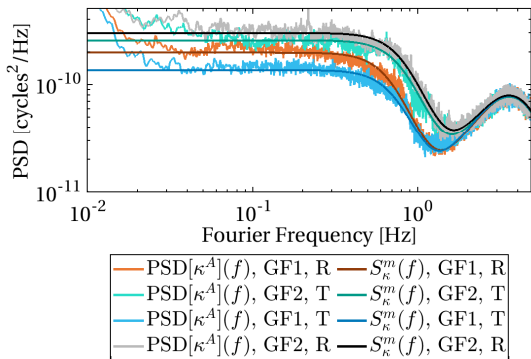


Figure 3.13. High-frequency part of the PSD of a single channel phase combination κ^D of both SC, cf. equation (3.35) together with the PSD fit model $S_\kappa^m(f)$, cf. equation (3.36). The data was measured on 2022-Sep-07 with GF-2 and on 2022-Sep-18 with GF-1 in reference role.

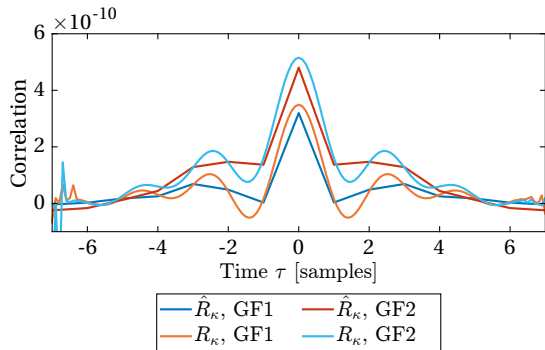


Figure 3.14. Analytical and numerical auto-correlation functions of the single channel combinations κ . The parameter estimation and numerical autocorrelation use measurement data from 2022-Sep-07. The inverse Fourier transform is not stable for evaluation times $|\tau| > 5$ samples, but safely be set to zero outside this interval.

can safely be set to zero outside this interval. Again, a large number of 20000 auto-correlations of consecutive data stretches with $N = 100$ samples ≈ 10 s was computed and averaged. The red and blue lines overlay well with the analytical solution. Using phase data from other days, where the A parameter is slightly different, the resulting patterns are similar in their shape but with a small bias in the magnitude for $\tau \approx 0$. Further mismatches between the two methods could arise from mis-modeling of $S_\kappa^m(f)$ in the spectral domain, for example, in the knee at approximately 1.5 Hz in figure 3.13. Still, the derived ACF matches well with the observed numerical autocorrelation from in-flight data and can be used in parameter estimations

3.4. Summary

Chapter 3 gave an introduction to the architecture of the LRI, its subunits and working principles, and, more briefly, the other GRACE-FO payloads. First measurements were presented. The ASD of the ranging signal was presented in figure 3.10, and the different noise contributions of the LRI have been explained based on previous studies. Section 3.3 gave a more thorough introduction to the measurement noise at high frequencies, including the derivation of noise models and autocorrelation functions for the LRI units in reference and transponder role, as well as for a particular linear combination of the four individual QPD channels. Later sections will use these models for parameter estimations in a least squares sense.

The Interferometric Phase Observable

4

“ *Time is relative. Its only worth depends upon what we do as it is passing.* ”

— ALBERT EINSTEIN —

Theoretical physicist who revolutionized the understanding of our universe

4.1. Relativistic Description of the Phase Observable

The previous section provided an intuitive picture of the LRI working principle through the beams' frequencies. However, the LRI actually measures the phase of the interference pattern, being the frequency integral. To describe the phase observables in a relativistic framework, the approach by [Yan et al. \(2021\)](#) is followed closely to assess potential relativistic effects on the conversion factor between the measured phase and the range. This description in terms of phase is preferred since it is invariant in the context of general relativity, i. e., independent of the coordinate system, in contrast to the frequency.

In GRACE-FO data analysis, four coordinate systems are of relevance: the local Lorentz frames of reference and transponder satellites, which have their proper time τ_R and τ_T and the origin at the satellite center-of-mass, respectively, and the geocentric non-rotating coordinate system with coordinate time t usually realized through GPS time. This quasi-inertial geocentric celestial reference frame (GCRF) is usually used in satellite gravimetry to perform orbit integration. In contrast, the co-rotating terrestrial reference frame is used to perform the gravity field recovery. Following the description in [Ashby et al. \(1986\)](#), the coordinate time t of the GCRF is assumed to be realized by clocks on the geoid, in contrast to the geocentric coordinate time (TCG) where the clocks are far away from Earth.

The roundtrip ranging scheme of the LRI in its ideal case without measurement noise is depicted in a Minkowski diagram in figure 4.1. It will be explained in detail in the following. The phase of the reference laser (RLAS) (cf. equation (2.6)) in the frame of the reference satellite can also be written as

$$\Phi_R(\tau_R'', \text{RLAS}) := \int_0^{\tau_R''} \nu_R(\tau_R) d\tau_R + \text{const.}, \quad (4.1)$$

where the arguments (τ_R, RLAS) specify a four-dimensional space-time event in general relativity with the time τ_R and the local laser position RLAS, ν_R is the instantaneous laser frequency and τ_R'' indicates the measurement epoch. The absolute value of the phase is neither accessible nor relevant here, which is emphasized by the constant term.

The phase value of a particular event $E = (\tau_R(E), \text{RLAS})$, when light with the phase $\Phi_R(E)$ is produced and emitted at the reference laser, will propagate towards the transponder satellite. In the local Lorentz frame of the transponder satellite, the

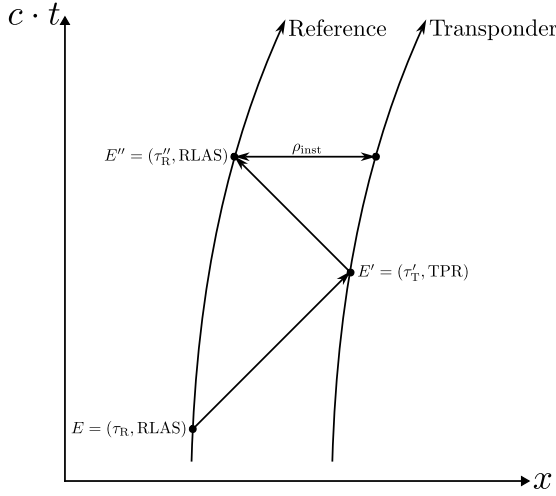


Figure 4.1. Minkowski-Diagram of the LRI roundtrip measurement. The light is emitted from the reference unit at the event E , at the position of the reference laser (RLAS). It is then received and re-emitted at E' at the transponder photoreceiver position (TPR). The non-instantaneous roundtrip phase is measured at E'' , again at the RLAS position, but a few milliseconds later. For reference, the instantaneous biased range is depicted as well. x denotes the spatial coordinates.

event $E' = (\tau_T(E'), \text{TPR})$ is defined as the reception at the transponder photoreceiver (TPR). The phase of the beatnote at the TPR is given as the phase difference of both interfering light fields, i. e.

$$\varphi_T(E') = \Phi_T(E') - \Phi_R(E') = f_{\text{off}}^T \tau_T^{\text{USO}}(E') + \delta_T(E'). \quad (4.2)$$

That measurement is used as feedback in the transponders' laser frequency control loop (cf. section 3.1), which means that $\dot{\varphi}_T(\tau_T^{\text{USO}})$ is kept at f_{off}^T . The phase derivative $\dot{\varphi}_T$ is defined w. r. t. the local time of the USO τ_T^{USO} , which is an electrical realization of the proper time τ_T that may exhibit noise and errors. As these errors are correctable in post-processing (using the CLK1B data product), the proper time realizations τ_R^{USO} and τ_T^{USO} are regarded as error-free in the following. Imperfections in the control loop, e. g., due to the limited gain or bandwidth, may result in phase deviations δ_T . Due to the frame invariance of the phase and the way the events E and E' were defined, one can use that the phase $\Phi_R(E')$ at the transponder detector at the reception event is equal to the phase on the reference laser at the emission event, i. e.,

$$\Phi_R(E') = \Phi_R(\tau_R(E), \text{RLAS}) = \Phi_R(E). \quad (4.3)$$

Note that equations (4.1) and (4.2) can be used to derive the phase (and frequency) of the transponder laser, which is a function of the reference laser.

The phase value of the transponder laser $\Phi_T(E')$ at the instance of detection was also split at the beamsplitter and will propagate back to the reference satellite. $E'' = (\tau_R(E''), \text{RPR})$ labels the event when this phase is impinging on the reference photoreceiver (RPR) and the corresponding phase of the beatnote on the reference photoreceiver reads

$$\varphi_R(E'') = \Phi_T(E'') - \Phi_R(E''). \quad (4.4)$$

The phase of the local oscillator field $\Phi_R(E'')$ was emitted at the reference laser a short time before that, the exact delay is given by the light propagation time $\Delta\tau_R^{[a_{R''}+b_{R''}]}$ for the optical path lengths a_R and b_R in the reference frame (cf. figure 3.2). The two primes indicate that these quantities refer to the time when the measurement occurs

on the reference side. Thus,

$$\Phi_{\text{R}}(E'') = \Phi_{\text{R}}(\tau_{\text{R}}(E'') - \Delta\tau_{\text{R}}^{[a_{\text{R}''}+b_{\text{R}''}]}, \text{RLAS}) . \quad (4.5)$$

The received light on the transponder satellite can be rewritten in terms of the reference laser phase plus a contribution from the transponder frequency-locked loop, i. e.

$$\begin{aligned} \Phi_{\text{T}}(E'') &= \Phi_{\text{R}}(\tau_{\text{R}}(E), \text{RLAS}) \\ &\quad + f_{\text{off}}^{\text{T}} \tau_{\text{T}}(E') + \delta_{\text{T}}(E') \end{aligned} \quad (4.6)$$

The relation between the light reception time $\tau_{\text{R}}(E'')$, i. e., the measurement time on reference, and light emission time $\tau_{\text{R}}(E)$ in terms of the light paths a , b and ℓ in figure 3.2 is

$$\tau_{\text{R}}(E'') - \tau_{\text{R}}(E) \quad (4.7)$$

$$= (\tau_{\text{R}}(E'') - \tau_{\text{R}}(E')) + (\tau_{\text{R}}(E') - \tau_{\text{R}}(E)) \quad (4.8)$$

$$= \Delta\tau_{\text{R}}^{[-b_{\text{T}'}+\ell_{\text{T}'\text{R}''}+b_{\text{R}''}]} + \Delta\tau_{\text{R}}^{[a_{\text{R}}+\ell_{\text{RT}'}+b_{\text{T}'}]} \quad (4.9)$$

$$= \Delta\tau_{\text{R}}^{[\ell_{\text{RT}'}+\ell_{\text{T}'\text{R}''}]} + \Delta\tau_{\text{R}}^{[a_{\text{R}}+b_{\text{R}''}]} . \quad (4.10)$$

The round-trip propagation time for light on the racetrack $\Delta\tau_{\text{R}}^{[\ell_{\text{RT}'}+\ell_{\text{T}'\text{R}''}]}$ as apparent in the local Lorentz frame of the reference satellite contains the ranging information and will be written in a short form as $\Delta\tau_{\text{R}}^{[\text{rt}]}$ later on. Again, the primes indicate roughly when light paths or satellite states are evaluated, e. g., double prime means the measurement time, one prime means approx. 220 km/ $c_0 \approx 0.73$ ms earlier and no prime means 1.46 ms earlier than the measurement epoch. Finally, by using equation (4.5) and equation (4.6) in equation (4.4) and employing the definition for the laser phase (cf. equation (4.1)), one obtains with the help of equation (4.10)

$$\begin{aligned} \varphi_{\text{R}}(\tau_{\text{R}}'') &= - \int_{\tau_{\text{R}}'' - \Delta\tau_{\text{R}}^{[\text{rt}]} - \Delta\tau_{\text{R}}^{[a_{\text{R}}+b_{\text{R}''}]} }^{\tau_{\text{R}}'' - \Delta\tau_{\text{R}}^{[a_{\text{R}''}+b_{\text{R}''}]}} \nu_{\text{R}}(\tau_{\text{R}}) \, d\tau_{\text{R}} \\ &\quad + f_{\text{off}}^{\text{T}} \tau_{\text{T}}(E') + \delta_{\text{T}}(E') + \text{const.} \end{aligned} \quad (4.11)$$

where the short form $\tau_{\text{R}}'' = \tau_{\text{R}}(E'')$ was used. The first line of equation (4.11) illustrates that the phase of the beatnote on the reference satellite φ_{R} contains the elapsed phase between start and end time given by the lower and upper bound of the integral, respectively. This result is consistent with the expression given in Sheard et al. (2012), though a constant laser frequency was assumed there.

The light propagation time $\Delta\tau_{\text{R}}^{[b_{\text{R}''}]}$ for path length b_{R} appears in both integral bounds with two primes, i. e., at the same epoch. This means that variations in that path between beamsplitter and photodiode do not cause phase variations due to common-mode rejection because that segment is traversed by both beams. The b_{R} -terms appear because the phase measurement at the photoreceiver is actually defined at the beamsplitter. However, there is a negligible delay until the information arrives at the detector. Delays appear with larger magnitude also in later stages of data processing, e. g., filter delays, and need to be accounted for in data processing (see Müller (2017) for more details).

The terms related to path length a_R in equation (4.11) are evaluated at different instances of time, which are separated by the round-trip delay of approx. 1.46 ms. The phase variations on this path delivering light to the beamsplitter over such short time scales can be safely omitted (Sheard et al., 2012).

The transponder phase measurement is mainly a trivial phase ramp:

$$\varphi_T(\tau_T(t)) = f_{\text{off}}^T \tau_T(t) + \delta_T(\tau_T(t)) . \quad (4.12)$$

The average phase over all four QPD channels on the reference and transponder satellites, φ_R and φ_T , are reported as so-called piston phase in the GRACE-FO LRI Level-1A data product (LRI1A) (Wen et al., 2019). The phase measurements exhibit sporadic phase jumps (or glitches) when some attitude control thrusters are activated (Abich et al., 2019; Misfeldt, 2019). Most of the jumps or steps appear simultaneously up to the light travel time on both satellites and have been accounted for in the mathematical description by the δ_T -term. By fitting a model to the individual phase jump in the transponder phase data, one can subtract the same model amplitudes from reference and transponder phase, but with different delay due to light travel time (Abich et al., 2019). Other effects that are removed from the phase, such as single event upsets (SEUs) will be discussed later in chapter 9. We denote these deglitched phase time series as φ_T^{DGL} and φ_R^{DGL} and compute the LRI ranging phase (also sometimes denoted as piston phase) as

$$\varphi_{\text{LRI}}(\tau_R(t)) = \varphi_T^{\text{DGL}}(\tau_T(t - \Delta t_{\text{estim}}^{[\ell_{T'R''}]}) - \varphi_R^{\text{DGL}}(\tau_R(t)) \quad (4.13)$$

$$\Rightarrow \varphi_{\text{LRI}}(t) = \varphi_T^{\text{DGL}}(t_R - \Delta t_{\text{estim}}^{[\ell_{T'R''}]}) - \varphi_R^{\text{DGL}}(t_R) . \quad (4.14)$$

To form the phase difference described in equation (4.13), one has to bring the phase values from LRI1A to the same time-grid by means of interpolation. We recommend to first convert the time tags of the reference τ_R and transponder τ_T into coordinate time (t_R and t_T) by using LLK1B, the datation reports from LHK1A, adding the constant phase delay of the downsampling filter (Wen et al., 2019), and then interpolate the transponder phase onto the time-grid of the reference, because the transponder measurement exhibits less variations. Further, the (approximate) light travel time from transponder to reference $\Delta t_{\text{estim}}^{[\ell_{T'R''}]}$ is used, which can be computed from the GPS positions of the satellites. Note that by converting the local LRI time τ_R into GPS time t_R , they are no longer regularly sampled and the resulting phase φ_{LRI} needs to be interpolated once more to derive the regularly sampled reference time-tags t in coordinate time for the final LRI1B data product. Equation (4.14) can directly be used in data processing using the LRI1A data product.

However, in order to understand the physical content of the computed ranging phase $\varphi_{\text{LRI}}(t)$, equation (4.14) is rewritten using the definitions of equations (4.11) and (4.12)

$$\varphi_{\text{LRI}}(t) = \int_{t_R - \Delta t_{\text{rt}}}^{t_R} \nu_R^G(t'_R) dt'_R + q_R , \quad (4.15)$$

where q_R denotes an arbitrary and unknown phase bias. Note that the absolute laser frequency ν_R^G in the coordinate frame is used here. The relation between the frequency of the laser source ν_R and the apparent frequency in the Earth-centered GCRF system

$\nu_{\text{R}}^{\text{G}}$ is

$$\nu_{\text{R}}^{\text{G}} = \nu_{\text{R}} \cdot \frac{d\tau_{\text{R}}}{dt} , \quad (4.16)$$

though the distinction between those is rather of academic interest, since they deviate just at the parts-per-billion level, as discussed in the following. The dominant DC and 1/rev errors are evaluated by assuming $\nu_{\text{R}}^{\text{G}} = \nu_{\text{R}}$ and considering $v = 7.7 \text{ km/s}$, $GM = 3.986 \cdot 10^{14} \text{ m}^3/\text{s}^2$ and $r = (6378 + 490) \text{ km}$ for the GRACE-FO orbit. The fractional clock error at DC frequency is given by (Müller, 2017, eq. 2.14)

$$\frac{d\tau}{dt} - 1 \approx -\frac{v^2}{2c_0^2} - \frac{GM}{rc_0^2} \approx -1 \cdot 10^{-9} . \quad (4.17)$$

This numerical value translates in a DC frequency difference of

$$\frac{\nu_{\text{R}}^{\text{G}}}{\nu_{\text{R}}} = \frac{d\tau}{dt} \quad \Rightarrow \quad \nu_{\text{R}}^{\text{G}} - \nu_{\text{R}} \approx 300 \text{ kHz} . \quad (4.18)$$

From GNI1B orbit data and equation (4.17), one can furthermore infer that the variations of $d\tau/dt$ are below 10^{-11} at the orbital frequency (Müller et al., 2022), giving a 1/rev error of approximately

$$\nu_{\text{R}}^{\text{G}} - \nu_{\text{R}} \approx 3 \text{ kHz} \cos(2\pi f_{\text{orb}} \cdot t) , \quad (4.19)$$

which is again well below the accuracy goal of 10^{-7} or better.

The derivative of equation (4.15), which is the phase rate, is given by (Müller et al., 2022)

$$\frac{d\varphi_{\text{LRI}}(t)}{dt} = \frac{d}{dt} \left(\int_{t-\Delta t^{[\text{rt}]}(t)}^t \nu_{\text{R}}^{\text{G}}(t') dt' + q_{\text{R}} \right) \quad (4.20)$$

$$= \frac{d\Delta t^{[\text{rt}]}}{dt} \cdot \nu_{\text{R}}^{\text{G}}(t - \Delta t^{[\text{rt}]}(t)) + \nu_{\text{R}}^{\text{G}}(t) - \nu_{\text{R}}^{\text{G}}(t - \Delta t^{[\text{rt}]}(t)) . \quad (4.21)$$

From this expression, the physical contributors to the ranging phase can be seen. The first term contains the desired ranging information, i. e., the round-trip propagation time $\Delta t^{[\text{rt}]}$ multiplied by the laser frequency $\nu_{\text{R}}^{\text{G}}$ at the emission event. The latter two terms can be regarded as a phase error due to laser frequency changes between the emission and reception time of the photon. A handy approximation for a slowly varying laser frequency $\nu(t + \Delta t^{[\text{rt}]}) \approx \nu(t)$ in both, coordinate time and proper time, is given by

$$\varphi_{\text{LRI}}(t) \approx \Delta t^{[\text{rt}]}(t) \nu_{\text{R}}^{\text{G}}(t) + q_{\text{R}} = \Delta \tau_{\text{R}}^{[\text{rt}]}(t) \nu_{\text{R}}(t) + q_{\text{R}} . \quad (4.22)$$

The equivalence of proper time quantities and coordinate time quantities in equation (4.22) follows from the phase-invariance under coordinate transformation in general relativity (Shiozawa, 2004).

4.2. Relation between the Measured Phase and Biased Range

Gravity field recovery for GRACE-like missions, i. e., the conversion of range, accelerometer and orbit observations into gravity field coefficients, is usually based on the biased instantaneous inter-satellite range

$$\rho^{\text{inst}}(t) = |\vec{r}_A(t) - \vec{r}_B(t)| + \text{const.} \quad (4.23)$$

that is obtained using LRI or KBR measurements. However, due to the finite speed of light and the motion of the satellites during the light travel time, these range measurements yield a non-instantaneous biased range, in the LRI case proportional to the round-trip light travel time in the GCRF $\Delta t^{[\text{rt}]}$ or in the reference S/C timeframe $\Delta \tau_{\text{R}}^{[\text{rt}]}$.

The conversion between LRI-derived raw biased range $\rho_{\text{LRI}}^{\text{raw}}$ and instantaneous biased range is in general given by the light time correction (LTC), i. e.,

$$\rho_{\text{LRI}}^{\text{inst}}(t) = \rho_{\text{LRI}}^{\text{raw}}(t) + \rho_{\text{LRI}}^{\text{LTC}}(t) \quad (4.24)$$

$$= \frac{c_0 \Delta t^{[\text{rt}]}(t)}{2} + c_0 \mathcal{T}_{\text{TWR}}^{\text{G}}(t) \quad (4.25)$$

$$= \frac{c_0 \Delta \tau_{\text{R}}^{[\text{rt}]}(t)}{2} + c_0 \mathcal{T}_{\text{TWR}}(t), \quad (4.26)$$

where $c_0 \mathcal{T}_{\text{TWR}}^{\text{G}}$ is the common light time correction for the LRI, which is derived from orbit information (GNI1B) and for the GCRF (Yan et al., 2021). However, a similar correction $c_0 \mathcal{T}_{\text{TWR}}$ could be derived from orbit information also for the local Lorentz frame of the reference satellite. Here we assume the conventional approach, where the light time correction is based on a range from $\Delta t^{[\text{rt}]}$. We further need to rescale the ranging phase φ_{LRI} (cf. equation (4.15)) in units of cycles with the estimated wavelength $\lambda_{\text{est}}^{\text{G}} = c_0 / \nu_{\text{R,est}}^{\text{G}}$ as apparent in the GCRF in order to obtain the raw LRI range in meter as (Müller et al., 2022)

$$\rho_{\text{LRI}}^{\text{raw}}(t) = \frac{c_0}{2} \int_0^t \frac{d\varphi_{\text{LRI}}(t')}{dt'} \frac{1}{\nu_{\text{R}}^{\text{G}}(t' - \Delta t^{[\text{rt}]}(t'))} - \left(\frac{\nu_{\text{R}}^{\text{G}}(t')}{\nu_{\text{R}}^{\text{G}}(t' - \Delta t^{[\text{rt}]}(t'))} - 1 \right) dt' \quad (4.27)$$

$$= \frac{c_0}{2} \left(\Delta t^{[\text{rt}]}(t) - \Delta t^{[\text{rt}]}(0) \right) + \text{errors} . \quad (4.28)$$

Equation (4.27) provides the recipe to compute the raw and biased range as a function of the coordinate time t , which is available after precise orbit determination. The formula follows directly from the definition of the phase derivative (cf. equation (4.21)). The first term in the integral resembles the well-known relation

$$\rho(t) = \frac{c_0}{\nu} \varphi(t) , \quad (4.29)$$

and the second term accounts for the effect of a varying frequency $\nu_{\text{R}}^{\text{G}}(t)$. Equation (4.28) in turn provides the physical meaning of $\rho_{\text{LRI}}^{\text{raw}}$ as a time-of-flight measurement, whereby the errors include TTL (Wegener et al., 2020), laser frequency noise (Abich et al., 2019) and others.

A handy approximation of equation (4.27) is given as

$$\rho_{\text{LRI,approx}}^{\text{raw}}(t) = \frac{c_0}{2} \int_0^t \frac{d\varphi_{\text{LRI}}(t')/dt'}{\nu_{\text{R}}(t')} - \left(1 - \frac{d\Delta t_{\text{GPS}}^{\text{[rt]}}(t')}{dt'} \right) \cdot \frac{\dot{\nu}_{\text{R}}(t')}{\nu_{\text{R}}(t')} \Delta t_{\text{GPS}}^{\text{[rt]}}(t') dt' , \quad (4.30)$$

where the frequency ν_{R} is expressed in the local frame of the reference satellite, and all quantities are evaluated at the same time t . The subscript GPS indicates that the light travel time can be obtained from orbit information. The accuracy of this approximation has been analyzed in Müller et al. (2022).

4.3. Scale and Timing Errors in the Instantaneous Biased Range

Up to now, the representation neglects some error sources, namely a mismodeling of the laser frequency, which is expressed as a scale factor, and, secondly, clock errors. It was shown in equation (4.27), that the biased range can be computed from the phase measurements if the conversion factor, more precisely the absolute frequency $\nu_{\text{R}}^{\text{G}}(t)$ or wavelength $\lambda(t) = c_0/\nu_{\text{R}}^{\text{G}}(t)$, is known. However, knowledge errors of this conversion factor can be expressed through the difference of the estimated and the true value, which is called the scale factor

$$\varepsilon_{\text{SCF}}(t) = \frac{\nu_{\text{R,est}}^{\text{G}}(t) - \nu_{\text{R}}^{\text{G}}(t)}{\nu_{\text{R}}^{\text{G}}(t)} \quad \Leftrightarrow \quad \nu_{\text{R}}^{\text{G}}(t) = \frac{\nu_{\text{R,est}}^{\text{G}}(t)}{1 + \varepsilon_{\text{SCF}}(t)} . \quad (4.31)$$

By replacing $\nu_{\text{R}}^{\text{G}}$ in equation (4.27) with the definition of equation (4.31), an expression for the estimated range $\rho_{\text{LRI}}^{\text{raw,est}}$ is obtained. The error of this estimated range is

$$\rho_{\text{LRI}}^{\text{raw,est}}(t) - \rho_{\text{LRI}}^{\text{raw}}(t) \approx \varepsilon_{\text{SCF}}(t) \cdot L(t) , \quad (4.32)$$

of which the full derivation is published in Misfeldt et al. (2023b, eq. 9ff) and is thus not repeated here.

The second potential error contributor is a timeshift ζ of the measured data, which may arise from an unmodeled internal delay between the time tagging of the ranging data and the true time reference frame given by the GPS. In the case of the LRI, the time offset between GPS and LRI can be up to 1.5 s due to initialization of the LRP time (Wen et al., 2019). So-called datation reports are taken regularly to measure this initialization time offset. However, even after correcting for this offset, a small deviation ζ may remain, and the effect is linearized through

$$\rho_{\text{LRI}}^{\text{inst}}(t + \zeta) \approx \rho_{\text{LRI}}^{\text{inst}}(t) + \zeta \cdot \dot{\rho}(t) . \quad (4.33)$$

By combining the two effects, the total error of the LRI measured signal w. r. t. the truth is

$$\rho_{\text{LRI}}^{\text{inst}}(t) - \rho_{\text{true}}^{\text{inst}}(t) \approx \varepsilon_{\text{SCF}}(t) \cdot L(t) + \zeta \cdot \dot{\rho}(t) . \quad (4.34)$$

For the LRI, typical values of the scale factor ε_{SCF} are on the order of 10^{-6} whereas the timeshift $\zeta \approx 50 \mu\text{s}$. The corresponding errors are shown for a given amplitude spectral density of ranging data in figure 4.2. Both error sources are close to the LRI noise requirement between 0.6 . . . 3 mHz, which sets a requirement for the knowledge of

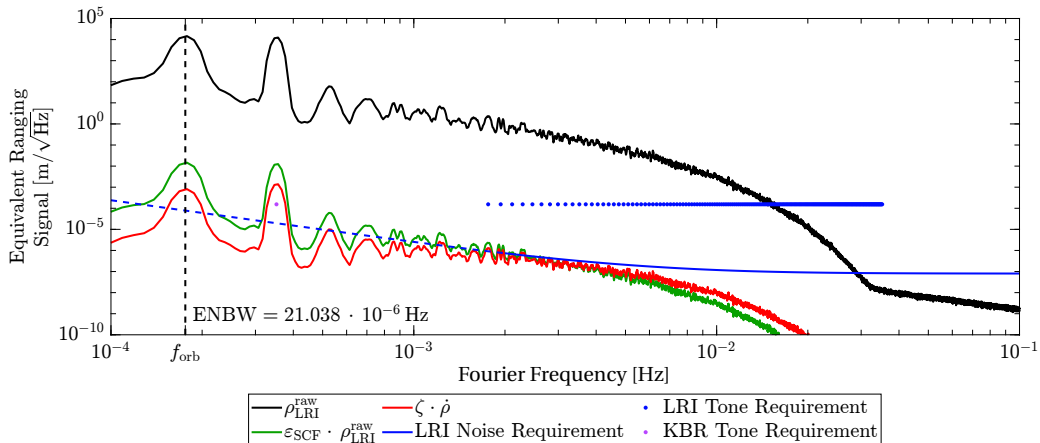


Figure 4.2. Typical ASD of the LRI ranging signal (black) and effective errors arising from a static scale factor error $\varepsilon_{\text{SCF}} = 10^{-6}$ (green) and timeshift $\zeta = 50 \mu\text{s}$ (red, cf. equation (4.33)). Also shown is the noise requirement of the LRI (blue line), which is strictly applicable only for frequencies above 2 mHz, but it was extrapolated towards lower frequencies (blue dashed segment). The dots denote a $1 \mu\text{m}_{\text{peak}}$ tone amplitude, being the tone error requirement for KBR and LRI at specific frequencies (2/rev for KBR, 10/rev . . . 200/rev for LRI). The ranging measurement is dominated by laser frequency noise at the highest frequencies (above 30 mHz) and by the differential gravitational and non-gravitational forces below.

both, scale factor (e. g. at the level of 10^{-7} to 10^{-8}) and timeshift (a few microseconds or better).

At Fourier frequencies below 0.6 mHz, the spectrum is dominated by sinusoidal errors at integer multiples of the orbital frequency $f_{\text{orb}} \approx 0.18 \text{ mHz}$. For these peaks, the tone error requirement of $1 \mu\text{m}_{\text{peak}}$ holds (Kornfeld et al., 2019) at 2/rev for the MWI (purple dot) and at n/rev with $10 \leq n \leq 200$ frequencies for the LRI (blue dots). Here, the LRI tone error requirement is not specified below 10/rev, as the instrument is only a technology demonstrator. However, future instruments might inherit the 2/rev requirement from the MWI and thus it is shown here. For correct representation, the tone requirement is rescaled to a level of $1 \mu\text{m}_{\text{peak}}/\sqrt{2\text{ENBW}} \approx 154 \mu\text{m}/\sqrt{\text{Hz}}$ (Heinzel et al., 2002) by using the equivalent noise bandwidth (ENBW) of $\approx 21 \mu\text{Hz}$ that was used to compute the spectral density traces. The displayed errors (red and green) are close to the tone requirement at 2/rev frequencies.

Laser Frequency Determination for the GRACE-FO LRI

“ The heart of science is the measurement. ”

— ERIK BRYNJOLFSSON —

Author and Professor at Stanford University

Some parts of this section were published by the author of this thesis in [Misfeldt et al. \(2023b\)](#), but the content is rewritten and extended to cover the full year 2022. This allows also to determine in-flight models for GF-2, which was in reference role only for four weeks in 2018 before, but for more than half a year in 2022.

For two reasons, precise interferometric ranging measurements need knowledge of the absolute laser frequency. First, as it is directly apparent from equation (3.10), any laser frequency variations in the measurement band (above 2 mHz) will couple linearly with the absolute spacecraft separation L . These variations are suppressed by implementing an optical reference cavity and the PDH scheme to lock the laser frequency to this reference. The stability of the cavity in the LRI has already been discussed in section 3.1. Secondly, not only these in-band variations are essential, but also knowledge of the absolute frequency is needed to relate the phase measurement to a (biased) range, cf. equation (4.27).

In this chapter, several ways to determine the absolute laser frequency of the LRI lasers are discussed and compared, namely the cross-calibration method (section 5.1), the cavity model (section 5.2) and the telemetry-based model (section 5.3). The performance of those models is compared through the range error; the direct difference of KBR-LRI range measurements gives just that. Furthermore, section 5.5 provides a model for a possible thermal coupling to correct tone errors in the measurement.

5.1. Cross-Calibration using the MWI

For the success of GRACE-FO, knowledge of the absolute laser frequency of the LRI was of minor importance, as it can be calibrated against the primary ranging instrument, the MWI, which also measures the biased inter-spacecraft range simultaneously. The instantaneous KBR range is defined as

$$\rho_{\text{KBR}}^{\text{inst}}(t) = \rho_{\text{KBR}}^{\text{raw}}(t) + \rho_{\text{KBR}}^{\text{LTC}}(t) + \rho_{\text{KBR}}^{\text{AOC}}(t) , \quad (5.1)$$

where $\rho_{\text{KBR}}^{\text{raw}}$ denotes the ionosphere-free K/Ka-band range, and the other two terms are error corrections for the light time correction (LTC) and antenna offset correction (AOC). All of them are given in the KBR1B data product ([Wen et al., 2019](#)). It is safe to assume that the KBR frequency is well known, as it is derived from the USO, whose frequency is in turn derived during precise orbit determination and referenced to the GPS. The fractional USO frequency variations due to relativity are at a level of 10^{-11} , mainly at 1/rev ([Müller et al., 2022](#)). However, they are irrelevant here, as this section only concerns variations at lower frequencies.

For calibrating the LRI frequency, the residuals of daily arcs of LRI phase measurement and the KBR range are minimized, i. e.,

$$\left| \left| \rho_{\text{KBR}}^{\text{inst}}(t) - \langle \lambda_{\text{est}}^{\text{SDS}} \rangle \cdot (\varphi_{\text{LRI}}(t) + \zeta \cdot \dot{\varphi}_{\text{LRI}}(t)) - \rho_{\text{LRI}}^{\text{LTC}} \right| \right| \rightarrow 0 . \quad (5.2)$$

A linearized form of the time shift was employed, cf. equation (4.33). Further, a modified form of equation (4.31) is employed to describe the wavelength, i. e.,

$$\langle \lambda_{\text{est}}^{\text{SDS}} \rangle(t_{\text{daily}}) = (1 + \langle \varepsilon_{\text{SCF}}^{\text{SDS}} \rangle(t_{\text{daily}})) \cdot \lambda_0^{\text{SDS}} , \quad (5.3)$$

where $\lambda_0^{\text{SDS}} = c_0/\nu^{\text{SDS}}$ is a ground-measured value given through the nominal laser frequencies (Wen et al., 2019)

$$\nu_1^{\text{SDS}} = 281\,616\,393 \text{ MHz} \quad \text{and} \quad \nu_2^{\text{SDS}} = 281\,615\,684 \text{ MHz} \quad (5.4)$$

for GF-1 and GF-2, respectively. However, as these values were determined pre-flight, they do not represent the best knowledge of the actual laser frequency and are sort of arbitrary. Equation (5.2) assumes a daily constant laser wavelength, which essentially decomposes the scale factor ε_{SCF} into a static and a time-variable part as

$$\varepsilon_{\text{SCF}}(t) = \langle \varepsilon_{\text{SCF}} \rangle(t_{\text{daily}}) + \delta\varepsilon_{\text{SCF}}(t) \quad (5.5)$$

of which only the static part $\langle \varepsilon_{\text{SCF}} \rangle$ is determined daily with discontinuities at the day boundaries. The time-variable part $\delta\varepsilon_{\text{SCF}}(t)$ remains unknown.

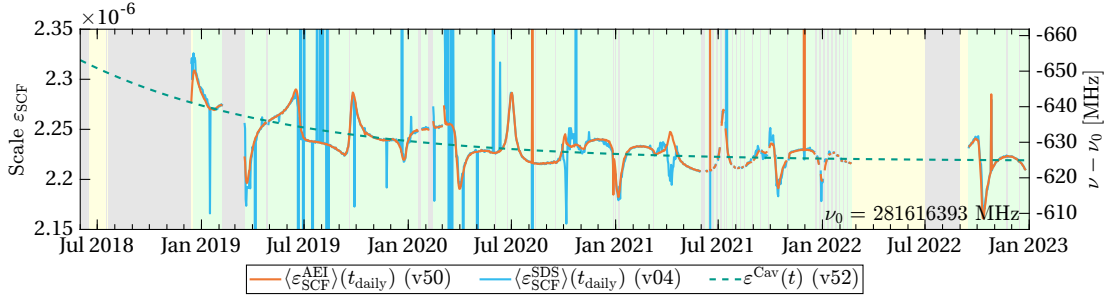
With the approach of equation (5.2) and the simplification of a constant daily wavelength, the conversion from phase to range, cf. equation (4.27), simplifies to

$$\rho_{\text{LRI}}^{\text{SDS}}(t) = \frac{c_0}{2} \frac{1 + \langle \varepsilon_{\text{SCF}}^{\text{SDS}} \rangle(t_{\text{daily}})}{\nu_0} \cdot \varphi_{\text{LRI}}(t) . \quad (5.6)$$

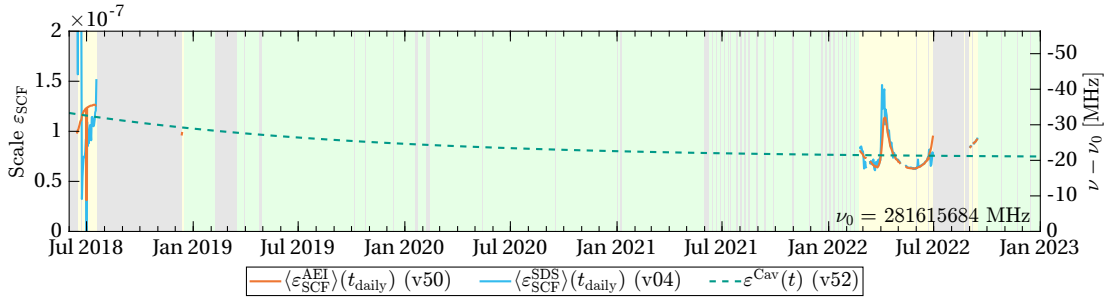
This cross-calibration is performed by the science data system (SDS) to derive the nominal LRI1B data product in version v04 (Wen et al., 2019). The value of the scale factor $\langle \varepsilon_{\text{SCF}} \rangle$ is reported in the `iono_corr` column of the data product, whereas the time shift ζ is applied through the time-correction product LLK1B.

Figure 5.1 shows the scale factor $\langle \varepsilon_{\text{SCF}}^{\text{SDS}} \rangle$ as given in the LRI1B-v04 data product (blue) alongside an in-house recomputation and validation of the v04 product, internally called LRI1B-v50 (orange). The top panel shows the segments with GF-1 in reference role and the bottom panel for GF-2. The two subplots cover the period from launch until the end of 2022. Often, GF-1 acts as the LRI reference (green background). For the times with a yellow background, GF-2 was in the reference role. The data gaps are due to spacecraft-related outages or operational modes in which the LRI cannot maintain the laser link (gray). The recomputation of the scale factor matches well with the SDS results but shows fewer outliers, especially before 27 June 2020. After that date, the phase jump removal algorithm was adjusted by the SDS (Wen, 2020). Both traces show a slow drift that seems to converge, and peaks and dips occurring roughly every three months, indicating an apparent change of the scale factor with a magnitude of $\pm 10^{-7}$ or ± 20 MHz in terms of the laser frequency. These variations are likely susceptibilities of the scale factor estimate to temperature-related tone errors, as discussed later in section 5.5. Notably, one can not distinguish which instrument contributes to those periodic variations, as usually only the difference between KBR and LRI is analyzed. However, the variations and their potential cause will be covered later in section 5.5.

5.2. CAVITY FREQUENCY DECAY



(a) Scale factor estimate of GF-1



(b) Scale factor estimate of GF-2

Figure 5.1. Scale Factor ε_{SCF} from cross-calibration (blue: official SDS LRI1B-v04 data; orange: in-house recomputation) and exponential fit model ε^{Cav} (green) for (a): GF-1 and (b): GF-2. The scale ε_{SCF} refers the nominal frequency ν_0 to the actually measured frequency, cf. right y-axis.

5.2. Cavity Frequency Decay

The slow drift found in the cross-calibration result of figure 5.1 was fitted as exponential decay of the form

$$\varepsilon^{\text{Cav}}(t) = \varepsilon_{\infty}^{\text{Cav}} - \varepsilon_0^{\text{Cav}} \exp(-\lambda^{\text{Cav}} \cdot t) \quad (5.7)$$

and is shown as the dashed curves in figure 5.1. The time t is GPS seconds past 22 May 2018, 00:00:00 UTC, and the fit parameters are listed in table 5.1. The standard error estimates of the parameters for GF-1 are smaller than for GF-2, as there is more data with GF-1 in the reference role. This kind of change in the estimated scale factor suggests that the length of the cavity spacer material is slowly changing over time. Such exponential shrinkage (or: increasing frequency), as apparent here, has already been observed in similar cavity systems made from ultra-low expansion (ULE) materials, see e. g. Fox et al. (2004) and Sanjuan et al. (2019), and the suspected cause is aging of the spacer material (Alnis et al., 2008). This effect is a physical property of the cavity, which is sometimes also called the *cavity creep*. Of course, equation (5.7) can be converted into an equivalent frequency model ν^{Cav} through equation (4.31). The corresponding frequency rates, computed from the first derivative, are in the order of 900 mHz/s and 300 mHz/s at $t = 0$ for GF-1 and GF-2, respectively, and decrease to approximately 45 mHz/s and 33 mHz/s after three years and below 10 mHz/s after five years for both cavities. This exponential decaying model for the cavity resonance frequency was used to derive another LRI1B-equivalent data product called LRI1B-v52.

Table 5.1. Estimated exponential cavity model ε^{Cav} parameters and their uncertainties.

SC	$\varepsilon_{\infty}^{\text{Cav}}$	$\varepsilon_0^{\text{Cav}}$	λ^{Cav} [1/s]
GF-1	$2.218 \cdot 10^{-6}$ $\pm 2.522 \cdot 10^{-9}$	$-1.039 \cdot 10^{-7}$ $\pm 1.262 \cdot 10^{-8}$	$3.217 \cdot 10^{-8}$ $\pm 5.170 \cdot 10^{-9}$
GF-2	$7.326 \cdot 10^{-8}$ $\pm 1.648 \cdot 10^{-8}$	$-4.596 \cdot 10^{-8}$ $\pm 1.106 \cdot 10^{-8}$	$2.299 \cdot 10^{-8}$ $\pm 4.852 \cdot 10^{-8}$

The difference to the previously mentioned LRI1B-v50 is that this newly derived cavity frequency estimate replaces the scale factor from the cross-calibration method.

5.3. Laser-Telemetry Frequency Model

Another way to determine the absolute laser frequency is the telemetry-based model ν^{TM} , which has already been introduced in section 3.1.3. Its idea is to use the frequency actuator voltages and the overall RLU temperature as a proxy for the actual laser frequency variations. In this section, the format of the telemetry and the on-ground calibrations are explained in detail.

5.3.1. Laser Telemetry Description

The telemetry of the laser actuator signals is downlinked and published in the LHK1A and LHK1B data products (Wen et al., 2019). With the LRI in science or diagnostic mode, these data streams have a rate of 1 Hz and a resolution of 32 bit. Otherwise, the actuator signals are reported only once every 120s and with a resolution of 16 bit. In any case, the unsigned values x can be decoded to a signed value and normalized to the value range $(-1/2, 1/2]$ using the two's complement

$$\text{u2i}(x, N) = \begin{cases} x/2^N - 1, & \text{if } x \geq 2^{N-1} \\ x/2^N, & \text{if } x < 2^{N-1} \end{cases} \quad (5.8)$$

with N denoting the bit depth (16 or 32).

Two variables are attributed to each frequency actuator that will be denoted as `thermIL`, `thermOOL`, `pztIL`, and `pztOOL` in the following. The notations in-loop (IL) and out-of-loop (OOL) are somewhat misleading here, as they do not refer to different sensors as in conventional feedback control circuits but are two parts of the same signal which are summed up to form the final setpoint value. The OOL channel is used for manual control in an open-loop configuration, e. g., to drive a frequency ramp for locking to the cavity or during link acquisition. On transitioning from manual control to automatic control, e. g., on a successful acquisition scan, the OOL signal is fixed at the current value, and the IL channel then represents the evolution of the actuator value in closed-loop operation. The notation is used here to remain conformal with the official data products. The actuator range of the OOL channels is ± 9 V, whereas the IL channel is limited to ± 1 V, which adds up to a full actuator control signal range of ± 10 V. The nominal frequency coupling coefficients are 500 MHz/V for the thermal element and 5 MHz/V for the PZT. This yields total scan ranges of ± 10 V \cdot 500 MHz/V = ± 5 GHz for the thermal element and equivalently ± 50 MHz for the PZT element.

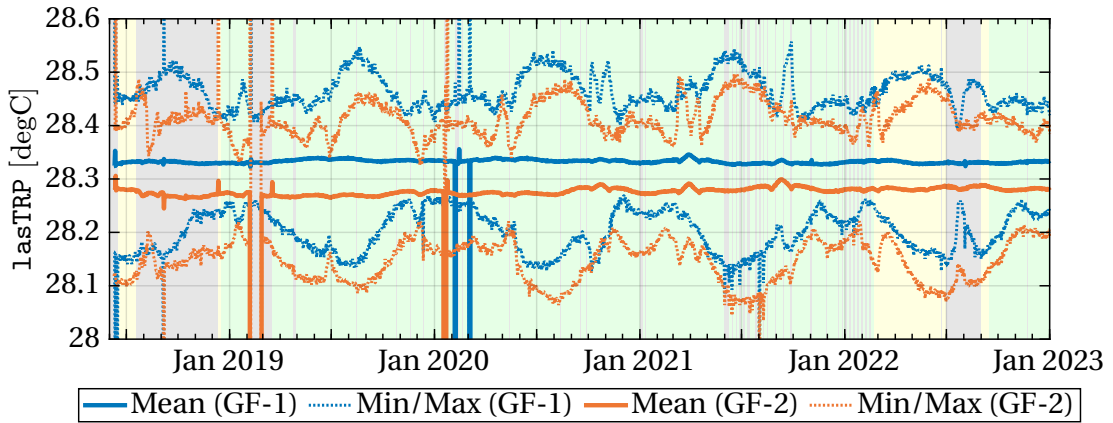


Figure 5.2. Daily Mean/Min/Max values for the 1asTRP thermistor on GF-1 and GF-2. The background coloring shows times of GF-1 as reference (green), GF-2 as reference (yellow), and LRI unlocked (gray).

The output frequency of the laser further depends on the temperature of the RLU, measured at the TRP at one of the feet of the housing (cf. figure 3.5). The nominal operating temperature of the laser is 26°C with a nominal frequency coupling of -12 MHz/K . Since the TRP of the RLU is on the outside of the housing, a time delay $\tau = 520\text{ s}$ is applied to the temperature measurements to account for the propagation time of outer temperature changes to the NPRO crystal. This numerical value was provided by the laser manufacturer Tesat Spacecom. By the time of writing, the RLU TRP temperature data is not publicly available in version 04 of the Level-1 data products by the SDS, but might at some point, to the authors' knowledge, be released within the HRT1B product. Figure 5.2 shows the time series of daily averaged/min/max values of the 1asTRP data. Over the whole mission time, the RLU temperature on both spacecraft is very stable, except for some periods in early 2019 and early 2020 where one or both LRI units were turned off completely. On GF-1, the average temperature (excluding the outliers) is at 28.33°C as opposed to 28.28°C on GF-2. On both spacecraft, variations of up to $\pm 0.25\text{ K}$ can be observed, related to orbital temperature variations. According to the nominal coupling of -12 MHz/K , the equivalent RLU frequency variations are on the order of $\mp 3\text{ MHz}$, or a fractional frequency variation of $\varepsilon_{\text{SCF}} \approx \delta\nu/\nu_0 \approx 1 \cdot 10^{-8}$, if the laser was free-running and not locked to the reference cavity.

As this analysis mainly concerns the very low frequencies at $1/\text{day}$ and below, a symmetric moving-mean filter with the length of eight times the orbital period $8/f_{\text{orb}} \approx 12\text{ h}$ is used to remove higher frequency components in the actuator signals.

5.3.2. Ground-Calibration Measurement Campaigns

During ground testing before launch, a laboratory setup was developed to verify and refine the frequency coupling coefficients of equation (3.11) by recording the laser's absolute frequency and the actuator setpoints while modulating the laser frequency. The absolute laser frequency was measured with a wavemeter, which is based on Fizeau in-

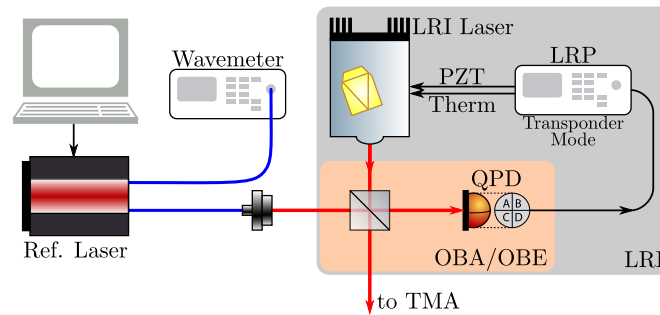


Figure 5.3. Laboratory setup for the LRI flight laser frequency calibration. Blue: Optical fibers; Red: laser beams in free space; Black: electric signals.

terferometry^[1]. Members of the LRI teams at JPL/NASA and AEI Hanover performed the measurements at the spacecraft level in 2017 and 2018. The author of this thesis was not involved in the experimental activities but re-analyzed the data later.

Wavemeter Calibration

Three wavemeters were used throughout the experimental activities. Two of them, a WS6-600 and a WS7-60, are manufactured by HighFinesse/Angstrom. The third one was a WA1500 by Burleigh. The latter was used directly before launch at the Vandenberg Air-Force Base (VAFB), and only very few data points were taken. It has an absolute accuracy of 600 MHz, just like the WS6-600. The accuracy of the WS7-60 is better by one order of magnitude, i. e., 60 MHz. The two HighFinesse devices feature a built-in neon lamp for calibration purposes.

At first, the wavemeter accuracy after the internal calibration was verified against an iodine standard. Further, the frequency of the reference laser and its frequency actuator coupling was characterized. These measurements are explained in more detail in appendix A for brevity. In summary, it was found that the data of the WS6-600 wavemeter is off by approximately -60 MHz on average and shows periodic features of 15 MHz (peak-to-peak) at a period of 300 s.

RLU Calibration Measurements

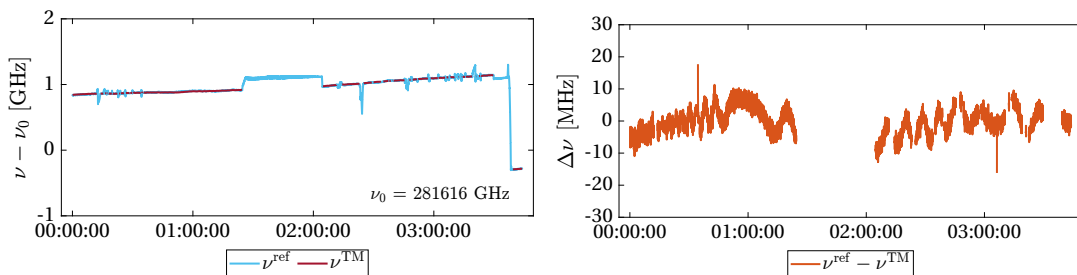
After verification of the wavemeter accuracy and the reference laser’s frequency actuator, the RLU was characterized. Figure 5.3 sketches the experimental setup of the RLU characterization measurement, which consisted of the LRI flight laser, the LRP, a frequency-controlled reference laser and a wavemeter. The LRI was in transponder mode, which means that it locks the local laser phase to the incoming beam and adds an 10 MHz offset. The incoming beam was generated from the reference laser, which belonged to the ground support equipment (GSE), and the wavemeter was connected

^[1]The working principle of a Fizeau wavelength meter is as follows: The beam under test propagates through two glass plates, which are under a small wedge angle, creating parallel and equidistant interference patterns on a camera chip. Fizeau interferometry does not need movable parts, which makes it suitable for portable devices, and it has a linear relationship between the beams’ wavelength and the distance between the lines of the interference pattern. For more information, see e. g. [Demtröder \(2014\)](#) and [Dobosz et al. \(2017\)](#).

5.3. LASER-TELEMETRY FREQUENCY MODEL

Table 5.2. Measurement campaigns of the RLU frequency calibration. The Identifier (ID) of the campaigns is used throughout the main text.

SC	ID	Date	Device	Note
GF-1	(i)	Nov 2017	WS6-600	DWS test procedure
GF-1	(ii)	Jan 2018	Burleigh WA1500	single data points only
GF-2	(1)	Jul 2017	WS7-60	discrete frequency steps
GF-2	(2)	Jul 2017	WS7-60	continuous frequency sweep
GF-2	(3)	Nov 2017	WS6-600	DWS test procedure
GF-2	(4)	Jan 2018	Burleigh WA1500	single data points only



(a) Measured frequency ν^{ref} and model ν^{TM} . (b) Frequency residuals $\nu^{\text{ref}} - \nu^{\text{TM}}$

Figure 5.4. Regression results for the GF-1 laser of measurement (i), cf. table 5.2. The gaps originate from lost-lock events of the LRI unit in transponder mode, when the reference laser (ν^{ref} in (a)) changed its frequency too fast. The raw telemetry recorded in parallel is shown in appendix B.

to this GSE laser. Due to the fixed 10 MHz offset of the LRI in transponder mode, its frequency is thus also known.

Multiple calibration sessions at the spacecraft level have been performed on both RLUs between July 2017 and January 2018. The GF-1 laser was calibrated twice, while the GF-2 laser was calibrated four times. A brief overview of the measurement and their date is shown in table 5.2. Experiments (i) and (3) were DWS tests, in which the frequency was recorded as an auxiliary channel. Furthermore, the setpoint of the reference laser was changed from time to time, causing the LRI unit to lose lock and switch into reacquisition mode, which explains some data gaps. A WS6-600 wavemeter by HighFinesse with an absolute accuracy of 600 MHz was used for these tests. Since experiments (ii) and (4) used a Burleigh WA1500, which had no digital output but only a display, not many data points were recorded in these tests. The GF-1 telemetry model was derived using experiment (i) solely. On GF-2, the laser was tested more often and used a WS7-60 wavemeter with higher accuracy (60 MHz).

Using these measurements, the coupling factors of equation (3.11) are determined through a least squares minimization, providing the models $\nu_{1/2}^{\text{TM}}$ for the two lasers. The regression results are shown in figure 5.4 for GF-1 and in figure 5.5 for GF-2. The subfigures (a) show the measured reference frequency ν^{ref} and the model ν^{TM} , which was obtained by estimating the parameters of equation (3.11) in a least-squares sense. The parameters of this estimation are shown in table 5.3 and deviate only slightly from the manufacturer’s design values. The residuals after minimization are shown in panels (b) of figures 5.4 and 5.5. All parts where the WS6-600 wavemeter was used show

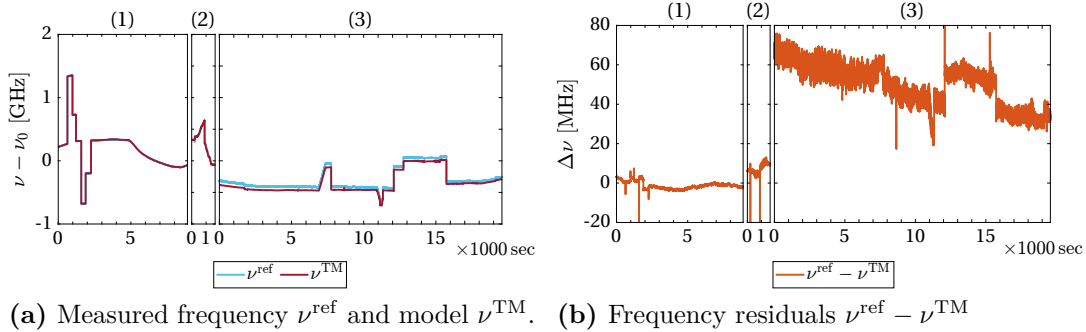


Figure 5.5. Regression results for the GF-2 laser. The numbering on top of the individual panels of each subfigure corresponds to the measurement campaigns, cf. table 5.2. Note the offset in the residuals in subfigure (b) when the less precise wavemeter WS6-600 was used in campaign no. (3). The average bias here is 50.056 ± 0.061 MHz. Other than in the previous figure, times where the LRI was unlocked from the reference laser are not shown here. The raw telemetry recorded in parallel is shown in appendix B.

higher noise and small oscillations in the residuals. While estimating the parameters for GF-2, a higher weight of 5:1 is applied to the data of the WS7-60, as it has a higher absolute accuracy. An offset of approximately 50 MHz was observed, which is consistent with the calibration of the wavemeters described in appendix A. For brevity, the measured actuator signals and RLU temperature are not shown here but can be found in appendix B.

5.3.3. Empirical Refinement with Flight Data

Figure 5.6 shows the afore described laser telemetry models $\nu_{1/2}^{\text{TM}}$ (dark blue and green) alongside the v50 frequency estimate from cross-calibration against the microwave $\nu_{\text{SCF}}^{\text{AEI}}$ (light blue). The subscripts 1/2 refer to GF-1 or GF-2, respectively. The curves were shifted down by 10 MHz whenever the particular spacecraft was in transponder role to remove the intended offset frequency in the plot. A frequency offset can be observed between the times with GF-1 and GF-2 in the reference role, indicated by the background coloring. The cavity resonance frequency of the GF-2 cavity is approximately 110 MHz below the one of GF-1, simply because of the manufacturing tolerances. Furthermore, the cavity frequency models $\nu_{1/2}^{\text{Cav}}$ are shown once more (black).

By design, the frequency difference of GF-1 and GF-2 is $\nu_{\text{T}} - \nu_{\text{R}} = f_{\text{off}} + f_{\text{D}}(t) \approx 10 \text{ MHz} \pm 2.35 \text{ MHz}$, with the transponder laser frequency ν_{T} being above the reference laser ν_{R} . However, the telemetry models differ by approximately ± 25 MHz at maximum, which is within the accuracy of the better wavemeter WS7-60, defining the model accuracy. A drift of roughly $40 \text{ MHz/year} \approx 1 \text{ Hz/s}$ between the telemetry models $\nu_{1/2}^{\text{TM}}$ and the reference given by the cross-calibration $\langle \nu_{\text{SCF}}^{\text{AEI}} \rangle$ (light blue) can be observed.

There are some gaps in the data (indicated by gray background coloring) caused by, e.g., regular nadir-pointing periods (June 2021 to September 2022), in which the LRI was not generating science data. The steep slopes and the dip in February and March 2020 in $\nu_{1/2}^{\text{TM}}$ originate from spacecraft-related non-science phases of the LRI, after which the units had to heat up to reach their nominal temperatures and thermal

5.3. LASER-TELEMETRY FREQUENCY MODEL

Table 5.3. Frequency coupling factors for the two LRI laser flight units. The design values from the laser specifications and fit results derived from on-ground measurements are shown. PZT and TRP coupling factors were not refined because the measurements were unsuitable for deriving these couplings. The manufacturer provided the static value $\Delta\nu_{\text{AirToVac}}$ representing the frequency change from air to vacuum environment. The shown uncertainties are the standard error of the variance-covariance matrix.

Coupling	Unit	Design Value	GF-1 (Fit)	GF-2 (Fit)
c_{pztIL}	[MHz]	10	-	-
c_{pztOOL}	[MHz]	90	-	-
c_{thermIL}	[MHz]	1000	1096 ± 0.226	1099 ± 0.348
c_{thermOOL}	[MHz]	9000	9007 ± 4.389	8862 ± 6.945
c_{lasTRP}	[MHz/K]	-12	-	-
$\nu_{0,\text{air}}$	[MHz]	281 614 803 (GF-1) 281 614 780 (GF-2)	281 614 716.494 ± 0.225	281 614 632.551 ± 0.276
$\Delta\nu_{\text{AirToVac}}$	[MHz]	37 (GF-1) 27 (GF-2)	-	-

equilibrium, which enters the telemetry-model through the laser’s TRP. It was found that the LRI acquired the laser link before thermal equilibrium was reached and that there are temperature transients observable at the lasers’ TRP (cf. figure 5.2). It seems that such large transients in the laser temperature are causing the simple model to fail and thus lead to steps in the $\nu_{1/2}^{\text{TM}}$ models, eventually through non-linear temperature dependencies. However, these steps are not physical as they would otherwise be visible in the cross-calibration estimate as well. Figure 5.7 shows the equivalent contributions from the thermal setpoints multiplied by their corresponding coupling factors, cf. table 5.3. The black dashed vertical lines indicate the time of the apparent steps, where the `thermIL` shows unusually high values and the `thermOOL` corresponding low values on acquisition.

The drift and steps are accounted for by an empirical correction term, whose parameters are again determined through a least-squares minimization of the deviations of the telemetry model and the current best estimate of the true cavity frequency, i. e., $\nu_{1/2}^{\text{TM}} - \nu_{\text{R}}^{\text{Cav}}$ against the modeled steps and drift. Here, the subscript R denotes the spacecraft in the reference role. The model reads

$$\nu^{\text{emp}}(t) = a \cdot (t - t_0) + \Delta\nu + \nu^{\text{step}}(t) , \quad (5.9)$$

where a is the drift in Hz/s, $\Delta\nu$ a static offset, that accounts for errors in $\nu_{0,\text{air}}$ of the telemetry model (cf. equation (3.11)) and $\nu^{\text{step}}(t)$ is defined as

$$\nu^{\text{step}}(t) = \nu_i^{\text{step}} \quad \text{if } t_i^{\text{step}} \leq t < t_{i+1}^{\text{step}} . \quad (5.10)$$

The estimated parameters are shown in tables 5.4a and 5.4b. The two lasers’ drift, more precisely the drift of the setpoints, is in the order of 1 Hz/s or equivalently 40 MHz/year. The steps are below 10 MHz each. In total, the empirically refined telemetry model (cf. equation (3.11)) reads

$$\nu_{1/2}^{\text{TME}}(t) = \nu_{1/2}^{\text{TM}}(t) - \nu_{1/2}^{\text{emp}}(t) \quad (5.11)$$

and is also shown in figure 5.6 in orange and red for GF-1 and GF-2, respectively. They now agree well with the cross-calibration method within 10 MHz. The need for

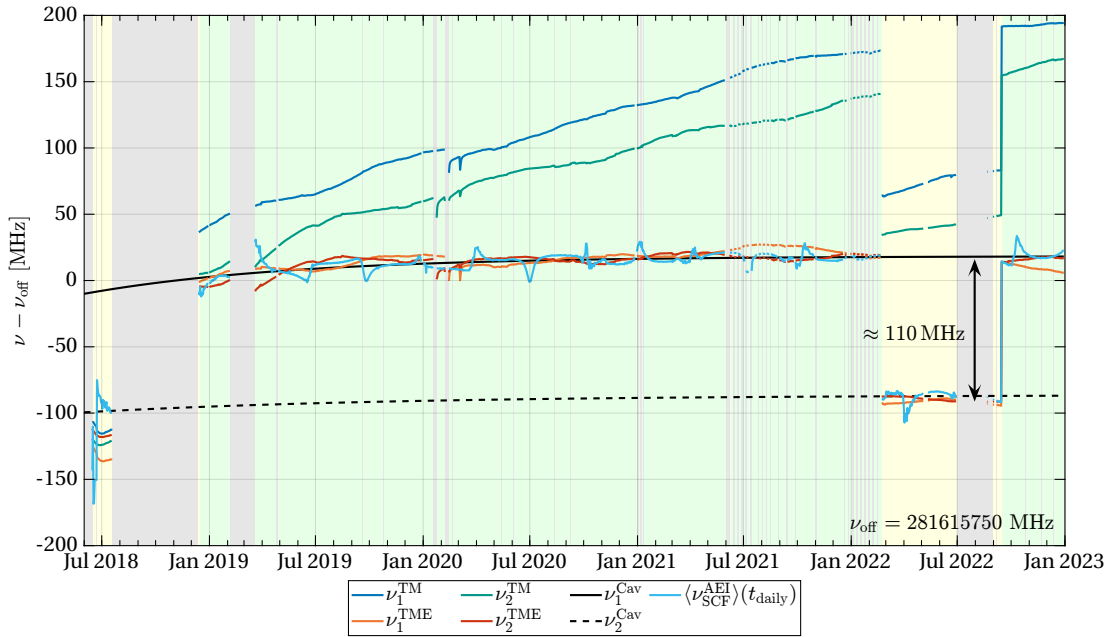


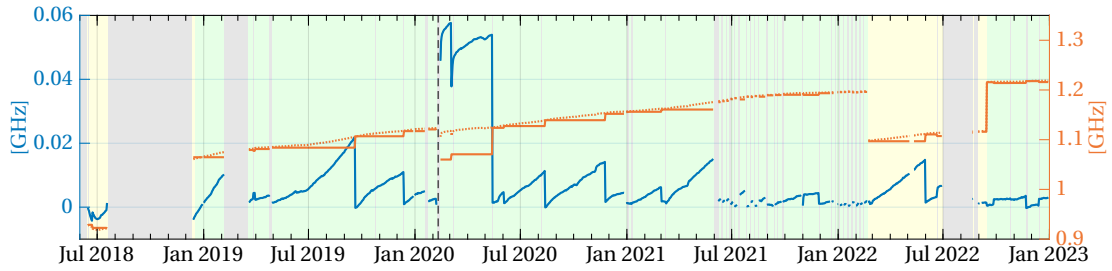
Figure 5.6. Laser frequency models ν^{TM} , ν^{TME} , ν^{Cav} and cross-calibration result over time for both SC. The background coloring shows times of GF-1 as reference (green), GF-2 as reference (yellow), and LRI unlocked (gray). The difference in the two cavity frequencies is approximately 110 MHz.

this empirical model makes the telemetry model still dependent on the microwave for the in-flight calibration. Further, ν^{TME} does neither show nor explain the seasonal variations in the cross-calibration estimate $\langle \nu_{\text{SCF}}^{\text{AEI}} \rangle$. The LRI ranging data product using this frequency model $\nu_{1/2}^{\text{TME}}$ to convert the measured phase to a range is called LRI1B-v51 in the following sections.

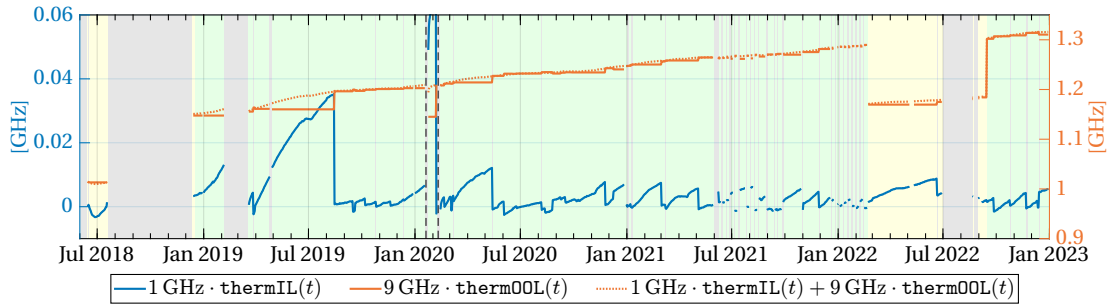
The hypothesis, raised in Misfeldt et al. (2023b) that this drift is an aging effect of the NPRO crystal of the RLUs was tested in a laboratory experiment, as there is little literature on aging-induced frequency changes of NPRO lasers. This experiment is described later in chapter 6. It is noteworthy that this drift is not represented in the actual cavity and laser frequency after stabilization but only in the PZT and thermal setpoints of the telemetry model since the laser is still locked to the reference cavity, which shows a much smaller drift (black solid and dashed lines in figure 5.6). Note that the telemetry model represents the setpoints changes that are needed to maintain the RLU output frequency at the cavity resonance. In contrast, the actual RLU laser frequency change from this aging effect is represented by $-\nu_{1/2}^{\text{emp}}$.

5.4. Comparison of the Models

In the next step, the three laser frequency models derived in the previous sections are compared at the level of LRI1B-equivalent data products. As a reminder, the official version by the SDS is called LRI1B-v04, while the in-house re-processing, also using the cross-calibration method of section 5.1, is called LRI1B-v50. However, as it introduces two empirical parameters each day and can not be derived independently from



(a) Frequency actuator signals on GF-1



(b) Frequency actuator signals on GF-2

Figure 5.7. Daily averaged thermal frequency actuations. (a): GF-1, (b): GF-2. Both show a trend over time. The background coloring shows times of GF-1 as reference (green), GF-2 as reference (yellow), and LRI unlocked (gray).

the KBR, it will not be considered further in the following comparison. LRI1B-v51 instead uses the laser telemetry model ν^{TME} (cf. equation (5.11)), which only needs initial calibration w. r. t. KBR and is independent thereafter. The exponential cavity model ν^{Cav} (cf. equation (5.7)) is used for LRI1B-v52. Last but not least, LRI1B-v53 uses the constant, predetermined values ν_0^{SDS} without any time-dependency (cf. equation (5.4)). Further differences between LRI1B-v04 and all LRI1B-v5X data products are the improved deglitching algorithm (Müller, 2021) and the LTC implementation according to Yan et al. (2021). More information about the LRI1B-v5X data products can be found in Müller (2021), Müller et al. (2022), and Misfeldt et al. (2023b) and on www.aei.mpg.de/grace-fo-ranging-datasets. The v5X data products were derived for the time span from June 2018 until the 1st of January 2023 for the following analysis.

5.4.1. The Range Error

The prefit range error $\rho_{\text{err},v5X}^{\text{pre}}$ is defined as the difference of the instantaneous ranges of LRI (in version v5X) and KBR as

$$\rho_{\text{err},v5X}^{\text{pre}}(t) = \rho_{\text{LRI},v5X}^{\text{inst}}(t) - \rho_{\text{KBR}}^{\text{inst}}(t) - \rho_{\text{KBR}}^{\text{FV}}(t), \quad (5.12)$$

where a correction term $\rho_{\text{KBR}}^{\text{FV}}$ arising from carrier frequency variations of the KBR is considered (Müller et al., 2022). This correction mainly contains signal at 1/rev and 2/rev and improves the consistency between SDS-derived KBR and AEI-derived LRI data products. The AEI-derived LRI ranging data products include such a correction

Table 5.4. Empirical parameters for the telemetry model, cf. equation (5.10). Time tags refer to midnight.

(a) Drift Parameters				(b) Steps in the Model			
Coupling	Unit	Value		i	t_i^{step}	ν_i^{step} [MHz]	
		GF-1	GF-2			GF-1	GF-2
a	[Hz/s]	1.189	1.061	1	22.05.2018 00:00:00	0	0
$\Delta\nu$	[MHz]	16.573	-9.626	2	24.01.2020 14:28:00	0	5.762
				3	14.02.2020 02:02:35	-0.224	5.762
				4	04.03.2020 14:14:26	-0.916	5.762
				5	01.01.2023 00:00:00	undefined	

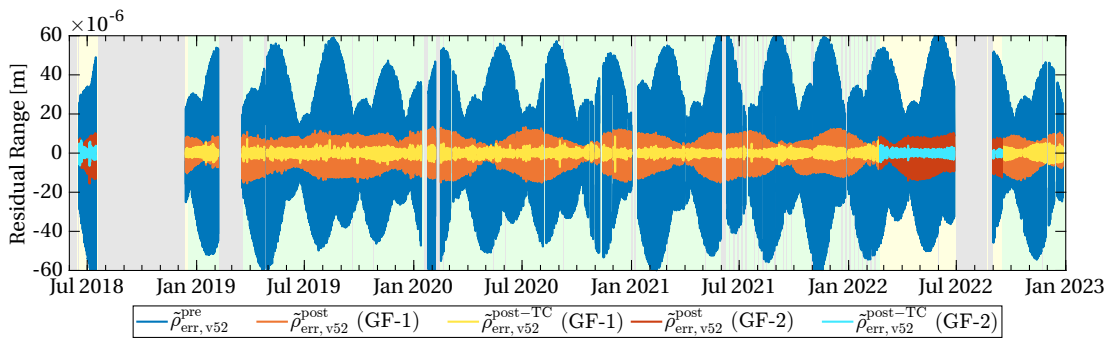


Figure 5.8. TC fit for both SC. The direct difference between KBR and LRI is shown in blue ($\tilde{\rho}_{\text{err}}^{\text{pre}}$), whereas the first stage of post-fit results, $\tilde{\rho}_{\text{err}}^{\text{post}}$, is shown in orange (GF-1) and red (GF-2). After estimating and subtracting the thermal coupling (TC), one obtains $\tilde{\rho}_{\text{err}}^{\text{post-TC}}$, shown as the yellow and cyan curves for GF-1 and GF-2, respectively. The distinction between the two SC is based on their role as reference or transponder. The results for v51 and v53 are shown in figure C.6 in appendix C.

already. However, the magnitude of this effect is small, and the results barely change when the correction is omitted.

The prefit range error, in general, exhibits long-term drifts in the order of a few $10 \mu\text{m}/\text{day}$, which are removed through a high-pass FIR filter with a cutoff frequency of $0.08 \text{ mHz} \approx f_{\text{orb}}/2$. The reason for this drift remains unknown and may be addressed in future studies. The filter does not affect the 1/rev, 2/rev, and higher frequencies, which the scale factor is most sensitive to. Half a day of data is cropped at the start and end of each continuous segment, i. e., at every loss of the interferometric link of either KBR or LRI, to remove the initialization period of the filter. Hence, even very short interruptions seem longer when represented graphically. The range error is decimated to a sampling rate of 3.3 mHz after another FIR anti-aliasing filter to save computational costs. In the following, filtered quantities are denoted with a tilde, e. g.,

$$\tilde{\rho}_{\text{err},v5X}^{\text{pre}} = \text{HPF}(\rho_{\text{err},v5X}^{\text{pre}}, 0.08 \text{ mHz}) . \quad (5.13)$$

The filtered pre-fit range errors for the LRI1B-v52 data products using ν^{Cav} are shown as blue traces in figure 5.8. The background coloring again indicates which SC is in reference role (green for GF-1, yellow for GF-2). The pre-fit residuals mainly oscillate at 1/rev and 2/rev frequencies, varying amplitude over the months. Aiming for small

5.4. COMPARISON OF THE MODELS

Table 5.5. Pre- and postfit rms of the range error and global parameter scale and timeshift estimates. The actual timeseries of LRI1B-v52, based on $\nu_{1/2}^{\text{Cav}}$ is shown in figure 5.8, v51 (based on $\nu_{1/2}^{\text{TME}}$) and v53 (based on the constant $\nu_{1/2}^{\text{SDS}}$) in figure C.6 of appendix C. The very last column references the tables listing the exact TC coupling coefficients. Different versions of the TC model exist for v52, which are described in more detail in the section 5.5.

v5X	SC	prefit		postfit			postfit incl. TC			Table
		$\tilde{\rho}_{\text{err}}^{\text{pre}}$ [$\mu\text{m rms}$]	$\tilde{\rho}_{\text{err}}^{\text{post}}$ [$\mu\text{m rms}$]	$\varepsilon_{\text{SCF}}^{\text{glo}}$	ζ^{glo} [μs]	$\tilde{\rho}_{\text{err}}^{\text{post-TC}}$ [$\mu\text{m rms}$]	$\varepsilon_{\text{SCF}}^{\text{glo}}$	ζ^{glo} [μs]		
v51	GF-1	25.068	6.807	$5.23 \cdot 10^{-9}$	71.24	3.730	$-1.21 \cdot 10^{-8}$	68.23	C.1a	
	GF-2	29.206	6.847	$-4.56 \cdot 10^{-8}$	70.77	1.774	$-2.08 \cdot 10^{-7}$	69.86	C.1b	
	GF-1	24.584	5.272	$-3.38 \cdot 10^{-10}$	71.18	1.188	$-1.10 \cdot 10^{-9}$	67.66	5.6a	
v52	GF-1	–	–	–	–	1.203	$3.01 \cdot 10^{-8}$	67.90	5.7a	
	GF-2	25.306	5.177	$-3.87 \cdot 10^{-9}$	70.85	0.930	$1.24 \cdot 10^{-7}$	68.44	5.6b	
	GF-2	–	–	–	–	1.104	$1.77 \cdot 10^{-7}$	68.63	5.7b	
v53	GF-2	–	–	–	–	1.359	$1.39 \cdot 10^{-9}$	68.09	5.8	
	GF-1	657.515	6.587	$2.23 \cdot 10^{-6}$	71.17	2.812	$2.46 \cdot 10^{-6}$	67.98	C.2a	
	GF-2	36.383	7.015	$8.06 \cdot 10^{-8}$	71.51	1.362	$4.60 \cdot 10^{-7}$	68.81	C.2b	

differences between KBR and LRI, the rms of the range error is used as a metric. Table 5.5 lists those prefit residuals in units of $\mu\text{m rms}$ for the three v5X releases. The residuals are 25...30 $\mu\text{m rms}$ in the cases of v51 and v52, respectively. v53 for GF-1 has a large pre-fit rms of 657 $\mu\text{m rms}$, since the initial laser frequency estimate ν_0^{SDS} of GF-1 is roughly 650 MHz from the in-flight truth, and thus the conversion from phase to range is unprecise. The on-ground frequency estimate for GF-2 is close to the truth, and thus the pre-fit rms is also at a smaller level of 36 $\mu\text{m rms}$ in v53. Since v52 shows the best results here, the following analysis will focus on this particular dataset. However, additional numbers, figures, and tables can be found in appendix C and will be mentioned at the appropriate places in the main text.

5.4.2. Global Scale and Timeshift Estimation

As a residual timeshift $\zeta \approx 70 \mu\text{s}$ between KBR and LRI is known (Müller et al., 2022), a first refinement of the range error $\tilde{\rho}_{\text{err}}^{\text{pre}}$ is performed by estimating a global static scale $\varepsilon_{\text{SCF}}^{\text{glo}}$ and also a global timeshift ζ^{glo} . This procedure is similar to the cross-calibration scheme (cf. section 5.1), but instead of estimating two parameters each day, only two global parameters for the complete period are determined here. With these estimates, the postfit range error reads

$$\tilde{\rho}_{\text{err},v5X}^{\text{post}}(t) = \left(1 + \varepsilon_{\text{SCF}}^{\text{glo}}\right) \cdot \tilde{\rho}_{\text{LRI},v5X}^{\text{inst}}(t + \zeta^{\text{glo}}) - \tilde{\rho}_{\text{KBR}}^{\text{inst}} - \tilde{\rho}_{\text{KBR}}^{\text{FV}}. \quad (5.14)$$

This estimation of only two parameters removes the unintended time delay and potential biases in the laser frequency models. The effect can again be linearized such that the correction term reads

$$\delta\tilde{\rho}_{\text{TC}}^{\text{glo}} = \varepsilon_{\text{SCF}}^{\text{glo}} \cdot \tilde{\rho}_{\text{LRI},v5X}^{\text{inst}}(t) + \zeta^{\text{glo}} \cdot \dot{\tilde{\rho}}_{\text{LRI},v5X}^{\text{inst}}(t). \quad (5.15)$$

The numerical values for these two global parameters are shown in columns 5 and 6 of table 5.5. Here, TC stands for thermal coupling and will be discussed in detail in the next section. The newly derived postfit range error is shown in figure 5.8 in orange

and red for GF-1 and GF-2, respectively. It already significantly lowers the rms error below $7 \mu\text{m}$ rms for all three v5X versions and both spacecraft; see the 4th column. The numerical value of the global scale parameter $\varepsilon_{\text{SCF}}^{\text{gl}}$ provides a metric of how close the respective model is to the KBR. Accordingly, the exponential cavity drift model $\varepsilon_{\text{SCF}}^{\text{Cav}}$ of v52 (cf. equation (5.7)) is accurate up to $-3.38 \cdot 10^{-10}$ for GF-1 and $-3.87 \cdot 10^{-9}$ for GF-2, while the other models need larger scale factor corrections.

It is expected that the KBR noise level is limiting the postfit range error. However, assuming a $10 \mu\text{m}/\sqrt{\text{Hz}}$ white noise in the KBR at low Fourier frequencies and a 3.3 mHz sampling rate, one obtains

$$10 \mu\text{m}/\sqrt{\text{Hz}} \cdot \sqrt{3.3 \text{ mHz}/2} \approx 0.4 \mu\text{m rms} , \quad (5.16)$$

which is the theoretical KBR noise limit expressed as an ASD. However, the range error of none of the three v5X datasets is reaching this theoretical limit. Therefore, potential ranging errors from thermal effects are investigated in the next section to reduce the KBR-LRI differences further.

5.5. Thermal Coupling in KBR-LRI Residuals

The thermal environment of the whole spacecraft and the individual units inside constantly change, with the largest variations appearing at 1/rev and 2/rev frequencies. These thermal variations might couple into the measured range of either KBR or LRI or both, commonly denoted as tone errors (Kornfeld et al., 2019). Two possible coupling mechanisms have been identified: First, the coupling could be in the (laser) frequency regime, like temperature changes of the cavity or USO, which acts as an additional scale factor term. Secondly, such errors might occur in the phase (or path length) regime, e. g., due to temperature-dependent alignment of optical components or temperature-driven effects in the electronics. In this section, linear coupling factors for the temperature sensors on both SC are estimated to reduce the KBR-LRI differences further, i. e., minimize $\tilde{\rho}_{\text{err}}^{\text{post}}$. The coupling factors have the units of 1/K for the (fractional) frequency regime and m/K for the phase regime. The TC term is denoted as $\tilde{\rho}_{\text{TC}}$. The postfit range error, including that TC, is defined as

$$\tilde{\rho}_{\text{err},v5X}^{\text{post-TC}}(t) = \tilde{\rho}_{\text{err},v5X}^{\text{post}}(t) - \tilde{\rho}_{\text{TC}}(t) , \quad (5.17)$$

with the TC being

$$\tilde{\rho}_{\text{TC}}(t) = \sum_i \delta \tilde{\rho}_{\text{TC},i}^{\text{freq}}(t) + \sum_i \delta \tilde{\rho}_{\text{TC},i}^{\text{phase}}(t) . \quad (5.18)$$

Each summand represents one of the two coupling mechanisms, and the i denotes contributions from different temperature sensors $T_i(t)$.

The temperature data T_i is retrieved from so-called OFFRED telemetry and is decimated to 3.3 mHz as the range error. In total, there are 161 thermistors on each SC, which are decomposed into $T_i(t) = T_i^{\text{AC}}(t) + T_i^{\text{DC}}(t)$ by high- and low-pass filtering at a cutoff frequency of 0.08 mHz again. With this frequency split, the DC part mainly contains static offsets and variations at periods of days and slower, while 1/rev variations and their higher harmonics dominate the AC part.

5.5.1. Coupling Mechanisms: Frequency and Phase Domain

The frequency-domain coupling is defined as

$$\delta\tilde{\rho}_{\text{TC},i}^{\text{freq}}(t) = \text{HPF} \left(L(t) \cdot \left(c_{1,i} \cdot T_i^{\text{AC/DC}}(t) + c_{2,i} \cdot \dot{T}_i^{\text{AC/DC}}(t) \right), 0.08 \text{ mHz} \right), \quad (5.19)$$

which is a modification of equation (4.34) where it was shown that scale errors (with $c_{1,i} \cdot T_i \approx \varepsilon_{\text{SCF}}$) couple with the absolute distance $L \approx 220 \text{ km}$ of the two spacecraft into the measured range. Again, the HPF is used to remove the long-term drifts in accordance and for the same reasoning as in the definition of the range error in equation (5.13). As a reminder, the filter removes long-term drifts but, importantly, maintains the 1/rev frequency, which has high relevance for the scale factor. The precise orbits from GPS (GNI1B-v04) are used to determine L . The cm-precision of GPS was found to be sufficient in comparison to the current rms residuals of $\tilde{\rho}_{\text{err}}^{\text{post}}$ in the order of a few μm , since the coupling coefficients are below 10^{-5} , yielding a precision of $0.1 \mu\text{m}$ or better. Following from the definition, the coefficients have the units $[c_{1,i}] = 1/\text{K}$ and $[c_{2,i}] = 1 \text{ s/K}$. They can easily be converted to approximate equivalent laser frequency couplings in units of Hz/K by multiplying with $\nu_0^{\text{SDS}} \approx 281 \text{ THz}$. Equation (5.19) again uses a linearization of a potential timeshift due to the potential propagation time of given temperature variations into the measurement. This timeshift can be computed through $\zeta_{T_i} = c_{2,i}/c_{1,i}$ with $[\zeta_{T_i}] = 1 \text{ s}$. It should be noted that a positive sign of this timeshift is not violating causality, as it can always be regarded as a modulus w. r. t. the orbital frequency.

In contrast, the definition of the phase-domain TC simply reads

$$\delta\tilde{\rho}_{\text{TC},i}^{\text{phase}} = \text{HPF} \left(c_{1,i} \cdot T_i^{\text{AC/DC}}(t) + c_{2,i} \cdot \dot{T}_i^{\text{AC/DC}}(t), 0.08 \text{ mHz} \right), \quad (5.20)$$

where the coefficients directly convert temperature variations into range variations with the units $[c_{1,i}] = 1 \text{ m/K}$ and $[c_{2,i}] = 1 \text{ s m/K}$. Once more, a potential timeshift is linearized, and the complete term is high-pass filtered.

The DC-part of the thermistor data contains a large bias and long-term variations and is thus expected to couple in the frequency regime because it produces prominent tones at 1/rev and 2/rev through its coupling with the distance L . If such a bias would couple in the phase regime, it would only cause a constant and hence irrelevant bias, which is suppressed by the filter in $\tilde{\rho}_{\text{TC},i}^{\text{phase}}$.

5.5.2. Unconstrained Parameter Estimation

Using an iterative approach, an algorithm searches for the sensors $T_i^{\text{AC/DC}}$, that minimize the rms of the postfit range error $\tilde{\rho}_{\text{err}}^{\text{post-TC}}$ the most. In every iteration, the two global parameters $\varepsilon_{\text{SCF}}^{\text{glo}}$ and ζ^{glo} are co-estimated together with the coupling coefficients $c_{1,i}$ and $c_{2,i}$ for each sensor $T_i^{\text{AC/DC}}$ on both SC and for both possible coupling mechanisms individually. In essence, in every iteration, $161 \text{ (sensors)} \times 2 \text{ (AC/DC)} \times 2 \text{ (phase/frequency mechanism)} \times 2 \text{ (spacecraft)} = 1228$ linear equations are solved. Their respective rms residuals of $\tilde{\rho}_{\text{err}}^{\text{post-TC}}$ are computed. Ultimately, the sensor i whose solution showed the smallest residual is chosen, meaning it reduced the difference between KBR and LRI the most. In the next iteration, the parameters of all previously added sensors will again be co-estimated, such that two columns extend the design matrix of the least squares estimation in every iteration. In this unconstrained estimation,

Table 5.6. Thermal coupling parameters for v52 using the exponential cavity frequency decay model ν_R^{Cav} as laser frequency model. The index i denotes the order of importance, i.e., the gain in reducing the rms residuals. The $\delta\tilde{\rho}$ type denotes the coupling in phase or frequency regime. Thus, the unit of c_1 is m/K if the phase-domain coupling was used, and 1/K if the frequency-domain coupling was used. The coefficient c_2 has units s m/K (AC) or s/K (DC). The last column $\zeta_T = c_2/c_1$ describes the timeshift of the temperature data in seconds.

(a) TC-v52 coefficients for GF-1 in reference role.

i	SC	Sensor	ID	Freq.	type	c_1	c_2	ζ_T [s]
1	GF-1	SaMzPx	THT10013	AC	phase	$-8.356 \cdot 10^{-8}$	$6.324 \cdot 10^{-6}$	-75.7
2	GF-2	BatTrp	THT10133	AC	freq	$-4.448 \cdot 10^{-11}$	$-1.822 \cdot 10^{-10}$	4.1
3	GF-1	Oct11	THT10143	AC	freq	$1.771 \cdot 10^{-11}$	$2.100 \cdot 10^{-9}$	118.6
4	GF-2	LriLas	THT10113	AC	phase	$-1.359 \cdot 10^{-5}$	$2.169 \cdot 10^{-3}$	-159.6
5	GF-2	Oct22	THT10157	AC	phase	$2.236 \cdot 10^{-6}$	$3.026 \cdot 10^{-4}$	135.3

(b) TC-v52 coefficients for GF-2 in reference role.

i	SC	Sensor	ID	Freq.	type	c_1	c_2	ζ_T [s]
1	GF-1	Act24	THT10128	AC	phase	$-1.117 \cdot 10^{-6}$	$-6.626 \cdot 10^{-3}$	5932.2
2	GF-1	RadRear	THT10029	AC	freq	$5.053 \cdot 10^{-13}$	$3.960 \cdot 10^{-10}$	783.5
3	GF-1	AccTrp	THT10043	DC	freq	$-6.099 \cdot 10^{-9}$	$1.199 \cdot 10^{-6}$	-196.6
4	GF-2	ImuIcu	THT10119	AC	phase	$-8.484 \cdot 10^{-7}$	$-1.264 \cdot 10^{-2}$	14898.6
5	GF-2	Act12	THT10108	AC	phase	$-2.833 \cdot 10^{-6}$	$4.018 \cdot 10^{-3}$	-1418.4

all sensors can couple in frequency and phase regimes, as defined by equations (5.19) and (5.20). Later on, other configurations will be tested.

The algorithm stops after adding five thermistors, giving 12 coefficients in total: the two global scale and timeshift parameters and two coefficients for each selected temperature sensor. Two independent TC models are derived: one for GF-1 in reference role, and another for GF-2 in reference role. This distinction may account for different behavior when the cavity is used on the satellites. However, the differences in the models between GF-1 and GF-2 may arise because there is less data available for GF-2 in the reference role.

After subtracting the full TC model, the KBR-LRI residuals $\tilde{\rho}_{\text{err}}^{\text{post-TC}}$ were reduced from 5...7 μm rms to 1...4 μm rms, and are shown in figure 5.8 for v52 (yellow for GF-1, cyan for GF-2). The best results could be achieved using LRI1B-v52 with 1.188 μm rms for GF-1 and 0.930 μm rms for GF-2. All resulting residual rms and global parameters are shown in the last four columns of table 5.5. As the approach of v52 shows the smallest residuals, only those thermistor coupling coefficients are shown in table 5.6, for brevity. The TC coefficients for v51 and v53 are shown in the appendix C.

As the OFFRED thermistor data is not publicly available, a range thermal coupling (RTC) data product is provided by the AEI at www.aei.mpg.de/grace-fo-ranging-datasets for the period from launch until 2022-Dez-31. Within that data product, the time series of the individual contributions of frequency-domain and phase-domain coupling ($\delta\tilde{\rho}_{\text{TC}}^{\text{freq}}$ and $\delta\tilde{\rho}_{\text{TC}}^{\text{phase}}$, cf. equations (5.19) and (5.20)) alongside a correction term arising from the global scale and time shift parameters $\delta\tilde{\rho}^{\text{glo}}$, cf. equation (5.18). The sum of the three contributions provides the full correction term to minimize the residuals

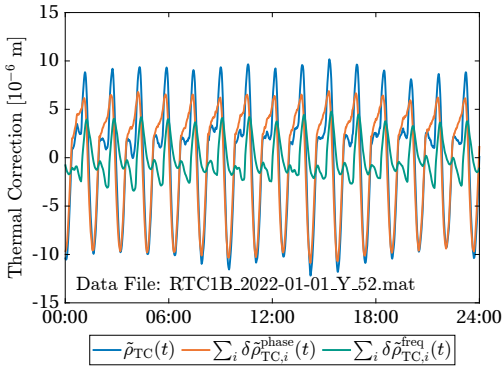


Figure 5.9. Thermal correction time series for 2022-Jan-01. This plot represents the RTC1B-v52 data product, which is also available at www.aei.mpg.de/grace-fo-ranging-datasets. The blue trace is the sum of the individual contributors in the phase and frequency domain, derived using the coupling factors the unconstrained fit, cf. table 5.6a.

between LRI and KBR. The data of that RTC1B data product is shown in figure 5.9 for 2022-Jan-01, with the total correction in blue and the two individual contributors in orange and green. The correction term $\delta \hat{\rho}^{\text{glo}}$ arising from the global scale $\varepsilon_{\text{SCF}}^{\text{glo}}$ and time shift ζ^{glo} is omitted in the plot. The correction term and, thus, the tone errors have a magnitude of $\pm 10 \mu\text{m}$ at 1/rev frequencies and some contributions at higher harmonics. That magnitude varies between $5 \mu\text{m}$ to $15 \mu\text{m}$ over time and is highly correlated with the β angle (not shown in figure 5.9).

Interestingly, neither the GF-1 nor GF-2 models use a sensor attached to the LRI directly. As the first sensor, having most relevance on reducing the residuals, both show a thermistor closely tied to the outer shell of the spacecraft, i. e., SaMzPx on GF-1, which is connected to the zenith-pointing solar array, and Act24 on GF-2, which is attached to one of the minus pitch attitude control thrusters (ACTs) and also points towards zenith direction, as well as Act12 (5th sensor on GF-2, plus pitch). It is expected that the underlying spacecraft interior’s thermal environment highly correlates to these sensors, as the SC top panels are directly heated by the sun and thus exhibit large temperature variations. The third thermistor in the GF-1 model is Oct11, at the rear side of the SC. As the rear is mainly illuminated (and thus heated) at β -angles close to zero, when the sun incidence vector is within the orbital plane of the SC, this coupling might strongly reduce the seasonal variations in the scale factor since the β -angle has a similar period of roughly 160 days. Notably, the first thermistor for all three v5X products on GF-1 is attached to the solar array (SaMz**), but none of the GF-2 models uses these. On GF-2 instead, more sensors connected to the accelerometer and the ACTs can be found. Only the model of v51 for GF-2 uses a thermistor attached to one of the LRI subunits, namely LriCavInt.

Comparing the values of table 5.6a for GF-1 to the ones published in Misfeldt et al. (2023b), for which the year 2022 was not included in the analysis, the two dominant sensors remain the same, and also Oct11 was already used there (as 5th sensor). As stated in the publication, it seems easy to find another set of sensors that performs similarly in terms of postfit rms because many thermistors are highly correlated. It should be noted that the iterative approach does not necessarily yield the absolute minimum of the postfit rms, which can only be found by computing the coupling coefficients for all possible combinations of five thermistors. However, that would require to solve

$$\binom{1228}{5} \approx 23 \cdot 10^{12} \quad (5.21)$$

systems of linear equations, which is impractical, and the iterative approach was thus chosen.

Table 5.7. Thermal coupling parameters for v52 using the exponential cavity frequency decay model ν_R^{Cav} as laser frequency model and enforcing the usage of the cavity internal thermistor.

(a) TC-v52 coefficients for GF-1 in reference role.

i	SC	Sensor	ID	Freq.	type	c_1	c_2	ζ_T [s]
1	GF-1	LriCavInt	THT10019	TF	freq	$-2.463 \cdot 10^{-9}$	$-3.212 \cdot 10^{-4}$	130 420.1
2	GF-1	SaMzPx	THT10013	AC	phase	$-1.036 \cdot 10^{-7}$	$-9.988 \cdot 10^{-6}$	96.4
3	GF-2	BatTrp	THT10133	AC	freq	$-2.821 \cdot 10^{-11}$	$-2.254 \cdot 10^{-8}$	798.9
4	GF-1	Oct11	THT10143	AC	freq	$2.419 \cdot 10^{-11}$	$-3.631 \cdot 10^{-9}$	-150.1
5	GF-1	MepMidPy	THT10153	AC	freq	$-1.383 \cdot 10^{-11}$	$1.677 \cdot 10^{-8}$	-1212.1

(b) TC-v52 coefficients for GF-2 in reference role.

i	SC	Sensor	ID	Freq.	type	c_1	c_2	ζ_T [s]
1	GF-2	LriCavInt	THT10019	TF	freq	$-4.761 \cdot 10^{-9}$	$-9.103 \cdot 10^{-4}$	191 192.1
2	GF-1	SaMzPx	THT10013	AC	freq	$-4.790 \cdot 10^{-13}$	$2.257 \cdot 10^{-11}$	-47.1
3	GF-2	RadRear	THT10029	AC	phase	$-3.409 \cdot 10^{-7}$	$1.740 \cdot 10^{-4}$	-510.4
4	GF-1	AccTrp	THT10043	DC	freq	$-5.728 \cdot 10^{-9}$	$-2.231 \cdot 10^{-6}$	389.6
5	GF-2	FgmB	THT10093	AC	freq	$-1.130 \cdot 10^{-11}$	$1.765 \cdot 10^{-8}$	-1561.6

5.5.3. Enforcing a Coupling of the Cavity

In the previous unconstrained estimation, all sensors were considered without any prior knowledge. In this second approach, the very first iteration of the algorithm is forced to use the cavity internal temperature (THT10019) with a frequency-type coupling, cf. equation (5.19). The cavity thermal noise is expected to be the limiting noise source at low frequencies (1 mHz) for the LRI. The specialty of this sensor is that the transmissivity transfer function TF of temperature variations at the sensor location into the cavity thermal shield (cf. figure 3.5) is known from the design of the shielding to be proportional to f^3 , written

$$\text{TF}(f) = \frac{1}{1 + \left(\frac{f}{f_c}\right)^3}, \quad (5.22)$$

with $f_c \approx 5 \mu\text{Hz}$. After applying this transfer function in Fourier space, the filtered time series of the cavity temperature is then plugged into equation (5.19) for the first iteration of the algorithm. The resulting thermal coupling coefficients are shown in table 5.7. Remarkably, the timeshift ζ_T for the cavity thermistor is in the order of 1.5 to 2 days for both GF-1 and GF-2, which the long propagation delay through the thermal shields can explain. Further, the global scale estimate $\varepsilon_{\text{SCF}}^{\text{gl}}$ is now $3 \cdot 10^{-8}$ for GF-1 and $-1.7 \cdot 10^{-7}$ for GF-2, much larger than before, indicating that the coupling with the cavity thermistor, as it has a significant DC bias, introduces a scale that is subsequently absorbed by the empirical global parameter. Further, the coupling factor for the cavity sensor in the order of $10^{-9}/\text{K}$ is much larger than the expected cavity coefficient of thermal expansion of $10^{-11}/\text{K}$ from pre-flight analysis and measurements. The actual effect of a varying cavity length seems to be masked by other more prominent tone error sources. Hence it is concluded that the cavities' temperature stability is not dominantly driving the difference between KBR and LRI and thus also not the TC, and that the actual tone errors introduced by the cavity can not be determined from flight data. The

Table 5.8. Thermal coupling parameters for GF-2-v52 using the exponential cavity frequency decay model ν_R^{Cav} as laser frequency model. Only T^{AC} is used in the fit.

i	SC	Sensor	ID	Freq.	type	c_1	c_2	ζ_T [s]
1	GF-1	Act24	THT10128	AC	phase	$-4.049 \cdot 10^{-6}$	$-3.093 \cdot 10^{-3}$	763.9
2	GF-1	RadRear	THT10029	AC	freq	$-2.548 \cdot 10^{-13}$	$7.782 \cdot 10^{-10}$	-3054.7
3	GF-1	LriCavInt	THT10019	AC	phase	$2.255 \cdot 10^{-6}$	$-4.375 \cdot 10^{-3}$	-1940.1
4	GF-1	ObcTrp	THT10076	AC	freq	$-1.978 \cdot 10^{-10}$	$1.100 \cdot 10^{-7}$	-556.4
5	GF-1	MwilpuB	THT10073	AC	freq	$9.258 \cdot 10^{-11}$	$-3.906 \cdot 10^{-8}$	-421.9

other sensors found by the algorithm are similar to the ones found in the unconstrained approach. The new coupling parameter sets show a slightly increased level of postfit residuals for both spacecraft, 1.203 μm rms and 1.104 μm rms, respectively, compared to the unconstrained fit (cf. table 5.5).

5.5.4. Enforcing AC Temperature Components (GF-2 only)

The TC models on GF-2, either in the unconstrained estimation or with the cavity thermistor, use the DC-part of AccTrp, that couples in the frequency domain. All other sensors are coupled with their AC components only. This sensor's contribution, which has a non-zero average value that couples with the total SC distance L , introduces large 1/rev variations. These are absorbed by an increase in the global scale factor $\varepsilon_{\text{SCF}}^{\text{glo}}$ from approximately $-3.9 \cdot 10^{-9}$ (postfit) to $1.2 \cdot 10^{-7}$ or $1.77 \cdot 10^{-7}$ (postfit inkl. TC), cf. table 5.5. However, this increase in the global scale correction parameter $\varepsilon_{\text{SCF}}^{\text{glo}}$ indicates an error in the laser frequency model that is smaller according to the estimation of that parameter without the TC. Therefore, this section derives another TC model, in which the usage of the T^{AC} frequency components only is enforced. The new coefficients are shown in table 5.8. In this case, the scale factor $\varepsilon_{\text{SCF}}^{\text{glo}} \approx 1.393 \cdot 10^{-9}$ remains small, and the global timeshift $\zeta^{\text{glo}} = 68.09 \mu\text{s}$ stays almost the same as before, cf. table 5.5. The postfit residuals are at a level of 1.359 μm rms, slightly higher than in the unconstrained case. However, the benefit is that the global scale factor refinement no longer anticorrelates with the tone errors.

5.5.5. Variations of the Tone Error Amplitudes

The total tone error amplitude can be assessed by computing the daily 1/rev and 2/rev amplitudes over the mission period. The tone error models are the unconstrained case on GF-1 (cf. table 5.6a) and the model with AC-components only on GF-2 (cf. table 5.8). Those parameter sets are also used for deriving the RTC1B data product.

Figure 5.10 shows the variability of the tone error contributions $\delta\tilde{\rho}^{\text{freq}}$ and $\delta\tilde{\rho}^{\text{freq}}$ at 1/rev and 2/rev frequencies. For this visualization, a fit of a sum of two sine waves with arbitrary amplitudes (c_1 and c_2) and phases (φ_1 and φ_2) at these frequencies. i. e.,

$$\tilde{\rho}_{\text{TC}}(t) = c_1 \sin(2\pi f_{\text{orb}}t + \varphi_2) + c_2 \sin(4\pi f_{\text{orb}}t + \varphi_4) \quad (5.23)$$

is performed on daily arcs. The orbital frequency is approximately $f_{\text{orb}} \approx 0.176 \text{ mHz}$. The resulting time series' of c_1 and c_2 are shown in the figure, in blue for the 1/rev frequency and pink for the 2/rev frequency. The tone error models have similar magnitudes, independently of the SC in the reference role. The 1/rev tone error magni-

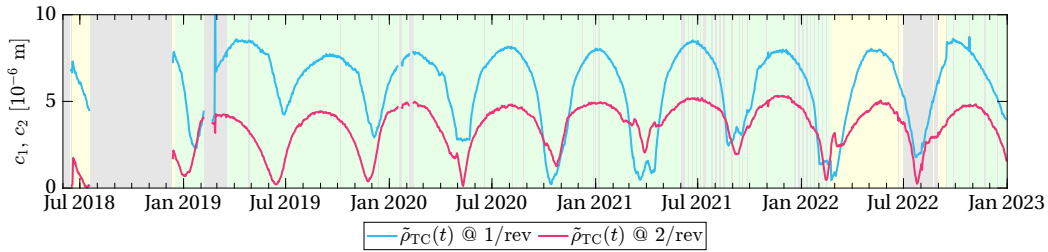


Figure 5.10. Daily estimates of the 1/rev and 2/rev tone error amplitudes c_1 and c_2 (cf. equation (5.23)) of the TC model, derived from the RTC1B data product.

tude varies between $0\ \mu\text{m}$ to $8\ \mu\text{m}$, while the 2/rev tone error is below $5\ \mu\text{m}$. These magnitudes are dominated by thermistors at the outer shell of the satellites, e.g., SaMzPx in the unconstrained models is attached to the solar arrays. These show large sinusoidal amplitudes at 1/rev, e.g., $80\ \text{K}$, that results in sinusoidal tone errors of $80\ \text{K} \cdot 10^{-7}\ \text{m/K} = 8\ \mu\text{m}$ at 1/rev frequencies.

As expected, the tone error magnitudes show strong seasonal variations, which are again related to the β angle between the orbital plane and the sun vector. The nominal requirement of tone errors within the KBR instrument is $2\ \mu\text{m}$ at 2/rev frequencies (Kornfeld et al., 2019), which these models exceed. However, it shall be noted that these assessments performed in this thesis are not solely related to the KBR instrument and that they might overestimate the actual tone error magnitudes by absorbing other unmodeled effects.

5.5.6. Variations of Scale Factor and Timeshift

Besides minimizing the residuals of the KBR-LRI difference $\rho_{\text{err}}^{\text{post-TC}}$, a secondary goal of this analysis is to reduce or explain the seasonal variations in the estimated scale factor $\langle \varepsilon_{\text{SCF}} \rangle(t_{\text{daily}})$, as apparent in figure 5.1 on page 53. Therefore, the scale and timeshift are estimated once more daily, but now these values are not meant to be used as a correction but only as a metric for the goodness of the frequency and TC models. The results are shown in figure 5.11, scale factor $\langle \varepsilon_{\text{SCF}} \rangle$ on the left and ζ on the right. The blue and cyan curves denote the residual scale factor ε_{SCF} using the range of LRI1B-v52 for GF-1 and GF-2, respectively, while the orange and pink curves include the thermal coupling correction. The corresponding figures for v51 and v53 can be found in appendix C. None of the frequency models (v51, v52, v53) can reduce the seasonal variations directly, but after applying the TC estimate, the variations are reduced by approximately one order of magnitude. This shows that the scale ε_{SCF} and timeshift ζ in LRI1B-v50 (and also in v04 by the SDS) partly absorb the effects of other measurement errors like the tone errors from the thermal coupling.

5.6. Discussion of Alternative Approaches for Future Gravity Missions

For future missions relying on an evolved LRI instrument, a different approach for determination of the scale factor or absolute laser frequency than the cross-calibration w. r. t. the MWI is needed. Those could be post-processing-based schemes, like the

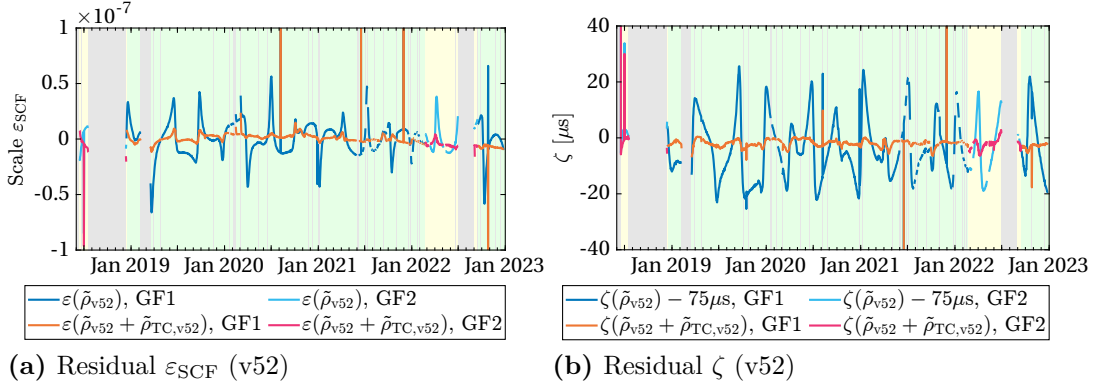


Figure 5.11. Residual scale ε_{SCF} and timeshift ζ of KBR-LRI in version v52 with and without the correction of $\tilde{\rho}_{\text{TC}}$ for both SC. The GF-1 model is shown in blue and orange, while the GF-2 ones are shown in cyan and pink. The seasonal variations are lowered significantly on both SC when applying the TC. Figures for v51 and v53 are shown in appendix C.

telemetry-based model $\nu^{\text{TME}}(t)$ shown in the previous sections (cf. section 5.3), or even include new units of the LRI system that directly measure the lasers' frequency. Table 5.9 briefly lists the current most promising alternatives and their benefits and costs.

The telemetry models $\nu_{1/2}^{\text{TME}}$, including the empirical correction $\nu_{1/2}^{\text{emp}}$ from in-flight measurements, reach an accuracy of approximately $60 \text{ MHz} \approx 200 \text{ ppb}$. Since the laser is thermally coupled to the satellite platform, temperature variations of the surrounding units couple into the setpoint-based model but not into the true frequency defined by the cavity within its thermal shield. For the LRI as a technology demonstrator, calibration of the laser frequency on-ground only had a moderate priority. However, an accuracy of 200 ppb should also be achievable through thorough on-ground calibration in future missions, especially regarding the -1 Hz/s drift of the laser setpoints. Characterizing the cavity frequency exponential ν^{Cav} pre-flight provides a second laser frequency estimate. Note that this cavity drift converged towards a static value approximately after one year in flight for the GRACE-FO LRI. Eventually, it might be beneficial not to use a newly manufactured cavity or at least to consider the drift.

An alternative to the telemetry and cavity models is to co-estimate the true laser frequency during GFR, as it is usually done for the accelerometer scales and biases (Helleputte et al., 2009; Klinger et al., 2016). But as the LRI scale uncertainty mainly influences the 1/rev and 2/rev frequencies, the co-estimated scale might be correlated to empirical parameters often introduced by the GFR processing strategies (Klinger et al., 2016).

Despite modeling or estimating the frequency, it can also be measured in flight with additional hardware. A broadly used technique is iodine spectroscopy, where the frequency-doubled laser is locked to a hyperfine transition line of molecular iodine, which has prominent hyperfine transition lines around 532 nm wavelength (Arie et al., 1992). This technology has also been used for calibration of the wavemeters for the RLU calibration (cf. appendices A and B). Laboratory experiments have shown absolute frequency repeatability levels below $1 \text{ kHz} \approx 3 \cdot 10^{-3} \text{ ppb}$ (Döringshoff et al., 2017). This method is probably the most accurate mean to determine the scale factor. Further,

Table 5.9. Comparison table of the methods to determine the absolute laser frequency ν_R or scale factor ε_{SCF} .

Method	Accuracy	Pros (+) / Cons (-)
Cross-Correlation to MWI (v50)		<ul style="list-style-type: none"> - Not feasible without MWI - Estimated frequency susceptible to ranging tone errors in GRACE-FO MWI and LRI
Telemetry Model (v51)	60 MHz (200 ppb)	<ul style="list-style-type: none"> + No changes of flight hardware required - Thorough calibration of laser and cavity required - Low accuracy, may serve as backup option
Exponential Cavity Model (v52)	20 MHz (67 ppb)	<ul style="list-style-type: none"> + No changes of flight hardware required - Precise long-term calibration required
Estimation during GFR ^[1]		<ul style="list-style-type: none"> + No changes of flight hardware required - Laser frequency highly correlated to $C_{2,0}$ gravity coefficient - Susceptible to instrument tone errors and to errors from GFR (e.g., temporal aliasing, gravity background model errors) - May have correlations to other empirical parameters (e.g., for accelerometer)
Iodine Cell ^[2]	1 kHz ($3 \cdot 10^{-3}$ ppb)	<ul style="list-style-type: none"> + Highest accuracy, well established standard + High TRL, already flown in sounding rocket - High mass and (optical) power demands due to frequency doubling
Novel Spectroscopy Unit	unknown	<ul style="list-style-type: none"> + Possible molecule candidates: $^{133}\text{CS}_2$ or C_2HD^[3]. - No frequency doubling required, existing transition near 1064 nm - Low TRL
FSR Readout ^[4]	3 MHz (10 ppb)	<ul style="list-style-type: none"> + Sufficient accuracy + Minor changes of existing optoelectronics, additional RF electronics to generate modulations for EOM required

^[1]See [Flechtner et al. \(2023\)](#) (project internal document)

^[2]See [Schuldt et al. \(2017\)](#), [Döringshoff et al. \(2017\)](#), and [Döringshoff et al. \(2019\)](#)

^[3]See [Jeng et al. \(1998\)](#), [Ye et al. \(1996\)](#), and [Ma et al. \(1999\)](#)

^[4]See [Rees et al. \(2021\)](#) and [Rees et al. \(2022\)](#)

activities are ongoing to qualify such setups for the space environment ([Döringshoff et al., 2017](#)). However, saturated Doppler-free spectroscopy is likely incompatible with the available optical power from Tesat RLUs used in the LRI so far and anticipated for future instruments. Hence, optical amplifiers would be needed, drastically increasing the complexity and electric power consumption.

There is the possibility for a hybrid lock by using both a conventional spectroscopic locking to an iodine reference and an offset PDH lock to an optical cavity, acting within different frequency bands. This hybrid lock combines the stability of the cavity at high Fourier frequencies and the absolute laser frequency knowledge through the molecular reference ([Sanjuan et al., 2021](#)), but is also likely incompatible w.r.t. the power demands in a space-borne interferometer.

There exist molecules with transitions near 1064 nm like $^{133}\text{CS}_2$ ([Jeng et al., 1998](#)) or C_2HD ([Ye et al., 1996](#); [Ma et al., 1999](#)), which can be used for laser stabilization using frequency-modulation spectroscopy. The benefit of these molecules is that no frequency doubling would be needed as in the case of $^{127}\text{I}_2$. However, to the authors' knowledge, there are currently no efforts to implement these techniques into flight hardware.

The last approach presented here is based on an extension of the conventional and well-established PDH lock ([Rees et al., 2021](#)). A subcarrier with sidebands at approxi-

mately one free spectral range (FSR) is modulated onto the local oscillator light. This subcarrier resonates with the cavity at one FSR above and below the carrier frequency, and the sidebands generate a PDH-like error signal, additionally to the conventional PDH readout signal. As the frequency of the subcarrier is coherently derived from an USO frequency, which in turn is accurately retrieved by precise orbit determination (POD), this technique can provide an estimate for the FSR frequency of the cavity. The FSR of a cavity obeys the following linear relation to the cavity resonance frequency:

$$\nu^{\text{res}} = (n^{\text{mode}} + n^{\text{offset}}) \cdot f^{\text{FSR}} . \quad (5.24)$$

Here, n^{mode} is an integer mode number, f^{FSR} is in the order of 1 GHz to 3 GHz and depends on the cavity, and ν^{res} is the absolute cavity resonance frequency. The fractional offset $0 \leq n^{\text{offset}} < 1$ must be calibrated on ground (Rees et al., 2022). It is currently an open research question if this offset is constant in time and on which environmental parameters it depends. The principle has been demonstrated in laboratory experiments with an accuracy of roughly 3 MHz \approx 10 ppb. However, the knowledge and stability of the fractional offset n^{offset} is one driver for the precision and must be calibrated thoroughly. The advantage of this technique is that only minor changes to existing flight hardware are needed, e. g., the use of GHz EOMs instead of MHz. However, additional RF electronics to generate the EOM modulation signals are required. The FSR readout is currently the most probable solution for upcoming gravity missions.

5.7. Summary

This section discussed different ways to determine the absolute laser frequency of the GRACE-FO LRI. Besides assuming just a static pre-flight value of the laser frequency, three options have been introduced: A cross-calibration using the MWI as the reference, an exponential decay model of the cavity resonance frequency, and a telemetry-based model using on-ground calibrations. In principle, when the latter two are thoroughly characterized on ground, the models should be sufficient to derive the LRI laser frequency within 60 MHz in-flight and without the MWI. However, in GRACE-FO, none of these three methods is entirely independent of the MWI. However, the latter two options only had to be calibrated once in orbit and can be used stand-alone afterward. For the telemetry model, a previously unknown drift in the order of -1 Hz/s was found, which might arise from potential aging effects of the NPRO crystal or the electronics. However, it is assumed that proper ground calibration for future missions can overcome an in-flight parameter estimation. A possible difficulty not investigated within this thesis is the potential thermal susceptibility of the set points, which are currently assumed to remain static.

The three laser frequency models have been compared, firstly utilizing the range error $\tilde{\rho}_{\text{err}}^{\text{pre}}$ of the LRI range w. r. t. the microwave and secondly by the variability of the residual scale $\langle \varepsilon_{\text{SCF}} \rangle$ and timeshift ζ . It was found that introducing global parameters, i. e., parameters that are estimated only once for the complete available timespan, for the scale $\varepsilon_{\text{SCF}}^{\text{glo}}$ and timeshift ζ^{glo} reduced the range error to a similar degree for all three models and also for both SC in reference role, to about 6 μm rms, with a slight advantage for v52 employing the exponential cavity model, cf. table 5.5. The residual scale and timeshift variations from daily cross-correlation w. r. t. the microwave still show prominent seasonal variations.

Sinusoidal errors, called tone errors and e. g. arising from thermal coupling into the measurement at mainly 1/rev and 2/rev frequencies, alter the scale factor estimation and thus may introduce such seasonal features. Hence, a model for a tone error correction was defined that consists of two possible coupling mechanisms: One of which couples in the frequency domain (like the scale factor) with the coefficients having units of 1/K or equivalently MHz/K. The second possibility couples directly in the range domain with units m/K. In an iterative approach, a set of five thermistors, distributed among the two spacecraft, was determined separately for each LRI unit in reference role. Ultimately, the residuals of KBR-LRI using this correction $\tilde{\rho}_{TC}$ could be reduced to a level of 1 μm rms in the case of v52 and a bit higher for v51 and v53. Different versions of this TC model have been derived. The unconstrained fit, in which the AC and DC frequency parts of the temperature measurements could couple in both, frequency and phase regime, yielded the best results in minimizing the KBR-LRI residuals. No dominant coupling of the LRI cavity thermistor was found, concluding that the cavity resonance frequency is stable at the orbital frequency to not cause dominant tone errors. A modification was made to the model of GF-2, where a contribution of the AccTrp DC temperatures caused unphysically large 1/rev variations that were absorbed by an increase in the global scale estimate $\varepsilon_{SCF}^{\text{glo}}$ subsequently. Therefore, the DC parts of the thermistors were excluded from the fit to derive a new model using only the AC parts of the thermistors. With this modification, the 1/rev and 2/rev amplitudes of the tone errors are below 8 μm and 5 μm , respectively. Furthermore, the seasonal variations in the residual scale and timeshift errors vanished in principle, cf. figure 5.11.

Since no dominant coupling of the LRI cavity frequency (through the cavity temperature) was observed, it is arguable that the TC can be predominantly attributed to the KBR instrument, e. g., through thermally induced KBR phase center variations. In that case, the most precise inter-satellite ranging dataset is given by LRI1B-v52 with an additional global scale factor and timeshift estimations of the unconstrained fit (GF-1) and the AC-only fit (GF-2). The values are (cf. table 5.5)

$$\varepsilon_{SCF}^{\text{glo}} = \begin{cases} -1.10 \cdot 10^{-9} & \text{for GF-1} \\ 1.39 \cdot 10^{-9} & \text{for GF-2} \end{cases} \quad \zeta^{\text{glo}} = \begin{cases} 67.66 \mu\text{s} & \text{for GF-1} \\ 68.09 \mu\text{s} & \text{for GF-2} \end{cases}, \quad (5.25)$$

where the residuals to the KBR instrument are 1.188 μm rms and 1.359 μm rms, respectively. This global scale factor correction is a static and minor correction to the cavity frequency model ν^{Cav} in the order of 0.3 MHz (GF-1) and 30 MHz (GF-2). The timeshift ζ^{glo} represents the timing offset of the LRI w. r. t. the KBR instrument. It should be noted that there is not much data with GF-2 in the reference role, and therefore the models are not as well determined as for GF-1. The TC correction is provided in the RTC1B-v52 data product available at www.aei.mpg.de/grace-fo-ranging-datasets.

Finally, the estimated accuracy of the cavity exponential and telemetry models is compared to other possible determination schemes for future gravity missions, concluding that such models might be a backup solution.

Experimental Verification of the RLU Frequency Drift

6

“*Scientists have become the bearers of the torch of
discovery in our quest for knowledge.*”

— STEPHEN W. HAWKING —

The World’s Most Famous Astrophysicist

This section describes a laboratory experiment to measure a linear frequency drift of a Tesat reference laser units (RLUs). Such a drift was observed in LRI flight data in section 5.3.3 by comparing the laser frequency model ν^{TM} , that uses the downlinked telemetry to compute the laser frequency, with the frequency estimate from correlating the LRI and KBR range measurements. The telemetry model for both laser units drifted at a rate of -1 Hz/s over a period of more than four years. The idea of the experiment in a laboratory of the AEI was to observe the beatnote frequency between an available RLU and an iodine-locked laser as the absolute frequency reference over a long period for a constant thermal setting.

6.1. RLU-EM Description and EGSE Construction

An RLU engineering model (EM) of the LISA Pathfinder mission, delivered to the AEI in 2006, was recommissioned and used as a device under test. This RLU-EM is an earlier version of the ones built into the LRI with reduced optical power and stability requirements, a narrower frequency control range, and no PMH temperature telecommand. Its optical output power is $14 \text{ mW} \pm 30\%$ and the nominal optical frequency at 24°C is $281\,604.64$ GHz, compliant to the iodine 1104 line (Windisch et al., 2007). The frequency can be controlled by up to ± 2.5 GHz by employing a thermal actuator at the NPRO crystal and by another ± 24 MHz range via a piezoelectric transducer.

As there was no controller and power supply for this particular RLU available, an electronic ground support equipment (EGSE) was designed and built for this experiment to implement the TM/TC interface of the laser. The telemetry of the RLU contains two analog channels: the current consumption of the pump diode (CURRENT_BENCH), the optical output power (LASER_POWER), as well two digital channels, where RLU_ON_OK indicates if the RLU is ready to receive the RLU_ON telecommand and RLU_FREQ_OK shows the status of the NPRO crystal temperature control loop. If the latter is active, the optical frequency of the light output fulfills the specified stability. On the other hand, the telecommands are comprised of one digital channel, the RLU_ON master switch for activating the optical output, and three analog channels: frequency tuning through FAST_FREQ and SLOW_FREQ, which act on the PZT and thermal elements internally (cf. section 5.3.1) and a SLOW_POWER control that adjusts the optical output power, i. e., the pump power of the LDB.

The EGSE was designed to enable control via the telecommand channels and data recording of the laser’s telemetry on a connected computer. The connection between

the computer and the EGSE was established through a serial USB interface of an ESP32 microcontroller, which also monitors the total runtime of the laser diode.

The circuit diagram and PCB place plans were created in EAGLE, a CAD software for electronics design. Commercial components were used for digital-to-analog conversion and vice versa: ADS1115 and MCP4728, programmable through an I²C interface and feature multiple channels at a high data rate. The analog TM/TC channels were amplified using operational amplifiers of type OP07L and corresponding resistors to match the required input voltage ranges of the RLU signal interface. The digital TM/TC channels rely on the RS422, a differential two-wire protocol. Space-qualified drivers and receivers are commercially available, of which the AM26C31M (driver) and AM26C32M (receiver) by Texas Instruments are non-space-qualified equivalents used in the EGSE.

The software of the microcontroller was written in the `Arduino` language, which is based on `C++`. All logic for fail-safe operation of the RLU, i. e., checking the user input for validity, is implemented within the microcontroller and is thus independent of the computer connection. For controlling the EGSE and recording the telemetry, a graphical user interface (GUI) was implemented in `Python` – all telecommands can be set, except for the `SLOW_FREQ` and `FAST_FREQ` channels, which need higher data rates than the microcontroller can provide. They are thus passed through to a LEMO connector to enable frequency using a function generator. For the `SLOW_POWER` signal, there is an internal jumper that can be configured to either set the setpoint through the GUI and the EGSE or by an external voltage source through a LEMO connector as well. A power-stabilizing control loop using an external photodiode voltage as a reference is planned for the future.

The GUI furthermore has an integration for a temperature board commonly used in the laboratories at the AEI. It features eight channels that can be read out at a rate of approximately 3 Hz. The data retrieved from this board is also shown in the GUI and, as a safety feature, one of the sensors can be used as thermal reference for the RLU. An individual operational temperature range can be defined and the GUI can automatically deactivate the laser, if the reference point temperature exceeds this range.

By now, this EGSE has proven to be reliable after more than two years of use in the laboratory. A potential extension of the EGSE, already included in the circuit design, is to use it as a pass-through box for testing a new phasemeter in development. The EGSE may validate the signals the phasemeter sets and only pass them to the RLU if they are within the requirements. A second EGSE box was shipped and successfully commissioned at an industrial partner to operate a new RLU in the context of developing the LRIs for future missions.

Images of the EGSE during construction, the RLU in the laboratory as well as a screenshot of the GUI, are shown in figures 6.1 to 6.3.

6.2. Experimental Setup

The experimental setup shown in figure 6.4 employs an iodine-locked laser^[1] as a frequency reference. The stabilization to a transition of the ¹²⁷I₂ molecule is achieved

^[1]Laser: Prometheus P20NE; Iodine Cell: I2 MTS V2.0, both by InnoLight GmbH

6.2. EXPERIMENTAL SETUP

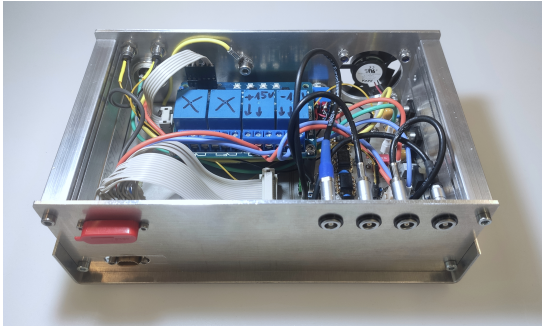


Figure 6.1. Photograph of the RLU EGSE during construction. The two front panel connectors on the left-hand side are the power- and signal interfaces between the EGSE and the RLU. The four LEMO connectors on the right-hand side are signal inputs for the frequency and power control.

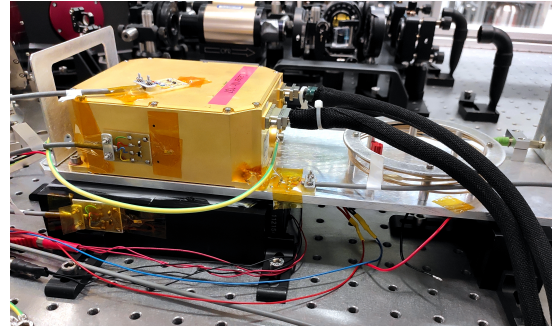


Figure 6.2. Photograph of the RLU-EM mounted on the Peltier cooled baseplate. Right of the RLU is a fiber reel. Several thermistors are attached to the RLU, the baseplate, and the heat sink. Fans provide additional cooling of the heat sink.

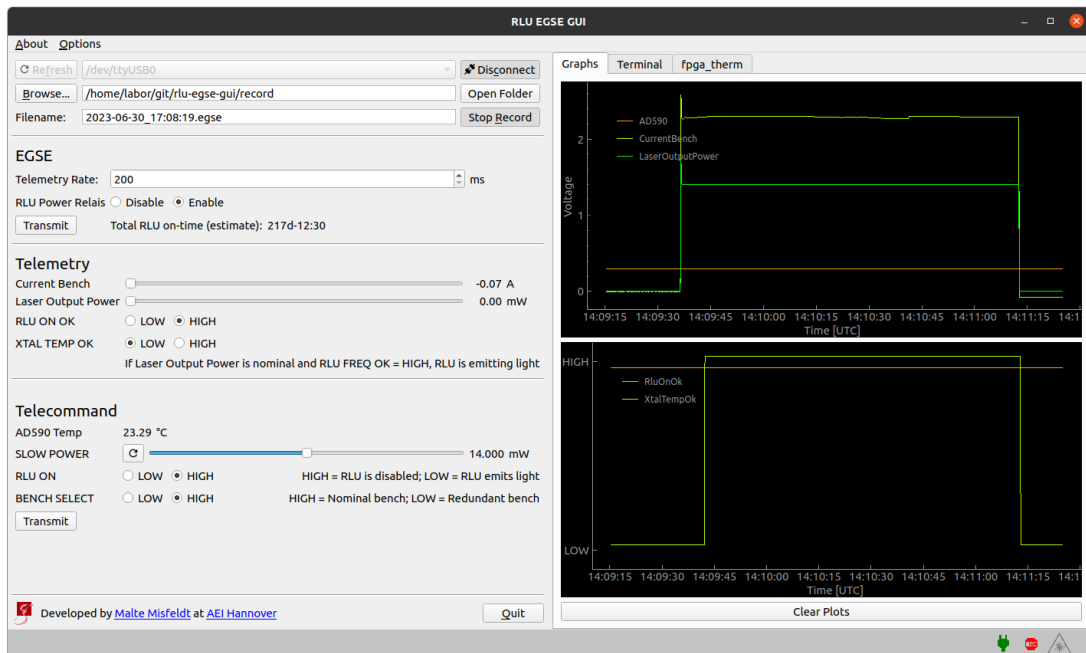


Figure 6.3. Screenshot of the RLU EGSE GUI running in the laboratory at AEI Hannover. Prior to this shot, the RLU was turned on for a few seconds. The graphs in the upper panel show the current consumption and optical output power over time. In the lower graphs panel, the RLU_FREQ_OK (which was called XTAL_TEMP_OK earlier) indicates that the frequency of the optical output has already stabilized only a few seconds after the activation.

through Doppler-free modulation transfer spectroscopy (MTS) (Shirley, 1982; Hall et al., 1999). A fraction of the iodine-locked laser light at 1064 nm is frequency doubled for the locking since the iodine transitions are near 532 nm. The beatnote frequency between the RLU and the iodine laser is in the range of 10 GHz due to the nominal frequency of the RLU and the limited frequency range of the iodine laser. The frequency is measured using a high-speed InGaAs photodiode^[1] and tracked gby a spectrum analyzer^[2]. Additionally, the absolute frequency of the RLU was measured using a wavelength meter^[3]. During the experiment, the optical output power was kept at the nominal level of 14 mW and the PZT and thermal setpoints of the RLU were held at 0 V by connecting 50 Ω terminators to the respective differential TM/TC channels at the EGSE. The absolute laser frequency during the experiment is determined in two ways:

1. Direct wavemeter measurement of $\nu_{\text{WM}}^{\text{RLU}}$ with an absolute accuracy of 60 MHz
2. Subsequent measurement of:
 - the iodine frequency $\nu_{\text{WM}}^{\text{I}}$ with the wavemeter, i. e., determination of the iodine transition, and
 - measuring the relative beat frequency f_b of the iodine and the RLU with the spectrum analyzer.

This scheme provides the RLU frequency as

$$\nu_b^{\text{RLU}} = \nu_{\text{WM}}^{\text{I}} - f_b . \quad (6.1)$$

The two-fold measurement scheme was chosen to avoid device-dependent errors of either the wavemeter or the spectrum analyzer. The wavemeter measurement of the iodine frequency $\nu_{\text{WM}}^{\text{I}}$ provides an estimate within ± 60 MHz. By comparing the measurement to a look-up table of known iodine transitions (BIPM, 2007), the true iodine transition and its frequency can be deduced under the assumption of a stable iodine frequency lock. Throughout the measurement campaigns, the iodine was locked to the a_1 transition of line number 1107 most of the time, but also to the a_{10} and a_{15} transitions as well as a_1 of line number 1108. They all are within a few hundred MHz of each other. Their exact frequencies are listed in table 6.1.

In May 2023, the whole setup was rebuilt as a fully fiber-integrated setup, employing commercial polarizing fiber beam splitters, attenuators, and a fiber-coupled photo detector^[4], which simplifies the setup as no beam alignment on the mirrors and photodetector is needed.

The baseplate of the RLU was initially mounted on four 25x25 mm Peltier elements for temperature control to maintain a stable RLU TRP temperature, which mainly needs cooling for dissipating the internally generated heat. A commercial Peltier controller with a manual setpoint setting was employed. The Peltier elements are mounted on a heatsink with fans for increased airflow. The temperatures of the RLU TRP, top, and side surfaces, the heatsink, the laboratory air, as well as the custom-built EGSE

^[1]Model 1437 by New Focus Inc.; 25 GHz bandwidth

^[2]Model FSL18 by Rohde & Schwarz GmbH & Co. KG; 18 GHz bandwidth

^[3]Model WS7-60 by HighFinesse; A similar one was used for the LRI ground calibration, cf. section 5.3.2.

^[4]Model 1414 by Newport Inc.; 25 GHz bandwidth

6.3. RLU-EM CALIBRATION

Table 6.1. Frequencies of some selected $^{127}\text{I}_2$ transitions (BIPM, 2007). The last column refers to the equivalent transition frequency at 1064 nm. Line 1104 is closest to the nominal RLU frequency, but is beyond the frequency range of the available iodine laser. Lines 1107 and 1108 were thus chosen, producing a approximately 10 GHz beatnote with the RLU. Line 1110 was used for calibration for the wavemeter, cf. appendix A.

Line No	Transition	Component	ν [kHz]	$\nu/2$ [kHz]
1104	R(57) 32-0	a_1	563 209 276 628	281 604 638 314
		a_1	563 228 033 107	281 614 016 553.5
1107	R(86) 33-0	a_{10}	563 228 605 369	281 614 302 684.5
		a_{15}	563 228 890 490	281 614 445 245.0
		a_1	563 229 788 749.6	281 614 894 374.8
1110	R(56) 32-0	a_1	563 259 651 971	281 629 825 985.5
		a_{10}	563 260 223 513	281 630 111 756.5

laser controller were monitored and recorded using an eight-channel temperature board developed in-house. An incident in mid-2023, in which the Peltier controlled had a malfunction, led to another modification of the setup with a thermoelectric liquid chiller^[1] and the RLU mounted to a water-cooled breadboard. The liquid chiller does not allow as fast temperature gradients as the Peltier elements. Still, it features an analog input port to manipulate the temperature setpoint continuously, e. g., through a connected frequency generator.

6.3. RLU-EM Calibration

6.3.1. Optical Power to Frequency Coupling

There is a cross-coupling between the optical output power and the frequency, calibrated via the measurement shown in figure 6.5. The SLOW_POWER setpoint (dashed light blue) was changed systematically during calibration, while the laser frequency ($\nu_{\text{RLU}}^{\text{WM}}$; dashed green) and beam power (P^{WM} ; not shown) were measured using the wavemeter (WM). Firstly, the measured optical beam power at the wavemeter was calibrated using linear regression to the optical power setpoints, resulting in the calibrated power ($P_{\text{RLU}}(P^{\text{WM}})$; blue). This calibration is needed, as the total optical power is not present at the wavemeter due to the beam splitters, coupling efficiencies, and an additional fiber attenuator placed before it (not shown in figure 6.4). The calibrated beam power was subsequently used to derive the frequency coupling, using linear regression w. r. t. the measured laser frequency $\nu_{\text{RLU}}^{\text{WM}}$, which results in a model of the laser frequency in dependence of the laser power ($\nu_{\text{RLU}}(P_{\text{RLU}})$; solid blue). As the wavemeter measurements, especially the power measurement, are quite noisy, a moving-mean filter with a length of 10 samples was applied to the data before the fit. The retrieved coupling coefficient is -310.537 MHz/mW or equivalently -130.425 MHz/V at the SLOW_POWER telecommand of the RLU interface (Windisch et al., 2007). The tuning range is -10 V to 10 V with a nominal power coupling of $3\% \cdot P_{\text{nom}}/\text{V} = 3\% \cdot 14 \text{ mW}/\text{V} = 0.42 \text{ mW}/\text{V}$. The retrieved coupling coefficient compares well to a calibration measurement from 2007, in which a value of -120 MHz/V was measured.

^[1]LK220 by Thorlabs

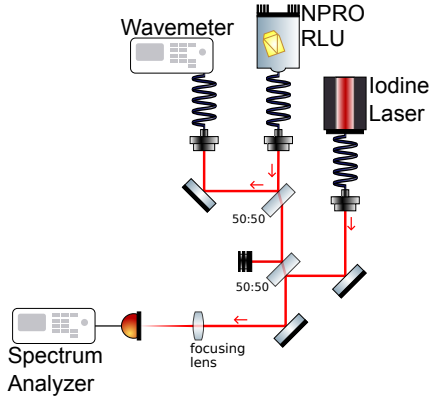


Figure 6.4. Experimental setup for the RLU frequency stability experiment. The photodiode and a spectrum analyzer measure the beat frequency between both lasers. The absolute RLU frequency is tracked in parallel with the wavemeter.

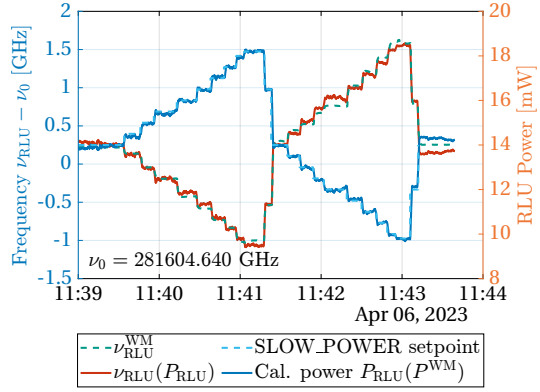


Figure 6.5. Calibration measurement of the RLU-EM: Optical frequency vs. optical power. The wavemeter (WM) measurements were smoothed with a 10-sample moving mean filter.

6.3.2. Temperature to Frequency Coupling

The dependence of the optical frequency on the RLU TRP temperature was characterized in mid-2023 after the liquid chiller was installed. Two calibration measurements are performed, both stimulate the RLU TRP temperature setpoint with a sine wave with a period of 3 hours and 8 h, respectively. The temperature setpoint varied from 23 °C to 27 °C, and the wavemeter and the spectrum analyzer recorded the laser frequency, as shown in figure 6.6. The two columns of the figure denote the two calibration measurements: on the left-hand side with the shorter oscillation period and on the right-hand side with the longer period. The bottom row shows the temperature data of the out-of-loop thermistor at the TRP. Small oscillations on short timescales originate from imperfect PID controller settings of the liquid chiller, which were adjusted during the second measurement. They have been adapted during the measurement to reduce those oscillations. The top row shows the frequency measurement from the beat with the iodine (blue), biased by the RLU design frequency of $\nu_0^{\text{RLU}} = 281\,604.64$ GHz. The orange trace is computed as a linear fit through a least squares adjustment and obeys the equation

$$\nu_{\text{model}} = c_{\text{TRP}} \cdot T_{\text{TRP}}(t) + \tau \cdot \dot{T}_{\text{TRP}} + \text{const.} , \quad (6.2)$$

where the second term is a linearization of a potential time shift that accounts for a propagation delay of TRP temperature variations into the frequency. Its numerical value is found to be small, around $\tau = -6.8$ s. The short notation

$$T'_{\text{TRP}}(t) = T_{\text{TRP}}(t - \tau) - 24\text{ }^\circ\text{C} \quad (6.3)$$

is used in the legend of figure 6.6, where 24 °C is the nominal operating temperature of the RLU. The temperature-to-frequency coupling of this particular RLU was found to be

$$c_{\text{TRP}} = -235.916 \pm 0.138 \text{ MHz/K} , \quad (6.4)$$

which is significantly higher than the -12 MHz/K, which are the specification for the two RLUs built into the GRACE-FO LRI. However, the RLU-EM is not operated in

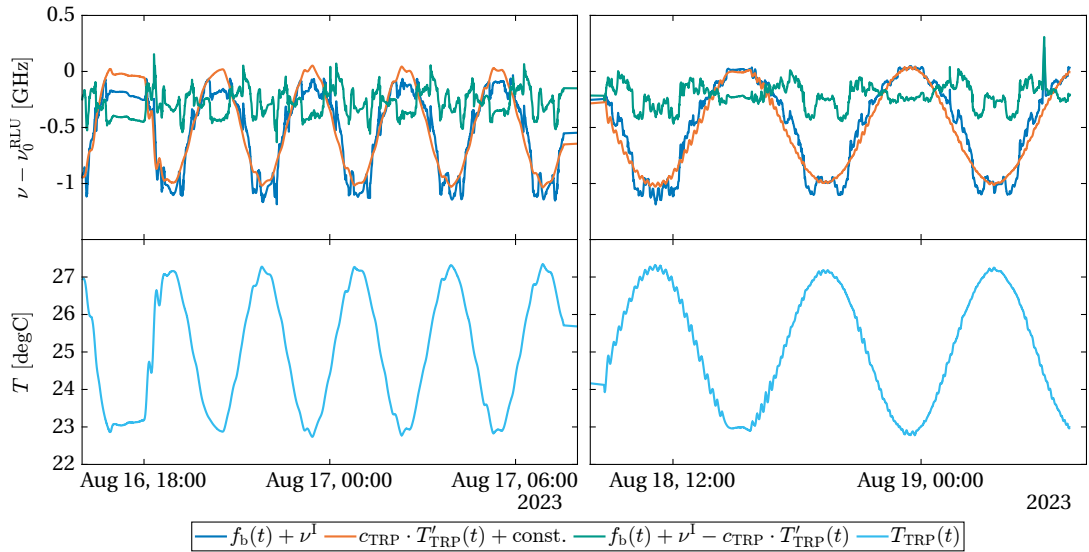


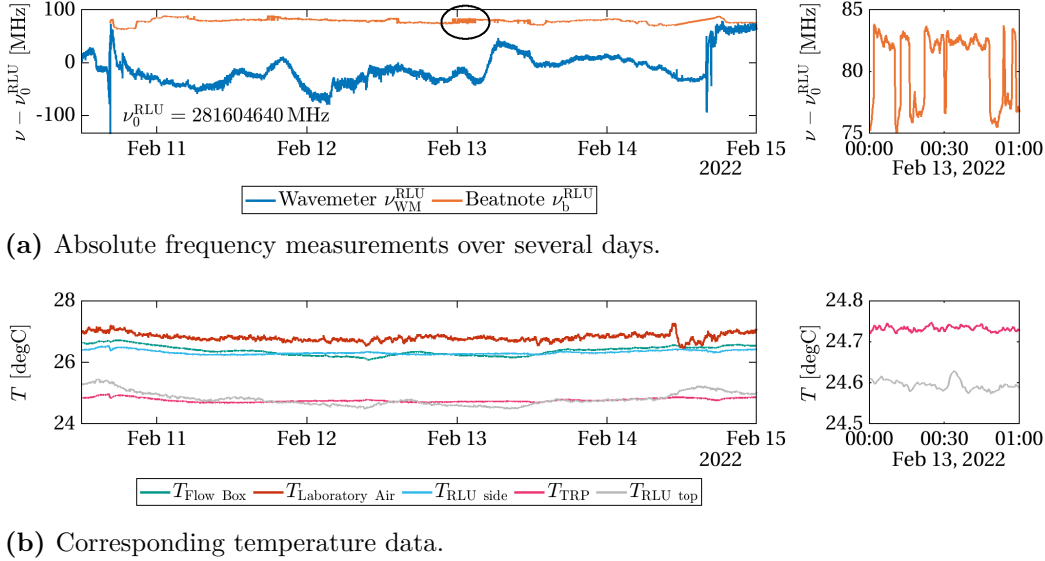
Figure 6.6. Temperature calibration measurement of the RLU-EM. $T'_{TRP} = T_{TRP}(t - \tau) - 24\text{ }^\circ\text{C}$ denotes the biased and time-shifted temperature at the TRP. The top row shows the measured frequency (blue), the thermal coupling model (orange), and the model residuals (green). The second row shows the variations of the RLU TRP. The sinusoidal temperature modulation has a period of 3 hours in the left column and 8 hours in the right. The short time-scale temperature variations originate from non-ideal PID controller settings of the liquid chiller.

a vacuum. Therefore, temperature fluctuations of the environment couple not only through the thermal interface, which is the contact area of the housing's feet with the base plate, but also through the air surrounding the device. A possible adaption of the experiment is to move the RLU-EM into a vacuum chamber to have better thermal stability. The corrected frequency, including the thermal coupling model, is shown in green. There are visible steps at all temperature levels with magnitudes up to a few 100 MHz. These frequency steps or hops are almost instantaneous and have already been observed in previous tests for this particular RLU-EM (Tröbs et al., 2007).

6.4. Measurement Campaigns

The RLU-EM frequency was measured several times between the end of 2021 and mid-2023. For every measurement campaign, which usually lasts for a few hours to days, the absolute frequency from the wavemeter ν_{WM}^{RLU} and beatnote measurement ν_b^{RLU} are recorded with the wavemeter and the spectrum analyzer, respectively. The iodine frequency ν^I is also measured with the wavemeter directly before each measurement, and the corresponding transition line is determined from the list of known transition frequencies, cf. table 6.1. This allows converting the beatnote frequency into an absolute frequency in accordance with equation (6.1).

An exemplary measurement, taken in February 2022, is shown in figure 6.7. This measurement's duration is more than four days. The top panel shows the two frequency measurements: the direct wavemeter measurement in blue and the indirect but more accurate beatnote measurement in orange. Obviously, the wavemeter data is less accu-



(a) Absolute frequency measurements over several days.

(b) Corresponding temperature data.

Figure 6.7. Example of an RLU-EM frequency calibration measurement, taken in February 2022. (a) Absolute frequency measurement $\nu_{\text{WM}}^{\text{RLU}}$ of the RLU-EM frequency using the WS7-60 wavemeter (blue) alongside the beatnote measurement $\nu_{\text{b}}^{\text{WM}} = \nu^{\text{I}} - f_{\text{b}}$ between the RLU-EM and the iodine laser. (b) Temperatures of the laboratory and the RLU-EM during that time. The small boxes on the right-hand side show a zoom into the region encircled in black. Here, the RLU-EM frequency shows repeated steps of approx. 10 MHz.

rate than the relative beatnote measurement, as it shows higher high-frequency noise, in the order of a few MHz, and its long-term variations are much larger, around ± 50 MHz from peak to peak, and those slow variations do not correlate with the beatnote measurement. It can be safely assumed that these variations are not common-mode in both lasers, the RLU and the iodine-locked reference laser, and thus are measurement errors of the wavemeter. Such variations, likely correlated to the environmental temperature, humidity, or air pressure, have been previously observed for that particular device. The standard deviation of the wavemeter measurement is approximately ± 30 MHz, whereas the standard deviation of the beatnote measurement is ± 5 MHz.

The smaller panels in figure 6.7 show a zoom into the measurement, showing one hour of data on 2022-Feb-13. In this period, the laser frequency again shows repeated steps up and down by approximately 10 MHz. Although not shown in the zoom, those steps are also visible in the wavemeter data and can thus be attributed to the RLU-EM. The temperature at the TRP was stabilized within 0.05 K around the setpoint of 24.6°C during that period. Such bi-modal behavior has been observed repeatedly for this laser, and the amplitude of the steps reaches up to 100 MHz. These features complicate the data analysis of each measurement, as they seem to be uncorrelated to the TRP temperature and other environmental metrics like the humidity level.

To assess if a long-term drift is present in the optical frequency of this RLU-EM, the average frequency over the individual measurement campaigns is calculated, yielding $\langle \nu_{\text{WM}}^{\text{RLU}} \rangle = 281\,604\,629.472$ MHz for the absolute wavemeter measurement and $\langle \nu_{\text{b}}^{\text{RLU}} \rangle = 281\,604\,719.286$ MHz for the beat measurement for the above example, during which the iodine laser was locked to the a_1 component of the R(106) 34-0 transition (line no 1108, cf. table 6.1) at $\nu^{\text{I}} = 281\,614\,894.3748$ MHz. The angled brackets, $\langle \cdot \rangle$, denote the average over the measurement time.

Table 6.2. Long-term measurement results of the RLU-EM optical frequency. The temperature and frequency values denote the average over the whole measurement dataset. The corresponding locked iodine line of the reference laser is provided as a reference. The data is shown in figure 6.8a

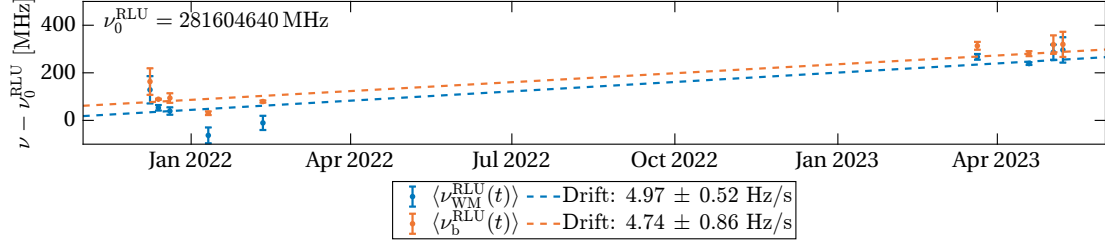
Date	$\langle T_{\text{TRP}} \rangle$ [degC]	$\langle \nu_{\text{WM}}^{\text{RLU}} \rangle$ [MHz]	$\langle \nu_b^{\text{RLU}} \rangle$ [MHz]	Line
2021-Dec-08	24.73 ± 0.20	281604768.604 ± 57.418	281604803.175 ± 55.816	1108, a_1
2021-Dec-13	25.10 ± 0.02	281604692.981 ± 11.582	281604728.955 ± 2.314	1108, a_1
2021-Dec-20	25.03 ± 0.11	281604679.343 ± 15.502	281604733.959 ± 20.082	1108, a_1
2022-Jan-10	25.44 ± 0.03	281604577.020 ± 33.282	281604670.166 ± 7.679	1108, a_1
2022-Feb-10	24.78 ± 0.06	281604629.472 ± 29.849	281604719.286 ± 4.593	1107, a_1
2023-Mar-20	23.91 ± 0.13	281604907.138 ± 11.936	281604953.646 ± 16.505	1107, a_{10}
2023-Apr-18	24.64 ± 0.03	281604878.870 ± 5.807	281604920.460 ± 10.490	1107, a_1
2023-May-02	24.01 ± 0.24	281604926.725 ± 31.859	281604958.582 ± 38.759	1107, a_1
2023-May-08	23.88 ± 0.25	281604936.220 ± 53.317	281604959.574 ± 52.817	1107, a_1

Table 6.2 lists the averaged frequencies of the different campaigns. They are furthermore shown in the top panel of figure 6.8a. A linear drift is fitted to both, the wavemeter and the beatnote measurements, and drawn as dashed lines. The reciprocal squared standard deviations, as given in table 6.2, are used as weighting parameters in the least squares estimation for the linear drift. As observed before, the wavemeter data is a few dozen MHz lower, which is caused by the limited absolute accuracy of the device. Furthermore, a linear drift of approximately +5 Hz/s can be observed.

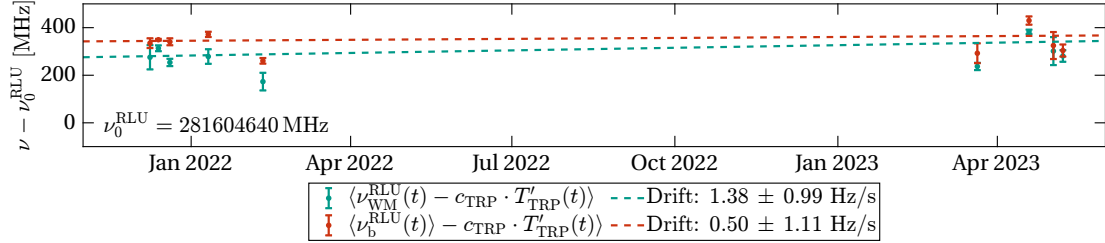
It was found in section 6.3.2 that the RLU-EM optical frequency is susceptible to its thermal environment, specifically with a coupling factor of $c_{\text{TRP}} \approx -236 \text{ MHz/K}$. However, the individual measurements have not been recorded at the same temperature each. Therefore, the raw frequency data has to be corrected by a temperature correction term given by

$$\nu_{\text{TRP}} = c_{\text{TRP}} \cdot T'_{\text{TRP}}(t) . \quad (6.5)$$

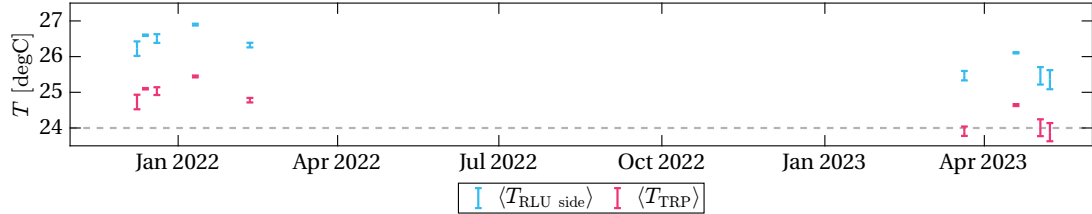
The frequency estimates after that correction are shown in figure 6.8b and exhibit a drift of approximately $+0.5 \pm 1.1 \text{ Hz/s}$ when using the more accurate beatnote measurements.



(a) Measured frequencies $\nu_{\text{WM}}^{\text{RLU}}$ (blue) and $\nu_{\text{b}}^{\text{RLU}}$ (orange). The wavemeter measurement is slightly lower than the beatnote with reference to the iodine standard. Both show an apparent drift of approximately +5 Hz/s.



(b) Frequencies corrected with the measured temperature data, using the calibrated temperature coupling c_{TRP} . After the correction, the drift is less prominent, at about $+0.50 \pm 1.11$ Hz/s for the beatnote measurement (red) and $+1.38 \pm 0.99$ Hz/s for the wavemeter measurement (green).



(c) Temperatures and their standard deviation during the respective frequency measurements. On average, the temperature was lower at the measurements in 2023. The pink data shows the RLU-EM TRP. The dashed gray line indicates the nominal RLU-EM temperature of 24 °C.

Figure 6.8. Frequency drift results after 1.5 years of measurements for the RLU-EM. (a) shows the raw measurements, indicating a +5 Hz/s drift. (b) includes the temperature coupling correction, as derived in section 6.3.2. The overall drift over the whole period reduces to about 0.5 ± 1.1 Hz/s. (c) shows the average temperature during the individual measurements at the RLU-EM TRP and on its side surface.

6.5. Discussion and Summary

The laser telemetry-based frequency models of the two RLUs within the GRACE-FO LRI show a frequency drift in the order of 1 Hz/s to 1.2 Hz/s, or equivalently approximately 40 MHz/year, over the course of almost five years, cf. table 5.4a in section 5.3.3. Since the RLU lasers are frequency-locked to a reference (cavity or frequency-offset lock, depending on their role), it is reasonable to assume that the free-running laser at a fixed thermal and PZT setting would show a -1.2 Hz/s to -1 Hz/s drift. Hence, a companion experiment was conducted in a laboratory to see if such a drift could be observed with an older RLU engineering model from a previous space mission. The susceptibility of the RLU-EM optical frequency to temperature variations at the TRP was calibrated and found to be -235.916 MHz/K. Similarly, the coupling of the optical power setpoint into the frequency was calibrated, yielding a coupling coefficient of -310.5 MHz/mW, which is in accordance with previous calibrations.

Within 18 months, the free-running frequency of this RLU-EM showed an increase of approximately 250 MHz, yielding a drift rate of approximately $+5$ Hz/s, which is much larger and with a different sign than observed in-flight. However, this drift almost vanished after considering a temperature coupling effect with a remaining frequency drift rate of 0.5 ± 1.1 Hz/s. The analysis of this experiment is complicated by frequent steps in the frequency that reach magnitudes up to several hundred MHz.

With this experiment, a drift in the RLU-EM could neither be confirmed nor excluded. Hence, it is still unclear if the drift observed in the GRACE-FO LRI telemetry is an actual frequency change of the RLU, e. g., caused by aging of the NPRO crystal. Another hypothesis would be purely electronic effect in the RLU or LRP electronics. However, if the drift is entirely attributed to the `SLOW_FREQ` telemetry channel, which has a nominal frequency coupling of 500 MHz/V for the GRACE-FO RLUs (cf. section 5.3.1), that would yield a drift of 40 MHz/year $\cdot 1/500$ V/MHz ≈ 80 mV/year or 0.8% /year of the full control range. That drift would only exceed the overall frequency control range in some tens of years, however, the magnitude sounds unreasonably high for a drift in the frequency controller electronics.

Repeating the experiment in a thermal vacuum chamber may be helpful for even better temperature stability. Additionally, the TRP of the RLU-EM provides a better estimate for the overall RLU-EM temperature in a vacuum environment, as the laser unit is not dissipating heat through the surrounding air but only through the contact points with the heat sink. It is further anticipated that a potential drift is detectable after a shorter observation time than a year due to better thermal control. However, it is unclear if the frequency hops remain even under more stable environmental conditions.

For future space missions, a qualification of this potential frequency drift with the particular laser flight models in a vacuum environment is needed, should a telemetry-based laser frequency model be used to determine the LRI scale factor or as a backup for a dedicated technical solution like the FSR locking scheme, which has been briefly introduced in section 5.6.

“Measure what is measurable, and make measurable what is not so.”

— GALILEO GALILEI —
Astronomer and Physicist

The triple mirror assembly (TMA), as introduced in section 3.1.6, is a critical part of the LRI instrument. It is routing the beam coming from the optical bench towards the distant spacecraft while enabling a lateral offset of 600 mm to circumpass the cold-gas tanks (Sheard et al., 2012). The manufacturing and integration accuracy is a performance driver of the whole LRI instrument, as any misalignment of the mirrors degrades the received optical power at the distant spacecraft, and any offset of the virtual mirror intersection point from the SC center of rotation contributes to TTL errors (Wegener et al., 2020). Parts of this section are currently being prepared for publication in (Misfeldt et al., 2023c).

During the mission, several so-called DWS scans have been performed. These are usually octagon-shaped patterns in the two pointing angles, pitch θ_{dws} and yaw ψ_{dws} , which are added as offsets onto the DWS control loop setpoints on one of the SC. In normal operations, these offsets are zero. However, when these offsets are non-zero, the outgoing beam is not anti-parallel to the incoming one but has an angular deviation. Hence, the distant spacecraft does not receive the central part of the beams' amplitude profile but maps the far-field beam intensity distribution throughout the scan, which implies a drop in the received beam power and thus the CNR, cf. equation (2.46) at the remote SC. These scans are particularly designed and used to assess the co-alignment of the TMA mirrors. If the TMA has non-zero co-alignment errors, θ_{tma} and ψ_{tma} , the beatnote amplitude on the receiving spacecraft is not maximized at $(\theta_{\text{dws}}, \psi_{\text{dws}}) = (0, 0)$, but at $(\theta_{\text{dws}}, \psi_{\text{dws}}) = (-\theta_{\text{tma}}, -\psi_{\text{tma}})$. However, many more aspects of the LRI, like heterodyne efficiency variations and a particular form of tilt-to-length coupling, can be analyzed from the scans. The following sections will at first present different types of DWS scans before the TMA co-alignment and other aspects are discussed.

7.1. DWS Scan Types

The first results of these measurements have been analyzed by the LRI team at AEI and first been published in Misfeldt (2019). However, more DWS scans have been performed regularly since. There are six different types of DWS scans in total, whose properties are listed in table 7.1. The corresponding DWS setpoint angles as time series and the spatial field of regard are shown in appendix D for all of these types. They mainly differ in pattern, number of setpoints, and the maximum DWS excursion angle. The first type is a pattern of concentric, equidistant octagons and consists of 168 setpoints and was designed for determination of the TMA co-alignment errors, see section 7.2. The pattern is rastered from the inside to the outside, with a maximum excursion of

Table 7.1. Description of the different DWS scan types. N defines the number of setpoints, $\gamma_{\text{dws}}^{\text{max}}$ is the maximum deflection angle, t_{hold} is the hold-time per setpoint. Notes: (*) 300 μrad was the design amplitude, however due to DWS setpoint wrapping in the LRP, the maximum value is at about 200 μrad . See appendix E for the exact spatial scan patterns.

Type	N	$\gamma_{\text{dws}}^{\text{max}}$ [μrad]	t_{hold} [s]	Shape	Description
1	168	100	30	Octagon	Initial design of the DWS scan
2	25	100	30	Octagon	Reduced Octagon pattern
3	1000	100	2	Random	Random pattern for phase front analysis
4	100	300*	120	Spokes	Low-CNR Pre-Test: Four Spokes in $\pm\psi$ and $\pm\theta$ directions
5	60	180	390	Circle	Low-CNR Test: Five concentric circles at $\gamma_{\text{dws}} = [60, 125, 150, 170, 180] \mu\text{rad}$
6	15	100	10	Steps	Radial spokes every 45° ; $\gamma_{\text{dws}} = 100 \mu\text{rad}$ per step

$\gamma_{\text{dws}}^{\text{max}} = \sqrt{(\psi_{\text{dws}}^{\text{max}})^2 + (\theta_{\text{dws}}^{\text{max}})^2} = 100 \mu\text{rad}$, which is equivalent to a beam pointing offset of $100 \mu\text{rad} \cdot 200 \text{ km} \approx 20 \text{ m}$ w. r. t. to the LOS at the longitudinal position of the distant SC. The second type is a reduced version of the first pattern with 25 setpoints only, but also with $\gamma_{\text{dws}}^{\text{max}} = 100 \mu\text{rad}$. The third type consists of 1000 randomly distributed setpoints within a circle of $\gamma_{\text{dws}}^{\text{max}} = 100 \mu\text{rad}$ and is used for phase front derivation, which is discussed later in section 7.4. The same is true for type six, which consists of eight steps of $100 \mu\text{rad}$ in 45° angles from the center and back. The fourth and fifth types are designed to test the low-CNR tracking capabilities of the LRP, which this thesis does not discuss further.

7.2. Far-Field Beam Properties and TMA Co-Alignment Errors

The beatnote amplitude \mathcal{A}_b on the receiving side is determined from the coherent sum of the amplitudes and phases in the four DPLLs as introduced in equation (2.37) and section 2.3.1. With the set of DWS setpoint angles of the transmitting SC and the beatnote amplitude \mathcal{A}_b of the receiving SC, one can model the far-field beam intensity profile and gain information about the beam properties and the TMA co-alignment.

During ground testing before launch, the measured TMA co-alignment error γ_{tma} exceeded the requirement of 50 μrad (LRI OPLB v19.0) on both TMAs. The co-alignment error of the TMA is typically expressed through the half-cone angle

$$\gamma_{\text{tma}} = \sqrt{\psi_{\text{tma}}^2 + \theta_{\text{tma}}^2} . \quad (7.1)$$

The latest ground measurement result before launch was performed in March 2018 and is shown in figure 7.3. It was found that moisture accumulated within the gluing pockets after assembly. The glue was used to support the optical bonding of the mirror substrates. However, the LRI functionality was still guaranteed in nominal conditions. Furthermore, the co-alignment was expected to improve after launch while slowly outgassing moisture.

7.2.1. Elliptical Gaussian Beam Model

In a simple approach, the beam intensity profile can be regarded as an elliptical or astigmatic Gaussian beam. Its normalized beam intensity $\mathcal{A}^{\text{SAGB}}$ can be expressed in accordance to equation (2.23) as

$$\mathcal{A}^{\text{SAGB}}(\psi', \theta') = \exp \left\{ - \left(\frac{\psi'}{\Theta_1} \right)^2 - \left(\frac{\theta'}{\Theta_2} \right)^2 \right\}. \quad (7.2)$$

The angles $(\theta', \psi')^T$ are defined as

$$\begin{pmatrix} \psi' \\ \theta' \end{pmatrix} = \begin{pmatrix} \cos \vartheta & \sin \vartheta \\ -\sin \vartheta & \cos \vartheta \end{pmatrix} \cdot \begin{pmatrix} \psi_{\text{dws}} - \psi_0 \\ \theta_{\text{dws}} - \theta_0 \end{pmatrix} \quad (7.3)$$

that represent the DWS-derived beam pointing angles yaw ψ_{dws} and pitch θ_{dws} as defined in the LRI optical frame through equation (2.43), and converted into the beams' principal axes frame through a rotation by the angle ϑ . Consequently, ψ_0 and θ_0 are the offset values at which the received power in the distant spacecraft is the highest, which are equivalent to the negative TMA co-alignment errors of the scanning SC. Θ_i are the divergence angles of the beam within that rotated frame, which are directly related to the waist sizes of the Gaussian beam through equation (2.10).

The Gaussian beam model is defined by its parameters $\{\mathcal{A}_0, \theta_0, \psi_0, \Theta_1, \Theta_2, \vartheta\}$, where \mathcal{A}_0 is a scaling factor, that is proportional to the received beam power. These free parameters are ultimately estimated by minimizing

$$\chi^2 = \sum_i \left(\mathcal{A}_0 \cdot \mathcal{A}^{\text{SAGB}}(\psi'(t_i), \theta'(t_i)) - \mathcal{A}_b(t_i) \right)^2 \quad (7.4)$$

with t_i denoting the sample of the measured time series.

7.2.2. Amplitude Profile Estimation and Discussion of Results

The far-field beam parameters can be determined from all the DWS scans that have been performed in principle. However, types 1 and 5 are most suited for this purpose, as their setpoints' spatial distribution covers the intensity profile most regularly and with many sample points, as seen in figure 7.2. Type 2 is also suited but has fewer sample points ($N = 25$), while types 4 and 6 only measure 4 or 8 spokes over the entire Gaussian profile. Type 3 has a very short hold time of $t_{\text{hold}} = 2$ s per setpoint, which is non-ideal for this analysis, as the \mathcal{I} and \mathcal{Q} values of the DPLLs are only stored at a rate of 0.1 Hz and errors are introduced by the interpolation. Therefore, the beam parameters were determined for all scans of types 1, 2, and 5 by minimizing equation (7.4) with a nonlinear minimizer^[1]. The results are shown in table 7.2.

An exemplary fit result for scan no. 1 is shown in figure 7.1 in the time domain and in figure 7.2 as a 3-dimensional representation of the beam intensity. This particular scan was executed in June 2018 on GF-1. The shown beam pointing angles are derived from the DWS signals and are measured on GF-1, while the amplitude is measured on the receiving spacecraft, GF-2, using the coherent sum of the four phasemeter channels

^[1]The MATLAB function `fminunc` uses a quasi-Newton method (Mathworks, Inc., 2023).

Table 7.2. Fit Parameters of all in-flight DWS Scans of types 1, 2, and 5. The absolute distance L is obtained from the GNVIB data products, and the temperature is measured at the TMA TRP. Both denote the average value over the scan duration. The meaning of the scan types is given in table 7.1. The parameter estimates for types 3, 4, and 6 are not reliable due to the fast setpoint changes and therefore excluded from this table. The TMA co-alignment errors are the negative values of θ_0 and ψ_0 .

No.	SC	Date	Type	$\theta_0 = -\theta_{tma}$ [μ rad]	$\psi_0 = -\psi_{tma}$ [μ rad]	γ_{tma} [μ rad]	Θ_1 [μ rad]	Θ_2 [μ rad]	ϑ [rad]	\mathcal{A}_0 [a.u.]	rms [a.u.]	L [km]	T [$^{\circ}$ C]
1	GF-1	2018-Jul-18	1	47.39 \pm 16.75	1.27 \pm 13.63	47.41	146.62 \pm 33.79	124.13 \pm 21.38	0.676 \pm 0.764	10.54 \pm 0.76	0.131	215.24	14.65
2	GF-1	2019-Jun-13	2	5.78 \pm 8.14	9.56 \pm 9.86	11.17	143.70 \pm 23.21	128.54 \pm 16.63	0.227 \pm 0.909	14.61 \pm 0.91	0.227	175.25	20.19
3	GF-1	2019-Jun-14	2	6.00 \pm 7.75	9.66 \pm 9.27	11.37	145.04 \pm 21.58	128.13 \pm 15.69	0.246 \pm 0.765	14.64 \pm 0.84	0.198	175.42	19.34
4	GF-1	2019-Oct-10	1	6.00 \pm 7.19	4.79 \pm 8.37	7.67	139.33 \pm 22.98	125.46 \pm 17.16	0.253 \pm 0.925	14.43 \pm 0.92	0.186	181.12	17.61
5	GF-1	2021-Jul-15	5	8.88 \pm 16.08	-12.82 \pm 16.05	15.59	132.26 \pm 26.36	125.69 \pm 25.52	0.442 \pm 2.624	12.35 \pm 2.15	0.549	205.13	17.59
6	GF-1	2022-Dec-15	5	13.01 \pm 13.88	-12.77 \pm 13.85	18.23	132.15 \pm 23.10	125.06 \pm 21.89	0.480 \pm 2.090	15.36 \pm 2.31	0.637	175.38	17.41
7	GF-2	2018-Jul-18	1	-4.37 \pm 9.75	52.37 \pm 16.56	52.55	144.25 \pm 25.67	127.40 \pm 17.86	0.016 \pm 0.830	11.01 \pm 0.62	0.089	215.26	14.67
8	GF-2	2019-Jun-14	2	-0.50 \pm 5.83	5.91 \pm 6.53	5.93	133.17 \pm 14.14	124.23 \pm 11.81	0.144 \pm 1.027	13.74 \pm 0.65	0.114	175.26	14.63
9	GF-2	2019-Jun-14	2	-0.03 \pm 5.95	5.23 \pm 6.64	5.23	133.60 \pm 14.80	124.77 \pm 12.03	0.109 \pm 1.048	13.57 \pm 0.66	0.115	175.21	14.62
10	GF-2	2019-Sep-26	1	1.03 \pm 5.79	5.93 \pm 6.49	6.01	129.09 \pm 16.28	120.88 \pm 13.66	0.094 \pm 1.196	13.09 \pm 0.73	0.112	181.08	14.66
11	GF-2	2019-Oct-10	1	-2.16 \pm 6.45	10.43 \pm 7.46	10.66	134.01 \pm 19.05	124.42 \pm 15.57	0.057 \pm 1.166	12.87 \pm 0.76	0.123	181.08	17.32
12	GF-2	2022-Dec-15	5	8.55 \pm 9.31	-12.43 \pm 9.29	15.09	130.58 \pm 14.24	124.16 \pm 14.15	0.186 \pm 1.574	13.73 \pm 1.47	0.223	175.38	17.40

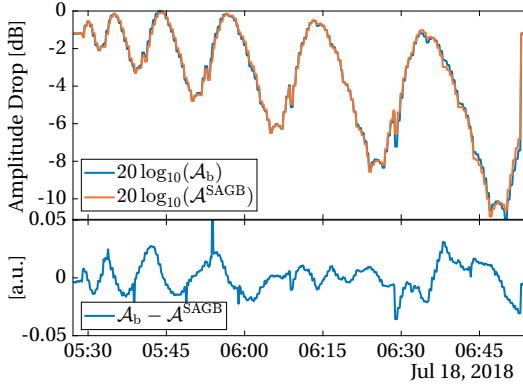


Figure 7.1. DWS Scan on GF-1 in June 2018 (Scan No. 1) in time-domain. **Top:** The measured beatnote amplitude on GF-2 and the estimated model, cf. equation (7.2). **Bottom:** The residuals, normalized to the maximum value of the measurement, are below 5%.

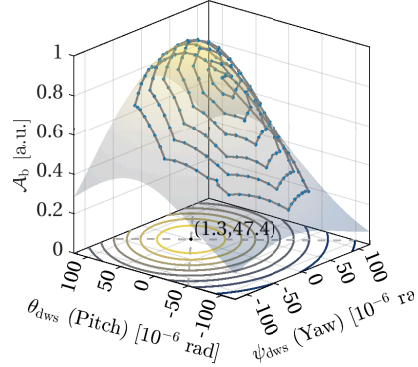


Figure 7.2. Amplitude profile of GF-1 in June 2018 (Scan No. 1). The amplitude is measured on GF-2 by means of the normalized DPLL \mathcal{I} values, cf. equation (2.37). The angles are obtained from the DWS signals on GF-1. The model is estimated following equation (7.2).

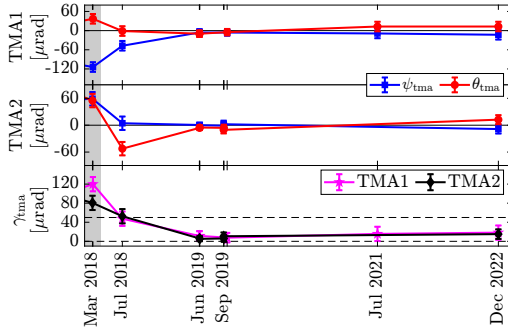


Figure 7.3. Variations of the TMA co-alignment angles (θ : Pitch; ψ : Yaw) from the last on-ground verification in 2018 until December 2022. **Top:** TMA of GF-1. **Center:** TMA of GF-2. **Bottom:** γ_{tma} for both TMAs, cf. equation (7.1). The gray area marks the period before launch. Josep Sanjuan kindly provided the ground measurements.

$\mathcal{A}_b = |\mathcal{A}_{cs}|$, cf. equation (2.37). The blue dots and gray connecting lines denote the measured data. The colored surface results from the parameter estimation show the Gaussian profile, cf. equation (7.2). The model matches the data well, with small residuals. The maximum amplitude is located at $(\psi_{\text{dws}}, \theta_{\text{dws}}) = (1.3, 47.4) \mu\text{rad}$, which could be attributed to a TMA co-alignment error of $(\psi_{\text{tma}}, \theta_{\text{tma}}) = (-1.3, -47.4) \mu\text{rad}$. Other potential but minor contributors to a non-centered location of the beam intensity maximum could be higher-order mode contents, uncalibrated offsets in the DWS controller, and residual beam-pointing from imperfectly wedged optical components. The dashed lines in the xy-plane denote the principal axes of the Gaussian beam, and the two axes have a divergence of $146 \mu\text{rad}$ and $124 \mu\text{rad}$, respectively. The estimated beam parameters for this and all other in-flight DWS scans are shown in table 7.2. Furthermore, the progression of the TMA co-alignment errors over time, starting with the last on-ground measurement, is shown in figure 7.3. The top and middle panels show the individual TMA angles of the two flight units, while the third panel shows the combined co-alignment error γ_{tma} and the $50 \mu\text{rad}$ requirement. After the co-alignment angles have been above the requirement in the ground tests on both TMA, they quickly recovered in orbit, likely due to outgassing of the accumulated moisture. The first in-orbit measurement, conducted in July 2018, showed a reduced $\gamma_{\text{tma}} \approx 50 \mu\text{rad}$ for both

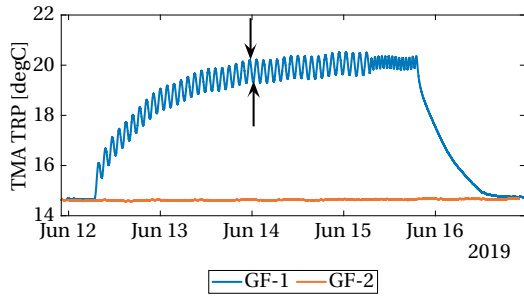


Figure 7.4. TMA TRP temperature variations in June 2019. The two arrows denote the times when the reduced DWS scans (type 2, no. 2 and 3) were conducted.

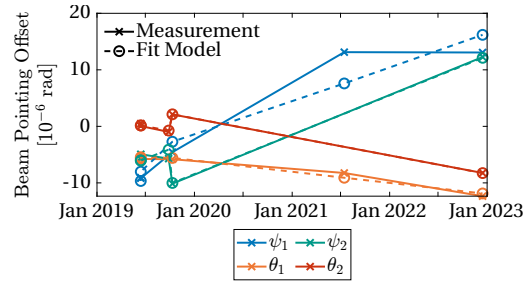


Figure 7.5. Beam pointing offsets ψ_{tma} and θ_{tma} of both SC over time. The solid lines and crosses show the individual scan results, and the dashed lines and circles show linear regression results regarding the varying TMA temperature, cf. equation (7.7) and table 7.3.

spacecraft, see figure 7.3. After June 2019, all measurements, which were approximately repeated twice a year, resulted in a co-alignment error of $\gamma_{\text{tma}} \approx 10 \mu\text{rad}$ on both SC, well below the requirement. Both beams show slight ellipticity with divergence angles in the order of $120 \mu\text{rad}$ to $150 \mu\text{rad}$. The absolute beatnote amplitude parameter \mathcal{A}_0 scales with the spacecraft separation L through the received optical beam power, cf. equation (2.47).

7.2.3. Temperature Stability of the TMA Co-Alignment

On 2019-Jun-14 a thermal cycling of the accelerometer was performed. Since the TMA is rigidly mounted to the ACC housing, its temperature followed the excitations. The measured temperature at the TMA TRP on GF-1, delivered in the OFFRED data as sensor THT10063, first shows a raise from roughly 14.6°C to 20°C and then a sinusoidal modulation of $\pm 0.5^\circ\text{C}$, as shown in figure 7.4. Within these variations, two short DWS scans (type 2), one at a high temperature and the other at a low temperature, separated by approximately 1 h, have been recorded. The average TMA temperatures throughout the scans were 20.19°C and 19.34°C , respectively. This allows computing the TMA temperature coupling as





$$c_{\psi_{\text{tma},1}} = -0.29 \mu\text{rad}/\text{K} \quad \text{and} \quad c_{\theta_{\text{tma},1}} = -0.22 \mu\text{rad}/\text{K} . \quad (7.5)$$

It should be noted that these coupling factors likely have large uncertainties due to the fast temperature variations and the fact that the TMA structure might not reach a thermal equilibrium state. Two scans were executed in GF-2 as well, but the TMA temperature did not change. Yet, a similar assessment can also be done on GF-2 for the two scans in September and October 2019, two weeks apart, as the TMA temperature was raised from approximately 14.6°C to 17.3°C . Here, the temperature coefficients are

$$c_{\psi_{\text{tma},2}} = 1.69 \mu\text{rad}/\text{K} \quad \text{and} \quad c_{\theta_{\text{tma},2}} = -1.20 \mu\text{rad}/\text{K} . \quad (7.6)$$

Unfortunately, there was no DWS scan on GF-1 in September 2019; hence, a direct comparison between the two SC is not possible. However, estimating the coupling

Table 7.3. Parameter estimates for the temperature coupling of the TMA. The fit model is shown in equation (7.7). The index of the angle denotes the SC, while ψ and θ denote the yaw and pitch axes, respectively. The color coding refers to the time-domain representation of these results shown in figure 7.5.

Angle	α_0 [μrad]	c_α [$\mu\text{rad}/\text{K}$]	c_{drift} [nrad/day]
ψ_1 	23.812 ± 53.219	-1.964 ± 2.692	15.944 ± 5.944
θ_1 	2.478 ± 8.350	-0.301 ± 0.422	-5.463 ± 0.933
ψ_2 	20.380 ± 9.360	-2.316 ± 0.643	19.211 ± 1.742
θ_2 	-12.847 ± 2.010	1.128 ± 0.138	-9.025 ± 0.374

factors through a weighted linear regression between the measured co-alignment errors and the corresponding temperature for the in-flight scans listed table 7.2 is possible. The regression function combines a static offset with a temperature coupling and a linear drift as

$$\alpha = \alpha_0 + c_\alpha \cdot T_{\text{tma}} + c_{\text{drift}} \cdot (t - t_0) , \quad (7.7)$$

where α denotes the measured beam pointing angles ψ_{tma} and θ_{tma} from the DWS scans as shown in table 7.2. The time refers to $t_0 = 2018\text{-May-22}$ at midnight. The parameters α_0 , c_α , and c_{drift} are determined independently for all four angles. An offset temperature T_0 , that biases the measurement as $T - T_0$, is not estimated, meaning that the α_0 parameter refers to a hypothetical co-alignment error at a TMA temperature of 0°C . The results of this regression are shown in figure 7.5 and table 7.3. The weighting in the least squares estimation is chosen as the inverse squared standard deviations of the angle estimates, cf. table 7.2, and of course, the first measurement on both SC was excluded, as it dominantly shows the co-alignment error due to the accumulated moisture. Not all assessments on both TMAs meet the temperature requirement of $1 \mu\text{rad}/\text{K}$ (Fleddermann et al., 2014). However, it should be noted that the data points used for this estimation have been collected with large temporal gaps in between and might be corrupted by various other effects. Further, as already mentioned earlier, the estimated pointing offsets of the intensity profiles' maximum are entirely attributed to the TMA co-alignment in this analysis; however, they might also be caused by other effects like non-gaussianity of the beams or offsets in the DWS readout. Also, the TMA temperature axis is neither sampled densely nor evenly, and the temperature stimulus is only 3 K at maximum.

7.3. Local Heterodyne Efficiency

This section describes the dependency of the heterodyne efficiency η_{het} on the relative angle α_{tx} between the two interfering beams. According to equation (2.47), the beatnote amplitude \mathcal{A}_b linearly depends on the square-root of the heterodyne efficiency $\sqrt{\eta_{\text{het}}}$. Consequently, the CNR, as it is proportional to \mathcal{A}_b^2 , is linearly dependent on η_{het} . The heterodyne efficiency itself depends on the relative angle of the two interfering beams, as introduced in section 2.3.5. The CNR thus directly measures the heterodyne efficiency variations if the relative beam angle changes and all other quantities, i. e., the local and received beam power, remain constant. Luckily, this is the exact case on the scanning

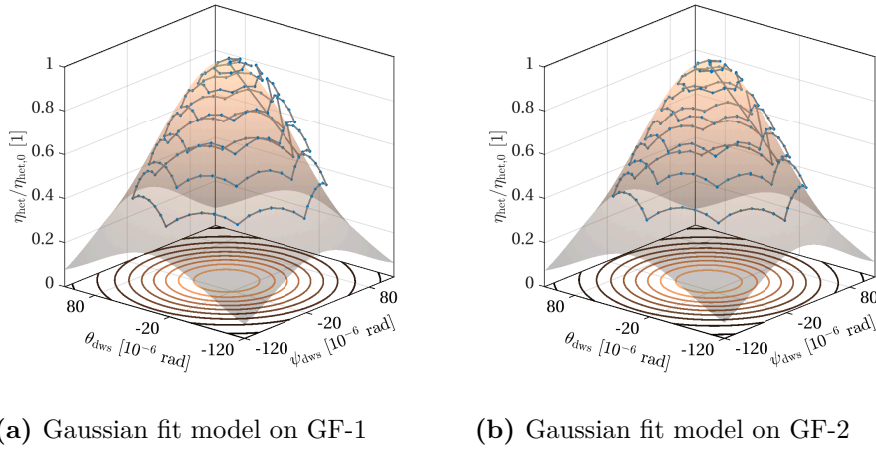


Figure 7.6. Spatial distribution of the heterodyne efficiency on GF-1 and GF-2. Shown are fits no. 1 and 7 recorded on 2018-Jul-18 of type 1 (cf. table 7.1). The y-axes are in units of the maximum heterodyne efficiency $\eta_{\text{het},0}$.

SC during a DWS scan. Therefore, the DWS scans can not only be used to assess the beam amplitude profile in the far field but also to investigate the local heterodyne efficiency. In the case of amplitude profile determination, the DWS controller deflects the local beam, and the amplitude profile is sensed through the CNR at the distant spacecraft. Now, for determining the heterodyne efficiency, the angles and CNR are both recorded on the local spacecraft, where the DWS offsets are commanded.

The radially symmetric definition for the angular dependency of the heterodyne efficiency, cf. equation (2.55), can simply be expanded to a 2-dimensional description in terms of the beam pointing angles yaw and pitch, ψ'_{dws} and θ'_{dws} , cf. equation (2.43). They are again transformed from the LRI optical frame into the principal beam axis frame through equation (7.3), as indicated by the primes. The heterodyne efficiency model thus reads

$$\eta_{\text{het}}(\psi'_{\text{dws}}, \theta'_{\text{dws}}) = \eta_{\text{het},0} \exp \left(-2 \frac{(\psi'_{\text{dws}} - \psi'_0)^2}{(\Theta_{\psi} f_{\text{cpd}}(w_0(\Theta_{\psi})/r_{\text{rx,ap}}))^2} - 2 \frac{(\theta'_{\text{dws}} - \theta'_0)^2}{(\Theta_{\theta} f_{\text{cpd}}(w_0(\Theta_{\theta})/r_{\text{rx,ap}}))^2} \right). \quad (7.8)$$

Again, $r_{\text{rx,ap}} = 4 \text{ mm}$ is the radius of the receiving aperture and $\Theta_{[\psi,\theta]}$ are the local beams' divergence angles. The local beams' waist radius, where the intensity drops to the $\approx 13.5\%$ level, is defined as $w_0(\Theta) \approx 2.5 \text{ mm}$ through the beam divergence Θ , cf. equation (2.10). The polynomial function $f_{\text{cpd}}(w_0(\Theta)/r_{\text{rx,ap}})$ takes a value of approximately approximately 1.1 for the LRI parameters, cf. equation (2.55). Furthermore, potential offsets in the DWS controller are introduced through ψ'_0 and θ'_0 .

This section verifies the analytical model of the heterodyne efficiency drop, cf. equation (7.8), with in-flight data from the DWS scans no. 1, 4, 7, 10, and 11, cf. table 7.2. These scans are of type 1, featuring the octagon pattern with a maximum relative pointing angle of $100 \mu\text{rad}$ and 168 setpoints. Each spacecraft conducted one of the

Table 7.4. Model parameters for the heterodyne efficiency models, cf. equations (7.8) and (7.14), based on the octagon-shaped DWS scans of type 1 on both spacecraft. Two parameter sets are given per scan, with and without estimating the non-gaussian part. This non-gaussian part is much smaller on GF-2 than on GF-1. The error estimates denote the standard error of the variance-covariance matrix.

No.	SC	ψ'_0 [μ rad]	Θ_ψ [μ rad]	b_ψ [%]	θ'_0 [μ rad]	Θ_θ [μ rad]	b_θ [%]	ϑ [rad]	rms [%]
1	GF-1	4.92 ± 25.27	142.28 ± 82.63	–	0.31 ± 24.32	138.31 ± 80.90	–	0.07 ± 16.98	0.83
		4.71 ± 17.64	135.07 ± 80.82	2.27 ± 42.39	0.28 ± 16.88	130.94 ± 80.30	2.56 ± 42.37	0.02 ± 3.83	0.83
4	GF-1	4.66 ± 22.44	136.20 ± 75.69	–	0.35 ± 21.70	132.27 ± 74.76	–	0.04 ± 15.77	0.62
		4.50 ± 14.89	129.82 ± 71.19	2.04 ± 37.33	0.34 ± 14.34	125.77 ± 70.92	2.26 ± 37.45	0.03 ± 3.77	0.62
7	GF-2	1.46 ± 16.83	138.46 ± 55.33	–	-0.10 ± 15.74	130.48 ± 54.21	–	0.07 ± 5.71	0.67
		1.46 ± 16.47	137.50 ± 75.04	0.31 ± 37.51	-0.10 ± 15.40	129.52 ± 73.99	0.32 ± 37.33	0.06 ± 5.56	0.67
10	GF-2	1.50 ± 17.37	130.87 ± 60.05	–	-0.29 ± 16.56	123.30 ± 60.70	–	-0.02 ± 6.53	0.79
		1.50 ± 17.37	131.47 ± 82.75	-0.20 ± 40.60	-0.29 ± 16.56	123.89 ± 83.16	-0.19 ± 40.91	-0.02 ± 6.44	0.79
11	GF-2	1.49 ± 17.00	136.70 ± 57.54	–	-0.34 ± 16.16	129.01 ± 57.11	–	0.01 ± 6.02	0.70
		1.48 ± 16.51	135.51 ± 77.58	0.34 ± 37.18	-0.34 ± 15.71	127.79 ± 77.18	0.45 ± 38.11	0.00 ± 5.80	0.70

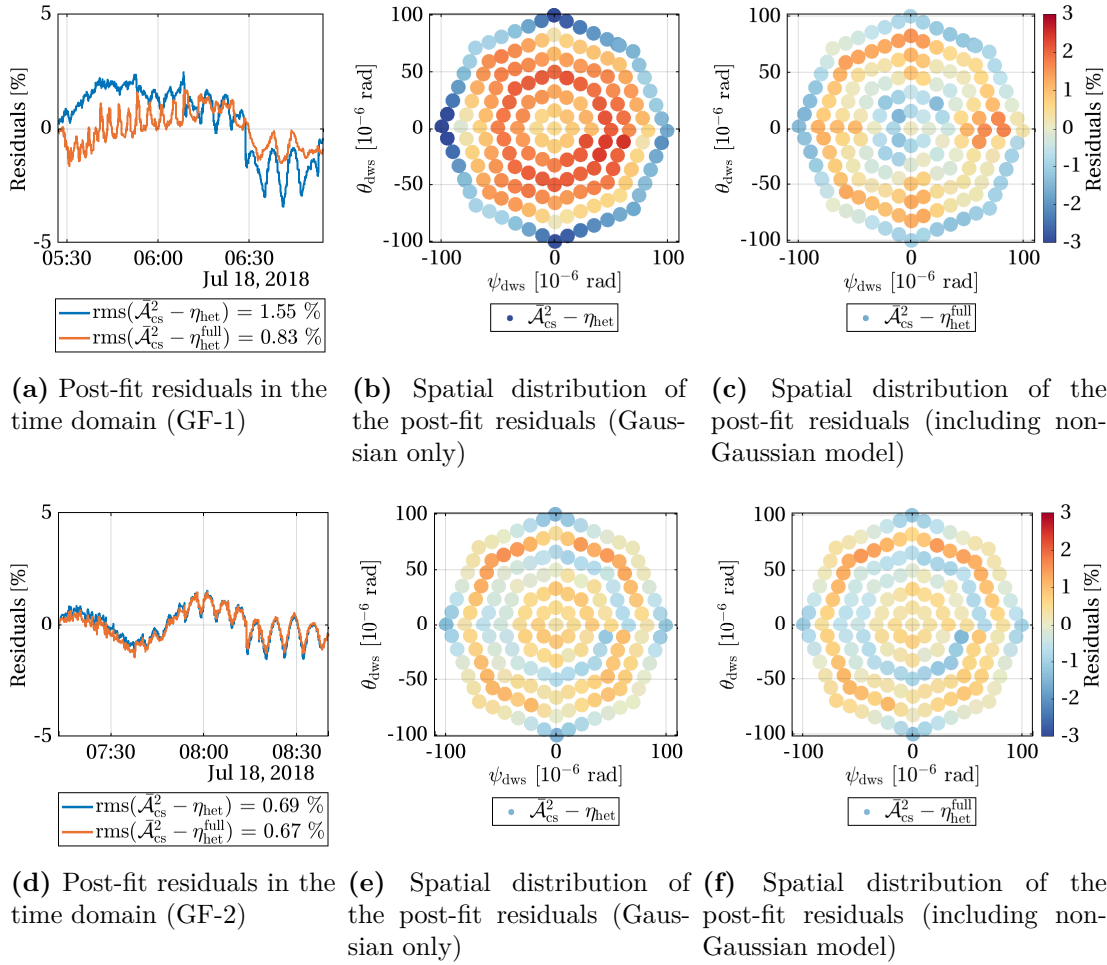


Figure 7.7. Post-fit residuals of the heterodyne efficiency on GF-1 and GF-2. Scans 1 and 7 of type 1 are shown, recorded on 2018-Jul-18 (cf. tables 7.1 and 7.2). Top row: GF-1; Bottom row: GF-2. Left column: postfit residuals in the time domain; Center column: Spatial distribution of the residuals after the purely Gaussian fit; Right column: Spatial distribution of the residuals including the non-gaussian fit.

scans in July 2018, and the others were recorded in October 2019.

All parameters of the heterodyne efficiency model are again determined through a nonlinear optimizer^[1]. In total, five parameters are estimated: the beam divergences Θ_ψ and Θ_θ , the DWS angle offsets ψ'_0 and θ'_0 , and the rotation of the beams' principal axis w. r. t. the DWS axes. The total amplitude is not estimated, as the model is fitted against the normalized beatnote amplitude $\bar{\mathcal{A}}_b^2$, and hence $\eta_{\text{het},0} = 1$.

The estimated parameters are shown in table 7.4. The DWS controller offsets, ψ'_0 and θ'_0 , are small, i. e., below $5 \mu\text{rad}$. Their exact value might be an artifact of a non-optimal model, as their expected value would be zero. The divergence angles of the astigmatic Gaussian beam are in the order of $125 \mu\text{rad}$ to $140 \mu\text{rad}$, with the divergence in yaw being larger than in pitch direction, $\Theta_\psi > \Theta_\theta$, as already observed in the

^[1]Again, the MATLAB function `fminunc` was used.

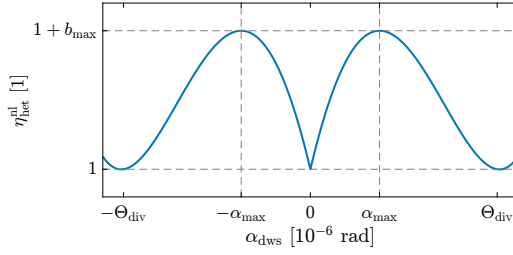


Figure 7.8. Unit-less function for the non-gaussianity of the heterodyne efficiency, cf. equation (7.9). The parameter α_{\max} varies the position of the maximum, whose amplitude is given by b_{\max} . The function equals one at $\alpha_{\text{dws}} = 0$ and $\alpha_{\text{dws}} = \Theta_{\text{div}}$.

previous section for the amplitude profile determination. The rotation of the beams' principal axes w. r. t. the DWS axis is small as well, below 0.08 rad in all measurements. The post-fit residuals rms, i. e., the rms of the difference between the actual data and the model, is larger for GF-1 than for GF-2, approximately by a factor of two. The standard error estimates are high for all parameters, indicating a non-optimal model.

The two subplots of figure 7.6 show the (normalized) beatnote amplitude, or the heterodyne efficiency drop, of the scanning spacecraft (GF-1 in (a), GF-2 in (b)) over the two DWS-derived beam pointing angles ψ_{dws} and θ_{dws} . The blue dots and gray lines show the measured data, while the colored surface shows the parameter estimation result. The model matches better on GF-2 than on GF-1, which is also visible from the post-fit residuals, which are shown in blue in subfigures (a) and (d) of figure 7.7. On GF-1, the post-fit residuals are at a level of 1.55 % rms of the total amplitude, while it is only 0.69 % rms on GF-2. Subfigures (b) and (e) show the post-fit residuals over the beam pointing angles in a spatial plot. On GF-1, figure 7.7b, the model clearly underestimates the heterodyne efficiency loss at beam pointing angles around $50 \mu\text{rad}$ (red colors), while it overestimates at larger angles (blue colors). Such model errors are expected as the beams are not perfectly Gaussian. To also estimate this non-gaussian fraction, an empirical model is introduced. Along one direction α_{dws} , it reads

$$\eta_{\text{het}}^{\text{ng}}(\alpha_{\text{dws}}) = 1 + c_1 |\alpha_{\text{dws}}| + c_2 \alpha_{\text{dws}}^2 + c_3 \alpha_{\text{dws}}^4 \quad (7.9)$$

with

$$c_1 = 2\alpha_{\max} b_{\max} (\Theta_{\text{div}}^2 - 2\alpha_{\max}^2) / c_4 \quad (7.10)$$

$$c_2 = b_{\max} (4\alpha_{\max}^3 - \Theta_{\text{div}}^3) / c_4 \quad (7.11)$$

$$c_3 = b_{\max} (\Theta_{\text{div}} - 2\alpha_{\max}) / c_4 \quad (7.12)$$

$$c_4 = \alpha_{\max}^2 (\alpha_{\max} - \Theta_{\text{div}})^2 (2\alpha_{\max} + \Theta_{\text{div}}) . \quad (7.13)$$

The function is exemplarily shown in figure 7.8. It is designed such that $\eta_{\text{het}}^{\text{nl}}(0) = \eta_{\text{het}}^{\text{nl}}(\Theta_{\text{div}}) = 1$, and $\eta_{\text{het}}^{\text{nl}}(\alpha_{\max}) = 1 + b_{\max}$. Furthermore, it shall have an extremum at α_{\max} , i. e., $\partial \eta_{\text{het}}^{\text{ng}}(\alpha) / \partial \alpha|_{\alpha_{\max}} = 0$. The model parameter b_{\max} is estimated individually for both beam principal axes, while the angular excursion of this maximum value is fixed at $\alpha_{\max} = 50 \mu\text{rad}$. Hence, the full heterodyne efficiency model reads

$$\eta_{\text{het}}^{\text{full}} = \eta_{\text{het}}(\psi'_{\text{dws}}, \theta'_{\text{dws}}) \cdot \eta_{\text{het}}^{\text{ng}}(\psi'_{\text{dws}}) \cdot \eta_{\text{het}}^{\text{ng}}(\theta'_{\text{dws}}) . \quad (7.14)$$

The post-fit residuals on GF-1, as shown in orange in figure 7.7a, are reduced from 1.55 % rms to 0.83 % rms by estimating the additional parameter. These non-Gaussian parameter has a magnitude of $2\% \cdot \eta_{\text{het},0}$ on GF-1. On GF-2 instead, the effect is

much smaller, and the empirical model does not reduce the residuals significantly; see figure 7.7d. All estimated parameters are also shown in the second line for each scan in table 7.4.

The non-gaussian model $\eta_{\text{het}}^{\text{full}}$ allows quantifying the heterodyne efficiency between the local oscillator beam and the received flat-top beam on the optical bench of the LRI. The Gaussian model has an accuracy within $\pm 3\%$ for angular offsets below $100\ \mu\text{rad}$ between the two phase fronts. These deviations are partly modeled with the empirical refinement $\eta_{\text{het}}^{\text{ng}}$. Further, the beam divergence angles estimated within this approach are consistent with the ones in the far-field from the previous section. These analytical and empirically refined models, η_{het} and $\eta_{\text{het}}^{\text{full}}$, can be useful for the design of future LRI-like instruments, e. g., to derive an accurate optical link budget.

7.4. Phase Variations during DWS Scans

This section investigates variations in the ranging phase during the DWS scans. These scans modulate the pointing of the beams, which might cause optical path length changes, while the geometric path length is preserved. There is an inherent difference to tilt-to-length coupling, which refers to rotations of the whole spacecraft, not only of the beam. The effect described in the following is not measurable in normal operations, as the DWS control loop always ensures the alignment of the beams w. r. t. the line of sight. However, as the beam pointing varies during DWS scans, and this effect becomes, in principle, measurable.

7.4.1. Beam Pointing-to-Pathlength Coupling: Linear and Quadratic

Three scans specialized for determination of this coupling have been performed on both spacecraft. One of them is scan type 3 (cf. table 7.1), with 1000 setpoints randomly sampled in Cartesian space with an average step magnitude of $90\ \mu\text{rad}$, as proposed in Misfeldt (2019) and executed in 2019; the exact scan design is shown in appendix D. Its total duration is 2000 s. Two more scans of type 6 have been performed in 2021 and 2022. These scans only have eight setpoints, and their execution duration is 160 s. It should be noted that the raw ranging phase, i. e., without phase jump removal, is used, as some observed phase steps are wrongly interpreted as phase jumps and removed. The few phase jumps at thruster events during the scans are manually chopped off. Furthermore, the round-trip range is taken instead of the half-roundtrip range, as the beam pointing-to-pathlength effect occurs only in one of the two paths and would be divided by two otherwise.

The DWS signals and, thus, the calibrated beam pointing angles ψ_{dws} and θ_{dws} in yaw and pitch, respectively, can be retrieved from the phase measurements of the scanning spacecraft independent of the reference/transponder role, while the ranging phase is always taken from the SC in the reference role. Only the ranging phase at a 10 Hz data rate is needed for this analysis, and thus, the hold time of the individual setpoints was decreased significantly to 2 s for scan type 3 compared to the DWS scans of type 1 and 2.

The phase variations under rotation are modeled as a second-order polynomial in both angles, ψ_{dws} and θ_{dws} , to account for the spherical shape of the phase under small

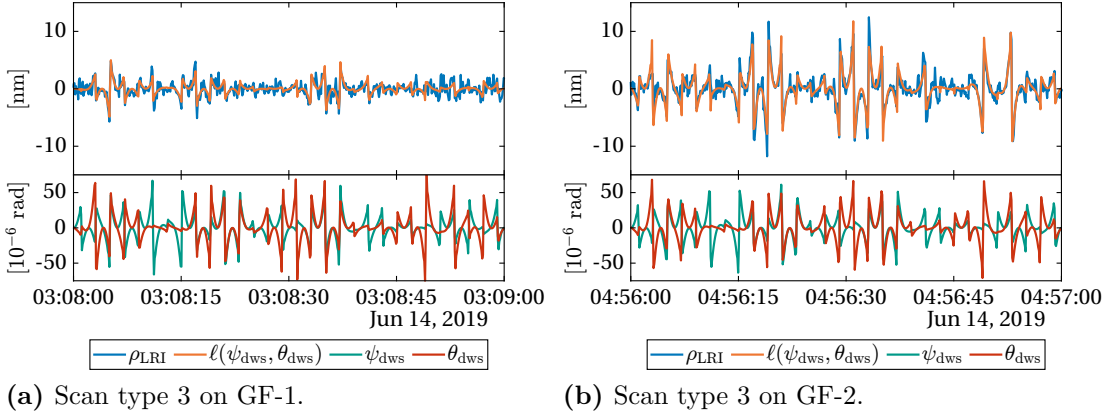


Figure 7.9. Small section of the DWS scans for phase front determination in the time domain. The top panels show the high-pass filtered ranging signal HPF $[\rho_{\text{LRI}}, f_c]$ (blue) and the fit model ℓ (orange), cf. equation (7.15). The high-pass filtered pointing angles ψ_{dws} and θ_{dws} , yaw and pitch, are shown on the bottom. (a) GF-1 scanning, (b) GF-2 scanning.

beam-pointing angles. The model ℓ reads

$$\ell(\psi_{\text{dws}}, \theta_{\text{dws}}) = c_0 + c_{l,\psi}\psi_{\text{dws}} + c_{l,\theta}\theta_{\text{dws}} + c_{q,\psi}\psi_{\text{dws}}^2 + c_{q,\theta}\theta_{\text{dws}}^2 + \text{const.} \quad (7.15)$$

The linear and quadratic coupling factors of equation (7.15) are estimated through a linear least squares fit that aims to minimize the difference of that model to the measured range ρ_{LRI} for data recorded during execution of the particular scans.

A highpass filter at $f_c = 0.35$ Hz is applied to ranging signal ρ_{LRI} and also to the beam pointing angles, ψ_{dws} and θ_{dws} , respectively. This filter removes the gravitational signal in the ranging data and renders the static offset c_0 in equation (7.15) unnecessary. The frequency of the low-pass filter cutoff f_c was determined through a parameter study to minimize the post-fit residuals of $\text{rms}(\ell - \text{HPF}[\rho_{\text{LRI}}, f_c])$. No weighting is applied in the parameter estimation, as the LRI ranging noise from the cavity lock at high frequencies is sufficiently white, cf. figure 3.10.

A short segment of scan type 3, executed in June 2019, is shown in figure 7.9 for both SC. Although the DWS setpoints (red and green, lower subplots) are commanded in discrete steps, they appear as peaks in figure 7.9 due to the high-pass filter. The ranging data ρ_{LRI} (blue, upper subplot) during the scan clearly shows excitations whenever the DWS setpoints are changed, and the estimated model ℓ (orange) follows the blue trace well. It is already apparent from the magnitude of the steps in the ranging data, which are in the order of 5 nm on GF-1 and 10 nm on GF-2, that the phase front on GF-2 has a stronger pointing-to-pathlength coupling or higher parasitic beam walk than GF-1.

The estimated parameters, shown in table 7.5, are in the order of $c_l \approx 20 \dots 35 \mu\text{m}/\text{rad}$ on GF-1 and $c_l \approx 25 \dots 110 \mu\text{m}/\text{rad}$ on GF-2 under non-zero beam pointing angles of up to $100 \mu\text{rad}$. The quadratic coupling reaches values in the order of $|c_q| < 0.5 \text{ m}/\text{rad}^2$ on GF-1 and $c_q < 2 \text{ m}/\text{rad}^2$ on GF-2. The uncertainties are calculated through Gaussian error propagation from the standard error of the variance-covariance matrix of the least squares minimization. The first scan on both spacecraft has the highest confidence, as more setpoints were commanded compared to the later scans. An additional parameter, which corresponds to a rotation of the DWS axes yaw and pitch w. r. t. the beams'

Table 7.5. Beam pointing-to-pathlength coupling factors for the scans of type 3 and 6 (cf. table 7.1). R denotes the spacecraft in reference role, TX the spacecraft where the scan pattern is commanded. The error estimates are the standard error of the variance-covariance matrix.

Type	R	TX	$c_{l,\psi}$ [$\mu\text{m}/\text{rad}$]	$c_{q,\psi}$ [m/rad^2]	$c_{l,\theta}$ [$\mu\text{m}/\text{rad}$]	$c_{q,\theta}$ [m/rad^2]
3	GF-1	GF-1	22.74 ± 0.41	0.37 ± 0.01	25.84 ± 0.42	-0.23 ± 0.01
6	GF-1	GF-1	23.94 ± 3.68	0.57 ± 0.04	32.12 ± 3.73	-0.15 ± 0.05
6	GF-1	GF-1	25.59 ± 3.04	0.46 ± 0.04	35.53 ± 3.10	-0.24 ± 0.04
3	GF-1	GF-2	24.12 ± 0.62	1.08 ± 0.01	107.72 ± 0.66	1.15 ± 0.01
6	GF-1	GF-2	46.56 ± 4.32	1.47 ± 0.06	38.05 ± 4.48	1.69 ± 0.06
6	GF-1	GF-2	50.72 ± 3.74	1.84 ± 0.05	63.65 ± 7.45	1.55 ± 0.10

principal axes coordinate system, can be implemented through equation (7.3). However, that results in non-linearity of equation (7.15) in the angles. Both variants have been implemented in software, but no advantage of the non-linear model was found. Hence, only the results of the linear method without the additional rotation are shown in table 7.5.

In regular operations, the FSM control loop ensures small DWS signals and thus small beam pointing angles, and also, the angular jitter of the FSM is small, with white noise in the order of $1 \mu\text{rad}/\sqrt{\text{Hz}}$. Hence, this potential noise source of the LRI is at the picometer level and, thus, not decreasing the instruments' performance.

7.4.2. Beam Pointing-to-Pathlength Coupling: Beam Waist Offsets

To first order, the beams propagating between the two spacecraft can be regarded as Gaussian beams. Hence, they have a spherical phase-front in the far-field, i. e., when the propagation distance is much larger than the Rayleigh range $z \gg z_R \approx 18.5 \text{ m}$, cf. section 2.2. Therefore, their electric field's phase at the distant spacecraft's receiving aperture does not change under small rotations or pointing variations. However, this only holds if the center of the spherical phase fronts is co-located with the rotation's pivot point, meaning the beams' waist is co-located at the reflective surface of the FSM, or in other words, that the radius of the phase front's curvature equals the geometric path length from the FSM to the distant receiving aperture. Any offset of the beam waist will induce phase changes on pointing variations as theoretically investigated in (Wanner et al., 2014; Schuster et al., 2015). This section attempts to derive such waist offset parameters given the observed phase variations of the previous section, assuming that other effects like additional phase variations due to the local beam deflection (e. g. beam walk), and heterodyne efficiency changes on the scanning spacecraft are zero. This is obviously not true; thus, the provided numbers can be regarded as an upper limit for this particular effect.

First assessments of the waist offsets have been published in (Misfeldt, 2019), but there have been more scans since, and also the theoretical derivation of the effect was revised. In the old analysis, the phase of a simulated beam with a non-zero waist offset was compared to a beam without this offset. The relative phase information was gained by subtracting the estimated phase of these two theoretical beams. However, a different approach is chosen for the scope of this re-analysis.

A spherical and a parabolic model for the beam's phase at the distant spacecraft are compared in the following. Afterwards, the effect of a non-zero waist offset is studied in the case of a spherical phase front.

Gaussian and Spherical Wave Models

This section calculates the difference of the paraxial approximation of the Gaussian beam's phase, equation (2.24), with respect to spherical phase fronts. Both models are, close to the propagation axis, reasonable choices for the phase of the beams of the LRI, although the truth is likely somewhere in between. The following equations are w.l.o.g. given for radially symmetric beams but can, in principle, be extended for elliptical beams as well. The phase fronts in the two pictures are defined as (cf. equation (2.24))

$$\Phi_p(\vec{r}) = k \cdot \left(z + \frac{x^2 + y^2}{2R(z)} \right) + \text{const.} \quad (7.16)$$

$$\Phi_s(\vec{r}) = k \cdot \sqrt{x^2 + y^2 + z^2} + \text{const.} \quad (7.17)$$

with the subscript p denoting the parabolic approximation and s the spherical form, and using the definition of the beam radius $R(z)$ of equation (2.11). The Gouy phase of the parabolic approximation is not explicitly written in equation (7.16). It yields a static contribution of $\eta_g(L)/k \approx \lambda/4$, cf. equation (2.12), which is, however, attributed to the constant offset.

The absolute beam pointing angle γ' consists of a quantity that is proportional to the DWS set point, and unknown offsets, e.g., due to TMA co-alignment errors or higher order mode contents of the Gaussian beams, and is abbreviated as

$$\gamma' = \sqrt{(\psi_{\text{dws}} + \psi_{\text{off}})^2 + (\theta_{\text{dws}} + \theta_{\text{off}})^2} \quad (7.18)$$

for a two-dimensional description, where ψ represents angles in the yaw, and θ in pitch axis. With this definition, the evaluation point \vec{r}'_{ap} , i.e., the position of the distant spacecrafts' receiving aperture w.r.t. the beam waist position \vec{r}_{waist} , expressed in the beams coordinate system, reads

$$\vec{r}'_{\text{ap}} = \hat{R}_{\gamma'} \cdot \vec{r}_{\text{ap}} - \vec{r}_{\text{waist}} \quad (7.19)$$

$$= \begin{pmatrix} \cos(\gamma') & \sin(\gamma') \\ -\sin(\gamma') & \cos(\gamma') \end{pmatrix} \cdot \begin{pmatrix} 0 \\ L \end{pmatrix} - \begin{pmatrix} 0 \\ \Delta z \end{pmatrix} \quad (7.20)$$

$$= \begin{pmatrix} L \sin(\gamma') \\ L \cos(\gamma') - \Delta z \end{pmatrix}, \quad (7.21)$$

where the second dimension denotes the propagation axis and the first dimension denotes one of the two orthogonal axes. Again, this symmetric description can easily be extended. Further, Δz denotes the waist position along the propagation axis. The definitions are sketched in figure 7.10. In the ideal case of $\Delta z = 0$ (blue phase fronts in the figure), the center of phase front curvature is co-located with the center of the beams' rotation, or in other words, the waist of the beam is located at the surface of

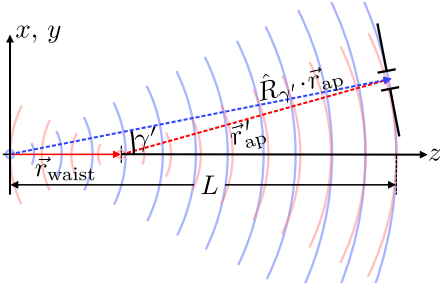


Figure 7.10. Two spherical phase fronts, one with a waist offset $|\vec{r}'_{\text{waist}}| = \Delta z$ along the propagation axis. The lines of equal phase (light red and blue) have different curvature at the receiving aperture in the distance L , which is measurable under varying beam pointing. $\hat{R}_{\gamma'} \cdot \vec{r}'_{\text{ap}}$ is the aperture position w.r.t. the center of the nominal beam (blue), and \vec{r}'_{ap} (cf. equation (7.19)) denotes the aperture position w.r.t. the beam with the offset.

the FSM. Obviously,

$$\Phi_s(\vec{r}'_{\text{ap}}) = k\sqrt{\Delta z^2 + L^2 - 2\Delta z L \cos(\gamma')} + \text{const.} \quad (7.22)$$

$$\Rightarrow \Phi_s(\vec{r}'_{\text{ap}})\Big|_{\Delta z=0} = k \cdot |L| + \text{const.} \quad \forall \gamma' \quad (7.23)$$

resembles the expected result of spherical symmetry for any beam pointing offset. The parabolic phase front approximation instead reads as

$$\Phi_p(\vec{r}'_{\text{ap}}) = k \cdot \left((L \cos(\gamma') - \Delta z) + \frac{L \sin^2(\gamma')}{2R(L \cos(\gamma') - \Delta z)} \right) + \text{const.} , \quad (7.24)$$

which does not yield an easily interpretable form. Therefore, to assess the differences between the spherical and parabolic case for a non-zero $\Delta z \neq 0$, a Taylor series \mathcal{T} of equations (7.22) and (7.24) in the two angles $\gamma_{\text{dws}} \approx 0$ and $\gamma_{\text{off}} \approx 0$ is computed. Note that the angles are treated individually in the series expansion, not in their short-hand notation γ' . The constant offset $L - \Delta z$ is subtracted, as it is not of interest, and the limit of $L \rightarrow \infty$ is considered for all other terms. These simplifications yield the variations of the (spherical) phase upon beam pointing variations as

$$\ell_s(\gamma_{\text{dws}}) = \lim_{L \rightarrow \infty} \mathcal{T}[\Phi_s(\vec{r}'_{\text{ap}})/k - (L - \Delta z)]\Big|_{\gamma_{\text{dws}} \approx 0, \gamma_{\text{off}} \approx 0} \quad (7.25)$$

$$\approx \frac{\Delta z}{2} \gamma_{\text{off}}^2 + \gamma_{\text{dws}} \gamma_{\text{off}} \Delta z + \gamma_{\text{dws}}^2 \left(\frac{\Delta z}{2} - \frac{\Delta z}{4} \gamma_{\text{off}}^2 \right) + \text{const.} \quad (7.26)$$

$$= c_0 + c_{l,\gamma} \gamma_{\text{dws}} + c_{q,\gamma} \gamma_{\text{dws}}^2 + \text{const.} . \quad (7.27)$$

A similar expression can be obtained by expanding the parabolic expression Φ_p , although more assumptions have to be made, i.e., that $\Delta z/L \approx 0$ and $z_R/L \approx 0$. However, those are given for the LRI, where L is in the order of 200 km. This parabolic equation reads

$$\ell_p(\gamma_{\text{dws}}) = \mathcal{T}[\Phi_p(\vec{r}'_{\text{ap}})/k - (L - \Delta z)]\Big|_{\gamma_{\text{dws}} \approx 0, \gamma_{\text{off}} \approx 0, \Delta z/L \approx 0, z_R/L \approx 0} \quad (7.28)$$

$$\approx \frac{\Delta z}{2} \gamma_{\text{off}}^2 + \gamma_{\text{dws}} \gamma_{\text{off}} \Delta z + \gamma_{\text{dws}}^2 \left(\frac{\Delta z}{2} - \left(2\Delta z + \frac{3}{4}L \right) \gamma_{\text{off}}^2 \right) + \text{const.} . \quad (7.29)$$

This expression, however, diverges in the limit of $L \rightarrow \infty$ due to the additional last term. The difference between the spherical and the parabolic model is

$$\ell_s - \ell_p = \frac{3}{4} \gamma_{\text{dws}}^2 \gamma_{\text{off}}^2 (3\Delta z + L) + \text{const.} . \quad (7.30)$$

The contribution of the Gouy phase to the parabolic model under such a beam rotation can be calculated as

$$\left[\eta_g(L) - \eta_g(L \cos(\gamma') - \Delta z)\right]/k \approx 3 \cdot 10^{-10} \text{ nm} \quad (7.31)$$

for a choice of $L = 220 \text{ km}$, $\gamma' = 250 \mu\text{rad}$ and $\Delta z = z_R$, which is negligibly small and therefore neglected further.

Estimating the Beam Waist Offset from DWS Scans

For the remainder of this section 7.4, the spherical model ℓ_s , i. e., equation (7.26) is used further, as it requires fewer assumptions in the derivation than for the parabolic model ℓ_p (equation (7.29)).

The first term of equation (7.26) is constant, while the other two terms denote a linear and quadratic coupling in γ_{dws} . It is consequently simplified in equation (7.27), using generic coupling coefficients c_l and c_q , where l, q denote the linear and quadratic couplings, respectively. Despite these linear and quadratic coupling terms in γ_{dws} , there is the very last term, which is quadratic in both, the beam pointing angle γ_{dws} and unknown offset angle γ_{off} , but linear in the waist offset Δz . It has a similar form as found for two tilted interfering Gaussian beams, see e. g., [Wanner et al. \(2014\)](#) and [Schuster et al. \(2015\)](#). In the cited references, the term is regarded as small. However, it will be preserved in the following.

It is easy to see that this form of pointing-to-pathlength coupling only arises, if $\Delta z \neq 0$; otherwise, the measured path length is simply $\ell_s|_{\Delta z=0} = L$ for all arbitrary γ_{dws} and γ_{off} ^[1]. A generalized expression of equation (7.27) for an astigmatic beam, using the DWS-derived beam pointing angles yaw ψ_{dws} and pitch θ_{dws} instead of a one-dimensional description using γ_{dws} , was already given in the previous section, cf. equation (7.15), and the linear and quadratic coupling factors $c_{l, [\psi, \theta]}$ have already been determined, see table 7.5. The beam parameters of interest, namely the beam pointing offsets $\psi_{\text{off}}, \theta_{\text{off}}$ and the beam waist offset $\Delta z_{[\psi, \theta]}$, can therefore be obtained by combining equations (7.26) and (7.27) and solving the quadratic equations in γ_{dws} for the waist offset Δz and the offset angle γ_{off}

$$[\psi_{\text{off}}, \theta_{\text{off}}] = \frac{1}{c_{l, [\psi, \theta]}} (2c_{q, [\psi, \theta]} \pm \sqrt{2c_{l, [\psi, \theta]}^2 + 4c_{q, [\psi, \theta]}^2}) \quad (7.32)$$

$$\Delta z_{[\psi, \theta]} = -c_{q, [\psi, \theta]} \pm \sqrt{\frac{c_{l, [\psi, \theta]}^2}{2} + c_{q, [\psi, \theta]}^2}, \quad (7.33)$$

where the symmetric description in terms of γ was not expanded into the two beams' principal axes ψ and θ , which have independent parameter sets. Only one solution yields a physical result, depending on the signs of the estimated coefficients.

The resulting parameters are given in table 7.6. The given error estimates are derived through error propagation of the standard error of the variance-covariance matrix. The exact error propagation formulas, as they are of minor importance and easily derived, are given in appendix F. The offset Δz of the waist position w. r. t. the center of rotations is on GF-1 is approximately -1 m in the yaw-axis, and 0.4 m in the pitch-axis. On GF-2

^[1]Note that the parabolic expression ℓ_p also features the non-zero term $3/4L\gamma_{\text{dws}}^2\gamma_{\text{off}}^2$, that does not vanish at $\Delta z = 0$.

Table 7.6. Beam waist offset parameters from DWS scans for the scans of type 3 and 6 (cf. table 7.1). R denotes the spacecraft in reference role, TX the spacecraft where DWS setpoints ψ_{dws} and θ_{dws} , i. e., the scan pattern, are commanded. The beam properties are determined through equations (7.32) and (7.33) using the fit parameters of table 7.5. The error estimates are determined through error propagation of the standard error of the variance-covariance matrix.

Type	R	TX	ψ_{tma} [μrad]	Δz_{ψ} [m]	θ_{tma} [μrad]	Δz_{θ} [m]
3	GF-1	GF-1	-30.695 ± 1.045	-0.741 ± 0.015	55.444 ± 2.303	0.466 ± 0.016
6	GF-1	GF-1	-21.122 ± 5.121	-1.133 ± 0.086	104.110 ± 36.432	0.309 ± 0.094
6	GF-1	GF-1	-27.888 ± 5.535	-0.917 ± 0.080	75.327 ± 16.093	0.472 ± 0.080
3	GF-1	GF-2	-11.206 ± 0.447	-2.153 ± 0.022	-46.631 ± 0.648	-2.310 ± 0.024
6	GF-1	GF-2	-15.802 ± 2.280	-2.946 ± 0.111	-11.227 ± 2.019	-3.389 ± 0.117
6	GF-1	GF-2	-13.792 ± 1.568	-3.677 ± 0.095	-20.496 ± 3.834	-3.106 ± 0.201

instead, they are in the order -3m in both axes. This offset ultimately causes the coupling of pointing deviations into the path length signal. This result is in accordance with pre-flight assessments, as it is assumed that the waist position can be determined well below one Rayleigh range, which is in the order of $z_R \approx 18.5\text{m}$ for the LRI beam parameters. The beam pointing offsets, being a secondary output of this analysis, shows a larger value than estimated previously in section 7.2. In comparison, the dedicated scan for the far-field amplitude profile provided TMA co-alignment values in the order of $5\mu\text{rad}$ to $10\mu\text{rad}$ in June 2019 (cf. table 7.2). The results of this section using the phase change are in the order of up to $100\mu\text{rad}$. However, the two methods, using the amplitude profile or the phase information, are not expected to yield the same result since the phase typically contains more information like parasitic phase changes from beam-walk on the QPDs, local phase changes, and higher order mode contents, for example. The analysis neglected these, and hence, the provided values for the beams' waist and pointing offsets can only be regarded as an upper bound.

7.5. Summary

The TMA within the LRI is a critical component with performance-driving requirements. The integration within the spacecraft, i. e., the co-location of the virtual vertex point of the three mirrors with the SC center of mass, as well as the co-alignment of the three mirror planes, define the performance in two ways: The co-location is the driver for TTL coupling, while the co-alignment is responsible for the pointing and thus the received beam power and CNR at the distant spacecraft. The first of these two effects was analyzed in Wegener et al. (2020), and the latter one within this chapter.

Before launch, a critical co-alignment error of the TMA mirrors that exceeded the requirement of $\gamma_{\text{tma}} < 50\mu\text{rad}$ was found, caused by accumulated moisture in the glue pockets. However, the in-orbit measurements of the TMA co-alignment error showed a recovery within a few months after launch, cf. table 7.2 and figure 7.3. After that, the TMA co-alignment errors are close to zero, well below the requirement. An attempt to verify the temperature coupling of the mirror alignment was performed. In the presented estimation, the temperature coupling of the co-alignment is below $\pm 2.5\mu\text{rad/K}$ in all axes, exceeding the requirement of $\pm 1\mu\text{rad/K}$. However, the temperature stimulus

of the TMA is small over the mission duration, and the estimates thus have large error bars.

Despite the TMA characterization and verification, the DWS scans have proven to be a valuable method for determining various properties of the laser beams, like their divergence angles and the corresponding amplitude profile in the far field. Furthermore, the local heterodyne efficiency is investigated, and a non-Gaussian contribution to the heterodyne efficiency under beam pointing variations is quantified to be smaller than 2.5% of the total beam power on GF-1 and 0.5% on GF-2, see table 7.4.

The last investigation concerned the phase front in the far field. It was shown that beam pointing variations during the DWS scans couple linearly and quadratically into the measured ranging phase, and this effect was named beam pointing-to-pathlength coupling. The magnitude of this pointing-to-pathlength coupling is up to $110 \mu\text{m}/\text{rad}$, with a quadratic contribution of up to $1.9 \text{ m}/\text{rad}^2$, as shown in table 7.5. This coupling might have many origins, of which a particular one was studied further: An offset of the beams' waist position w.r.t. the FSM might lead to phase variations in the measurement. An upper bound for the waist offset is determined to be within 1 m of the FSM rotation point for both beam axes on GF-1, and on the order of -3 m on both axes on GF-2. As the pointing is usually maintained below $1 \mu\text{rad}/\sqrt{\text{Hz}}$ by the DWS-FSM control loop, this coupling is below $1 \text{ nm}/\sqrt{\text{Hz}}$ in nominal operations. It should be noted that this kind of pointing-to-pathlength coupling is inherently different from TTL, which is caused by geometric path length changes due to satellite rotations, as e.g. investigated by Wegener et al. (2020), instead of optical path length changes due to beam pointing variations.

“ *A laser is a solution seeking a problem.* ”

— THEODORE MAIMAN —

American Physicist and Inventor of the Laser

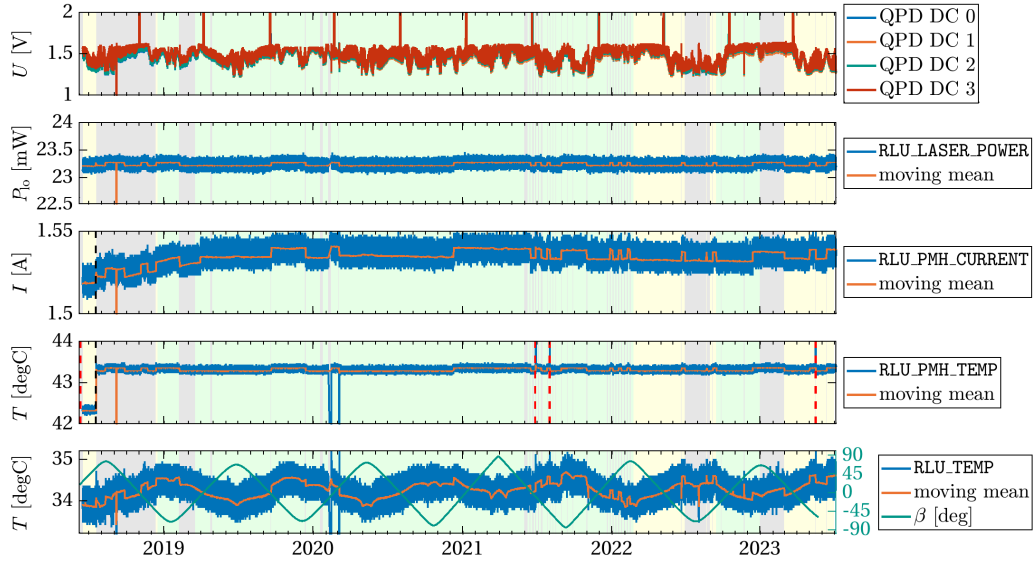
The reliability and stability of the reference laser units (RLUs), in terms of laser frequency and optical power, is vital for operating the LRI. Both spacecraft carry one RLU and an optical reference cavity, as introduced in section 3.1.3. The absolute laser frequency and very-low-frequency variations, which occur on the time scales of months and years, have already been investigated in chapter 5. This chapter investigates the RLU telemetry apart from its optical long-term frequency stability.

8.1. Time-Variability of the RLU Telemetry Channels

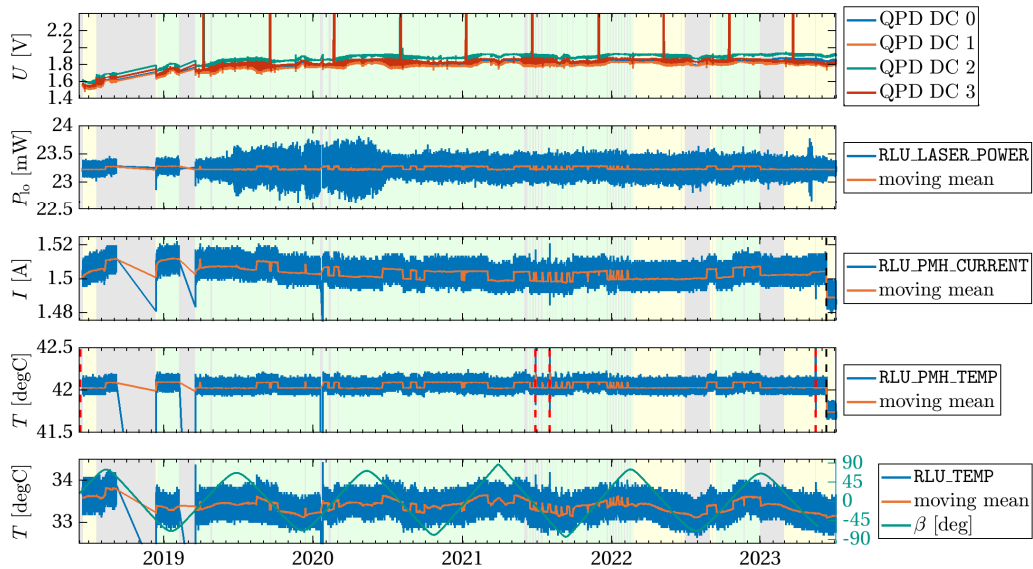
The laser telemetry is important to assess the general LRI status and performance. Moreover, it may indicate signs of degradation of the laser unit. The laser telemetry channels have been briefly introduced in section 3.1.3 and will be discussed in more detail now. The RLUs feature a telecommand and telemetry (TM/TC) interface with digital and analog channels. The analog telecommands (TCA) are used for setting the optical output power (RLU_LASER_POWER) and the frequency through the thermal and piezo actuators (RLU_SLOW_FREQ and RLU_FAST_FREQ). Furthermore, the temperature of the pump module head (PMH), which consists of two cold-redundant laser diode benches (LDBs), can be controlled through the RLU_PMH_TEMP channel. The optical output power, the PMH temperature, and the RLU internal temperature (RLU_TEMP) can be read through analog telemetry channels. The digital part of the interface is used to enable the optical output of the RLU (RLU_ON) and to set the active LDB (RLU_BENCH_SELECT). Until now, both RLUs still operate on the nominal LDB, and no switch to the redundant one has been performed.

Figures 8.1a and 8.1b show the progression of those RLU telemetry channels over the mission lifetime for GF-1 and GF-2, respectively. The RLU telemetry data originates from the so-called `ADCSamples` packet of the housekeeping telemetry and are recorded once every 120 s. The data product in which the data is published is called LHK1A or LHK1B (Wen et al., 2019). The analog telemetry is read out using an 8-channel 12-bit ADC, and the conversion from ADC counts to engineering units has been performed on the ground using the calibration table, determined before launch (JPL LRI Team, 2018).

The top panel shows the DC values of the summed QPD channels. Remember that the photocurrents generated by the photodiode quadrants are split into an AC and DC part, cf. section 2.3. These DC signals vary slightly over time, presumably due to temperature variations of the QPD. Furthermore, sharp peaks can be observed roughly every six months when the orbital plane of the SC is such that the sunlight directly



(a) RLU telemetry and QPD DC values on GF-1



(b) RLU telemetry and QPD DC values on GF-2

Figure 8.1. QPD DC Power and RLU telemetry over five years for (a) GF-1 and (b) GF-2. The red vertical lines denote the times of PMH scans (4 per spacecraft), the black lines denote PMH temperature setpoint changes (1 per spacecraft; see section 8.3). The background coloring denotes which SC was in reference role (green: GF-1, yellow: GF-2) or if the LRI tracking was suspended (gray).

enters the LRI baffles and impinges on the QPD. These are commonly denoted as sun-blinding periods where $\beta \approx 0^\circ$, with β being the angle between the sun vector and the orbital plane. Each spacecraft is blinded for about 30s per orbit for three days. The blinding occurs with a 180° orbital phase shift between the two SC, as they are oriented differently in the orbital plane, with GF-1 being rotated around the yaw angle by 180° , cf. section 3.1.9.

The second panel shows the RLU laser power P_{1o} , which is measured within the RLU. The blue trace shows the raw signal, whereas the orange curve is low-pass filtered with a moving-mean filter. The average optical power remains constant over the time of five years. Hence, no sign of degradation is apparent here, and both RLU deliver about 23.25 mW optical power according to the RLU-internal photodiode. The laser power on GF-2 shows higher fluctuations between 2019 and mid-2020. None of the other channels show such an envelope, and the variations decreased again in mid-2020. Within the low-pass filtered signals, two plateau values are visible on both SC, and the laser power seems to toggle between these two values several times. This effect, which occurs in the subsequent panels, will be discussed later.

The third panel features the current consumption of the PMH. It is presumably measured as the voltage drop over a small resistor in the power supply of the PMH. On GF-1, the PMH draw 1.52 A at the beginning of the mission, which increased to 1.54 A within the first year. Such an increase can be expected through possible aging effects of the RLU and the pump diodes, and an increase in the current monitor is a sign of degradation of the pump diode (Windisch et al., 2007). The PMH current on GF-2 also showed a slight increase in the early mission phase, but the values slightly dropped afterward to an average of roughly 1.5 A. At the very end, there is a step downwards at the black vertical line, which marks the time of a change in the PMH temperature setting.

The PMH temperature is then shown in the fourth panel, where a similar step is apparent. The PMH seems to draw less current at that new temperature. A similar but smaller effect is visible on GF-1 in July 2019. The influence of the PMH temperature is explained in more detail in section 8.3 below.

In the last panel, the overall RLU temperature measured via a 10 k Ω NTC thermistor inside the RLU housing is shown. On GF-1, prominent variations seem anti-correlated to the β -angle between the orbital plane and the sun vector (shown in green, refer to the right axis). On GF-2, the correlation is positive. This can again be explained with the different orientation of the two SC in orbit and the laser being located closer to one side within the SC, cf. figure 3.9 on page 32. The peak amplitude of these low-frequency variations is in the order of ± 0.25 K. A bi-modal behavior is apparent in the telemetry, where the values toggle between a lower and higher value.

In the following, the bi-modal behavior of the RLU telemetry is investigated further. The top panel of figure 8.2 again shows the optical laser power as measured by the RLU on GF-2, but limited to the period between 2021-Dec-18 and 2022-Feb-25. The raw signal and a low-pass filtered version are shown again as well. During this period, regular nadir-pointing periods were performed for two consecutive days per week where the LRI is not in science mode, as indicated by the gray background coloring. During the nadir pointing, the LRI is typically commanded into the diagnostic mode, in which the FSM moves to its zero position and does not perform reacquisition scans. There is an apparent increase in the number of plateau changes reported in the laser optical

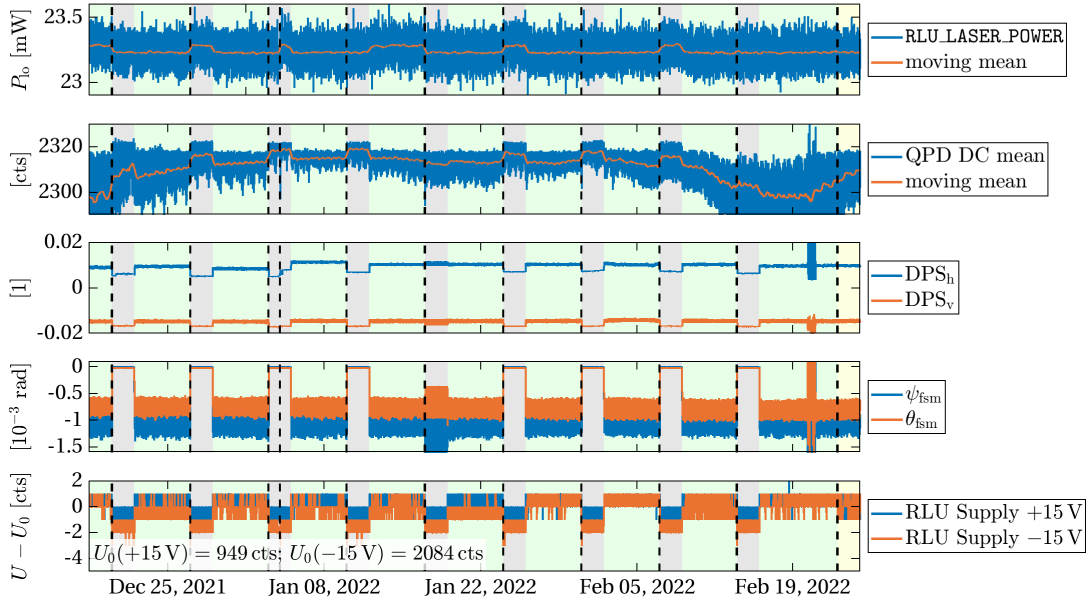


Figure 8.2. QPD DC, DPS, FSM, and RLU power supply signals on GF-2 during the nadir pointing mode periods in 2022. The green background indicates the phases in science mode, while the out-of-science phases are gray. The vertical black dashed lines denote reboots of the LRP.

power (orange trace in the first panel of figure 8.1b), which have a magnitude of approximately $0.05 \text{ mW} \approx 0.2\% \cdot P_o$. They occur instantaneously, although the orange trace in figure 8.2 (first panel) shows the plateau value changes with a slope due to the low-pass filter. The black vertical lines denote reboot times of the LRP, which is ultimately responsible for controlling the laser. It should be noted that the RLU turns off and on again if the LRP reboots. Remarkably, the plateaus often change at LRP and hence RLU reboots, and when the LRI transitions into science mode. In some instances, none of these two events triggered a plateau change, e. g., at the nadir-pointing period at the beginning of February 2022.

The second panel shows the DC power averaged over the four QPD channels on GF-2 once more. Whether or not the laser output power actually varies can be confirmed or disproved by comparing the mean QPD DC power over all channels, which is an independent measure of the optical power, to the RLU-internal optical power monitor from the laser telemetry. Small DC level changes of approximately $5 \text{ counts} \approx 0.2\% \cdot 2300 \text{ counts}$ can be observed, which always align with the nadir-pointing periods, in difference to the plateaus in the laser power signal above. Although the optical power variations in both measures have a similar magnitude of 0.2% , they do not seem to have the same cause. The plateaus within the QPD signal do correlate with steps in the DPS signals (third panel, cf. equations (2.44) and (2.45)) and significant steps of the FSM angles ψ_{fsm} (yaw) and θ_{fsm} (pitch; fourth panel). Every time the LRI is commanded out of science mode (gray background), the DPS signals show a step of approximately 5% , and also the FSM angles (fourth panel) show significant steps. In regular operation, the FSM has a static offset from its mechanical zero position that arises from integration tolerances of the LRI OBA into the spacecraft. This initial

pointing offset in two dimensions per SC was determined in space during the initial acquisition (Abich et al., 2019; Misfeldt, 2019). Whenever the LRI is commanded into diagnostic or idle modes, the FSM moves to its zero position. While rotating the mirror by large angles in the order of 1 mrad, it is likely that the QPD DC mean signal is influenced by residual beam walk on the QPD, which may not be suppressed entirely by the imaging system. From the DPS measurements, it is apparent that the beam spot moved such that 5% of the total optical power impinges at another half of the QPDs. Although the average optical beam power should be constant under beam walk on the circular photodiode, since the QPD diameter is larger than the beam spot size, there is a 45 μm slit between the QPD segments. These slits form a cross on the circular segmented photodiode. Therefore, the DC power measurements are incomplete due to a small portion of the total light power not impinging on the segments but in the slits, as the amount of light each photodiode segment receives, and hence the DPS signals, depends on the position of the beam spot.

In one instance, the LRI was not commanded into diagnostic mode but performed a reacquisition scan between 2022-Jan-08 and 2022-Jan-22, see the FSM angles in the bottom panel of figure 8.2. The reacquisition scan is centered around the initial pointing offsets, hence the angular step, and thus, the beam walk is smaller than for the other events. No steps in the mean QPD DC signal were observed but in the RLU telemetry channels like the laser power. This renders actual RLU optical power changes unlikely.

Additionally, no plateaus are visible in the non-RLU data streams digitized at the same eight-channel ADC. Two of these data streams are the cavity reflection and transmission power levels, another direct measure of the laser power. Hence, a variation in the ADC reference voltage, and thus a common value change in all ADC channels, can also be excluded as an explanation.

The RLU power supply voltage at ± 15 V is also monitored and shown in the last panel of figure 8.2. Although the conversion factor from ADC counts to a voltage is unknown to the author, relative changes can be observed: a drop of 1 count at transitions into the diagnostic mode. However, that change also occurs reliably at every mode transition from science into diagnostic mode and does not correlate with the plateau changes in the RLU laser power telemetry.

All of this leads to the conclusion that the value changes between two levels in the RLU telemetry do not affect the laser power but are artifacts of the RLU electronics, although the exact cause can not be named.

8.2. RLU Frequency Variations at High Frequencies

A low-pass filter is usually applied to suppress the high-frequency variations while deriving the laser frequency model from telemetry, that relates the telemetry values of the frequency servos to the absolute laser frequency, in chapter 5. In contrast, this section focuses on the high-frequency variability of the RLU laser frequency instead. It is, however, more of scientific and engineering interest, as the laser frequency is either stabilized to the reference cavity resonance (in reference role) or frequency-offset phase-locked to the incoming beam (in transponder role), cf. section 3.1. After that stabilization, the laser frequency fluctuations of the outgoing beam of the reference unit are suppressed to a level well below $30 \text{ Hz}/\sqrt{\text{Hz}} \cdot \text{NSF}(f)$. However, the control signals of the frequency stabilization servos, a thermal element and a PZT, represent

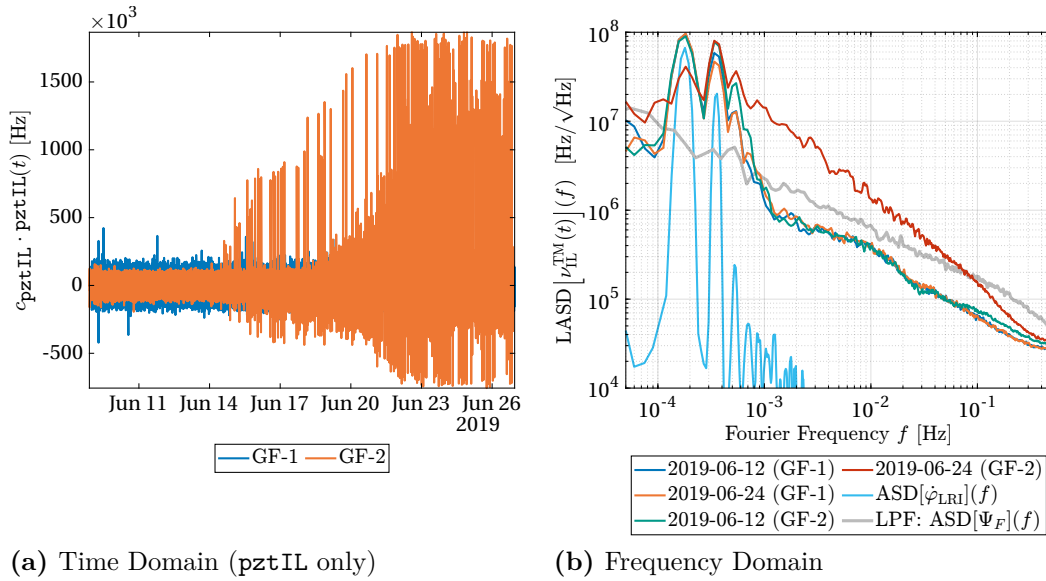


Figure 8.3. RLU free-running laser frequency noise estimate based on the telemetry model ν_{IL}^{TM} . **(a)** time-domain representation of the PZT actuator voltage times the coupling factor (GF-1 in blue, GF-2 in orange). The signal magnitude on GF-2 (transponder role) starts to increase on 2019-Jun-14. **(b)** ASDs of the in-loop contributors of the laser frequency ν_{IL}^{TM} . The GF-2 signal of 2019-Jun-22 (red) shows higher signal magnitudes above 0.5 mHz up to 20 mHz than on 2019-Oct-03 (green), before the increase. The spectra for GF-1 on both dates (blue, orange) do not differ. Equivalent Doppler frequency variations, calculated from the LRI ranging signal, are shown in light blue. A LISA Pathfinder frequency noise estimate Ψ_F of a free-running RLU is shown in gray. The data was kindly provided by Sarah Paczkowski.

the frequency variations needed to keep the RLU at that stable frequency. Therefore, the actuator signals directly represent the frequency difference between the cavities' resonance and the RLU free-running laser frequency on the reference spacecraft. The free-running frequency noise of the RLUs is orders of magnitude larger than the cavity frequency noise, and hence, the actuator signals solely represent the free-running RLU frequency noise. On the transponder spacecraft, the laser is locked to the incoming, cavity-stabilized beam from the reference spacecraft, which underwent a Doppler frequency shift due to the relative spacecraft motion, i. e., it contains the ranging signal of interest shown as ASD in figure 3.10.

This investigation started with the observation that the maximal magnitude of the `pztIL` control signal varies in time, exemplarily shown in figure 8.3a for June 2019. The frequency variations are computed from the PZT and thermal actuator signals as explained in section 3.1.3, using the refined coupling factors from table 5.3. The graph shows the sole effect of the `pztIL` signal, as it contains the high-frequency variations of interest; the blue trace is for GF-1, which also held the reference role, while the orange trace is for GF-2. The data spread of the signal on GF-2 suddenly increased from roughly ± 100 kHz to a range between -750 kHz to 1750 kHz, although only nominal operations were performed on the SC at that time. Figure 8.3b shows ASDs of the telemetry-based laser frequency $\nu^{TM}(t)$, cf. equation (3.11), or more precisely, the

estimate of RLU free-running frequency variations from the in-loop actuator, i. e.,

$$\nu_{\text{IL}}^{\text{TM}} = c_{\text{pztIL}} \cdot \text{pztIL}(t) + c_{\text{thermIL}} \cdot \text{thermIL}(t) . \quad (8.1)$$

The spectra for the full days of 2019-Jun-12 (blue and green; before the increase) and 2019-Jun-22 (orange and red; after the increase) are shown. The free-running RLU noise in this assessment is at a level of $10^6 \text{ Hz}/\sqrt{\text{Hz}}$ at 1 mHz and $10^4 \text{ Hz}/\sqrt{\text{Hz}}$ at 0.5 Hz. An ASD of the phase rate $\dot{\varphi}_{\text{LRI}}$, that represents the frequency variations due to the Doppler shifts, is shown in light blue for reference. It is clearly visible that the ranging phase signal is only recoverable due to the cavity lock since the free-running RLU laser frequency variations are orders of magnitude larger than the signal of interest for Fourier frequencies above 1 mHz. Therefore, the laser frequency actuator signals dominantly represent the free-running local oscillator noise, and the ranging signal of interest can be regarded as negligibly small.

A similar assessment of the free-running laser frequency noise has been performed for the RLU flown aboard LISA Pathfinder (Paczkowski, 2021), which is assumed to be very similar to the RLUs implemented within the LRI. On that mission, a dedicated interferometer measures the laser frequency noise. The results for the free-running laser frequency noise estimate Ψ_F of the LISA Pathfinder RLU by Paczkowski (2021) are shown as gray trace in figure 8.3b. They are approximately a factor of two higher than the LRI RLU laser frequency variations at high Fourier frequencies.

The amplitudes in the spectral densities for GF-2 on the two different days differ significantly above 1 mHz. This observation is used in the following, where equivalent rms frequency fluctuations $\delta\nu_{\text{rms}}$ in the frequency band between Fourier frequencies of $1 \text{ mHz} < f < f_s/2 \approx 500 \text{ mHz}$ are used as a proxy for the high-frequency free-running laser frequency noise. This newly introduced observable is computed as

$$\delta\nu_{\text{rms}}(t') = \left(\int_{1 \text{ mHz}}^{500 \text{ mHz}} \text{PSD} \left[\nu_{\text{IL}}^{\text{TM}}(t) \right] (f) df \right)^{1/2} , \quad (8.2)$$

where each PSD is computed over data chunks of six hours. For each evaluation time t' , t is a vector reaching from t' to $t' + 6 \text{ h}$. Consecutive segments overlap by 50%, hence the resulting $\delta\nu_{\text{rms}}(t')$ time series is sampled once per three hours. Only chunks with 100% data availability are used in this analysis, performed over the full mission lifetime. The resulting time series of equivalent RLU frequency fluctuations is shown in figure 8.4, blue for GF-1 and orange for GF-2.

The average free-running laser frequency noise, exemplarily computed for the year 2021, is at a level of 73 kHz rms for GF-1 and 78 kHz rms for GF-2. The standard deviation around the average, computed for the same period, is 5 kHz rms for both RLUs. The noise level of the RLU in reference mode is slightly below the transponder laser, i. e., the blue trace is slightly lower whenever GF-1 is in reference role (green background) and vice versa for with GF-2 in reference role (yellow background). This small difference between GF-1 and GF-2 can be attributed to multiple effects: Firstly, the transponder spacecraft copies the cavity-locked signal from the reference and additionally adds the frequency noise of the local phase lock, which is uncorrelated. Secondly, the differences between the roles can also originate from imperfect coupling factors c_{pztIL} , c_{thermIL} and the different cross-over frequency between the two actuators, cf. figure 3.4. The effect of the Doppler shift in the transponder frequency estimate is

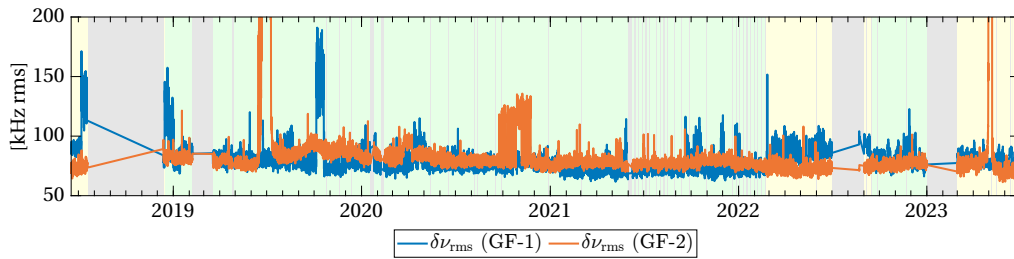


Figure 8.4. Equivalent rms RLU frequency fluctuations for GF-1 (blue) and GF-2 (orange). Some periods show elevated plateaus in the noise estimate. As before, the background coloring denotes which SC is in the reference role.

again much smaller in this frequency band, below 1 kHz rms. However, the 5 kHz rms difference between GF-1 and GF-2, that corresponds to 7 %, is marginal.

Three regions with increased RLU frequency noise can be identified per spacecraft: July 2018, December 2018, and October 2019 on GF-1 and June/July 2019, October/November 2020, and May 2023 on GF-2. While the non-nominal plateaus on GF-1 all have similar values at about 125 kHz rms to 150 kHz rms, the noise on GF-2 increases to almost 1 MHz rms in July 2019 (which led to the discovery, cf. figure 8.3a) and about 1.5 MHz rms in May 2023. Note that such high values are not shown on the axis of figure 8.4, but the increase in the orange curve is visible.

The free-running laser frequency noise of the LISA Pathfinder RLU is approximately a factor of two higher, at about 145 kHz rms in the same frequency band between 1 mHz to 500 mHz. This value was calculated from the trace shown in figure 8.3b. Just as the RLUs within LRI, it features short periods with increased free-running laser frequency noise that could not be explained so far (Paczkowski, 2021).

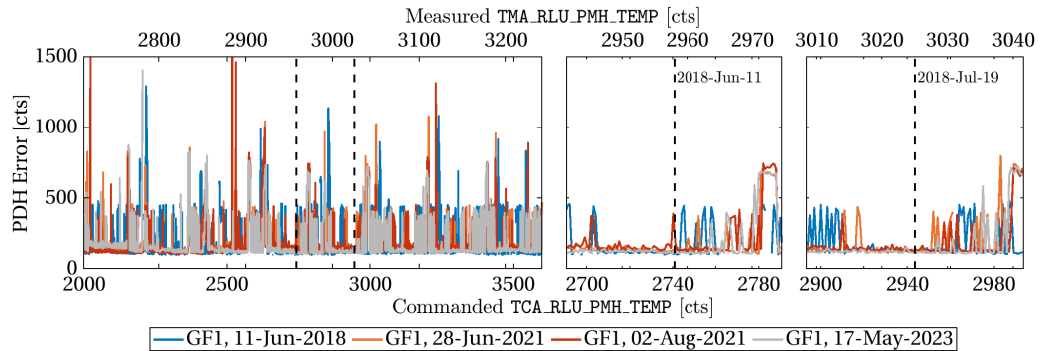
Generally, the intrinsic free-running laser frequency noise can vary for many reasons, such as temperature variations and non-ideal setpoints of the PMH temperature. This particular effect is investigated in the following section. However, in nominal operations, the free-running laser frequency noise is highly suppressed by the active laser stabilization on both SC and does not affect the ranging measurement’s noise.

8.3. Pump Module Head (PMH) Frequency Noise

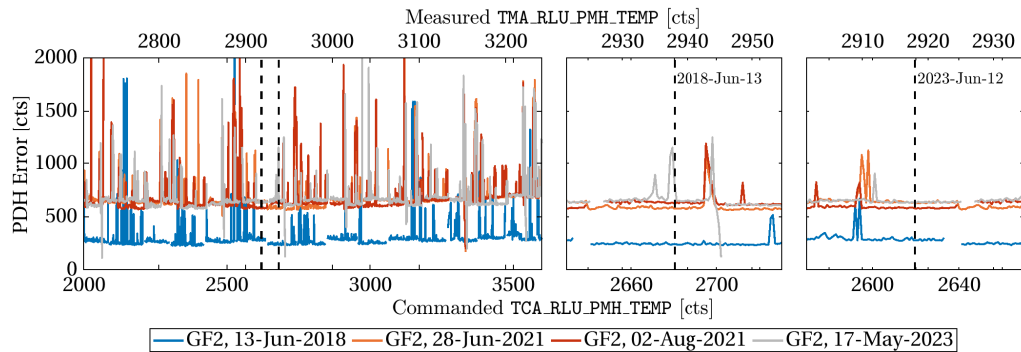
The stability of the RLU optical frequency strongly depends on the pump light going into the NPRO crystal. Typically, that pump light has a wavelength of approximately 808 nm, and it is provided by one of the two cold-redundant LDBs within the PMH. The PMH further includes heater modules and a thermistor.

Previous studies have shown that the NPRO laser frequency noise of an NPRO laser can be reduced by active stabilization of the pump current, i. e., the pump diode’s optical output power (Willke et al., 2000). It turns out that the temperature of the pump diode has a similar effect in the RLU, likely through RIN caused by temperature-driven conversion efficiency variations of the semiconductor pump diode. The frequency stability of the RLU can thus be improved by choosing a PMH temperature setpoint with lower RIN. As the temperature dependency of the LDBs RIN may vary over time, e. g., from aging processes of the pump diodes, it is helpful to review the choice of the temperature setpoint regularly.

8.3. PUMP MODULE HEAD (PMH) FREQUENCY NOISE



(a) Scans on GF-1.



(b) Scans on GF-2.

Figure 8.5. PMH scan results. The temperature of the RLU PMH is linearly increased. Lower values of the error signal indicate less laser frequency noise. Loss of the PDH lock is represented by gaps. The bottom axes denote the telecommanded RLU_PMH_TEMP, i. e., the heater voltage, whereas the top axes denotes the measured telemetry of an attached thermistor. The small panels show the surroundings of the commanded PMH setpoints (black, dashed, vertical lines) before and after the changes, respectively.

A specialized scan was executed several times on both SC to assess that high-frequency laser frequency noise. During this scan, the PMH temperature setpoint, denoted as TCA_RLU_PMH_TEMP and representing the voltage at the heating module, is slowly increased from 2000 counts to 3600 counts, which approximately translates to a change from 40 °C to 50 °C, although the absolute temperature is not of importance here. The RLU remains locked to the optical reference cavity during the scan. Note that the PMH temperature in principal only influences the LDB and should not alter the RLU output frequency, which is kept at the cavities' resonance. Several telemetry channels are collected while increasing the PMH temperature. One of them is the PDH error signal, or more precisely, the maximum value of the PDH error signal over the sampling rate during the PMH scans. The PDH error signal is a proxy for the noise in the PDH lock and thus of the laser frequency noise. Slow variations of the RLU are counteracted by the PDH lock and therefore suppressed. In contrast, laser frequency variations above the PDH lock's unity gain frequency appear in the PDH error signal. The other data channels comprise the RLU_PMH_CURRENT, RLU_LASER_POWER, the RLU thermal reference point temperature, and the power of light reflected by the cavity.

Figure 8.5 shows the PDH error signal as a function of the PMH temperature setpoint

TCA_RLU_PMH_TEMP (bottom axes) in the leftmost panel. The measured PMH temperature TMA_RLU_PMH_TEMP is also given for reference on the top axes. They differ, as the former is a measure of the voltage applied to the heater circuit, whereas the latter describes the resistance of an attached thermistor. Four scans have been taken on both SC: The first during the commissioning on 2018-Jun-11 and 2018-Jun-13, respectively (blue). Two more scans have been performed within a short time frame, between June and August 2021 (orange and red). The last one was completed on 2023-May-17 (gray). All scans show a distinct frequency noise floor, some peaks, and gaps. The goal of the scans is to find a broad region with a low PDH error signal in post-processing. The gaps originate from losing the PDH lock, and the peaks indicate a higher frequency noise.

On GF-1, the number of peaks is higher, with smaller quiet regions in between, which have a noise floor at roughly 200 counts. On GF-2, the noise floor increased significantly from approx. 300 counts to 600 counts after the first PMH scan, but there are fewer peaks and broader noise-free regions.

The right panels zoom in on the regions surrounding the dashed black lines, which indicate the commanded PMH temperature setpoints during nominal operation. On GF-1, it was set to roughly 2740 counts during the instruments' commissioning in June 2018, shown in the center panel in the top row of figure 8.5a. A noisy region is close to that temperature setting, as apparent from the blue peak at the vertical line labeled "2018-Jun-11". The setpoint was thus increased to approximately 2945 counts, where a broader noise-free region was at that time. The PDH error signal has changed by now, and the frequency noise again increased close to that new setpoint (cf. orange and gray in the upper right panel).

The set point at launch on GF-2 was at approximately 2665 counts, as shown in figure 8.5b in the overview and the center panel. That setpoint was at a noise-free region even after the overall noise increase between 2018 and 2021 (cf. blue curve vs. the others). In 2023, higher ranging noise was observed, and therefore, new PMH scans were recorded (gray). It turned out that two peaks appeared close to the PMH setpoint on GF-2 (black, dashed line in the center panel), and it was decided to lower the setting to 2615 counts. As apparent from the lower-right panel, the curves of all four scans are flat in that region. The phase noise in the ranging measurement lowered again as a consequence.

Monitoring the data in the future and eventually adjusting the setpoint again is recommended to avoid an operational state with high RLU laser frequency noise, which probably led to the effect described in the previous section 8.2.

8.4. Summary

A good understanding of the light source is essential in optical interferometric measurements. Therefore, this section covered several effects connected to the RLUs, apart from the determination of the absolute laser frequency of chapter 5.

At first, the telemetry provided by the RLU was investigated for the full mission period in section 8.1. The optical power and current draw do not show signs of degradation on both SC. However, there are small steps between two distinct modes in the measurements, which are revealed by low-pass filtering of the data streams. The toggling between the modes is mostly triggered by mode transitions into or out of the

science mode, but they do not occur at every mode transition. Several possible reasons for these steps have been investigated, but no correlation to other data streams was found, and thus, no explanation for that bi-modal behavior. For example, variations of the DC optical power levels at the QPD segments can be attributed to beam walk by analyzing the DPS signals and the FSM positions and not to optical power variations.

Section 8.2 concerned the observation that the frequency actuator signal `pztIL` sometimes shows higher variability, first discovered in June 2019. During these periods, the spectral density amplitudes of the telemetry-based laser frequency estimate are elevated for Fourier frequencies above 1 mHz, compared to the usual level. The integral over the amplitude spectral density from 1 mHz to 500 mHz is used as a proxy to describe the high-frequency laser frequency noise. The typical laser frequency noise level from this assessment is at about 75 kHz rms for both RLUs. When the non-nominal PZT signal was found in the beginning, the noise level was 1 MHz rms, much higher than usual. The changes between the two noise levels are instantaneous. Such a bi-modal laser frequency noise behavior was also observed for the RLU integrated on LISA Pathfinder, which has similar characteristics.

It should be noted that the frequency noise described here is canceled by the PDH lock to the cavity to below $30 \text{ Hz}/\sqrt{\text{Hz}}$ and typically does not disturb the ranging measurements. The effects observed are estimates from the actuator signals to keep the RLU locked to the cavity, or in other words, the negative free-running laser frequency noise.

This chapter's last section 8.3 discussed the PMH temperature setpoint. That temperature setpoint influences the relative intensity noise of the RLU's pump diode and, thus, the frequency noise at the optical output. An optimal setpoint, by means of low laser frequency noise, can be determined using so-called PMH scans, in which the PMH temperature is scanned over a large range. The maximum error signal of the cavity lock over a fixed period is used as a proxy for the laser frequency noise.

Both SC executed four such scans, one during the commissioning of the LRI instrument, two in 2021, and one in 2023. It was found that the average frequency noise level on GF-2 increased by a factor of two between 2018 and 2021, while the noise floor on GF-1 remained constant. Furthermore, the PMH temperature setpoint was changed once on both spacecraft when the scan indicated that the current temperature setting was close to a noisy region. Continuous monitoring is recommended as the temperature dependency of the pump diode's laser frequency noise varies over time.

Disturbances from Radiation: Single Event Upsets

9

“Outer space, once a region of spirited international competition, is also a region of international cooperation.”

— JAMES ALFRED VAN ALLEN —
American Physicist

Parts of this section have already been published in [Misfeldt et al. \(2023a\)](#), but were now revised, updated, and extended for this thesis. Most importantly, the numerical autocorrelation functions in the theoretical framework were replaced with the analytical ones derived in section 3.3. Further, newly found events were added.

9.1. Radiation Environment in a Low-Earth Orbit

The LRI onboard the GRACE-FO satellites is naturally exposed to the charged particles from ionizing radiation originating solar or cosmic radiation. Some particles are trapped within the Earth’s magnetic field. As GRACE-FO orbits Earth within an altitude of approximately 500 km, the trapped particles in the Van Allen belts are most critical ([Van Allen, 1959](#)). These particle belts around the Earth were first discovered in 1958 using the NASA mission called Explorer 1. They extend 1000 km to 60 000 km above Earth’s surface ([Bakhtiyarov, 2015](#)), but these numbers vary depending on the solar activity. Their shape is supported by Earth’s magnetic field, which redirects the incoming high-speed ions from the sun and cosmic rays into these belts that encompass the Earth, effectively protecting hazardous radiation at Earth’s surface and enabling life as we know it. The belts are categorized into outer and inner belts. The former mainly contains energetic electrons, whereas protons and electrons dominate the latter. The particle energy in the inner belt can get larger than 100 MeV, and the belt can expand to about 200 km above Earth’s surface during strong solar activity ([Bakhtiyarov, 2015](#)). There is an offset between Earth’s geometric center and the belts’ center, causing the so-called south-atlantic anomaly (SAA), where the inner belt approaches Earth’s surface more closely than on average ([Daly, 1994](#)). Further, the interplay between the energetic particles trapped in the belts and the atmosphere causes the aurora at the poles ([Alfvén, 1958](#)).

As modern electronics are getting smaller and smaller, e. g., down to the size of a few atoms per magnetic data storage unit in laboratory experiments ([Loth et al., 2012](#)), interactions with single particles already have a localized loading effect, known as single event effects (SEE) ([Medina, 2015](#)). On the one hand, SEE can be hard errors, meaning that an electric device, like an integrated circuit, is permanently damaged. On the other hand, non-destructive SEE are called soft errors. They can be further distinguished as SEU (e. g. a memory cell changing its information, also known as bit flip), single event functional interrupt (SEFI) (e. g. a state machine jumping to an unexpected state), and single event transient (SET) (e. g. a transient current in an integrated circuit, that may alter the output of DC/DC converters or ADCs). Those effects are not only

generated by the direct impact of charged particles onto the electronic, as it is also possible that heavier nuclei are partially converted into secondary neutrons by collision with the spacecraft structure and that these numerous secondary neutrons cause SEEs (Maurer et al., 2008). Also, as the fabrication size of memory cells decreases, the sensitive circuit nodes are closer together, and their tolerable charge collected within the region of an ion strike gets smaller. Both effects can result in multiple upsets from a single ion (Maurer et al., 2008).

In the context of GRACE and GRACE-FO, SEEs are known to have caused frequent reboots (Webb et al., 2019b), GPS errors and, in the GRACE mission, a hard error SEE possibly caused a failure of one of the instrument control units (ICUs) through a broken DC/DC converter (Pritchard et al., 2002). This section investigates possible SEU from bitflips within the ranging phase of the LRI.

The LRI and, in particular, the LRP were built following spaceflight-typical risk assessment standards, like the guidelines of the European Cooperation for Space Standardization (ECSS, 2012). Regarding the risk of radiation-induced SEUs, the two FIR filters A and B are identified as the most probable source for radiation-induced SEUs, cf. figure 3.8 in section 3.1.7. These two filters are likely implemented within the processor of the LRP (Ware et al., 2006). The FIR filter within the FPGA is excluded from this analysis because the FPGA is expected to be less susceptible to radiation than the RAM of the processor (Samwel et al., 2019). Further, current space-qualified FPGAs even feature error detection and correction (EDAC) implemented in hardware, see e. g., the RTG4 FPGA series (Microchip Technology Inc., 2022).

9.2. Recent and Future Solar Activity

The sun and its activity are significant in Earth’s radiation environment. The solar activity undergoes a natural 11 year cycle, which was discovered in the 19th century already (Schwabe et al., 1844). The solar activity is measured by optically observing and counting the number of sunspots. The measurements are taken on multiple stations on Earth daily, and figure 9.1 shows these measurements and a monthly mean since 1975 (green and black). Further, the prediction and its uncertainty (blue) represent the expected cycle 25 at the beginning of 2020. This prediction is a consensus estimate from several studies. However, the measured solar activity does not follow this prediction. Recent investigations by McIntosh et al. (2023) provide an updated model that foresees an earlier and higher maximum activity in 2024.

The GRACE-FO satellites were launched in the minimum between cycles 24 and 25, and the solar activity started to increase in early 2020. Not only the radiation environment is influenced by solar activity, but also the air drag in low Earth orbit (LEO), as the atmosphere expands due to higher temperatures (NOAA SWPC, 2023). Given the higher solar activity, an increase in the number of SEUs detected within GRACE-FO can be expected, particularly in the LRI.

9.3. Simulation of SEUs in the LRI Phase Data

The phase measurement and subsequent decimation within the LRP have been introduced in section 3.1.7. In this section, the output of the 2-step FIR filtering and

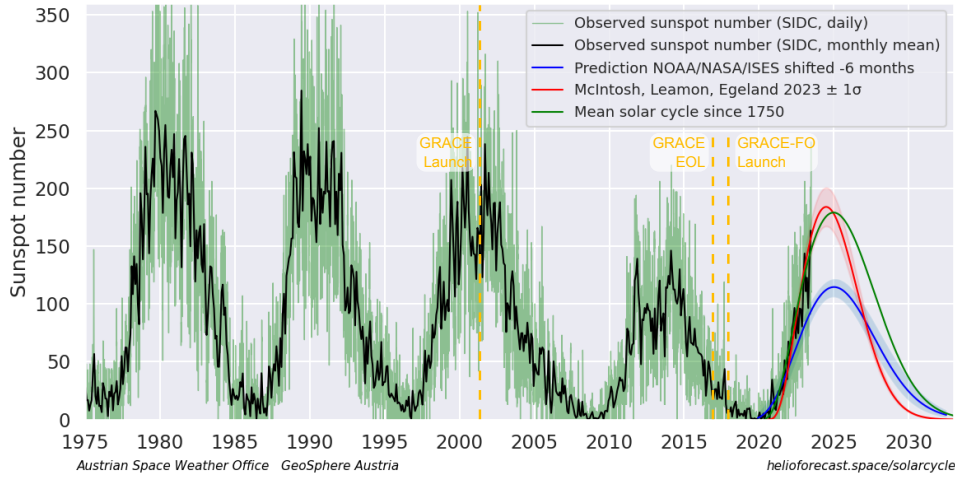


Figure 9.1. Daily and monthly sunspot numbers since 1975 (green and black) and predictions: Consensus prediction (blue) and updated model (red, McIntosh et al. (2023)). The vertical dashed lines roughly denote the dates of the GRACE launch and deorbiting, and the GRACE launch and the GRACE-FO launch. The smooth green curve shows the mean solar cycle since 1750. Image (modified) courtesy of the Australian Space Weather Office (2023).

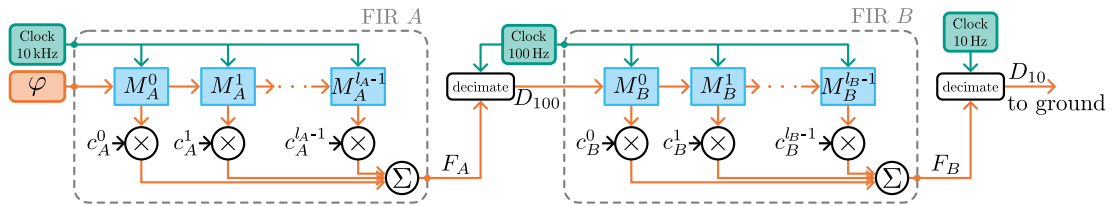


Figure 9.2. Block diagram of the two FIR filter stages as implemented for the simulation. Green denotes clock signals, orange denotes the phase data, and blue denotes memory cells. The FIR filter coefficients $c_{A/B}^j$ are multiplied with the data points in the registers $M_{A/B}^j$, and the filtered result $F_{A/B}$ is the sum of all multiplications. The dashed gray boxes implement equation (9.1).

decimation chain from 10 kHz down to 10 Hz is computed in a time-domain simulation, according to the block diagram in figure 9.2. The filter response at a given discrete time step t_i of the phase $\varphi(t)$ of either filter A or B is given by the sum over all products of the filter coefficients c^j with the value contained in the j -th register M^j , i. e.,

$$F_{A/B}[\varphi(t_i)] = \sum_{j=0}^{l-1} c_{A/B}^j \cdot \text{val}(M_{A/B}^j) = \sum_{j=0}^{l-1} c_{A/B}^j \cdot \varphi(t_{i-j}) \quad (9.1)$$

In this equation, l is the length of the filter or the number of the filter coefficients, l_A or l_B . The value of the j -th register M^j is the input data φ at j time steps before the measurement epoch t_i , i. e., $\text{val}(M_{A/B}^j) = \varphi(t_{i-j})$.

The simulation is performed with a trivial filter input of $\varphi \equiv 0$, i. e., without any ranging signal, to obtain just the disturbance from a bitflip. This disturbance would add linearly to the regularly filtered ranging signal due to the linearity of FIR filters.

Figure 9.2 depicts the simulated computation chain in a block diagram. The input data at 10 kHz is denoted as φ . It passes the first filter A with the outcome F_A , which is decimated by a factor of 100 to form D_{100} . That decimated signal is fed through filter B , whose outcome F_B is decimated by a factor of ten. The final result of the simulation is D_{10} , which represents the phase data transmitted to the ground.

Upon an artificial bitflip, the j -th register of either filter A or B is set from 0 to 1 during the execution of the simulation. The inverse bitflip from 1 to 0 can be obtained by inverting the simulation results, i. e., the D_{10} time series. An SEU in filter A will propagate through the subsequent filter and decimation stages. Manipulation of M_A^0 in filter A is equivalent to setting a single data point of the input phase φ to one. However, manipulation of higher registers, meaning a change of a register during filter execution, can not be replaced by an equivalent input data φ .

The free parameters of a simulation that computes the phases upon a bitflip are:

- The filter (A or B) affected by the SEU
- The occurrence time of the SEU, expressed as a sample or tick number $k_{A/B}$ at the filter's clock rate. Due to the fixed decimation rates from F_A or F_B to the 10 Hz output data rate, the filter output repeats after a fixed number of subsample time stamps, that corresponds to the decimation rates of each filter, i. e., $1000 = 100 \cdot 10$ or 10 for filters A and B , respectively. Thus, if the SEU occurs in filter A , $k_A \in [0, 1000) \subset \mathbb{N}_0$ is used and $k_B \in [0, 10) \subset \mathbb{N}_0$ for filter B .
- The affected register number $j_A \in [0, l_A) \subset \mathbb{N}_0$ or $j_B \in [0, l_B) \subset \mathbb{N}_0$. This number is usually provided in fractions of the full filter length $l_{A/B}$ within this thesis. The numerical value for the total number of registers $l_{A/B}$ and other details like the exact filter coefficients can not be disclosed here.
- The bit number $b \in [0, 64) \subset \mathbb{N}_0$ of the bitflip within the presumed 64-bit register (i. e., the 2^b magnitude of the flipped bit). For simulation, $b = 0$ is usually used. This parameter is a linear scale factor, and it is estimated later through a least squares algorithm, where the simulation result is rescaled to match the observations.

An exemplary simulation result is shown in figure 9.3, for an SEU in the first register $j_A = 0$ of filter A at time $k_A = 250$. The simulation of an SEU in the first register, with $j_A = 0$ and indicated in gray, effectively results in the impulse response of the filter F_A (orange, left panel). The green curve is the first decimation D_{100} , fed into filter B , whose output F_B is shown in red in the right panel. It appears delayed by about 0.7s due to the filters' group delay. The final output D_{10} is shown in cyan and represents the phase as it would be downlinked from the spacecraft. A different injection sample $k_A \neq 250$ would cause another delay of F_A w. r. t. the finite, decimated sample points, and thus a slightly different shape and amplitude in D_{100} and all subsequent data streams. There are 1000 unique patterns in the 10 Hz output data stream for a possible SEU in filter A and ten patterns for filter B , according to the sampling rate decimation factors. The ten patterns of filter B , which ultimately dominate the shape of the output D_{10} , are approximately a subset of the 1000 patterns of filter A . Note that figures 9.3 and 9.4 do not show the exact filter coefficients employed in-flight, as they can not be disclosed. However, the following analysis of LRI flight data uses the actual coefficients.

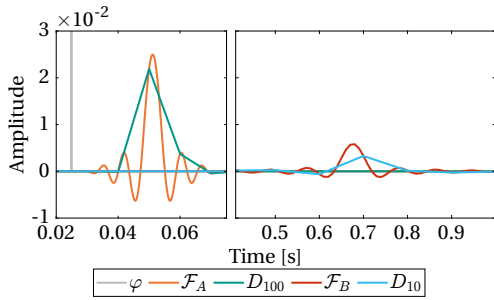


Figure 9.3. Simulated data throughout the filtering chain for an SEU in filter A with subsample time $k_A = 250$ and register number $M_A = 0$ and a magnitude of $b = 0$. The output of the first filter F_A (orange) is sampled at 10 kHz, the first decimation D_{100} (green) and the output of the second filter F_B (red) at 100 Hz, and the final output D_{10} (cyan) is sampled at 10 Hz. Left and right time-axes are in units of seconds, but note the different scales. The delay arises from the filters' phase delay. This example shows artificial filter coefficients, as the exact coefficients employed in flight can unfortunately not be disclosed here.

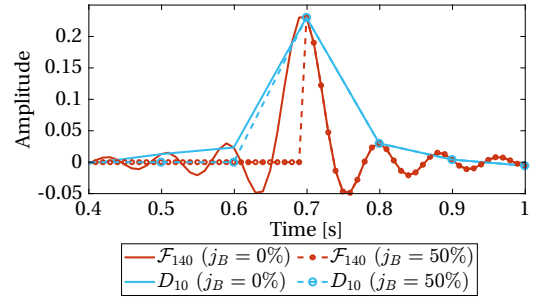


Figure 9.4. Simulated data showing the effect of an SEU in a higher register number of filter B and with $k_B = 8$. The solid lines depict the response of an impulse traveling through the full filter (i. e., for $j_B = 0$), while the dashed lines show the response for an SEU that affects the register $j_B = 50\%$ in the middle of the filter. Color coding as in figure 9.3. Note that the magnitude is larger than in figure 9.3, because this SEU was simulated in the second instead of the first FIR filter. Also, the traces appear to have shifted in time because of the differing subsample time k_B . F_A and D_{100} are zero and thus not shown here.

Given an SEU in filter A , the data D_{100} after that filter only has a few non-zero samples, and a single peak can approximately describe that. Therefore, the result after filter B approximates the filter's impulse response with minor deviations, as seen in figure 9.3. However, the results may vary if the SEU occurs within filter B . Two simulations of an SEU in filter B are shown in figure 9.4, one at $j_B = 0$ (solid lines) and one at $j_B = 50\%$ (dash-dotted). In the latter case, only parts of the impulse response are represented in the output, which looks cropped. The cropping effect in D_{10} does not occur for filter A due to the second filtering.

Two LUTs were created from the simulations for events either in filter A or B , where the injection sample number $k_{A/B}$ and the affected register $j_{A/B}$ of the SEU occurrence were varied over the parameter space listed above. A 15 sample ≈ 1.5 s segment of the output D_{10} after the second decimation is stored in the 3D-LUTs, which have the dimensions $1000 \times l_A \times 15$ and $10 \times l_B \times 15$, respectively. The first dimension represents the injection sample number $k_{A/B}$, and the second represents the register number $j_{A/B}$. The third dimension contains the simulation result D_{10} . The individual rows of the LUTs are denoted as $\text{LUT}_{A/B}^{k,j}$, where the subscript A/B is usually omitted in the following when both filters are meant.

9.4. Detection of SEUs in the LRI Phase Data

The SEU detection algorithm is part of the so-called `LriToolbox`, an in-house collection of MATLAB scripts at the AEI. The toolbox automatically processes and analyzes

LRI data in near-realtime and has been part of the author's master's project (Misfeldt, 2019). It features an extensive phase jump removal algorithm, which was necessary due to laser frequency noise induced by micro shocks caused by attitude control thruster activation (Abich et al., 2019). This algorithm was now extended to also include SEU detection and removal. In the first step of the existing implementation, all single-channel phase data of both SC are searched for outliers by detecting peaks larger than ± 30 mHz on the detrended phase rate, or peaks larger than $2 \cdot 10^{-4}$ cycles/s on the first derivative of the DWS combinations (cf. section 2.3.3). All these events are marked as phase disturbances before the second step's modeling and subtraction are performed. Other than actual phase jump events in the averaged ranging phase, SEUs only occur in a single channel, making them easily distinguishable. Further, an SEU produces a short-lived peak in the phase, whereas phase jumps have persistent steps caused by a non-zero integral of fast laser frequency variations at a finite sampling rate, cf. Misfeldt (2019). Short segments of $N \leq 30$ samples are extracted from the measured phase data stream once an SEU candidate is identified in a single channel and the single-channel phase combination $\kappa(t)$ as introduced in section 3.3.3 is computed.

The SEU model can be expressed through

$$\eta_i^{k,j}(a) = \eta_i^{k,j}(a, t_i) = a \cdot \text{LUT}^{k,j}(t_i) , \quad (9.2)$$

which essentially is one entry of the LUT scaled by an amplitude $a = 2^b$. Further, the residuals are defined as

$$\begin{aligned} r_i^{k,j}(\boldsymbol{\vartheta}) &= r \left((a, c_2, c_1, c_0)^\top, t_i \right) \\ &= \kappa_i - \eta_i^{k,j}(a) - c_2 \cdot t_i^2 - c_1 \cdot t_i - c_0 , \end{aligned} \quad (9.3)$$

where a second-order polynomial is subtracted to remove residual ranging signal or similar effects. Equation (9.3) defines the regression coefficients $\boldsymbol{\vartheta} = (a, c_2, c_1, c_0)^\top$.

For modeling the measured SEU event in the extracted phase combination κ , the best-fitting template of the LUT entries is determined with the framework of maximum likelihood estimation introduced in section 3.3.1. In this case, the residuals are defined by equation (9.3). As they are dependent on the parameters k and j , the minimum negative log-likelihood $\ell^{k,j}(\kappa | \hat{\boldsymbol{\vartheta}})$ and the corresponding optimal parameter estimates $\hat{\boldsymbol{\vartheta}}$ are estimated for all values of k and j . The best estimate for the SEU model is determined by finding the minimum of $\ell^{k,j}(\kappa | \hat{\boldsymbol{\vartheta}})$ in the two-dimensional $k \times j$ -sized grid. The fitting of the measured data κ to the templates η is done individually for both LUTs ($\text{LUT}_A^{k,j}$ and $\text{LUT}_B^{k,j}$) and the minimum values of the log-likelihood over the LUTs is identified to retrieve the most likely parameter set.

The amplitude, i. e., the significance or bit number of the flipped bit, and the flip direction ($0 \rightarrow 1$ if positive, or $1 \rightarrow 0$ if negative) can directly be obtained from the parameter a of the fit. The bit number b is given by

$$b = \log_2 \left(10 \cdot 2^{24} \cdot a \right) , \quad (9.4)$$

with $1/(10 \cdot 2^{24})$ being the least significant bit in units of phase cycles in the LRI phase measurement (Wen et al., 2019). Ideally, b yields an integer number that directly represents the affected bit; however, as stated in section 9.1, multiple bits can be affected at once and yield a fractional number.

9.5. Discussion of the SEU Events

The analyzed phase data spans from the beginning of the mission in June 2018 until the end of June 2023. Over that period, 32 SEU events were identified, whose estimated parameters are shown in table 9.1. Sixteen events were recorded on each spacecraft, GF-1 and GF-2. As the reference and transponder role is interchangeable, 19 events were recorded on the transponder unit and 13 on the reference unit. The four phase channels are almost uniformly affected (A: 8 events, B: 6, C: 9, D: 9), and filter A shows more events than filter B (22 vs. 10), which is expected, because filter A has more registers, $l_A \approx 3.6 \cdot l_B$, i. e., features a physically larger area in the electronics that can be hit by radiation. With a total time in science mode of the LRI of 75% and 32 detected events, roughly ten events can be expected per year. It should be noted that not every SEU event can be identified, as their magnitude might be below the detection threshold, hidden within the phase readout noise (on the transponder unit) or the laser frequency noise (on the reference unit). The smallest event identified is event #16 with a magnitude of only $3 \cdot 10^{-3}$ cycles, where the 29th bit flipped up, while the 22nd bit flipped down in a register at $j_A \approx 16\% \cdot l_A$ of filter A . The phase readout noise is in the order of 10^{-5} cycles at high frequencies (cf. equation (3.12)). The higher noise levels of the reference unit from the cavities' coating Brownian noise, cf. section 3.3, might also explain the higher detection count on the transponder unit. Figure 9.5 shows the SEU of event #1 (measurement κ^D , blue) and the corresponding, best-fitting simulation in orange. The scale a of the signal w. r. t. the normalized LUT template is $6.87 \cdot 10^9$, which can be converted into the bit significance through equation (9.4), yielding the bit number $b = 60$, that was altered in register $j_B \approx 67\% \cdot l_B$ of filter B . As explained earlier, it produced a cropped filter impulse response for SEUs in higher registers of the second filter, cf. figure 9.4. Further, the residuals after subtraction of the model are shown (green, right y-axis) and are in the order of 10^{-5} cycles, as expected. On the other hand, events #3 and #9, which are marked gray in the table, have large residuals after subtraction of the model. The shape of the residuals, shown in figure 9.6, suggests that there is a second SEU event, which happened approximately one sample later in time, which can be caused by secondary neutrons, as described in section 9.1. From the linearity of the FIR filter, two timewise separated events are a linear superposition of the individual events. However, a simple second iteration of the described algorithm over the residuals does not succeed, as the first iteration does not distinguish the events but only minimizes the residuals. Hence, it removes parts of both events, and the shape fed into the second iteration does not match the templates of the LUTs anymore. A simultaneous fitting of two SEU events with arbitrary time-delay in between would be necessary to handle these events. However, this largely increases the number of possible templates and the computational cost, and a different approach than template-based estimation would be needed. However, figure 9.7 shows a simulation with two SEU events in filter A at $j_{A,1} = 30\%$ (pink) and $j_{A,2} = 40\%$ (gray), separated by only one sample k_A at a rate of 10 kHz, and with different magnitudes $a_1 = 1 \cdot 10^4$ cycles and $a_2 = -1 \cdot 10^5$ cycles. After the first iteration of the SEU removal algorithm, the residuals of this simulated dataset have a similar shape compared to the example of event #3 shown in figure 9.6, but ten times smaller residuals.

Some results, marked yellow and green in table 9.1, have bit numbers b with a non-integer part larger than the 95% confidence interval. These events are likely created

Table 9.1. SEU parameters as detected in the LRI phase data. Ch: affected phase channel; a : magnitude in the phase data; k : sub-sample timing of the event; j : affected register (normalized); b : bit number; Dir: denotes the direction of the bitflip (\uparrow : $0 \rightarrow 1$ or \downarrow : $1 \rightarrow 0$). CI: A 95% confidence interval for the bit number b . The colored bit position cells are encoded as follows: **Green:** Fractional number can be well explained with two bitflips simultaneously. **Yellow:** Fractional number can be explained with more than two bitflips simultaneously. **Gray:** High residuals observed (see main text). The horizontal lines separate different years.

#	Event Time [UTC]	SC	Role	Ch	FIR	a	k	j [%]	Dir	Bit No. b int+frac	95% CI Bit No. b	Residuals [cycles rms]
1	09-Jul-2018 18:25:01	GF-1	T	D	B	$6.87 \cdot 10^9$	9	66	\uparrow	$60+1.43 \cdot 10^{-12}$	$\pm 4.36 \cdot 10^{-12}$	$1.31 \cdot 10^{-5}$
2	20-Jan-2019 09:31:55	GF-1	R	D	A	$2.02 \cdot 10^2$	296	31	\uparrow	$35-1.97 \cdot 10^{-2}$	$\pm 1.54 \cdot 10^{-4}$	$8.44 \cdot 10^{-6}$
3	01-Apr-2019 16:36:27	GF-2	T	B	A	$4.19 \cdot 10^5$	352	0	\downarrow	$46-3.23 \cdot 10^{-4}$	$\pm 6.41 \cdot 10^{-4}$	$7.41 \cdot 10^{-2}$
4	18-Apr-2019 23:38:38	GF-2	T	C	A	$5.50 \cdot 10^{10}$	165	37	\uparrow	$63+9.31 \cdot 10^{-13}$	$\pm 2.16 \cdot 10^{-12}$	$2.53 \cdot 10^{-5}$
5	09-Sep-2019 00:07:28	GF-2	T	A	B	$6.80 \cdot 10^0$	4	0	\downarrow	$30+8.75 \cdot 10^{-2}$	$\pm 3.78 \cdot 10^{-5}$	$7.32 \cdot 10^{-6}$
6	13-Nov-2019 23:31:24	GF-1	R	D	A	$2.80 \cdot 10^7$	346	61	\downarrow	$52+6.17 \cdot 10^{-2}$	$\pm 2.36 \cdot 10^{-8}$	$9.88 \cdot 10^{-6}$
7	20-Nov-2019 03:09:38	GF-1	R	A	A	$6.71 \cdot 10^6$	309	49	\downarrow	$50+7.24 \cdot 10^{-8}$	$\pm 1.15 \cdot 10^{-7}$	$1.09 \cdot 10^{-5}$
8	25-Nov-2019 15:30:17	GF-1	R	C	B	$1.02 \cdot 10^2$	1	65	\downarrow	$34-8.11 \cdot 10^{-5}$	$\pm 3.70 \cdot 10^{-4}$	$8.31 \cdot 10^{-6}$
9	06-Jan-2020 06:13:57	GF-2	T	C	B	$1.44 \cdot 10^4$	4	56	\downarrow	$41+1.32 \cdot 10^{-1}$	$\pm 4.89 \cdot 10^{-3}$	$1.71 \cdot 10^{-1}$
10	01-Feb-2020 16:24:25	GF-2	T	A	A	$4.59 \cdot 10^1$	299	31	\uparrow	$33-1.59 \cdot 10^{-1}$	$\pm 4.51 \cdot 10^{-4}$	$5.54 \cdot 10^{-6}$
11	22-Mar-2020 00:51:54	GF-1	R	A	A	$1.84 \cdot 10^2$	797	51	\uparrow	$35-1.51 \cdot 10^{-1}$	$\pm 1.53 \cdot 10^{-2}$	$3.88 \cdot 10^{-5}$
12	01-May-2020 08:07:03	GF-1	R	C	A	$2.56 \cdot 10^1$	646	0	\downarrow	$32-9.11 \cdot 10^{-4}$	$\pm 1.45 \cdot 10^{-3}$	$1.03 \cdot 10^{-5}$
13	30-May-2020 09:31:44	GF-1	R	A	A	$3.44 \cdot 10^0$	394	32	\downarrow	$59+3.16 \cdot 10^{-12}$	$\pm 1.19 \cdot 10^{-11}$	$1.03 \cdot 10^{-5}$
14	17-Aug-2020 23:27:50	GF-1	R	A	B	$3.91 \cdot 10^3$	1	86	\downarrow	$39+2.56 \cdot 10^{-1}$	$\pm 2.59 \cdot 10^{-3}$	$8.22 \cdot 10^{-6}$
15	07-Sep-2020 01:47:43	GF-2	T	A	B	$7.94 \cdot 10^2$	6	0	\uparrow	$37-4.50 \cdot 10^{-2}$	$\pm 1.09 \cdot 10^{-6}$	$2.36 \cdot 10^{-5}$
16	12-Sep-2020 02:17:38	GF-1	R	B	A	$3.20 \cdot 10^0$	972	0	\uparrow	$29-1.55 \cdot 10^{-4}$	$\pm 9.27 \cdot 10^{-3}$	$8.49 \cdot 10^{-6}$
17	11-Dec-2020 18:06:47	GF-2	T	D	A	$3.36 \cdot 10^6$	903	30	\uparrow	$49-5.33 \cdot 10^{-9}$	$\pm 8.11 \cdot 10^{-9}$	$9.27 \cdot 10^{-6}$
18	19-Dec-2020 04:44:29	GF-2	T	B	A	$1.82 \cdot 10^8$	381	74	\downarrow	$55-2.38 \cdot 10^{-1}$	$\pm 8.62 \cdot 10^{-9}$	$7.51 \cdot 10^{-6}$
19	09-Mar-2021 11:18:40	GF-2	T	D	B	$1.34 \cdot 10^7$	3	35	\downarrow	$51+1.01 \cdot 10^{-11}$	$\pm 4.07 \cdot 10^{-11}$	$1.60 \cdot 10^{-5}$
20	10-Mar-2021 18:20:28	GF-2	T	D	A	$3.28 \cdot 10^3$	218	47	\downarrow	$39+8.09 \cdot 10^{-5}$	$\pm 8.29 \cdot 10^{-5}$	$1.22 \cdot 10^{-5}$
21	12-Mar-2021 23:20:11	GF-2	R	C	A	$8.19 \cdot 10^2$	434	24	\uparrow	$37-3.22 \cdot 10^{-4}$	$\pm 3.04 \cdot 10^{-5}$	$8.07 \cdot 10^{-6}$
22	25-Jul-2021 00:27:50	GF-2	T	B	B	$1.34 \cdot 10^7$	0	23	\uparrow	$51+8.54 \cdot 10^{-11}$	$\pm 6.52 \cdot 10^{-11}$	$2.57 \cdot 10^{-5}$
23	30-Sep-2021 19:46:16	GF-2	T	A	A	$1.05 \cdot 10^5$	57	0	\uparrow	$44+2.30 \cdot 10^{-9}$	$\pm 5.02 \cdot 10^{-7}$	$2.16 \cdot 10^{-5}$
24	16-Nov-2021 16:25:26	GF-2	T	C	A	$2.10 \cdot 10^5$	18	7	\downarrow	$45+1.75 \cdot 10^{-7}$	$\pm 3.52 \cdot 10^{-7}$	$2.23 \cdot 10^{-5}$
25	05-Dec-2021 04:06:04	GF-1	R	C	A	$1.60 \cdot 10^3$	454	60	\uparrow	$38-3.05 \cdot 10^{-2}$	$\pm 3.30 \cdot 10^{-4}$	$9.12 \cdot 10^{-6}$
26	27-Jan-2022 22:21:58	GF-1	R	B	B	$1.34 \cdot 10^7$	7	32	\downarrow	$51-1.63 \cdot 10^{-11}$	$\pm 1.92 \cdot 10^{-11}$	$6.98 \cdot 10^{-6}$
27	04-Jun-2022 15:21:35	GF-1	T	D	A	$5.50 \cdot 10^{10}$	721	46	\uparrow	$63-2.67 \cdot 10^{-12}$	$\pm 4.23 \cdot 10^{-12}$	$1.07 \cdot 10^{-5}$
28	15-Oct-2022 02:21:21	GF-2	T	D	A	$3.85 \cdot 10^6$	94	72	\downarrow	$49+1.99 \cdot 10^{-1}$	$\pm 1.80 \cdot 10^{-6}$	$1.29 \cdot 10^{-5}$
29	16-Oct-2022 15:39:01	GF-1	T	D	A	$8.64 \cdot 10^{10}$	688	73	\downarrow	$64-3.48 \cdot 10^{-1}$	$\pm 6.31 \cdot 10^{-11}$	$6.82 \cdot 10^{-6}$
30	07-Nov-2022 12:32:14	GF-1	R	C	B	$3.17 \cdot 10^0$	8	67	\downarrow	$29-1.46 \cdot 10^{-2}$	$\pm 1.18 \cdot 10^{-2}$	$1.56 \cdot 10^{-5}$
31	22-Nov-2022 22:27:28	GF-2	T	B	A	$5.50 \cdot 10^{10}$	542	2	\uparrow	$63+3.55 \cdot 10^{-13}$	$\pm 1.38 \cdot 10^{-12}$	$1.93 \cdot 10^{-5}$
32	04-Jun-2023 22:13:14	GF-1	T	C	A	$2.75 \cdot 10^{10}$	823	6	\downarrow	$62+1.92 \cdot 10^{-13}$	$\pm 9.75 \cdot 10^{-13}$	$7.96 \cdot 10^{-6}$

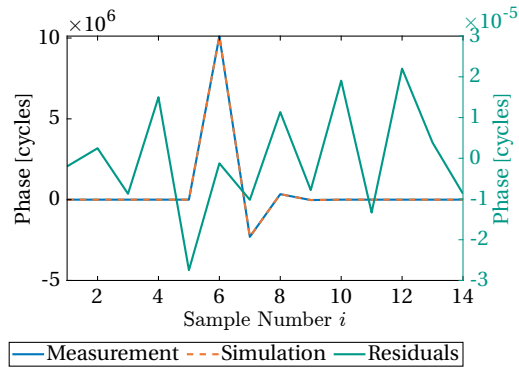


Figure 9.5. Example of an SEU fit with low residuals for event #1. The residuals (green) are in the order of 10^{-5} cycles.

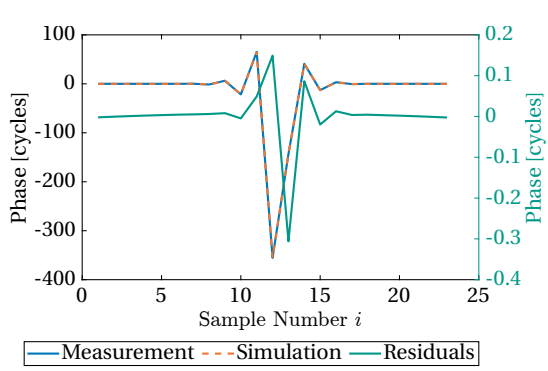


Figure 9.6. Example of an SEU fit with high residuals for event #3. The residuals are shaped like a second SEU.

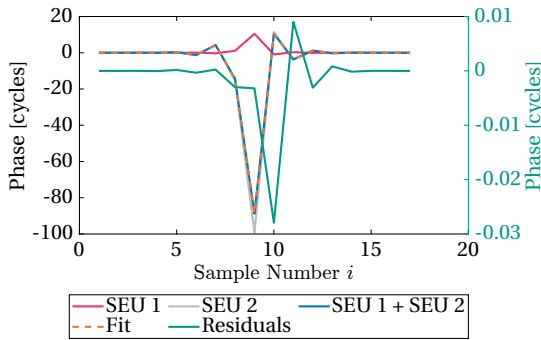


Figure 9.7. Simulation of two non-simultaneous SEU events (pink and gray) with a separation of 0.1 ms.

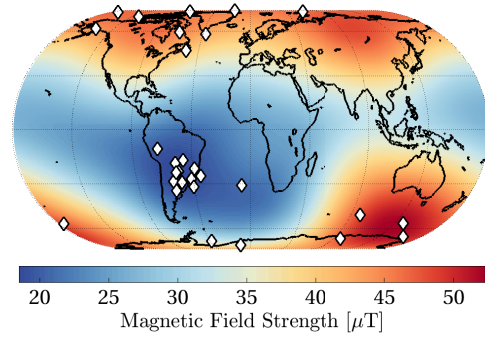


Figure 9.8. World map showing the location of the GRACE-FO spacecraft at occurrence of SEUs (diamonds). The colors represent the magnetic field strength in μT at 490 km above Earth's surface derived from the CHAOS-7 model.

by a particle with a trajectory inside the plane of the memory cell array, thus altering more than one bit. Such an effect would increase or decrease the bit number by specific fractional bit numbers, which can be computed by

$$\mathcal{O}_{\pm}(n) = \log_2(2^b \pm 2^{b-n}) - \log_2(2^b). \quad (9.5)$$

Here, b denotes the bit number of the most significant flipping bit, and n is the second flipped bit's position relative to the first one. The sign of the term depends if the two bits flip in the same or different directions. If more than two bits are affected, the fractional part is a superposition of the values of \mathcal{O} , shown in table 9.2.

Furthermore, the spacecraft location at the SEU events is shown in a world map in figure 9.8. The background coloring indicates the Earth's magnetic field strength at an altitude of 490 km above Earth's surface and was computed for the reference epoch January 2021 from the time-variable CHAOS-7 model (Finlay et al., 2020). This model is named after CHAMP, Ørsted, and SAC-C, all of which are or were magnetic observatories in space (Olsen et al., 2006). The most recent version 7, also includes data of the SWARM mission and ground data (Finlay et al., 2020). The detected SEU events

n	$\mathcal{O}_+(n)$	$\mathcal{O}_-(n)$
1	0.58496	-1
2	0.32193	-0.41504
3	0.16993	-0.19265
4	0.08746	-0.09311
5	0.04439	-0.04580
6	0.02237	-0.02272
7	0.01123	-0.01131
8	0.00562	-0.00565
9	0.00282	-0.00282
10	0.00141	-0.00141
11	0.00070	-0.00070
12	0.00035	-0.00035

Table 9.2. Fractional bit numbers for two bitflips simultaneously as a function of the separation between bit numbers. The number n denotes position $b - n$ of the second bit, relative to the one at position b , $b > n$.

clearly cluster within the SAA, where the charged particles, dominantly protons, and electrons, dive deepest into the atmosphere. Furthermore, many events were captured in polar regions, where the Earth’s magnetic field lines and, thus, also the Van Allen radiation belts arc downward towards Earth, providing less natural shielding (Samwel et al., 2019).

9.6. Summary

This section focused on radiation-induced disturbances in the electronics within the LRI processor, specifically on single event upsets within the buffers of the two anti-aliasing filters before decimating the measured phase data. The LRP architecture was introduced, and based on that, a simulation of SEU events was performed. The results from the simulation provided templates, which were then saved as a look-up table and used for identifying SEU events in actual phase data of the LRI, and the parameters were determined using the method of maximum likelihood estimation. In total, 32 events were identified in approximately four years of the mission, with an approximate time in science mode of the LRI instrument of 75%. The frequency of these events may ramp up with increasing solar cycle 25 in the coming years. The detected events cluster near the SAA and the poles, and some events did not only cause one bit to flip but multiple bits simultaneously.

SEU events in the phase data are short-lived (in the order of 1 s) and rare (roughly ten occasions per year), and thus, they are expected to have little influence on the gravity fields for now. Likely, most data processing centers identify these short segments containing the disturbance as outliers. However, this study shows the possibility of identifying and removing this particular source of measurement disturbances in post-processing. At the same time, future instruments might even overcome it by either implementing radiation-hardened memory, using error correction algorithms onboard, or using an algorithm similar to the one presented here in the processing centers on the ground.

The AEI has derived independent, LRI1B-equivalent data sets publicly available at <https://www.aei.mpg.de/grace-fo-ranging-datasets>. These data sets include the SEU removal algorithm presented within this section, among other algorithmic optimizations w. r. t. the official v04 releases by the SDS.

“ *We are running out of time and we must have a planetary solution to a planetary crisis.* ”

— ALBERT “AL” GORE JR. —

Environmentalist and 45th US vice president

This thesis presented comprehensive insights into data analysis of the Laser Ranging Interferometer aboard the GRACE Follow-On mission and attempted to deepen the instrument’s understanding. The LRI precisely measures the distance variations between two spacecraft with a noise level below $200 \text{ pm}/\sqrt{\text{Hz}}$ at Fourier frequencies of 5 Hz, over a baseline of $220 \pm 50 \text{ km}$. The LRI’s racetrack configuration consists of one unit on each spacecraft, with one denoted as the reference, where the ranging measurement takes place, and the other denoted as the active transponder. The transponder acts like an amplifying retroreflector that recreates the incoming light’s phase and adds a static frequency offset while the reference frequency is locked to an optical reference cavity employing the Pound-Drever-Hall method.

The theory part of this thesis presented ranging noise models at high Fourier frequencies above 1 Hz based on in-flight data and their power spectral densities and autocorrelation functions for the reference role, whose power spectral density is dominated by the cavity thermal noise and follows a $1/f$ shape and the transponder, which is limited by the phase readout noise that is described by a fourth-order polynomial here. Furthermore, a specific phase combination of the four quadrant photodiode phase channels, e. g., $\kappa^A = \varphi_A - (\varphi_B + \varphi_C + \varphi_D)/3$, is introduced that describes the uncorrelated noise of a single phase channel. A combination of a lowpass and a bandpass filter can be used to model the noise in this combination. These noise models were used later to weight the observations in least squares parameter estimations.

New formulas for a relativistic description of the phase observable in inter-satellite interferometers were presented, and the conversion of the measured interferometric phase to a range is discussed for an error-free case. Particular attention is drawn to frequency variations during the roundtrip propagation time of the photons. Importantly, a more sophisticated integral form of the well-known relation $\rho(t) = c_0/\nu \cdot \varphi(t)$ should be used when considering those laser frequency variations.

The theory chapters conclude by describing the two important quantities in the LRI data processing: a static offset in the time tags of the LRI phase measurement with respect to the KBR and the absolute laser frequency. Simple equations are derived to model the dominant order of errors of these quantities in the ranging measurement. It is highlighted that these errors increase the ranging noise in the measurement frequency band if they remain uncorrected.

One significant challenge in the data processing of LRI data is precisely determining the absolute laser frequency and the timing offset. The current scheme, employed by the science data system for generating the official LRI data product, performs an inter-

comparison between the two ranging instruments, the LRI and the KBR, which easily provides the scale factor ε_{SCF} and timing offset ζ between the two, which are in the order of $\varepsilon_{\text{SCF}} \approx 10^{-6}$ and $\zeta = 70 \mu\text{s}$. However, since the results of this intercomparison are used to derive the LRI level-1B data, the results might imprint KBR errors onto the LRI data. Furthermore, such intercomparison is not feasible if the KBR has a malfunction or in future missions with an LRI as the primary and only ranging instrument. Therefore, three new ways of determining the absolute laser frequency of the LRI have been investigated.

The first is based on deriving a model of the optical cavities' resonance frequencies, in particular accounting for settling effects, that has been quantified for the LRI cavities for the first time. On GF-1, it starts at approximately 281 615 743 MHz after launch and converges asymptotically against 281 615 768.376 MHz, whereas the drift on GF-2 is smaller with an initial value of 281 615 649 MHz and converging to 281 615 663.369 MHz after five years in orbit.

The second method relates the laser telemetry, i.e., the actuator voltages of the frequency servo, to the output frequency based on calibration measurements taken before launch. A previously uncalibrated drift in the absolute laser frequency at a rate between -1.2 Hz/s to -1 Hz/s was found. An attempt to measure such a drift with a comparable laser system in the laboratory was unfortunately not conclusive, as the repeatability of the measurement is limited by the thermal environment in the laboratory and the laser's susceptibility to temperature variations, which was measured to be -235.619 MHz/K . Furthermore, the measured laser frequency in the laboratory shows frequent steps of 10 MHz to 100 MHz. The following efforts in the laboratory might focus on developing a frequency-dependent transfer function for the temperature coupling into the absolute laser frequency and installing the laser within a thermal vacuum chamber for better thermal control. However, the knowledge from designing the laser controller electronics in this laboratory activity will propagate into the phasemeter design for future LRI-like instruments at the AEI.

The third method relies on static, pre-flight estimates of the laser frequency without further refinement or modeling. It can be regarded as a worst-case knowledge of the in-flight frequency and is not recommended but it served as a sanity check and an easy way to reproduce and validate the SDS approach.

The three new approaches to determining the laser frequency have been used to generate LRI Level-1B equivalent data sets. They have been compared to the KBR ranging data. It was found that the biased ranges of these new LRI1B and the KBR1B data sets differ by about $25 \mu\text{m}$ rms. This difference can be reduced to roughly $5 \mu\text{m}$ rms by estimating a single scale factor and time shift for the whole mission duration. In contrast, these two values are estimated once per day in the official data processing employing the KBR-LRI intercomparison.

Sinusoidal tone errors are a dominant ranging error source in GRACE-like missions. They arise, for example, from temperature variations that couple into the measurement chain and are difficult to disentangle from the actual ranging signal, especially at the orbital period. This thesis aims to set an upper limit on the magnitude of this particular error source by further minimizing the $5 \mu\text{m}$ rms difference between the KBR and LRI measurements. Two potential coupling mechanisms have been identified and modeled: a coupling in the phase domain, e.g., through thermal flexing of the satellite platform with a coupling factor with units of m/K , or in the frequency domain, e.g., through

frequency variations of the LRI or KBR oscillators, causing a coupling with units of MHz/K. Using this TC model, which consists of a set of 12 coefficients for the entire mission span, the residuals between KBR and LRI lower to approximately $1\ \mu\text{m}$ rms. The dominant coupling arises from thermistors attached to the solar array that is periodically directly heated by the sun. Therefore, they can be regarded as a proxy for the spacecraft's interior temperature. Neither the LRI cavity nor the laser couple dominantly as a tone error source; hence, one might argue that the TC is caused by the KBR instrument, for example, through thermally induced variations of the KBR phase center.

The 1/rev and 2/rev components of the TC model show peak amplitudes smaller than $8\ \mu\text{m}$ and $5\ \mu\text{m}$, respectively, but exhibit seasonal variations in amplitude and phase, that are correlated to the β -angle between the orbital plane of the spacecraft and the sun vector. Additionally, using the TC model reduces variations in the LRI scale factor from KBR-LRI cross-calibration. The three-monthly seasonal features, as apparent in the scale factor and time shift estimated from the daily KBR-LRI intercomparison in the official data processing, are likely produced by tone errors.

The presented methods for determining the absolute laser frequency were compared to available or currently developed techniques that might be implemented in a future gravity mission. Although an atomic or molecular transition, like an iodine standard, could provide the highest accuracy among the presented methods, the FSR readout scheme proposed by [Rees et al. \(2021\)](#) seems a good candidate for future missions since only minor modifications to existing flight hardware are required. Nevertheless, the laser telemetry-based model and the characterization of the cavity resonance might be pursued as alternative means to derive the absolute laser frequency and cross-validate the novel FSR readout technique to some extent.

A key component of the LRI is the so-called TMA, a structure that mimics a hollow corner cube and acts as a passive retroreflector. To ensure anti-parallelity of the incoming and outgoing beams, the orthogonal alignment of the three mirrors has to fulfill strict requirements. The mirror co-alignment can be measured in space using so-called DWS scans, where a deliberate offset is added onto the beam pointing. These scans have been performed repeatedly. It was shown that the TMA mirrors realigned in space after being misaligned before launch due to moisture accumulation, and now yield small residual beam pointing errors below $\pm 10\ \mu\text{rad}$, well below the requirement, and remain stable over time after moisture release. As a by-product, the spatial amplitude profile of the Gaussian beams in the far-field was characterized. It was further attempted to assess the temperature susceptibility of the TMA co-alignment. However, the temperature stimulus in orbit is small, and therefore, it is questionable if the obtained values of up to $\pm 2.5\ \mu\text{rad}/\text{K}$ are realistic and really exceed the requirement of $\pm 1\ \mu\text{m}/\text{K}$.

The DWS scans can further be used to assess various other properties of the laser beams and the interferometer. The heterodyne efficiency, for example, quantitatively describes the overlap or similarity of the two interfering beams. It varies under relative beam tip and tilt, and can be measured from the coherent sum of the individual channels' beatnote amplitudes. It showed the expected Gaussian profile to a large extent. A simple model for the non-Gaussian contribution was fitted as well and showed a non-Gaussian contribution below 2.5% peak, but that model should be further refined, as it did not improve the fit on GF-2.

It was found that the longitudinal path length signal changes during the DWS scans,

which is described as beam pointing-to-pathlength coupling. A specially designed DWS scan to assess this coupling was analyzed, and a linear coupling of at maximum $110 \mu\text{m}/\text{rad}$, and a quadratic contribution of up to $1.9 \text{m}/\text{rad}^2$ with the beam pointing offsets was found. With an angular jitter of the fast steering mirror of approximately $1 \mu\text{rad}/\sqrt{\text{Hz}}$ at high frequencies, this contributes to the overall LRI ranging noise at the picometer level. One possible explanation for the coupling coefficients is assessed: an offset in the order of 3.5m of the Gaussian beam's waist position with respect to the steering mirror's surface could explain such pathlength variations under beam pointing offsets. However, other effects like parasitic phase variations from beam-walk on the photodiodes and higher-order spatial mode contents might contribute as well but were omitted here. Thus, the presented waist offset values only provide an upper bound for this particular effect.

The reliability and stability of the RLUs is another key aspect of the LRI operation. Its telemetry channels are monitored over the course of the mission. Although the free-running laser frequency noise is suppressed by the PDH cavity lock, its magnitude can be assessed from the PDH servo voltages, dominantly from the `pztIL` signal. In nominal conditions, the free-running laser frequency noise is at a level of 75kHz rms for Fourier frequencies between 1mHz to 500mHz , which is comparable to the laser system flown on LISA Pathfinder. However, periods with an elevated frequency noise were revealed. This non-stationary behavior of the free-running laser frequency noise led to further investigation of the RLU frequency and telemetry. The frequency stability of the RLU depends on the thermal working point of the pump diodes. Designated measurements of the error signal in the cavity lock, while slowly ramping the diode temperature, reveal "sweet spots" with low laser frequency noise and regions with higher noise. The temperature of the sweet spots may vary over time, and these measurements have therefore been performed four times per both spacecraft: once at the instruments' commissioning in 2018, twice in mid-2021, and once more in mid-2023. It was observed that GF-1 operated at a non-ideal temperature setpoint in 2018, and thus, it was changed to a slightly different value. A similar setpoint change was performed in GF-2 in June 2023 after a higher noise level was observed in the ranging data. Continuous monitoring of the frequency noise will provide early signs of non-ideal temperature settings, or even degradation of the RLU. Furthermore, all RLU telemetry channels, which report the optical output power, current consumption, and internal temperatures, show a small bi-modal behavior with irregular hops. Although several potential sources for this behavior have been investigated, no clear evidence of the cause could be found.

Finally, SEUs were analyzed. These are sporadic effects in digital electronics, where a charged particle, for example, originating from cosmic radiation, interacts with the digital logic and changes the value of a memory cell. This effect is commonly called a bitflip. In the LRI, SEUs occur within the buffers of the phase decimation filters, resulting in short-lived peaks in the ranging phase data. These peaks can be easily detected, as they usually have a much larger magnitude than the measured phase variations. 32 SEU events have been identified within the LRI ranging data between launch and mid-2023. They were modeled and subtracted with low residual disturbances. Sometimes, multiple bits flip simultaneously or even with a small time offset. As solar activity is ramping towards the maximum of solar cycle 25 at the time of writing, the incidence rate is expected to rise accordingly.

This thesis primarily investigated the laser frequency of the LRI in many aspects, from a theoretical derivation of new formulas, in-flight data analysis, and even with a companion on-ground experiment. Secondly, the DWS scans have been investigated in great detail. Besides that, many small effects and disturbances in the LRI were investigated. Still, they typically only have a minor impact on the ranging measurement and, thus, on the recovered gravity fields. Therefore, they are rather of academic interest and to improve the future generations of the LRI. In conclusion, the LRI performs well after more than five years in orbit with low noise, few interruptions, and no visible signs of degradation. The work presented in this thesis significantly contributes to understanding the instrument and the data delivered by the LRI. It will help in the design and data analysis of future LRI-like inter-satellite interferometers for NGGM and GRACE-C – and for testing fundamental physics in space with upcoming experiments like the LISA, Taiji, or TianQin.

A. Wavemeter Calibration

In a first experiment, the accuracy of the wavemeter-internal calibration was reviewed by locking a laser, a Prometheus laser by Coherent, Inc. (Coherent, Inc., 2020), to an iodine hyperfine transition of an iodine cell manufactured by InnoLight. The equivalent wavelengths of the hyperfine lines of molecular iodine are in the range of 532 nm and as they are well known (Arie et al., 1992), they are commonly used as absolute frequency reference (see e.g. Schuldt et al. (2017)). The Bureau International des Poids et Mesures (BIPM) has released a list of recommended nominal frequencies, of which an excerpt is given in table 6.1.

The Prometheus laser features two fiber-coupled output ports: one port at 1064 nm and 500 mW and a secondary, frequency-doubled port at 532 nm with 20 mW optical power, that can directly be used for locking to an iodine cell. The frequency can be tuned over a range of 60 GHz (Coherent, Inc., 2020). For this calibration, the R(56)32-0 iodine transition was chosen.

The first calibration measurement, shown in figure A.1, kept the laser frequency locked to the a_1 component first, then changed to the a_{10} component and at the end locked back to the a_1 component. The average measured frequency of the two hyperfine components at 1064 nm is approximately 60 MHz below the nominal values of table 6.1. This bias was measured repeatedly.

The nominal difference frequency of the two components is

$$\delta\nu_{\text{vis}} = \nu_{a_{10}}^{1110} - \nu_{a_1}^{1110} = 571.542 \text{ MHz} \quad (\text{A.1})$$

$$\delta\nu_{\text{IR}} = \delta\nu_{\text{vis}}/2 = 285.771 \text{ MHz} , \quad (\text{A.2})$$

according to table 6.1 and the measurement showed a difference of 288.785 MHz, being only 3.014 MHz away from the nominal value of equation (A.2). Various settings for the exposure time of the wavemeter were tested with only a slight increase of noise for

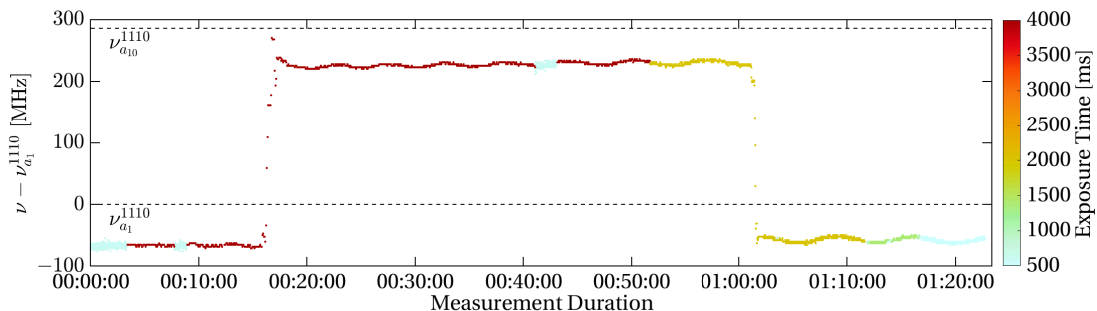


Figure A.1. Absolute frequency measurements of the reference laser locked to different hyperfine lines of an iodine cell. The apparent quantization of approximately 3 MHz arises from the finite resolution of 10^{-5} nm of the wavemeter WS6-600. Outliers were removed. The color indicates the wavemeter's exposure time.

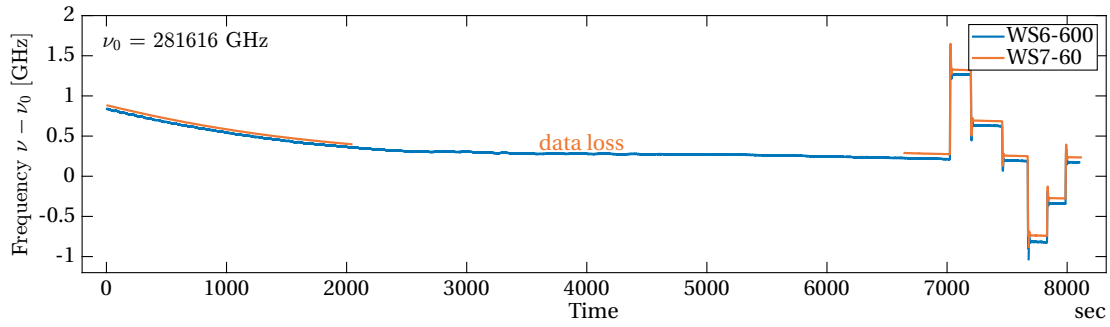


Figure A.2. OGSE laser frequency, measured with two wavemeters. 110 min waiting for thermal equilibrium, afterward active control by using the laser’s actuators. Outliers removed.

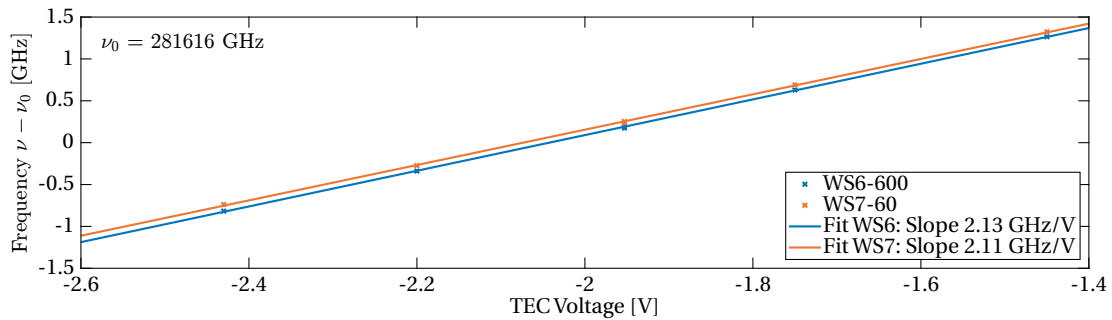


Figure A.3. Thermal Coupling calibration of the OGSE laser

low exposure times. Small oscillations with a magnitude of up to 15 MHz at a period of 300 s have also been observed repeatedly for this device.

Later at the integration facility, a second wavemeter, the WS7-60, was available alongside the former WS6-600. This allowed a comparison of the two devices, in which the offset of approximately 50 MHz of the WS6-600 was again observed, cf. figure A.2. Further, it was found that the optical ground support equipment (OGSE) laser takes about 60 min to reach thermal equilibrium after switching on.

Furthermore, the coupling of the thermoelectric element to the optical frequency was calibrated using the time series of figure A.2 and the thermal setpoints applied. With both wavemeters, a value of approximately 2.1 GHz/V was measured, see figure A.3.

B. RLU Calibration Actuator Signals

Shown in figures B.4 and B.5 are the actuator signals as recorded during the on-ground measurement campaigns. Here, (a) shows the PZT actuator setpoints, (b) the thermal actuator setpoints, (c) the temperature at the RLU TRP.

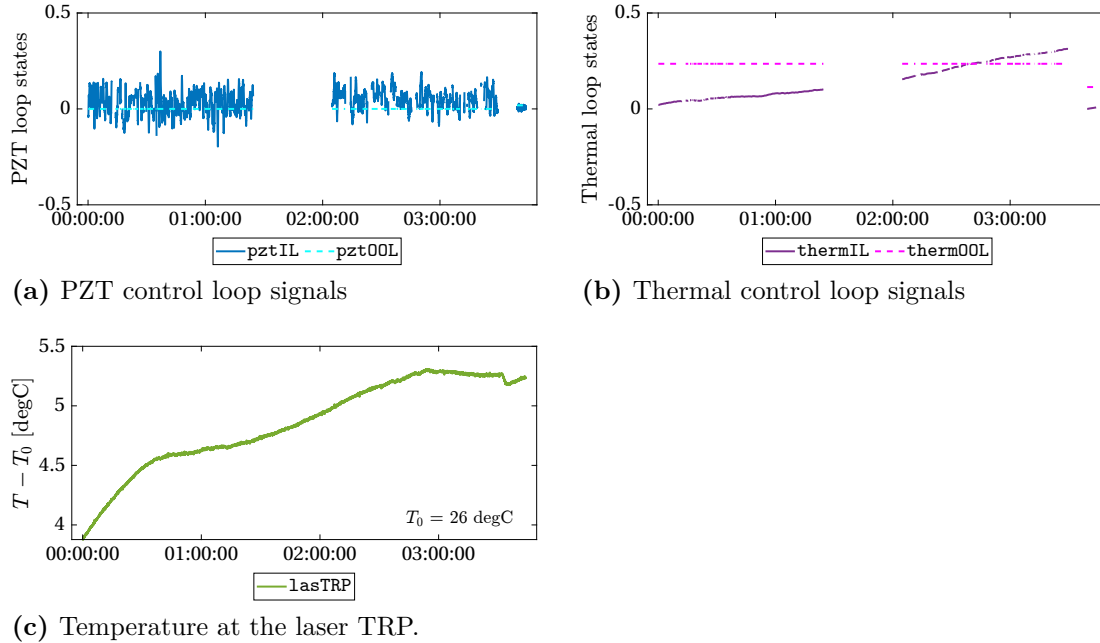


Figure B.4. Actuator signals of the on-ground measurements for GF-1, measurement (i). The gaps originate from lost-lock events of the LRI unit in transponder mode, when the reference laser changed its frequency too fast. The RLU TRP data in (c) was recorded independently of the LRP telemetry and thus shows no gaps.

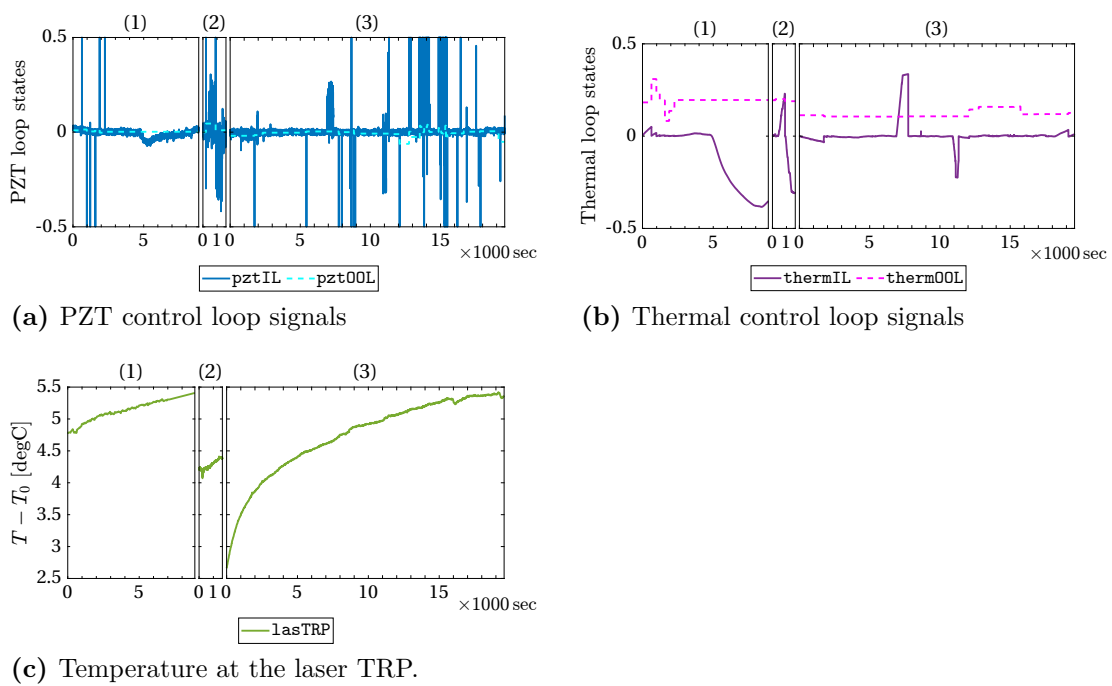
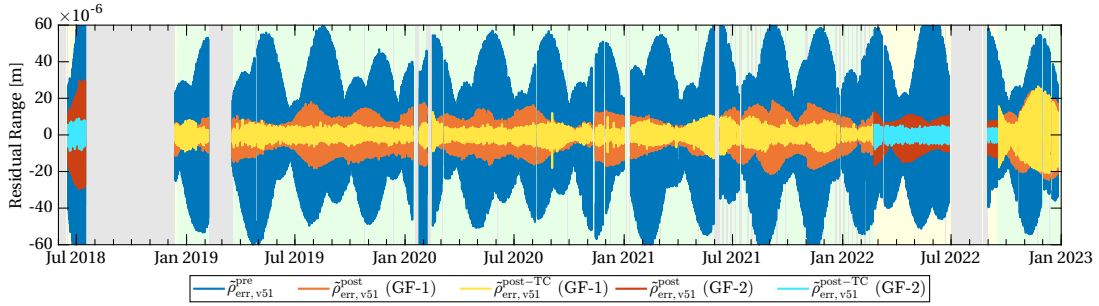


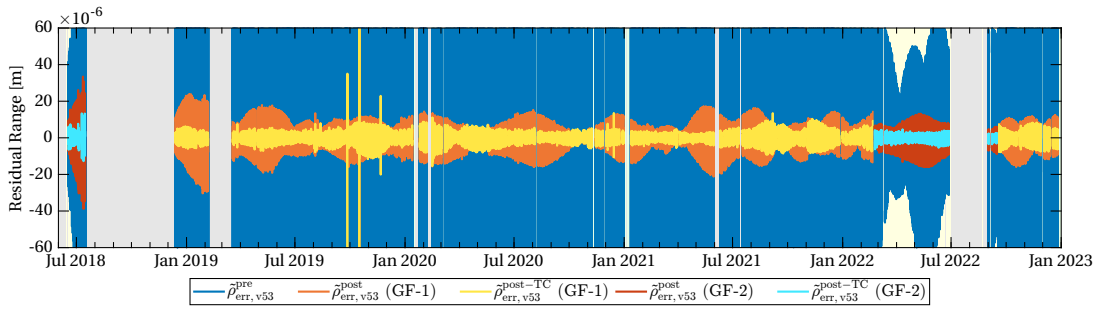
Figure B.5. Actuator signals of the on-ground measurements for GF-2. The numbering on top of the individual panels of each subfigure corresponds to the measurement campaigns, cf. table 5.2. Other than in the previous figure, times when the LRI was unlocked from the reference laser are not shown here.

C. Thermal Coupling Coefficients for v51 and v53

In the main text of section 5.5, the TC coupling coefficients of v51 and v53 were omitted for brevity. They are shown here in tables C.1 and C.2. One peculiarity in the GF-2 model for TC-v51 is that a special low-pass filter is used for the fifth sensor (LriCavInt), that implements a transfer function reproducing the effect the thermal shield surrounding the cavity.



(a) TC for v51



(b) TC for v53

Figure C.6. TC fit for both SC. The direct difference of KBR and LRI is shown in blue ($\tilde{\rho}_{\text{err}}^{\text{pre}}$), whereas the first stage of post-fit results, $\tilde{\rho}_{\text{err}}^{\text{post}}$, is shown in orange (GF-1) and red (GF-2). After estimating and subtracting the TC, one obtains $\tilde{\rho}_{\text{err}}^{\text{post-TC}}$, shown as the yellow and cyan curves for GF-1 and GF-2, respectively. The distinction between the two SC is made based on their role as reference or transponder.

Table C.1. Thermal coupling parameters for v51 using the telemetry-based laser frequency model $\nu_{1/2}^{\text{TM}}$ as laser frequency model. The index i denotes the order of importance, i.e., the gain in reducing the rms residuals. The $\delta\tilde{\rho}$ type denotes the coupling in phase or frequency regime. Thus, the unit of c_1 is m/K if the phase-domain coupling was used, and 1/K if the frequency-domain coupling was used. The coefficient c_2 has units s m/K (AC) or s/K (DC). The last column $\zeta_T = c_2/c_1$ describes the timeshift of the temperature data in seconds.

(a) TC-v51 coefficients for GF-1

i	SC	Sensor	ID	Freq.	type	c_1	c_2	ζ_T [s]
1	GF-1	SaMzPx	THT10013	AC	freq	$-5.235 \cdot 10^{-13}$	$5.203 \cdot 10^{-11}$	-99.4
2	GF-1	Pr21	THT10144	DC	freq	$-2.197 \cdot 10^{-9}$	$2.520 \cdot 10^{-6}$	-1146.6
3	GF-1	LriLpcMy	THT10022	DC	freq	$5.264 \cdot 10^{-9}$	$-4.302 \cdot 10^{-6}$	-817.4
4	GF-1	MepRearPy	THT10140	AC	freq	$-2.638 \cdot 10^{-11}$	$8.187 \cdot 10^{-9}$	-310.3
5	GF-2	Tank2	THT10151	DC	freq	$-4.294 \cdot 10^{-9}$	$-3.337 \cdot 10^{-6}$	777.1

(b) TC-v51 coefficients for GF-2

i	SC	Sensor	ID	Freq.	type	c_1	c_2	ζ_T [s]
1	GF-2	AccPanel	THT10052	DC	freq	$1.507 \cdot 10^{-8}$	$-3.210 \cdot 10^{-6}$	-213.1
2	GF-1	AccIcu	THT10117	AC	freq	$1.289 \cdot 10^{-10}$	$-7.915 \cdot 10^{-8}$	-613.8
3	GF-1	Act24	THT10128	AC	freq	$-1.371 \cdot 10^{-11}$	$-8.474 \cdot 10^{-9}$	618.2
4	GF-2	MwiUsoB	THT10071	AC	freq	$-3.387 \cdot 10^{-10}$	$-1.027 \cdot 10^{-7}$	303.2
5	GF-2	LriCavInt	THT10019	TF	freq	$-7.725 \cdot 10^{-9}$	$1.448 \cdot 10^{-4}$	-18 749.1

Table C.2. Thermal coupling parameters for v53 using the pre-calibrated fixed frequency value ν_0 as laser frequency model. The columns are as described in the above table.

(a) TC-v53 coefficients for GF-1

i	SC	Sensor	ID	Freq.	type	c_1	c_2	ζ_T [s]
1	GF-2	SaMzMx	THT10032	AC	phase	$-1.054 \cdot 10^{-7}$	$1.574 \cdot 10^{-5}$	-149.3
2	GF-2	AccTrp	THT10075	DC	freq	$-1.080 \cdot 10^{-8}$	$-6.467 \cdot 10^{-7}$	59.9
3	GF-2	LriLas	THT10113	AC	freq	$-1.580 \cdot 10^{-10}$	$-4.162 \cdot 10^{-10}$	2.6
4	GF-1	Tank1	THT10121	DC	freq	$4.115 \cdot 10^{-9}$	$-9.356 \cdot 10^{-6}$	-2273.3
5	GF-2	LriObe	THT10090	DC	freq	$-2.060 \cdot 10^{-9}$	$3.436 \cdot 10^{-6}$	-1668.2

(b) TC-v53 coefficients for GF-2

i	SC	Sensor	ID	Freq.	type	c_1	c_2	ζ_T [s]
1	GF-2	AccPanel	THT10084	DC	freq	$-3.143 \cdot 10^{-9}$	$-2.262 \cdot 10^{-6}$	719.8
2	GF-1	Act24	THT10128	AC	freq	$-9.379 \cdot 10^{-12}$	$-3.941 \cdot 10^{-8}$	4202.4
3	GF-1	AccTrp	THT10043	DC	freq	$-1.617 \cdot 10^{-8}$	$7.893 \cdot 10^{-6}$	-488.2
4	GF-1	MepRearMy	THT10154	AC	phase	$-4.702 \cdot 10^{-6}$	$1.578 \cdot 10^{-3}$	-335.6
5	GF-2	Act12	THT10108	AC	freq	$-1.078 \cdot 10^{-11}$	$2.631 \cdot 10^{-8}$	-2440.8

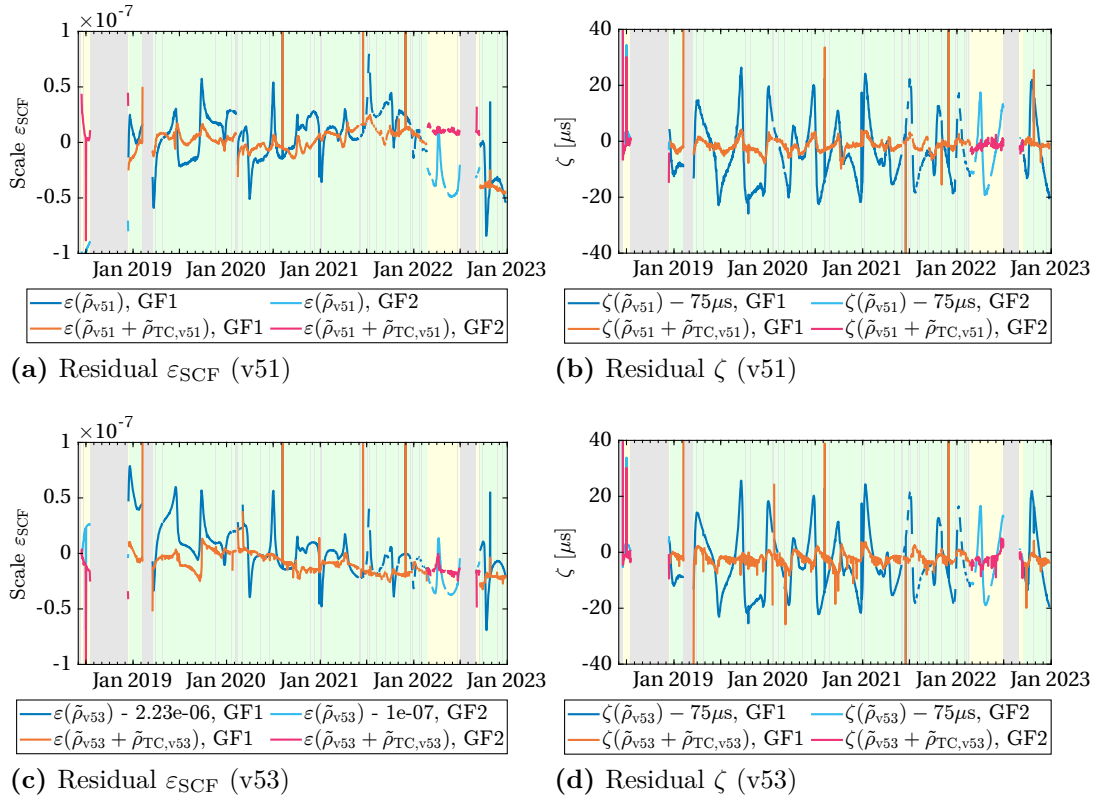


Figure C.7. Residual scale ε_{SCF} and timeshift ζ of KBR-LRI in versions v51 and v53 with and without the correction of $\tilde{\rho}_{\text{TC}}$ for both SC. The GF-1 model is shown in orange and blue, while the GF-2 ones are shown in pink and cyan. The seasonal variations are lowered significantly on both SC when applying the TC. In the scale of v53, the TC partially absorbs the effect of the exponential cavity drift, while in v51 some lower frequency variations of the telemetry model ν^{TME} are dominantly suppressed.

D. DWS Scan Design Patterns

While table 7.1 lists all different types of DWS scans performed, their test design in terms of setpoints' time series' and the spatial field of regard is shown in figures D.8 to D.13.

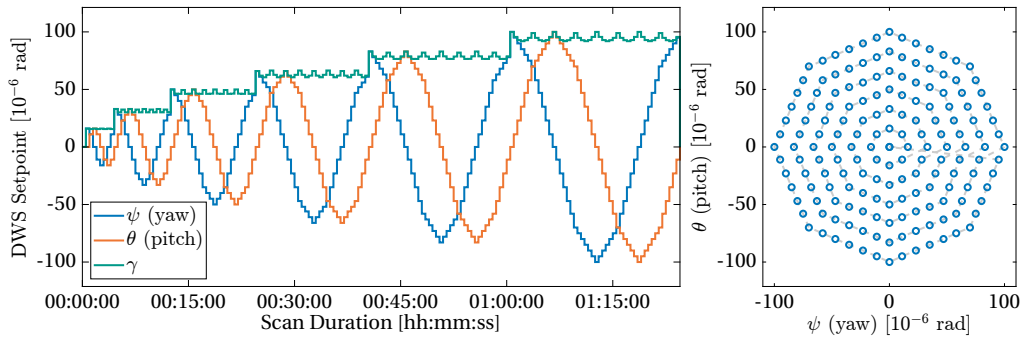


Figure D.8. DWS Scan Type 1

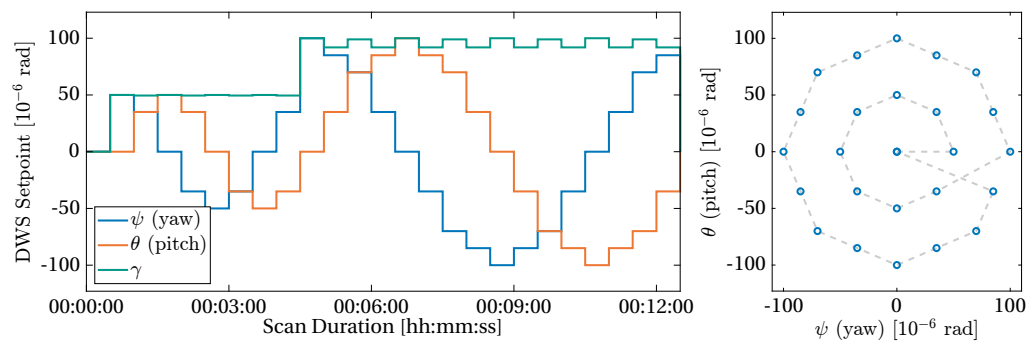


Figure D.9. DWS Scan Type 2

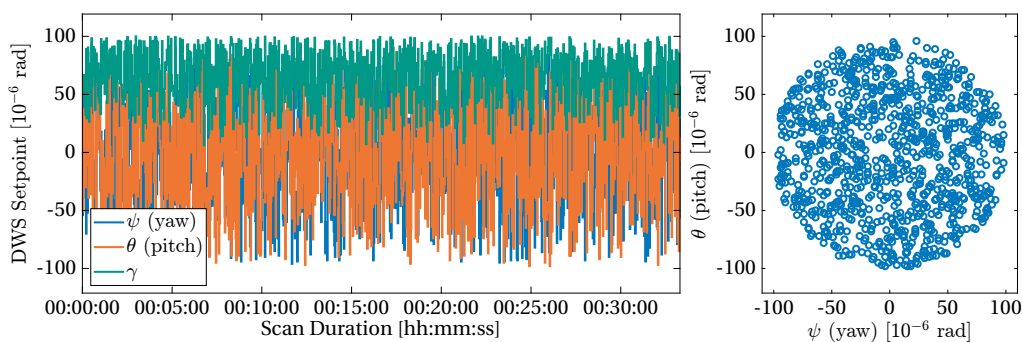


Figure D.10. DWS Scan Type 3

D. DWS SCAN DESIGN PATTERNS

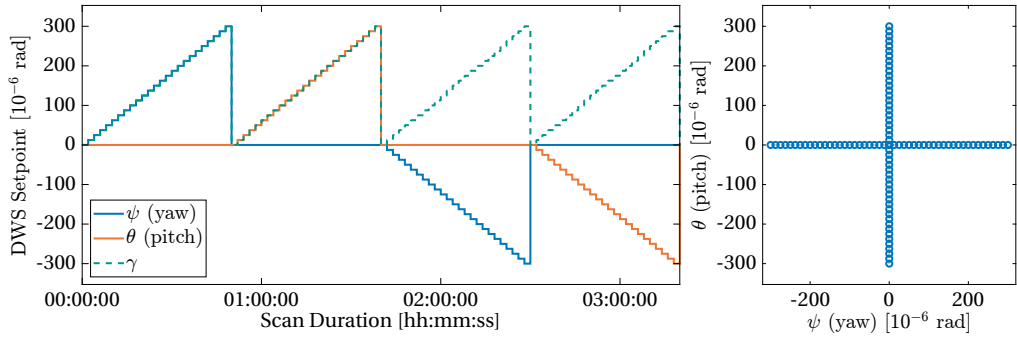


Figure D.11. DWS Scan Type 4

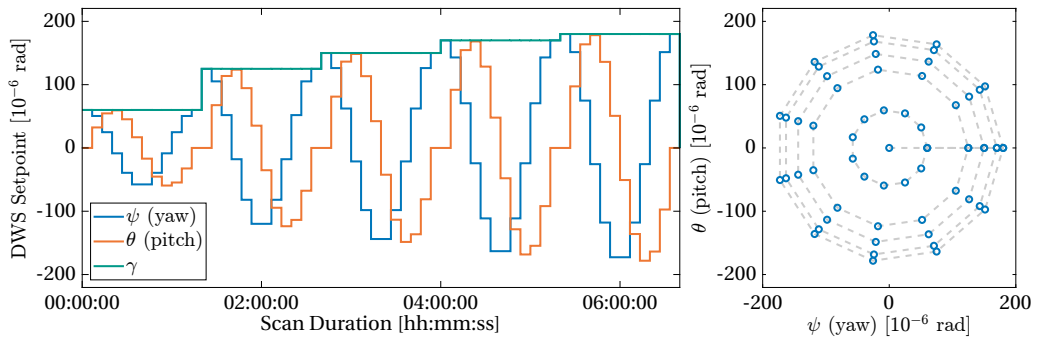


Figure D.12. DWS Scan Type 5

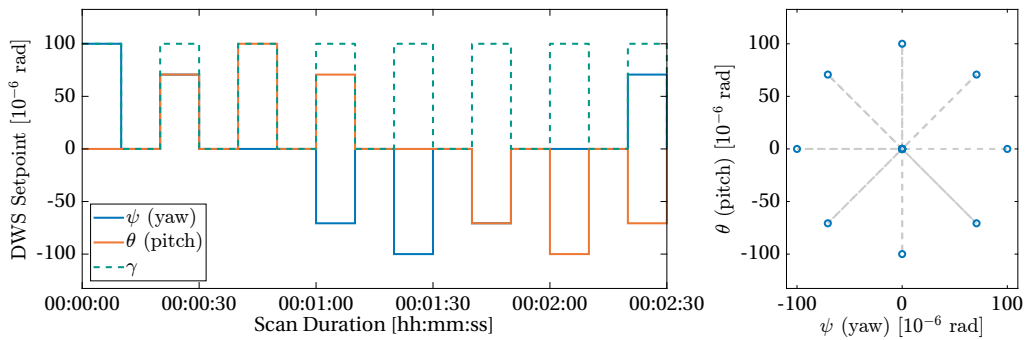


Figure D.13. DWS Scan Type 6

E. DWS Setpoint Wrapping

The Low-CNR pretest design (type 4 in table 7.1) was originally designed to have maximum excursions of $300 \mu\text{rad}$ in yaw and pitch angles, ψ and θ . However, the DWS technique has two wrapping limits:

1. The physical limit is at a full cycle of phase difference between the two beams. With magnification lenses with factor $m = 8$ before the QPD, one phase cycle corresponds to a DWS angle of about $200 \mu\text{rad}$, depending on the angle and spacecraft. A full calibration of the measured DWS signal in phase cycles to the resulting angles in μrad is given in Misfeldt (2019, sec. 4.4).
2. The DWS setpoint has a certain bit-depth, which corresponds to a maximum excursion angle of 1.15 cycles or equivalently approximately $\pm 232 \mu\text{rad}$.

Figure E.14 shows those limits at the example of the Low-CNR pretest performed on GF-1 on 2020-Aug-07. The LRI loses lock at $\gamma \approx 180 \mu\text{rad}$, when the CNR is below the LRP tracking limits.

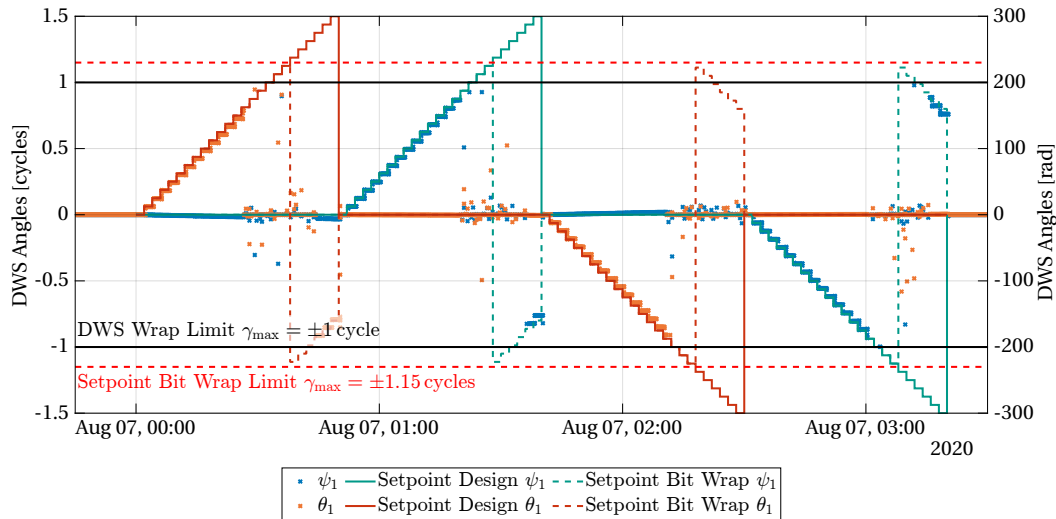


Figure E.14. Bit Wrapping of the DWS Setpoints. The actual DWS phase wrapping at 1 cycle can not be observed, as the LRI lost the link due to a low CNR at $\gamma \approx 180 \mu\text{rad}$

F. Error Propagation for the Phase Front Parameters

The uncertainties of the dependent quantities can be derived through uncertainty propagation. In general, the uncertainty u_x of a dependent quantity $x(y_1, y_2, \dots)$ can be derived through

$$u_x = \sum_i \sqrt{\left(\frac{\partial x}{\partial y_i} \cdot u_{y_i}\right)^2}. \quad (\text{A.3})$$

Here, u_{y_i} denotes the uncertainties of the independent variables y_i , that are given by the least squares parameter estimation. Applying the above formula to equations (7.32) and (7.33), one easily obtains

$$u_{\alpha_{\text{tma}}} = \left\{ \left[\left(\frac{\pm 2}{\sqrt{2c_l^2 + 4c_q^2}} - \frac{2c_q \pm \sqrt{2c_l^2 + 4c_q^2}}{c_l^2} \right) \cdot u_{c_l} \right]^2 + \left[\frac{1}{c_l} \left(2 \pm \frac{4c_q}{\sqrt{2c_l^2 + 4c_q^2}} \right) \cdot u_{c_q} \right]^2 \right\}^{1/2} \quad (\text{A.4})$$

and

$$u_{\Delta z} = \left\{ \left[\left(\frac{\pm c_l}{2\sqrt{\frac{c_l^2}{2} + c_q^2}} \right) \cdot u_{c_l} \right]^2 + \left[\left(\frac{\pm c_q}{\sqrt{\frac{c_l^2}{2} + c_q^2}} - 1 \right) \cdot u_{c_q} \right]^2 \right\}^{1/2}. \quad (\text{A.5})$$

Bibliography

- Abich, Klaus et al. (July 2019). “In-Orbit Performance of the GRACE Follow-on Laser Ranging Interferometer”. In: *Physical Review Letters* 123.3. DOI: [10.1103/physrevlett.123.031101](https://doi.org/10.1103/physrevlett.123.031101).
- Alfvén, H. (Jan. 1958). “On the Theory of Magnetic Storms and Aurorae”. In: *Tellus* 10.1, pp. 104–116. DOI: [10.3402/tellusa.v10i1.9213](https://doi.org/10.3402/tellusa.v10i1.9213).
- Alnis, J. et al. (May 2008). “Subhertz linewidth diode lasers by stabilization to vibrationally and thermally compensated ultralow-expansion glass Fabry-Pérot cavities”. In: *Physical Review A* 77.5, p. 053809. DOI: [10.1103/physreva.77.053809](https://doi.org/10.1103/physreva.77.053809).
- Álvarez, Anthony Dávila et al. (Sept. 2022). “A simplified gravitational reference sensor for satellite geodesy”. In: *Journal of Geodesy* 96.10. DOI: [10.1007/s00190-022-01659-0](https://doi.org/10.1007/s00190-022-01659-0).
- Amaro-Seoane, Pau et al. (2017). *Laser Interferometer Space Antenna*. DOI: [10.48550/ARXIV.1702.00786](https://doi.org/10.48550/ARXIV.1702.00786).
- Antonucci, F et al. (June 2012). “The LISA Pathfinder mission”. In: *Classical and Quantum Gravity* 29.12, p. 124014. DOI: [10.1088/0264-9381/29/12/124014](https://doi.org/10.1088/0264-9381/29/12/124014).
- Arie, Ady et al. (Sept. 1992). “Absolute frequency stabilization of diode-laser-pumped Nd:YAG lasers to hyperfine transitions in molecular iodine”. In: *Opt. Lett.* 17.17, pp. 1204–1206. DOI: [10.1364/OL.17.001204](https://doi.org/10.1364/OL.17.001204).
- Armano, M. et al. (May 2015). “The LISA Pathfinder Mission”. In: *Journal of Physics: Conference Series* 610, p. 012005. DOI: [10.1088/1742-6596/610/1/012005](https://doi.org/10.1088/1742-6596/610/1/012005).
- Armano, M. et al. (May 2017). “LISA Pathfinder: First steps to observing gravitational waves from space”. In: *Journal of Physics: Conference Series* 840, p. 012001. DOI: [10.1088/1742-6596/840/1/012001](https://doi.org/10.1088/1742-6596/840/1/012001).
- Armano, M. et al. (Oct. 2022). “Sensor noise in LISA Pathfinder: An extensive in-flight review of the angular and longitudinal interferometric measurement system”. In: *Physical Review D* 106.8, p. 082001. DOI: [10.1103/physrevd.106.082001](https://doi.org/10.1103/physrevd.106.082001).
- Ashby, Neil et al. (Oct. 1986). “Relativistic effects in local inertial frames”. In: *Physical Review D* 34.8, pp. 2246–2259. DOI: [10.1103/physrevd.34.2246](https://doi.org/10.1103/physrevd.34.2246).
- Australian Space Weather Office (2023). *Progression of solar cycle 25. Sunspot numbers including predictions*. [Online; accessed 28-July-2023]. URL: <https://heliocast.space/solarcycle>.
- Bachman, B. et al. (May 2017). “Flight phasemeter on the Laser Ranging Interferometer on the GRACE Follow-On mission”. In: *Journal of Physics: Conference Series* 840, p. 012011. ISSN: 1742-6596. DOI: [10.1088/1742-6596/840/1/012011](https://doi.org/10.1088/1742-6596/840/1/012011).
- Bakhtiyarov, Sayavur I. (2015). “Earth’s Natural Protective System: Van Allen Radiation Belts”. In: *Handbook of Cosmic Hazards and Planetary Defense*. Springer International Publishing, pp. 225–240. DOI: [10.1007/978-3-319-03952-7_19](https://doi.org/10.1007/978-3-319-03952-7_19).
- Barranco, Germán Fernández et al. (Mar. 2017). “Phase stability of photoreceivers in inter-satellite laser interferometers”. In: *Optics Express* 25.7, p. 7999. DOI: [10.1364/oe.25.007999](https://doi.org/10.1364/oe.25.007999).
- Bender, P. L. et al. (2008). “A Possible Dual-GRACE Mission with 90 Degree and 63 Degree Inclination Orbits”. In: *Proceedings of the 3rd International Symposium on Formation Flying, Missions and Technologies*.
- Bureau International des Poids et Mesures (Oct. 2007). *Recommended Values of Standard Frequencies for Applications Including the Practical Realization of the Metre and Secondary Representations of the Definition of the Second: Iodine ($\lambda = 532$ nm)*. BIPM. URL: https://www.bipm.org/documents/20126/41549514/M-e-P_I2_532.pdf/16c7ddb8-4854-9f16-34cc-5bcebe299ce8 (visited on 01/26/2023).
- Carraz, Olivier et al. (July 2023). “ESA activities and perspectives on Laser Tracking Instrument for NGGM/MAGIC mission”. In: *International Conference on Space Optics – ICSSO 2022*. Ed. by Kyriaki Minoglou et al. SPIE. DOI: [10.1117/12.2689654](https://doi.org/10.1117/12.2689654).

- Carter, William H. (Oct. 1972). “Electromagnetic Field of a Gaussian Beam with an Elliptical Cross Section”. In: *Journal of the Optical Society of America* 62.10, p. 1195. DOI: [10.1364/josa.62.001195](https://doi.org/10.1364/josa.62.001195).
- Cesare, Stefano et al. (June 2022). “Drag and Attitude Control for the Next Generation Gravity Mission”. In: *Remote Sensing* 14.12, p. 2916. DOI: [10.3390/rs14122916](https://doi.org/10.3390/rs14122916).
- Chatfield, C. (1975). *The Analysis of Time Series: Theory and Practice*. Springer US. DOI: [10.1007/978-1-4899-2925-9](https://doi.org/10.1007/978-1-4899-2925-9).
- Coherent, Inc. (2020). *Prometheus - Ultra-Narrow Linewidth CW DPSS Green Laser*. Coherent, Inc. URL: <https://www.coherent.com/resources/datasheet/lasers/prometheus-ds.pdf> (visited on 03/23/2020).
- Cossavella, F. et al. (2022). “Attitude Control on GRACE Follow-On: Experiences from the First Years in Orbit”. In: *Space Operations*. Springer International Publishing, pp. 493–517. DOI: [10.1007/978-3-030-94628-9_22](https://doi.org/10.1007/978-3-030-94628-9_22).
- Daly, E.J. (Jan. 1994). “The radiation belts”. In: *Radiation Physics and Chemistry* 43.1-2, pp. 1–17. DOI: [10.1016/0969-806x\(94\)90198-8](https://doi.org/10.1016/0969-806x(94)90198-8).
- Danzmann, Karsten et al. (Apr. 2003). “LISA technology concept, status, prospects”. In: *Classical and Quantum Gravity* 20.10, S1–S9. DOI: [10.1088/0264-9381/20/10/301](https://doi.org/10.1088/0264-9381/20/10/301).
- Demtröder, Wolfgang (2014). *Laser Spectroscopy 1*. Springer Berlin Heidelberg. DOI: [10.1007/978-3-642-53859-9](https://doi.org/10.1007/978-3-642-53859-9).
- Dobosz, Marek et al. (Nov. 2017). “Overview of the laser-wavelength measurement methods”. In: *Optics and Lasers in Engineering* 98, pp. 107–117. DOI: [10.1016/j.optlaseng.2017.06.006](https://doi.org/10.1016/j.optlaseng.2017.06.006).
- Döringshoff, K. et al. (2017). “A flight-like absolute optical frequency reference based on iodine for laser systems at 1064 nm”. In: 123. ISSN: 0946-2171. DOI: [10.1007/s00340-017-6756-1](https://doi.org/10.1007/s00340-017-6756-1).
- Döringshoff, Klaus et al. (May 2019). “Iodine Frequency Reference on a Sounding Rocket”. In: *Physical Review Applied* 11.5, p. 054068. DOI: [10.1103/physrevapplied.11.054068](https://doi.org/10.1103/physrevapplied.11.054068).
- Drever, R. W. P. et al. (June 1983). “Laser phase and frequency stabilization using an optical resonator”. In: *Applied Physics B* 31.2, pp. 97–105. ISSN: 1432-0649. DOI: [10.1007/BF00702605](https://doi.org/10.1007/BF00702605).
- Dubovitsky, Serge et al. (Nov. 2018). *Laser Ranging Interferometer User Manual*. Rev. D. NASA/JPL.
- Ed Hawkins (University of Reading) (Nov. 2, 2022). *Warming Stripes*. URL: www.showyourstripes.info.
- European Cooperation for Space Standardization (ECSS) (Oct. 2012). *Space Product Assurance: Radiation Hardness Assurance - EEE components*. Tech. rep. ECSS-Q-ST-60-15C. Requirements and Standards Division.
- Finlay, Christopher C. et al. (Oct. 2020). “The CHAOS-7 geomagnetic field model and observed changes in the South Atlantic Anomaly”. In: *Earth, Planets and Space* 72.1, p. 156. ISSN: 1880-5981. DOI: [10.1186/s40623-020-01252-9](https://doi.org/10.1186/s40623-020-01252-9).
- Flechtner, Frank et al. (Sept. 2015). “What Can be Expected from the GRACE-FO Laser Ranging Interferometer for Earth Science Applications?” In: *Surveys in Geophysics* 37.2, pp. 453–470. DOI: [10.1007/s10712-015-9338-y](https://doi.org/10.1007/s10712-015-9338-y).
- Flechtner, Frank et al. (June 14, 2023). *Deliverable D4 (v3.0). ESA RFP/3-17121/21/I-DT-lr*. Technical Note ESA RFP/3-17121/21/I-DT-lr. Version 3.0. AEI Hannover and GFZ Potsdam.
- Fleddermann, R. et al. (Sept. 2014). “Testing the GRACE follow-on triple mirror assembly”. In: *Classical and Quantum Gravity* 31.19, p. 195004. DOI: [10.1088/0264-9381/31/19/195004](https://doi.org/10.1088/0264-9381/31/19/195004).
- Fox, Richard et al. (2004). *Stable Optical Cavities for Wavelength References*.
- Frappart, Frédéric et al. (May 2018). “Monitoring Groundwater Storage Changes Using the Gravity Recovery and Climate Experiment (GRACE) Satellite Mission: A Review”. In: *Remote Sensing* 10.6, p. 829. DOI: [10.3390/rs10060829](https://doi.org/10.3390/rs10060829).
- Gegout, Pascal et al. (Sept. 1991). “Geodynamic parameters derived from 7 years of laser data on Lageos”. In: *Geophysical Research Letters* 18.9, pp. 1739–1742. DOI: [10.1029/91gl01801](https://doi.org/10.1029/91gl01801).

- Gerberding, Oliver (Feb. 2014). “Phase Readout for Satellite Interferometry”. PhD thesis. Institut für Gravitationsphysik.
- Ghobadi-Far, Khosro et al. (Aug. 2020). “GRACE Follow-On Laser Ranging Interferometer Measurements Uniquely Distinguish Short-Wavelength Gravitational Perturbations”. In: *Geophysical Research Letters* 47.16. DOI: [10.1029/2020gl089445](https://doi.org/10.1029/2020gl089445).
- Ghobadi-Far, Khosro et al. (Feb. 2022). “Along-Orbit Analysis of GRACE Follow-On Inter-Satellite Laser Ranging Measurements for Sub-Monthly Surface Mass Variations”. In: *Journal of Geophysical Research: Solid Earth* 127.2. DOI: [10.1029/2021jb022983](https://doi.org/10.1029/2021jb022983).
- Hall, J.L. et al. (Apr. 1999). “Stabilization and frequency measurement of the I/sub 2/-stabilized Nd:YAG laser”. In: *IEEE Transactions on Instrumentation and Measurement* 48.2, pp. 583–586. DOI: [10.1109/19.769663](https://doi.org/10.1109/19.769663).
- Han, Shin-Chan et al. (Aug. 2006). “Crustal Dilatation Observed by GRACE After the 2004 Sumatra-Andaman Earthquake”. In: *Science* 313.5787, pp. 658–662. DOI: [10.1126/science.1128661](https://doi.org/10.1126/science.1128661).
- Heinzel, G. et al. (2002). “Spectrum and spectral density estimation by the Discrete Fourier transform (DFT), including a comprehensive list of window functions and some new flat-top windows”. In: *Max Planck Society eDoc Server* 395068.0.
- Heinzel, Gerhard et al. (Nov. 2012). “Laser Ranging Interferometer for GRACE Follow-On”. In: *International Conference on Space Optics — ICSO 2012*. Ed. by Errico Armandillo et al. SPIE. DOI: [10.1117/12.2309099](https://doi.org/10.1117/12.2309099).
- Heinzel, Gerhard et al. (Nov. 2020). “Tracking Length and Differential-Wavefront-Sensing Signals from Quadrant Photodiodes in Heterodyne Interferometers with Digital Phase-Locked-Loop Readout”. In: *Physical Review Applied* 14.5, p. 054013. DOI: [10.1103/physrevapplied.14.054013](https://doi.org/10.1103/physrevapplied.14.054013).
- Helleputte, Tom Van et al. (June 2009). “CHAMP and GRACE accelerometer calibration by GPS-based orbit determination”. In: *Advances in Space Research* 43.12, pp. 1890–1896. DOI: [10.1016/j.asr.2009.02.017](https://doi.org/10.1016/j.asr.2009.02.017).
- Intergovernmental Panel on Climate Change (IPCC) (2022). “Sea Level Rise and Implications for Low-Lying Islands, Coasts and Communities”. In: *The Ocean and Cryosphere in a Changing Climate: Special Report of the Intergovernmental Panel on Climate Change*. Cambridge University Press, pp. 321–446. DOI: [10.1017/9781009157964.006](https://doi.org/10.1017/9781009157964.006).
- Jeng, Shie-Chang et al. (Oct. 1998). “Absolute frequencies of the ¹³³CS₂ transitions near 1064 nm”. In: *Optics Communications* 155.4-6, pp. 263–269. DOI: [10.1016/s0030-4018\(98\)00279-x](https://doi.org/10.1016/s0030-4018(98)00279-x).
- Jenkins, G. M. et al. (1968). *Spectral Analysis and Its Applications*. Holden-Day series in time series analysis and digital signal processing. Holden-Day. ISBN: 9780816244645.
- Jiménez Cisneros, B. E. et al. (2014). “Freshwater Resources. Part A: Global and Sectoral Aspects.” Contribution of Working Group II to the Fifth Assessment Report of the Intergovernmental Panel on Climate Change. In: *Climate Change 2014: Impacts, Adaptation, and Vulnerability. Part A: Global and Sectoral Aspects. Contribution of Working Group II to the Fifth Assessment Report of the Intergovernmental Panel on Climate Change*. Ed. by C. B. Field et al. .A: Global and Sectoral Aspects. Cambridge, United Kingdom; New York, NY, USA: Cambridge University Press, pp. 229–269.
- Jin, Shuanggen et al. (Dec. 2013). “Observing and understanding the Earth system variations from space geodesy”. In: *Journal of Geodynamics* 72, pp. 1–10. DOI: [10.1016/j.jog.2013.08.001](https://doi.org/10.1016/j.jog.2013.08.001).
- Johannessen, J. A. et al. (July 2003). “The European Gravity Field and Steady-State Ocean Circulation Explorer Satellite Mission: Its Impact on Geophysics”. In: *Surveys in Geophysics* 24.4, pp. 339–386. DOI: [10.1023/b:geop.0000004264.04667.5e](https://doi.org/10.1023/b:geop.0000004264.04667.5e).
- JPL LRI Team (2018). “LRI Calibration Plan Table v47”.
- Kane, Thomas J. et al. (Feb. 1985). “Monolithic, unidirectional single-mode Nd:YAG ring laser”. In: *Optics Letters* 10.2, p. 65. DOI: [10.1364/ol.10.000065](https://doi.org/10.1364/ol.10.000065).

- Klinger, Beate et al. (Nov. 2016). “The role of accelerometer data calibration within GRACE gravity field recovery: Results from ITSG-Grace2016”. In: *Advances in Space Research* 58.9, pp. 1597–1609. DOI: [10.1016/j.asr.2016.08.007](https://doi.org/10.1016/j.asr.2016.08.007).
- Koch, Alexander (2020). “Link acquisition and optimization for intersatellite laser interferometry”. en. PhD thesis. DOI: [10.15488/9799](https://doi.org/10.15488/9799).
- Koch, Karl-Rudolf (1999). *Parameter Estimation and Hypothesis Testing in Linear Models*. Springer Berlin Heidelberg. DOI: [10.1007/978-3-662-03976-2](https://doi.org/10.1007/978-3-662-03976-2).
- Kochkina, Evgenia (2013). “Stigmatic and Astigmatic Gaussian Beams in Fundamental Mode: Impact of Beam Model Choice on Interferometric Pathlength Signal Estimates”. PhD thesis. Leibniz Universität Hannover.
- Kornfeld, Richard P. et al. (2019). “GRACE-FO: The Gravity Recovery and Climate Experiment Follow-On Mission”. In: *Journal of Spacecraft and Rockets* 56.3, pp. 931–951. DOI: [10.2514/1.A34326](https://doi.org/10.2514/1.A34326).
- Landerer, Felix W. et al. (June 2020). “Extending the Global Mass Change Data Record: GRACE Follow-On Instrument and Science Data Performance”. In: *Geophysical Research Letters* 47.12. DOI: [10.1029/2020gl088306](https://doi.org/10.1029/2020gl088306).
- Langenbach, Harald et al. (June 2005). “Fast steering mirror for laser communication”. In: *Esa Special Publications* 591, pp. 27–33.
- Loth, Sebastian et al. (Jan. 2012). “Bistability in Atomic-Scale Antiferromagnets”. In: *Science* 335.6065, pp. 196–199. DOI: [10.1126/science.1214131](https://doi.org/10.1126/science.1214131).
- LRI Team (n.d.). *Optical Power Budget v19.0*. Tech. rep.
- Luo, Jun et al. (Jan. 2016). “TianQin: a space-borne gravitational wave detector”. In: *Classical and Quantum Gravity* 33.3, p. 035010. DOI: [10.1088/0264-9381/33/3/035010](https://doi.org/10.1088/0264-9381/33/3/035010).
- Luo, Jun et al. (Aug. 2020a). “The first round result from the TianQin-1 satellite”. In: *Classical and Quantum Gravity* 37.18, p. 185013. DOI: [10.1088/1361-6382/aba66a](https://doi.org/10.1088/1361-6382/aba66a).
- Luo, Ziren et al. (July 2020b). “The Taiji program: A concise overview”. In: *Progress of Theoretical and Experimental Physics* 2021.5. DOI: [10.1093/ptep/ptaa083](https://doi.org/10.1093/ptep/ptaa083).
- Ma, Long-Sheng et al. (Dec. 1999). “Ultrasensitive frequency-modulation spectroscopy enhanced by a high-finesse optical cavity: theory and application to overtone transitions of C₂H₂ and C₂HD”. In: *Journal of the Optical Society of America B* 16.12, p. 2255. DOI: [10.1364/josab.16.002255](https://doi.org/10.1364/josab.16.002255).
- Mahrtdt, Christoph (2014). “Laser link acquisition for the GRACE follow-on laser ranging interferometer”. PhD thesis. Leibniz Universität Hannover.
- Massotti, Luca et al. (Oct. 2021). “Next Generation Gravity Mission Elements of the Mass Change and Geoscience International Constellation: From Orbit Selection to Instrument and Mission Design”. In: *Remote Sensing* 13.19, p. 3935. DOI: [10.3390/rs13193935](https://doi.org/10.3390/rs13193935).
- Mathworks, Inc. (Aug. 28, 2023). *fminunc – Documentation*. [Online; accessed 28-August-2023]. URL: <https://de.mathworks.com/help/optim/ug/fminunc.html>.
- Maurer, Richard H. et al. (2008). “Harsh environments : space radiation environment, effects, and mitigation”. In: *Johns Hopkins Apl Technical Digest* 28, pp. 17–29.
- McIntosh, Scott W. et al. (Jan. 2023). “Deciphering solar magnetic activity: The (solar) hale cycle terminator of 2021”. In: *Frontiers in Astronomy and Space Sciences* 10. DOI: [10.3389/fspas.2023.1050523](https://doi.org/10.3389/fspas.2023.1050523).
- Medina, David F. (2015). “Solar Radiation and Spacecraft Shielding”. In: *Handbook of Cosmic Hazards and Planetary Defense*. Springer International Publishing, pp. 295–314. DOI: [10.1007/978-3-319-03952-7_10](https://doi.org/10.1007/978-3-319-03952-7_10).
- Merson, R. H. et al. (Sept. 1958). “Use of Artificial Satellites to Explore the Earth’s Gravitational Field: Results from Sputnik 2 (1957 β)”. In: *Nature* 182.4636, pp. 640–641. DOI: [10.1038/182640a0](https://doi.org/10.1038/182640a0).
- Microchip Technology Inc. (Oct. 6, 2022). *RTG4TM Radiation-Tolerant FPGAs*. URL: <https://www.microchip.com/en-us/products/fpgas-and-plds/radiation-tolerant-fpgas/rtg4-radiation-tolerant-fpgas> (visited on 10/06/2022).

- Misfeldt, Malte (June 2019). “Data Processing and Investigations for the GRACE Follow-On Laser Ranging Interferometer”. MA thesis. Institut für Gravitationsphysik, p. 121. DOI: [10.15488/9639](https://doi.org/10.15488/9639).
- Misfeldt, Malte et al. (June 2023a). “Disturbances from single event upsets in the GRACE follow-on laser ranging interferometer”. In: *Advances in Space Research* 72.6, pp. 2259–2269. DOI: [10.1016/j.asr.2023.06.038](https://doi.org/10.1016/j.asr.2023.06.038).
- Misfeldt, Malte et al. (Jan. 2023b). “Scale Factor Determination for the GRACE Follow-On Laser Ranging Interferometer Including Thermal Coupling”. In: *Remote Sensing* 15.3. ISSN: 2072-4292. DOI: [10.3390/rs15030570](https://doi.org/10.3390/rs15030570).
- Misfeldt, Malte et al. (2023c). “The Triple Mirror Assembly on the GRACE Follow-On Laser Ranging Interferometer”. In: (*in preparation*).
- Morrison, Euan et al. (Aug. 1994). “Automatic alignment of optical interferometers”. In: *Applied Optics* 33.22, pp. 5041–5049. DOI: [10.1364/AO.33.005041](https://doi.org/10.1364/AO.33.005041).
- Müller, Laura (2021). “Generation of Level 1 Data Products and Validating the Correctness of Currently Available Release 04 Data for the GRACE Follow-On Laser Ranging Interferometer”. en. MA thesis. Max Planck Institute for Gravitational Physics. DOI: [10.15488/11818](https://doi.org/10.15488/11818).
- Müller, Vitali (July 2017). “Design Considerations for Future Geodesy Missions and for Space Laser Interferometry”. PhD thesis. Leibniz Universität Hannover. DOI: [10.15488/9029](https://doi.org/10.15488/9029).
- Müller, Vitali et al. (Sept. 2022). “Comparing GRACE-FO KBR and LRI Ranging Data with Focus on Carrier Frequency Variations”. In: *Remote Sensing* 14.17, p. 4335. DOI: [10.3390/rs14174335](https://doi.org/10.3390/rs14174335).
- NASA Space Weather Prediction Center (Apr. 2023). *Solar Cycle Progression*. NASA. (Visited on 04/19/2023).
- NASA/JPL (Sept. 2018). *GRACE-FO Satellite Switching to Backup Instrument Processing Unit*. [Online; accessed 21-May-2019]. URL: <https://gracefo.jpl.nasa.gov/news/139/grace-fo-satellite-switching-to-backup-instrument-processing-unit/>.
- Nicklaus, K. et al. (2017). “Optical bench of the laser ranging interferometer on grace follow-on”. In: *International Conference on Space Optics — ICSO 2014*. Ed. by Zoran Sodnik et al. Vol. 10563. International Society for Optics and Photonics. SPIE, pp. 738–746. DOI: [10.1117/12.2304195](https://doi.org/10.1117/12.2304195).
- Nicklaus, Kolja et al. (June 2020). “Laser metrology concept consolidation for NGGM”. In: *CEAS Space Journal* 12.3, pp. 313–330. DOI: [10.1007/s12567-020-00324-6](https://doi.org/10.1007/s12567-020-00324-6).
- Nicklaus, Kolja et al. (Aug. 2022). “Towards NGGM: Laser Tracking Instrument for the Next Generation of Gravity Missions”. In: *Remote Sensing* 14.16, p. 4089. DOI: [10.3390/rs14164089](https://doi.org/10.3390/rs14164089).
- Olsen, Nils et al. (July 2006). “CHAOS-a model of the Earth’s magnetic field derived from CHAMP, Ørsted, and SAC-C magnetic satellite data”. In: *Geophysical Journal International* 166.1, pp. 67–75. DOI: [10.1111/j.1365-246x.2006.02959.x](https://doi.org/10.1111/j.1365-246x.2006.02959.x).
- Paczkowski, Sarah (2021). “Laser Frequency Stabilisation and Interferometer Path Length Differences during the LISA Pathfinder Satellite Mission”. en. PhD thesis. DOI: [10.15488/11130](https://doi.org/10.15488/11130).
- Pie, N. et al. (Dec. 2021). “Time Variable Earth Gravity Field Models From the First Spaceborne Laser Ranging Interferometer”. In: *Journal of Geophysical Research: Solid Earth* 126.12. DOI: [10.1029/2021jb022392](https://doi.org/10.1029/2021jb022392).
- Pritchard, B.E. et al. (2002). “Radiation effects predicted, observed, and compared for spacecraft systems”. In: *IEEE Radiation Effects Data Workshop*. IEEE. DOI: [10.1109/redw.2002.1045525](https://doi.org/10.1109/redw.2002.1045525).
- Rees, Emily Rose et al. (July 2021). “Absolute frequency readout derived from ULE cavity for next generation geodesy missions”. In: *Optics Express* 29.16, p. 26014. DOI: [10.1364/oe.434483](https://doi.org/10.1364/oe.434483).
- Rees, Emily Rose et al. (June 2022). “Absolute Frequency Readout of Cavity against Atomic Reference”. In: *Remote Sensing* 14.11, p. 2689. DOI: [10.3390/rs14112689](https://doi.org/10.3390/rs14112689).

- Reider, Georg A. (2016). *Photonics*. Springer International Publishing. ISBN: 9783319260761. DOI: [10.1007/978-3-319-26076-1](https://doi.org/10.1007/978-3-319-26076-1).
- Reigber, Ch et al. (Apr. 2003). “The CHAMP-only earth gravity field model EIGEN-2”. In: *Advances in Space Research* 31.8, pp. 1883–1888. DOI: [10.1016/s0273-1177\(03\)00162-5](https://doi.org/10.1016/s0273-1177(03)00162-5).
- Reigber, Christoph (1989). “Gravity field recovery from satellite tracking data”. In: *Theory of Satellite Geodesy and Gravity Field Determination*. Springer-Verlag, pp. 197–234. DOI: [10.1007/bfb0010552](https://doi.org/10.1007/bfb0010552).
- Rohde, Robert A. et al. (Dec. 2020). “The Berkeley Earth Land/Ocean Temperature Record”. In: *Earth System Science Data* 12.4, pp. 3469–3479. DOI: [10.5194/essd-12-3469-2020](https://doi.org/10.5194/essd-12-3469-2020).
- Rubincam, David Parry (Feb. 1984). “Postglacial rebound observed by Lageos and the effective viscosity of the lower mantle”. In: *Journal of Geophysical Research: Solid Earth* 89.B2, pp. 1077–1087. DOI: [10.1029/jb089ib02p01077](https://doi.org/10.1029/jb089ib02p01077).
- Rummel, R. et al. (Jan. 2002). “Dedicated gravity field missions—principles and aims”. In: *Journal of Geodynamics* 33.1-2, pp. 3–20. DOI: [10.1016/s0264-3707\(01\)00050-3](https://doi.org/10.1016/s0264-3707(01)00050-3).
- Rummel, Reiner (Feb. 2020). “Earth’s gravity from space”. In: *Rendiconti Lincei. Scienze Fisiche e Naturali* 31.S1, pp. 3–13. DOI: [10.1007/s12210-020-00889-8](https://doi.org/10.1007/s12210-020-00889-8).
- Samwel, Susan W. et al. (July 2019). “Space radiation impact on smallsats during maximum and minimum solar activity”. In: *Advances in Space Research* 64.1, pp. 239–251. DOI: [10.1016/j.asr.2019.03.025](https://doi.org/10.1016/j.asr.2019.03.025).
- Sanjuan, Jose et al. (Jan. 2021). “Simultaneous laser frequency stabilization to an optical cavity and an iodine frequency reference”. In: *Optics Letters* 46.2, p. 360. DOI: [10.1364/ol.413419](https://doi.org/10.1364/ol.413419).
- Sanjuan, Josep et al. (Nov. 2019). “Long-term stable optical cavity for special relativity tests in space”. In: *Optics Express* 27.25, p. 36206. DOI: [10.1364/oe.27.036206](https://doi.org/10.1364/oe.27.036206).
- Schuldt, Thilo et al. (Jan. 2017). “Development of a compact optical absolute frequency reference for space with 1e-15 instability”. In: *Applied Optics* 56.4, p. 1101. DOI: [10.1364/ao.56.001101](https://doi.org/10.1364/ao.56.001101).
- Schuster, Sönke et al. (Feb. 2015). “Vanishing tilt-to-length coupling for a singular case in two-beam laser interferometers with Gaussian beams”. In: *Applied Optics* 54.5, p. 1010. DOI: [10.1364/ao.54.001010](https://doi.org/10.1364/ao.54.001010).
- Schwabe, Heinrich et al. (1844). “Sonnen-Beobachtungen im Jahre 1843”. In: *Astronomische Nachrichten* 21.15, pp. 234–235. DOI: [10.1002/asna.18440211505](https://doi.org/10.1002/asna.18440211505).
- Schwarze, Thomas S. (2018). “Phase extraction for laser interferometry in space : phase readout schemes and optical testing”. en. PhD thesis. DOI: [10.15488/4233](https://doi.org/10.15488/4233).
- Sheard, B. S. et al. (Dec. 2012). “Intersatellite laser ranging instrument for the GRACE follow-on mission”. In: *Journal of Geodesy* 86.12, pp. 1083–1095. ISSN: 1432-1394. DOI: [10.1007/s00190-012-0566-3](https://doi.org/10.1007/s00190-012-0566-3).
- Shiozawa, Toshiyuki (2004). *Classical Relativistic Electrodynamics*. Springer Berlin Heidelberg. DOI: [10.1007/978-3-662-06261-6](https://doi.org/10.1007/978-3-662-06261-6).
- Shirley, Jon H. (Nov. 1982). “Modulation transfer processes in optical heterodyne saturation spectroscopy”. In: *Optics Letters* 7.11, p. 537. DOI: [10.1364/ol.7.000537](https://doi.org/10.1364/ol.7.000537).
- Spero, Robert (Mar. 2021). “Point-mass sensitivity of gravimetric satellites”. In: *Advances in Space Research* 67.5, pp. 1656–1664. DOI: [10.1016/j.asr.2020.12.019](https://doi.org/10.1016/j.asr.2020.12.019).
- Tapley, B. D. et al. (2003). “Large scale ocean circulation from the GRACE GGM01 Geoid”. In: *Geophysical Research Letters* 30.22. DOI: [10.1029/2003GL018622](https://doi.org/10.1029/2003GL018622).
- Tapley, B. D. et al. (2004). “The gravity recovery and climate experiment: Mission overview and early results”. In: *Geophysical Research Letters* 31.9. DOI: [10.1029/2004GL019920](https://doi.org/10.1029/2004GL019920).
- Tapley, Byron D. et al. (Apr. 2019). “Contributions of GRACE to understanding climate change”. In: *Nature Climate Change* 9.5, pp. 358–369. DOI: [10.1038/s41558-019-0456-2](https://doi.org/10.1038/s41558-019-0456-2).
- Thompson, R. et al. (May 2011). “A flight-like optical reference cavity for GRACE follow-on laser frequency stabilization”. In: *Joint Conference of the IEEE International Frequency Control and the European Frequency and Time Forum (FCS) Proceedings*. IEEE. DOI: [10.1109/fcs.2011.5977873](https://doi.org/10.1109/fcs.2011.5977873).

- Tröbs, Michael et al. (Jan. 12, 2007). *LTP reference laser unit engineering model frequency hops (S2-AEI-TN-3036)*. Tech. rep. Max-Planck Institute for Gravitational Physics (Albert-Einstein-Institute).
- Van Allen, James A. (1959). “Radiation Belts around the Earth”. In: *Scientific American* 200.3, pp. 39–47. ISSN: 00368733, 19467087.
- Velicogna, Isabella et al. (Apr. 2020). “Continuity of Ice Sheet Mass Loss in Greenland and Antarctica From the GRACE and GRACE Follow-On Missions”. In: *Geophysical Research Letters* 47.8. DOI: [10.1029/2020gl087291](https://doi.org/10.1029/2020gl087291).
- Wand, Vinzenz et al. (2006). “LISA Phasemeter development”. In: *AIP Conference Proceedings*. AIP. DOI: [10.1063/1.2405118](https://doi.org/10.1063/1.2405118).
- Wang, Changqing et al. (July 2015). “Monthly gravity field recovery from GRACE orbits and K-band measurements using variational equations approach”. In: *Geodesy and Geodynamics* 6.4, pp. 253–260. DOI: [10.1016/j.geog.2015.05.010](https://doi.org/10.1016/j.geog.2015.05.010).
- Wanner, Gudrun et al. (May 2014). “Analytical description of interference between two misaligned and mismatched complete Gaussian beams”. In: *Applied Optics* 53.14, p. 3043. DOI: [10.1364/ao.53.003043](https://doi.org/10.1364/ao.53.003043).
- Ware, B. et al. (2006). “Phase Measurement System for Inter-Spacecraft Laser Metrology”. In: *Earth Science Technology Conference ESTC*.
- Webb, Frank et al. (2018). *GRACE FO SDS Newsletter No. 1. Report: Oct-Nov 2018 (No. 1)*. [Online; accessed 22-June-2019]. URL: https://media.gfz-potsdam.de/gfz/sec12/pdf/GRACE_FO_SDS_NL_11_2018.pdf.
- Webb, Frank et al. (2019a). *GRACE FO SDS Newsletter No. 11. Report: Jan 2020 (No. 11)*. [Online; accessed 05-July-2023]. URL: https://www.gfz-potsdam.de/fileadmin/gfz/sec12/pdf/GRACE-FO/GRACE_FO_SDS_newsletter_No11.pdf.
- Webb, Frank et al. (2019b). *GRACE FO SDS Newsletter No. 3. Report: Apr-May 2019 (No. 3)*. [Online; accessed 05-July-2023]. URL: https://media.gfz-potsdam.de/gfz/sec12/pdf/GRACE_FO_SDS_NL_11_2018.pdf.
- Wegener, Henry et al. (July 2020). “Tilt-to-Length Coupling in the GRACE Follow-On Laser Ranging Interferometer”. In: *Journal of Spacecraft and Rockets*, pp. 1–10. DOI: [10.2514/1.a34790](https://doi.org/10.2514/1.a34790).
- Wegener, Henry Paul (2022). “Analysis of tilt-to-length coupling in the GRACE follow-on laser ranging interferometer”. en. PhD thesis. Institut für Gravitationsphysik. DOI: [10.15488/11984](https://doi.org/10.15488/11984).
- Wen, Hui Ying (July 20, 2020). *GRACE-FO L1 Release Notes*. Ed. by Hui Ying Wen. Jet Propulsion Laboratory.
- Wen, Hui Ying et al. (Nov. 2019). *GRACE-FO Level-1 Data Product User Handbook*. JPL D-56935, Version of September 11, 2019. Jet Propulsion Laboratory.
- Wiese, D. (Jan. 2011). “Optimizing Two Pairs of GRACE-like Satellites for Recovering Temporal Gravity Variations”. In.
- Wiese, David et al. (Mar. 2021). “The NASA Mass Change Designated Observable Study: Progress and Future Plans”. In: *Proceedings of the EGU General Assembly 2021*. Copernicus GmbH. DOI: [10.5194/egusphere-egu21-8088](https://doi.org/10.5194/egusphere-egu21-8088).
- Willke, B. et al. (July 2000). “Frequency stabilization of a monolithic Nd:YAG ring laser by controlling the power of the laser-diode pump source”. In: *Optics Letters* 25.14, p. 1019. DOI: [10.1364/ol.25.001019](https://doi.org/10.1364/ol.25.001019).
- Windisch, Steve et al. (Apr. 2, 2007). *Interface description for LTP RLU EM*. Tech. rep. LTP- TESAT-SPE-0091. TESAT-Spacecom. 24 pp.
- WMO (2021). *2021 State of Climate Services: Water*. en.
- Wörner, Lisa et al. (Jan. 2023). “MaQuIs - Mars Quantum Gravity Mission”. In: DOI: [10.22541/essoar.167397424.46877056/v1](https://doi.org/10.22541/essoar.167397424.46877056/v1).
- Wouters, Bert et al. (May 2019). “Global Glacier Mass Loss During the GRACE Satellite Mission (2002-2016)”. In: *Frontiers in Earth Science* 7. DOI: [10.3389/feart.2019.00096](https://doi.org/10.3389/feart.2019.00096).

- Wu, Yue-Liang et al. (Feb. 2021). “China’s first step towards probing the expanding universe and the nature of gravity using a space borne gravitational wave antenna”. In: *Communications Physics* 4.1. DOI: [10.1038/s42005-021-00529-z](https://doi.org/10.1038/s42005-021-00529-z).
- Xiao, Yun et al. (Mar. 2023). “Performance and application of the Chinese satellite-to-satellite tracking gravimetry system”. In: *Chinese Science Bulletin*. DOI: [10.1360/tb-2022-1057](https://doi.org/10.1360/tb-2022-1057).
- Yan, Yihao et al. (Apr. 2021). “Revisiting the light time correction in gravimetric missions like GRACE and GRACE follow-on”. In: *Journal of Geodesy* 95.5. DOI: [10.1007/s00190-021-01498-5](https://doi.org/10.1007/s00190-021-01498-5).
- Ye, Jun et al. (July 1996). “Sub-Doppler optical frequency reference at 1064 μm by means of ultrasensitive cavity-enhanced frequency modulation spectroscopy of a C_2HD overtone transition”. In: *Optics Letters* 21.13, p. 1000. DOI: [10.1364/ol.21.001000](https://doi.org/10.1364/ol.21.001000).
- Yoder, C. F. et al. (June 1983). “Secular variation of Earth’s gravitational harmonic J2 coefficient from Lageos and nontidal acceleration of Earth rotation”. In: *Nature* 303.5920, pp. 757–762. DOI: [10.1038/303757a0](https://doi.org/10.1038/303757a0).
- Zuber, Maria T. et al. (Feb. 2013). “Gravity Field of the Moon from the Gravity Recovery and Interior Laboratory (GRAIL) Mission”. In: *Science* 339.6120, pp. 668–671. DOI: [10.1126/science.1231507](https://doi.org/10.1126/science.1231507).

Acknowledgements

When I started studying physics back in 2013, I was always asked “What are you going to work afterwards?” and my usual answer was: “Everything is possible. My primary goal is a PhD”. Now, ten years later, this is about to happen, and it makes me feel proud. However, this would not have been possible without many people’s support.

A big thank you to Karsten Danzmann for creating such a wonderful institute with uncounted possibilities to conduct interesting research at the quantum frontier, develop personally, and satisfy my curiosity.

To Gerhard Heinzl, I greatly respect your inexhaustible knowledge, comprehension, and unbroken motivation, even if your work drifts increasingly into bureaucracy. Thanks for the exciting discussions, drinks in the park, and trips to China.

And to Vitali Müller, your open-minded way of leading the LRI activities is an inspiration. I enjoy working with you every day, all the numerous trips around the world that we shared, and that you are smiling and laughing every day.

I feel honored that Torsten Mayer-Gürr and Kirk McKenzie are the referees for my thesis. Furthermore, thanks to Klemens Hammerer for being the chair of my defense. In this context, I’d also like to thank Birgit Ohlendorf for her support in fighting the bureaucratic aspects of a PhD. Another thank you to all the colleagues who read parts of this thesis, had many valuable comments, and found even more stupid typos.

All of my work was also greatly supported by Laura Müller, who is doing great in implementing our groups’ findings into the AEI-LRI1B data product. Also, thanks to all current and former members of our LRI group.

I am also grateful to the LRI team at the JPL for their professional cooperation and regular fruitful discussions. A special thanks to the GRACE-FO TPM study team around Frank Flechtner for the always nice and friendly meetings, discussions, and laughter at Oberpfaffenhofen, Potsdam, and at ESTEC.

To all the ones I met and made friends with at the numerous conferences I attended.

Despite that freaking Covid situation over large parts of my PhD, I had a great time working at the AEI, which is only possible with all the lovely colleagues, e. g., the Kranoleum and Mensa groups, the “AEI crew”, the AEI/IQO soccer team, the IWOS-CIA, the Christmas Band and many more. Among these people, a special thanks goes to Joscha Heinze and Marie-Sophie Dorothee Hartig for withstanding the lockdowns with a good TV show and lots of hiking activities. I also would like to thank Pascal Andreas Grafe for the late-night after-work drinks and discussions about phasemeters and sail-trimming. Lastly, thanks to Nina and Christoph Heimo Bode for pushing me toward Roundnet.

Third thesis, third acknowledgment: My Bachelor and Master studies would not have been possible without the Grøbe. Ist das jetzt ein bisschen klar g’worden, ja?

I owe deep gratitude to my friends and family outside of academia. Although I am very much into my research and spend a lot of time with it, I always enjoy every minute with you.

Last but not least, Norina, thank you for your love, support, and your way of seeing the world. I really look forward to our loooong vacation!